

REPORT DOCUMENTATION PAGE			Form Approved OMB No. 0704-0188	
Public reporting burden for this collection of information is estimated to average 1 hour per response, including the time for reviewing instructions, searching existing data sources, gathering and maintaining the data needed, and completing and reviewing this collection of information. Send comments regarding this burden estimate or any other aspect of this collection of information, including suggestions for reducing this burden to Department of Defense, Washington Headquarters Services, Directorate for Information Operations and Reports (0704-0188), 1215 Jefferson Davis Highway, Suite 1204, Arlington, VA 22202-4302. Respondents should be aware that notwithstanding any other provision of law, no person shall be subject to any penalty for failing to comply with a collection of information if it does not display a currently valid OMB control number. PLEASE DO NOT RETURN YOUR FORM TO THE ABOVE ADDRESS.				
1. REPORT DATE (DD-MM-YYYY) 09-04-2012		2. REPORT TYPE Final		3. DATES COVERED (From - To) Feb. 1, 2009-Nov. 30, 2011
4. TITLE AND SUBTITLE Advanced Concurrent-Multiband, Multibeam, Aperture-Synthesis with Intelligent Processing for Urban Operation Sensing			5a. CONTRACT NUMBER FA9550-09-1-0104	
			5b. GRANT NUMBER	
			5c. PROGRAM ELEMENT NUMBER	
6. AUTHOR(S) Cam Nguyen			5d. PROJECT NUMBER	
			5e. TASK NUMBER	
			5f. WORK UNIT NUMBER	
7. PERFORMING ORGANIZATION NAME(S) AND ADDRESS(ES) Texas Engineering Experiment Station 1470 William D Fitch Pky College Station, TX 77845- 4645			8. PERFORMING ORGANIZATION REPORT NUMBER	
9. SPONSORING / MONITORING AGENCY NAME(S) AND ADDRESS(ES) AFOSR 875 N. Randolph St. Suite 325, Room 3112 Arlington, VA 22203			10. SPONSOR/MONITOR'S ACRONYM(S) AFOSR	
			11. SPONSOR/MONITOR'S REPORT NUMBER(S) AFRL-OSR-VA-TR-2012-1147	
12. DISTRIBUTION / AVAILABILITY STATEMENT Distribution A: Approved for Public Release				
13. SUPPLEMENTARY NOTES				
14. ABSTRACT Sensor Hardware: Basic hardware research for concurrent dual-band dual-polarization radar was conducted, resulting in various novel architectures with unprecedented performance. The system is designed using a 0.18-μm SiGe BiCMOS process in single chips and is extremely small. The entire system is estimated to have a size of only 12mmx8mm and 5cmx5cm without and with 6-element antenna array, respectively. Various components and subsystems, e.g., the concurrent dual-band transmitter and tri-band tri-output synthesizer, have been completely developed or designed with unprecedented performance. Signal Processing and Software: The research and development of signal processing and software for the multiband sensor was completed. New hardware (HW) software (SW) codesign paradigm was developed for the purposes of adaptive processing of cross-polarization sensor data obtained from multiple sensor modalities aimed at collaborative high-resolution sensing, detection, localization and identification of point-type and distributed targets in urban environments. The unified HW/SW codesign techniques capable of operation in uncertain operational scenarios for a variety of admissible sensor array configurations outperform the existing adaptive radar imaging algorithms both in resolution and convergence rate. The elaborated "Virtual Remote Sensing Laboratory" SW was integrated with the prospective synthesized simulated sensor HW model for demonstration of the superior capabilities of the overall prospective multimode sensor system via extensive simulation studies.				
15. SUBJECT TERMS Multiband radar, multiband sensor				
16. SECURITY CLASSIFICATION OF:			17. LIMITATION OF ABSTRACT UU	18. NUMBER OF PAGES 199
a. REPORT U	b. ABSTRACT U	c. THIS PAGE U		
				19b. TELEPHONE NUMBER (include area code) 979-845-7469

EXECUTIVE SUMMARY

1. Performance

A. Sensor Hardware

The architecture and specifications for the concurrent dual-band multi-channel dual-polarization 24.5/35 GHz radar system have been developed and analyzed. The system is designed using Jazz 0.18- μm SiGe BiCMOS process in single chips and is extremely small. The entire system is estimated to have a size of only 12mmx8mm without the antenna array. With the 6-element antenna array, the complete chip is about 5cmx5cm. This radar system, once fully developed, is the first ever-developed millimeter-wave concurrent dual-band multi-channel dual-polarization radar system on SiGe BiCMOS. Various components and subsystems of the system have been completely developed or designed and scheduled for fabrication.

Transmitter (TX): All the components of the concurrent dual-band 24.5/35 GHz TX have been developed with unprecedented performance, and the complete TX has been designed and is currently being fabricated using Jazz 0.18- μm SiGe BiCMOS process.

Receiver (RX): Several components of the concurrent dual-band 24.5/35 GHz RX have been developed with unprecedented performance. A concurrent dual-band 24.5/35 GHz RX has been designed using Jazz 0.18- μm SiGe BiCMOS process and scheduled for fabrication.

Antenna Array: The concurrent dual-band dual-polarization 24.5/35 GHz antenna array have been designed using multi-layer liquid crystal polymer (CLP) substrates and scheduled for fabrication.

TR/CAL Switch and Attenuator: The concurrent dual-band dual-polarization transmit-receive/calibration (TR/CAL) switch has been designed using Jazz 0.18- μm SiGe BiCMOS process and scheduled for fabrication. The attenuator across 10-43 GHz has been developed using Jazz 0.18- μm SiGe BiCMOS process with unprecedented performance.

Synthesizer: All components of the synthesizer and the complete synthesizer have been developed using Jazz 0.18- μm CMOS process with unprecedented performance.

B. Sensor Signal Processing and Software

The research and development of signal processing and software for the proposed sensor has been completed. New hardware (HW) software (SW) codesign paradigm was developed for the purposes of adaptive processing of cross-polarization sensor data obtained from multiple sensor modalities aimed at collaborative high-resolution sensing, detection, localization and identification of point-type and distributed targets in urban environments. The unified HW/SW codesign techniques capable to operate in uncertain operational scenarios for a variety of admissible sensor array configurations outperform the existing adaptive radar imaging algorithms both in resolution and convergence rate. The elaborated “Virtual Remote Sensing Laboratory” SW was integrated with the prospective synthesized simulated sensor HW model for

demonstration of the superior capabilities of the overall prospective multimode sensor system via extensive simulation studies.

C. Comments

The proposed concurrent dual-band multi-channel dual-polarization 24.5/35 GHz radar system on single silicon chip is very complex. Its design is extremely challenging and the development of this radar integrating hardware and software requires significant efforts with substantial funding. Although we are not able to finish this project within 32 months, as can be seen in this report, we have made considerable progress and achieved significant milestones in this research during this duration, from developing novel hardware to innovative signal processing. During this research, significant delays have been encountered due to unexpected (and out of our control) delays by an outside CMOS foundry that fabricated the circuits.

The proposed system including hardware and software would represent the first millimeter-wave concurrent multiband multi-polarization radar in fully integrated SiGe BiCMOS chips for military applications, and we believe that its contribution is enormous for the DoD missions. With the significant efforts and achievement we have made during the past 32 months, this research should be continued to fully develop the system.

2. PhD Dissertations

Two PhD students are currently completing their research and dissertations under this project. They are scheduled to defend the following dissertations in May and Aug. 2012:

Sanghun Lee (May 2012): A Fully Integrated Concurrent Multi-Band Multi-Output CMOS Synthesizer for Multi-Band Microwave Systems

Various components and the entire concurrent tri-band 3.5/7/21 GHz synthesizer have been developed using 0.18- μm CMOS process to support the proposed system. These components and the synthesizer were implemented with novel architectures and represent the state of the art with unprecedented performance. This synthesizer has a size of only 1.9mmx0.94mm and is the first fully integrated CMOS synthesizer that provides concurrent tri-band tri-output using a single VCO and a single frequency divider with enhanced and tunable locking range, and enhanced 2nd harmonic suppression.

Cuong Huynh (Aug. 2012): Research and Development of a Concurrent Dual-Band SiGe BiCMOS Millimeter-Wave Transmitter for Radar, Sensing and Communication Systems

The concurrent dual-band 24.5/35 GHz transmitter and constituent components have been developed using 0.18- μm SiGe BiCMOS process. They were realized with novel architectures and represent the state of the art with unprecedented performance. The total size for this TX is only 2mmx4.5mm. This is the first ever-developed millimeter-wave concurrent dual-band TX on SiGe BiCMOS.

3. Patent Application

C. Huynh and C. Nguyen, “Ultra-High-Isolation Switches for RF Communication and Radar Systems,” Patent Application, 2011.

4. People Involved and Publications

Professor C. Nguyen, Professor Y. Shkvarko, PhD students: Sanghun Lee, Cuong Huynh, Jaeyoung Lee, Juseok Bae, Donghyun Lee.

Journal Publications and Submission:

1. C. Huynh and C. Nguyen, “New Ultra-High-Isolation RF Switch Architecture and Its Use for a 10-38 GHz 0.18- μ m BiCMOS Ultra-Wideband Switch,” *IEEE Trans. on Microwave Theory and Techniques*, Vol. MTT-59, Feb. 2011, pp. 345-353.
2. S. Lee, S. Jang and C. Nguyen, “Low-Power-Consumption Wide-Locking-Range Dual-Injection-Locked $\frac{1}{2}$ Divider through Simultaneous Optimization of VCO Loaded Q and Current,” Submitted to *IEEE Trans. on Microwave Theory and Techniques*.
3. S. Lee and C. Nguyen, “Self-Injection-Locked 0.18- μ m BiCMOS 1/3 Frequency Divider with Improved Locking Range, Phase Noise and Sensitivity,” Submitted to *IEEE Microwave and Wireless Components Letters*.
4. S. Lee, S. Jang and C. Nguyen, “New Divide-by-3 Injection-Locked Frequency Divider Utilizing Self-Injection Technique for Locking Range Enhancement,” Submitted to *IEEE Microwave and Wireless Components Letters*.
5. C. Huynh and C. Nguyen, “Design of a 0.18- μ m SiGe BiCMOS 25/37-GHz Concurrent Dual-Band Power Amplifier Using Synthetic Impedance Matching Network,” Submitted to *IEEE Trans. on Microwave Theory and Techniques*.
6. S. Lee and C. Nguyen, “A Fully Integrated Concurrent Multiband Multi-Output Phase-Locked Loop with Enhanced and Tunable Locking Range for Concurrent Multiband Microwave Systems,” Submitted to *IEEE Trans. on Microwave Theory and Techniques*.
7. C. Huynh and C. Nguyen, “A 0.18- μ m SiGe BiCMOS 35-GHz RF-Pulse Former for Short-Range High-Data-Rate Communication and High-Resolution Radar Systems,” To be submitted to *IEEE Microwave and Wireless Components Letters*.
8. C. Huynh and C. Nguyen, “An Ultra-Wideband Microwave/Millimeter-Wave 0.18- μ m SiGe BiCMOS Active Balun,” To be submitted to *IEEE Microwave and Wireless Components Letters*.

9. C. Huynh and C. Nguyen, "An Ultra-High-Isolation 0.18- μm SiGe BiCMOS 22-29 GHz T/R Module Including Power and Low-Noise Amplifiers for Communications and Radar," To be submitted to *IEEE Trans. on Microwave Theory and Techniques*.
10. C. Huynh and C. Nguyen, "On the Design and Development of a Fully Integrated SiGe BiCMOS Concurrent Dual-Band Dual-Mode K/Ka-Band Transmitter for Multiband Radar and Communication Systems," To be submitted to *IEEE Trans. on Microwave Theory and Techniques*.
11. J. Bae and C. Nguyen, "A 0.18- μm SiGe BiCMOS 10-67 GHz Switch-Attenuator with High Switching Isolation and Large Attenuation Range," To be submitted to *IEEE Trans. on Microwave Theory and Techniques*.
12. J. Lee and C. Nguyen, "Design of a 0.18- μm SiGe BiCMOS Concurrent Tri-Band Low-Noise Amplifier for Multiband Ku/K/Ka-Band Radar Systems," To be submitted to *IEEE Trans. on Microwave Theory and Techniques*.
13. Castillo-Atoche A., Shkvarko Y.V., Torres-Roman D., and Perez-Meana H., "Convex Regularization-Based Hardware/Software Co-design for Real-Time Enhancement of Remote Sensing Imagery", *Journal of Real Time Image Processing*, USA, Vol. 2009, No. 4, DOI 10.1007/s 11554-009-0115-3, pp. 261-272, 2009.
14. Castillo-Atoche A., Torres-Roman D., and Shkvarko Y.V., "Reconfigurable Architecture of Systolic Array Processors for Real Time Remote Sensing Image Enhancement/ Reconstruction", *WSEAS Transactions on Signal Processing*, Vol. 5, No. 8, pp. 293–303, 2009.
15. Shkvarko Y.V., "Unifying Experiment Design and Convex Regularization Techniques for Enhanced Imaging With Uncertain Remote Sensing Data---Part I: Theory", *IEEE Transactions on Geoscience and Remote Sensing*, Vol. 48, No. 1, pp. 82–95, Jan 2010.
16. Shkvarko Y.V., "Unifying Experiment Design and Convex Regularization Techniques for Enhanced Imaging With Uncertain Remote Sensing Data---Part II: Adaptive Implementation and Performance Issues", *IEEE Transactions on Geoscience and Remote Sensing*, Vol. 48, No. 1, pp. 96–111, Jan 2010.
17. Castillo-Atoche A., Torres-Roman D., and Shkvarko Y.V., "Experiment Design Regularization-Based Hardware/Software Codesign for Real-Time Enhanced Imaging in Uncertain Remote Sensing Environment", *EURASIP Journal on Advances in Signal Processing*, Vol. 2010, Article ID 254040, pp. 1–21, 2010.
18. Castillo-Atoche A., Torres-Roman D., and Shkvarko Y.V., "Towards Real Time Implementation of Reconstructive Signal Processing Algorithms Using Systolic Array Coprocessors", *Journal of Systems Architecture*, Vol. 56 (2010), pp. 327–339, 2010.

19. Shkvarko Y.V., Tuxpan J., and Santos S.R., "Dynamic Experiment Design Regularization Approach to Adaptive Imaging with Array Radar/SAR Systems", *Sensors*, Vol. 2011, No. 11, pp. 4483-4511, 2011.
20. Shkvarko Y.V., Santos S.R., and Tuxpan J., "Resolution Enhanced Radar/SAR Imaging: An Experiment Design Framework Combined With Neural Network-Adapted Variational Analysis Regularization", *EURASIP Journal of Advances in Signal Processing*, Vol. 2011, In press, pp. 1-16, 2011.

Conference Presentations:

1. C. Huynh and C. Nguyen, "Ultra-Broadband 0.18- μm BiCMOS Active Baluns for Extremely Wideband RF Applications," 2011 IEEE International Symposium on Antennas and Propagation, Spokane, Washington, July 2011.
2. C. Huynh and C. Nguyen, "Ultra-High-Isolation BiCMOS Switch for Extremely Wideband Microwave and Millimeter-Wave Systems," 36th International Conf. on Infrared, Millimeter, and Terahertz Waves, Houston, Texas, Oct. 2011.
3. S. Lee and C. Nguyen, "0.18- μm BiCMOS Divide-by-3 Injection-Locked Frequency Divider Implementing Phase Tuning for Enhanced Locking Range," 2012 Symposium on Wireless and Microwave Circuits and Systems, Waco, Texas, Mar. 2012.
4. S. Lee and C. Nguyen, "A Self-Injection-Locked 0.18- μm BiCMOS 1/3 Frequency Divider with Improved Locking Range, Phase Noise and Sensitivity," 2012 Symposium on Wireless and Microwave Circuits and Systems, Waco, Texas, Mar. 2012.
5. S. Lee and C. Nguyen, "Low-Power Wide-Locking-Range Dual-Injection-Locked 0.18- μm BiCMOS 1/2 Divider with Simultaneous Optimization of VCO Loaded Q and Current," 2012 Symposium on Wireless and Microwave Circuits and Systems, Waco, Texas, Mar. 2012.
6. C. Huynh and C. Nguyen, "An Ultra-Broadband 0.18- μm BiCMOS Active Balun," 2012 Symposium on Wireless and Microwave Circuits and Systems, Waco, Texas, Mar. 2012.
7. C. Huynh and C. Nguyen, "An Ultra-High-Isolation, Ultra-Wide-Band Microwave and Millimeter-Wave BiCMOS Switch," 2012 Symposium on Wireless and Microwave Circuits and Systems, Waco, Texas, Mar. 2012.
8. J. Lee and C. Nguyen, "SiGe BiCMOS Concurrent Dual-band LNAs with Integrated Notch Filter," 2012 Symposium on Wireless and Microwave Circuits and Systems, Waco, Texas, Mar. 2012.
9. Shkvarko Y. and Castillo-Atoche A., "Descriptive Experiment Design Unified with Convex Regularization for High-Resolution Radar/SAR Imaging", 2009 International Radar Symposium (IRS 2009), Hamburg, Germany, pp. 763-768, Sep. 2009.

10. Castillo-Atoche A., Torres-Roman D., and Shkvarko Y., "Reconfigurable Architecture of Systolic Array processors for Remote Sensing Applications", 2009 9th WSEAS Intern. Conference on Signal Speech and Image Processing (SSIP'09), Budapest, Hungary, ISBN: 978-960-474-114-4, pp. 162-167, Sep. 2009.
11. Shkvarko Y., Tuxpan J., and Santos S., "Near Real Time Enhancement of Fractional SAR Imagery Based on Robust Descriptive Experiment Design Regularization Framework", 2010 8th European Conference on Synthetic Aperture Radar (EUSAR'2010), Aachen, Germany, ISBN: 978-8007-3272-2, pp. 24-27, June 2010.
12. Shkvarko Y. and Espadas V.E., "Experiment Design Framework for Super-High Resolution Imaging With the GOESTAR Configured Sensor Array Data", 2010 International Kharkov Symposium on Physics and Engineering of Microwaves, Millimeter and Submillimeter Waves (MSMW'2010), Kharkov, Ukraine, ISBN: 978-1-4244-7898-9, 3 pp., June 2010.
13. Shkvarko Y., Tuxpan J., Santos S., "Aggregated Convex Regularization and Variational Analysis Technique for Enhancement of MM Waveband Remote Sensing Imagery", International Symposium MSMW'2010, Kharkov, Ukraine, ISBN: 978-1-4244-7898-9, 3pp., June 2010.
14. Shkvarko Y., Castillo B., Tuxpan J., and Castro D., "High-Resolution Radar/SAR Imaging: An Experiment design Framework Combined With Variational Analysis Regularization", WORLDCOMP'2011: The 11th Int. Conf. on Image Processing, Computer Vision and Pattern Recognition (IPCV'11), Las Vegas, USA, Vol. IPCV-II, pp. 652-658., July 2011.
15. Shkvarko Y., Tuxpan J., and Castro D., "Bayesian Dynamic Experiment Design Regularization Framework for High-Resolution Radar/SAR Imaging", International Radar Symposium (IRS'2011), Leipzig, Germany, pp. 359-364, Sept. 2011.
16. Shkvarko Y.V., Santos S.R., Tuxpan J., and Espadas V.E., "Modified Hopfield Neural Network Computational Technique for Real-Time Enhancement of Multimode Radar/SAR Imagery", International Radar Symposium (IRS'2011), Leipzig, Germany, pp. 385-390, Sept. 2011.
17. Shkvarko Y.V., Espadas V.E., and Castro D.E., "Descriptive Experiment Design Optimization of GeoSTAR Configured Multisensor Imaging Radar", 4th International Radio Electronics Forum (4th IREF'2011), Kharkov, Ukraine, Vol. I, pp. 76-81, Oct. 2011.

1. PROJECT OBJECTIVE

This project aims to conduct basic research and development of a novel compact, low-cost, multi-polarization, multi-band multi-sensor synthetic aperture radar (SAR) array accompanied by an innovative intelligent signal processing and software for accurate sensing of ground moving targets in urban environments and structures in real time. The project consists of two major tasks. The Sensor Hardware integrates electrically two modalities in K and Ka band allowing them to function together concurrently as a single sensor over multiband. The hardware will be realized using low-cost miniature RF integrated circuits, making feasible distributions of large array of sensors “covertly” over many places such as buildings or installation in moveable platforms like UAV for cost-effective, wireless sensing and surveillance. The Signal Processing and Software addresses both collaborative remote sensing and distributed sensor network data acquisition capable of intelligent processing and information fusion from properly selected different mobile and locally distributed modalities and data for speedy search, discovery, identification and mapping of multiple and distributed targets in complex urban environments and structures with low false alarm rates.

2. PERFORMANCE

The performance in this project is described in two parts according to the tasks conducted in this research:

Part A - Research and Development of Sensor Hardware

Part B - Research and Development of Signal Processing and Software

PART A – RESEARCH AND DEVELOPMENT OF SENSOR HARDWARE

Summary of Performance:

The architecture and specifications for the concurrent dual-band multi-channel dual-polarization 24.5/35 GHz radar system have been developed and analyzed. The system is designed using Jazz 0.18- μm SiGe BiCMOS process in single chips and is extremely small. The entire system is estimated to have a size of only 12mmx8mm without the antenna array. With the 6-element antenna array, the complete chip is about 5cmx5cm. This radar system, once fully developed, is the first ever-developed millimeter-wave concurrent dual-band multi-channel dual-polarization radar system on SiGe BiCMOS. Various components and subsystems of the system have been completely developed or designed and scheduled for fabrication.

Transmitter (TX): All the components of the concurrent dual-band 24.5/35 GHz TX have been developed with unprecedented performance, and the complete TX has been designed and is currently being fabricated using Jazz 0.18- μm SiGe BiCMOS process.

Receiver (RX): Several components of the concurrent dual-band 24.5/35 GHz RX have been developed with unprecedented performance. A concurrent dual-band 24.5/35 GHz RX has been designed using Jazz 0.18- μm SiGe BiCMOS process and scheduled for fabrication.

Antenna Array: The concurrent dual-band dual-polarization 24.5/35 GHz antenna array have been designed using multi-layer liquid crystal polymer (CLP) substrates and scheduled for fabrication.

TR/CAL Switch and Attenuator: The concurrent dual-band dual-polarization transmit-receive/calibration (TR/CAL) switch has been designed using Jazz 0.18- μm SiGe BiCMOS process and scheduled for fabrication. The attenuator across 10-43 GHz has been developed using Jazz 0.18- μm SiGe BiCMOS process with unprecedented performance.

Synthesizer: All components of the synthesizer and the complete synthesizer have been developed using Jazz 0.18- μm CMOS process with unprecedented performance.

1. SYSTEM ARCHITECTURE

Fig. 1 shows the block diagram of the sensor. It consists of a multichannel multi-concurrent-band antenna-transceiver, digital signal processing (DSP), and display.

The **Antenna-Transceiver** consists of multiple dual-polarization antennas, transmit-receive and calibration switches (TR/CAL Switch), transmitter (TX), receiver (RX) and synthesizer.

The **TX** consists of upconverters (UCT), band-pass filters (BPF), switches, baluns and power amplifiers (PA). Although only one TX is shown in the system, multi-channel TX can also be implemented in which PA's are used on all the output arms of the power divider to amplify the signals going to the antennas. The TX's principle is based upon the concept of generating a carrier-based ultra-wideband (UWB) signal by gating a single-tone signal with a small time

window, thereby only producing signal during a small time period. A switching procedure implementing a novel RF leaking cancellation technique, in which the RF leaking signal through a switch is suppressed by combining with its replica using a balun, is adopted in the proposed TX to achieve extremely high isolation switching needed in UWB signal generation. The TX generates signals “concurrently” in K and Ka band to feed the antenna(s) through a power divider and TR/CAL Switch. The transmitting signals are also fed to each of the RX channels through another TR/CAL Switch to provide signals for RX calibration. The **RX** has multiple channels of identical receiver front-ends working concurrently in K and Ka band. Each channel has two separate identical receivers, each consisting of separate bandpass filter (BPF), low-noise amplifier (LNA), voltage-gain-control amplifier (VGA), and common single-pole multi-throw (SPNT) switch, mixers, automatic gain control baseband amplifier (AGC), and analog-to-digital converter (ADC). The **Synthesizer** generates multiple signals of different frequencies concurrently to feed both TX and RX simultaneously. The **DSP** performs all the necessary processing and operation for the entire sensor. The **DSP** is described in Part B of the report.

The **TX** transmits signals in K- and Ka-band simultaneously to the TR/CAL Switch. The TR/CAL Switch along with the dual-polarized antenna allows both horizontally and vertically polarized signals to be transmitted toward targets. Multi-band signals of orthogonal polarizations are transmitted to achieve not only more detailed target information but also polarization diversity, all leading to optimum detection and characterization capabilities. The horizontally and vertically polarized reflected signals at all frequencies are captured by the **RX** via the dual-polarized antennas and another TR/CAL Switch. The horizontally polarized and vertically polarized received signals are separated from each other. Each signal is amplified by the LNA and VGA, selected by the SPNT Switch, down-converted to intermediate-frequency (IF) and then base-band signals, amplified and digitized before going into the **DSP**. The **DSP** performs various functions such as executing the multi-beam operation, processing the measured complex cross correlations between receivers, and reconstructing the distribution of power received by the receivers. The sensor acquires all four polarization images with the same geometry and from the same point. The reflected echoes of multi-polarization are properly selected, fused and jointly processed by the multichannel receiver accompanied by the **DSP software** to achieve accurate and rapid detection, identification, location and tracking of all targets, and environment characterization over a large area. With (near) real-time processing, the operation is completed very quickly.

There are two significantly new basic hardware research activities especially worthwhile to be mentioned here: One is the “basic research of novel concurrency techniques” for sensors and another is the development of an innovative multi-beam and synthetically large aperture technique. These very important basic researches will have a profound impact to military sensors, particularly for urban warfare operations, where multifunction, multi-operation, multi-mission over complex targets and environments with miniature systems become essential.

The concurrency techniques allow all the components including antennas, and hence the sensor with a single RF front-end, to work concurrently in multiple bands. This is a basic and unique feature of our hardware approach as compared to the conventional approach which integrates two (or more) bands together with all the components combined physically, just like different systems tied together (e.g., parallel through a multiplexer), which is extremely difficult to realize

in practice – particularly when more bands are involved. Another word, our approach integrates multi-band together “**electrically**”, instead of **physically** as done in the conventional approach. Therefore, the total RF components remain essentially the same as those for a single-band system, leading to optimum size, cost and power consumption for the system. The ability of operating multiple bands simultaneously increases the diversity of the transmitter and receiver, and hence system – especially needed when operating in environments with severe multi-path fading such as urban settings or mountainous terrains which hinder the sensing capability. Effectively, our research in concurrency will lead a novel system frame-work capable of multi-function and multi-mission concurrency by “electrically” combining systems operating in different bands into a “single” unit in a very efficient way. It should be noted that we do “not” achieve the concurrency by employing components working over an extremely wide bandwidth covering both desired and undesired frequency ranges in the multi-band (i.e., all-pass), as doing so will “not” lead to an overall optimum system architecture and performance due to various problems such as increased power consumptions resulting from undesired operating bandwidths, degraded RF power-efficiency, increased circuit and hence system complexity, increased interference with other RF operations, generation of (unwanted) RF radiation in non-interested bands and increased RF emission leading to RF environment pollution and less stealthy operations, etc. Instead, our concurrency techniques will enable all the components and hence the sensor to work “only” within the desired bandwidths in these bands (i.e., in multiple band-pass windows.) Research in “concurrency” for both RF components and systems, particularly across such widely separate bands that are considered as different modes, however, is expected to result in numerous benefits for surveillance.

The multi-beam-and-synthetically-large-aperture technique enables the sensor to generate multiple beams simultaneously with a synthetic aperture much larger than the actual aperture, resulting in beam-width much narrower than that produced by conventional arrays with the same number of elements, and hence very fine angle resolution. This allows large areas to be searched rapidly from a given position of a moving platform “without” physically moving the antennas or using external beam-control devices such as phase shifters as in conventional phased arrays, largely eliminating errors due to these components and ultimately help improving the system performance. Note that the achieved “synthetic aperture” is an inherent characteristic of our (aperture-synthesis-based) sensor “in addition to” the synthetic aperture achieved in conventional SAR operation through the movement of antennas by the sensor’s carrying platform such as UAV.

The system is capable of achieving the system “**agility**.” It can change the frequency, waveform and beam formation to accommodate different real-world situations. “Agility” is important for sensing. For instance, our TX can change the pulse width and PRF of transmitting signals as well form different transmitting beams through the multi-antenna. Our RX can also alter the beam formation through its multi-output in conjunction with multiple cross-correlators and multi-antenna. All these can be done interactively through the DSP.

It is important to note that the multi-sensor system with its multi-modality signal/data processing fusion, although based on RF, is viewed as consisting of “**different types or modes**” of sensors. The reason is we will use frequencies which are widely separate – for instance, 24.5 and 36 GHz that are around 1.5λ apart. This frequency separation is close to the difference between electro-

optic (EO) and infrared sensors which are considered as two different modes. More over, the scattering phenomenon and the polarization effects at 24.5 and 35 GHz are very different. It is noted that the 1.5λ difference is in the high RF range, which is much more significant than in low RF ranges (e.g., going from 3 to 4.5 GHz may not make much difference since the scattering/polarization effects at these frequencies are not significantly different, as compared to going from 24.5 to 35 GHz

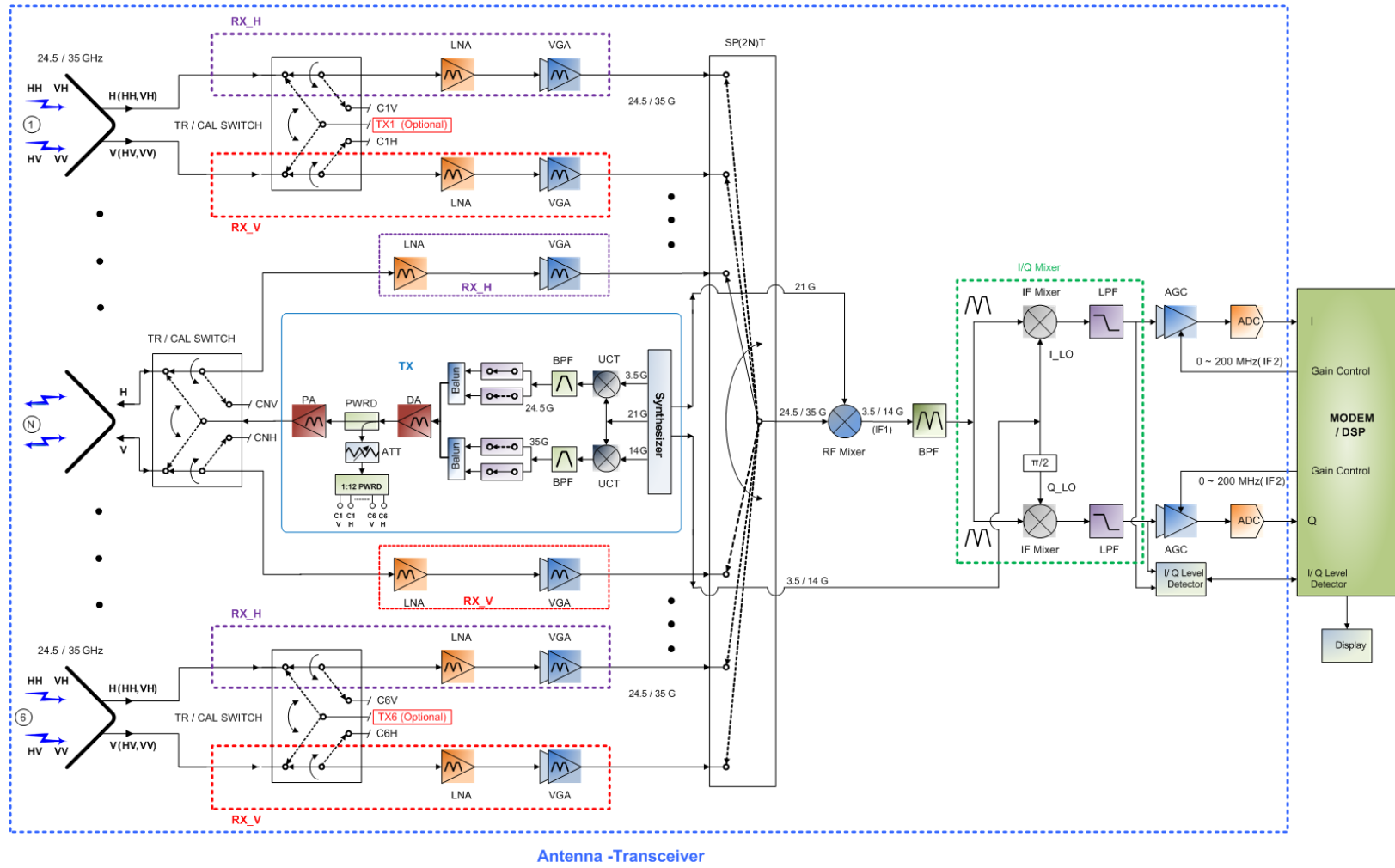


Fig. 1. Multi-sensor system operating concurrently in 2 bands (K and Ka).

2. TRANSMITTER

Summary of Performance: The architecture and specifications for the concurrent dual-band 24.5/35 GHz transmitter (TX) have been developed and analyzed. All components of the TX have been developed with very good performance. Several of them represent the state of the art with unprecedented performance. The entire concurrent dual-band 24.5/35 GHz TX has been designed and is currently being fabricated using Jazz 0.18- μm SiGe BiCMOS process. The total size for this TX is only 2mmx4.5mm. This is the first ever-developed millimeter-wave concurrent dual-band TX on SiGe BiCMOS. Once the TX is fully tested and evaluated, it can be integrated with other subsystems including receivers, antenna array and other circuits, as well as with the developed signal processing software, to form the entire concurrent multiband sensor proposed in this project.

2.1 Transmitter Architecture

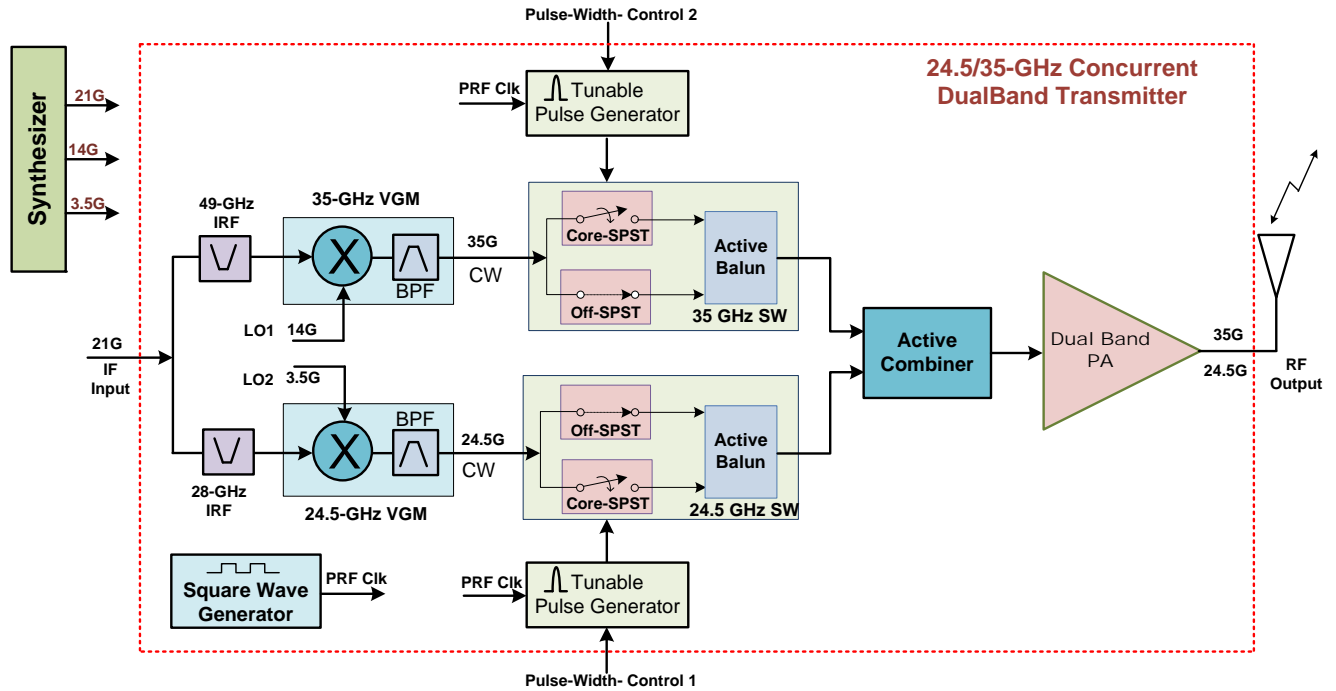


Fig. 2. Transmitter architecture.

Figure 1 shows the transmitter architecture as seen in the system architecture shown in Fig. 1. It is designed to generate narrow RF pulses at 24.5 and 35 GHz concurrently. The transmitter consists of two image reject filters (IRF) at 28 and 49 GHz, two up-conversion variable gain mixers (VGM) at 24.5 and 35 GHz, two ultra-high-isolation RF SPST switches, two tunable pulse generators (PG), one PRF square-wave generator, one active combiner and one concurrent dual-band power amplifier.

The 24.5- and 35-GHz VGMs produce 24.5 and 35 GHz CW signals, respectively, from the 21-GHz IF, and 3.5- and 14-GHz LO signals. The 24.5- and 35-GHz RF switches are turned on and off by the impulses generated from PG1 and PG2 to produce the 24.5 and 35-GHz RF pulses, respectively. The width of the impulses generated from PG1 and PG2, and hence that of the RF

pulses generated from the RF switches, can be independently tuned by the pulse-width-control-1 and pulse-width-control-2 signals. These RF pulses are then combined in the active combiner and amplified by the concurrent dual-band 24.5/35 GHz power amplifier.

Design of the transmitter and its components are described in the following sections. In these sections, the 24.5- and 35-GHz channels refer to the signal path from the IF input to RF output which produces and amplifies the 24.5- and 35-GHz signals, respectively. The 24.5-GHz channel consists of 28-GHz IRF, 24.5-GHz VGM, 24.5-GHz RF switch, combiner and dual-band PA and the 35-GHz channel consists of 49-GHz IRF, 35-GHz VGM, 35-GHz RF switch, combiner and dual-band PA.

2.2 Image Rejection Filter (IRF)

The 24.5-GHz CW signal is generated by mixing 21-GHz IF and 3.5-GHz LO in the 24.5-GHz VGM while the 35-GHz CW signal is generated by mixing 21-GHz IF and 14-GHz LO in the 35-GHz VGM. The 28-GHz IRF is basically a band-stop filter and is designed to reject the 28-GHz image signal leaking from the 35-GHz channel, and the 49-GHz IRF is designed to reject the 49-GHz image signal leaking from the 24.5-GHz channel.

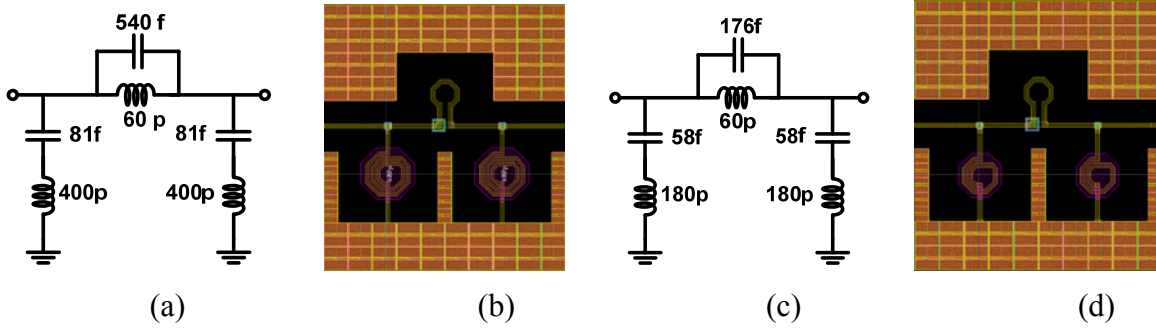


Fig. 3. Schematic and layout of the 28-GHz IRF (a, b) and 49-GHz IRF (c, d).

Fig. 3 shows the schematic and layout of the 28- and 49-GHz IRFs. The insertion loss at 21 GHz and rejection at the image frequency are summarized in the Table 1.

Table 1 - 28- and 49-GHz IRF performance

	Insertion loss at 21 GHz (dB)	Rejection at Image Frequency (dB)
28-GHz IRF	1.6	46
49-GHz IRF	0.3	50

2.3 Variable Gain Mixers (VGM)

2.3.1 24.5-GHz VGM

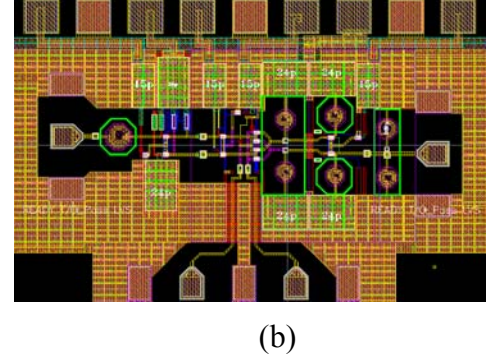
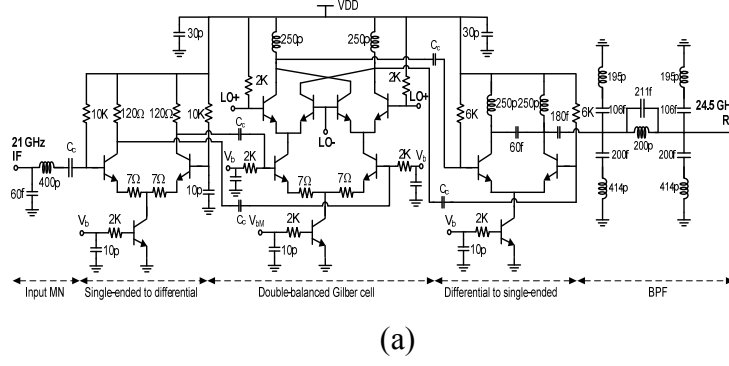


Fig. 4. 24.5-GHz VGM schematic (a) and layout (b).

Fig. 4 shows the schematic and layout of the 24.5-GHz VGM designed to generate the 24.5-GHz signal from the 21-GHz IF and 3.5-GHz LO signals. It consists of an input matching network, single-ended to differential balun, double-balanced Gilbert mixer cell, differential to single-ended balun and band pass filter (BPF). The double-balanced Gilbert mixer cell is chosen instead of a single-balanced cell to enhance the IF-to-RF and LO-to-RF isolation. The BPF passes the 24.5-GHz tone, suppresses the low sideband tone at 17.5-GHz and cross-channel coupling at 35 GHz. The simulation results show that the PBF exhibits an insertion loss of 2.3 dB at 24.5 GHz, and rejection of 55 and 42 dB at 17.5 and 35 GHz, respectively. The whole VGM is optimized to have high gain and linearity.

Fig. 5 shows the gain, 24.5-GHz output power, IF-to-RF isolation, LO-to-RF isolation, low sideband rejection, and output signal spectrum. The simulation results show that the 24.5-GHz VGM exhibits a maximum gain of 27.9 dB, 1-dB output power compression $P_{out,1dB}$ of 1.93 dBm, noise figure of 6.7 dB, low sideband rejection of 56 dB, IF-RF isolation higher than 14.8 dB, LO-RF isolation higher than 66 dB, and good input and output matching. These results are summarized in the Table 2. The VGM output signal spectrum in Fig. 5(b) shows a 24.5-GHz tone with power of 1.28 dBm and the harmonic and inter-modulation products with suppression of more than 25 dBc. By changing the bias voltage V_{bM} from 0.78 to 1.3 V, the gain of the VGM changes from -10 dB to +27.9 dB.

Table 2 - 24.5-GHz VGM performance

Gain (dB)	Low-sideband Rejection (dB)	IF-RF Isolation (dB)	LO-RF Isolation (dB)	$P_{out,1dB}$ (dBm)	$P_{in,1dB}$ (dBm)	NF (dB)	IF Return Loss (dB)	RF Return Loss (dB)
27.9	>56	> 14.8	>66	+1.93	-25	6.7	13	10.1

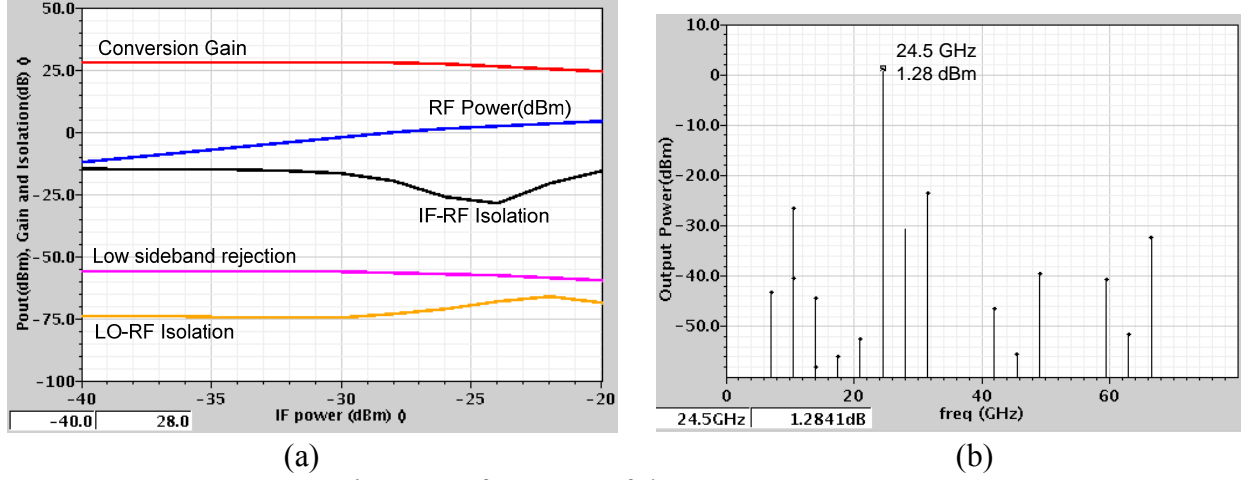


Fig. 5. Performance of the 24.5-GHz VGM.

2.3.2 35-GHz VGM

Fig. 6 shows schematic and layout of the 35-GHz VGM designed to generate the 35-GHz signal from the 21-GHz IF and 14-GHz LO signals. It consists of an input matching network, single-ended to differential balun, double-balanced Gilbert mixer cell, differential to single-ended balun and band pass filter (BPF). The BPF passes the 35-GHz tone, suppresses the low-sideband tone at 7-GHz and cross-channel coupling at 24.5 GHz. The simulation results show that the PBF exhibits the insertion loss of 3 dB at 35 GHz and rejection of 31 and 26 dB at 7 and 24.5 GHz, respectively.

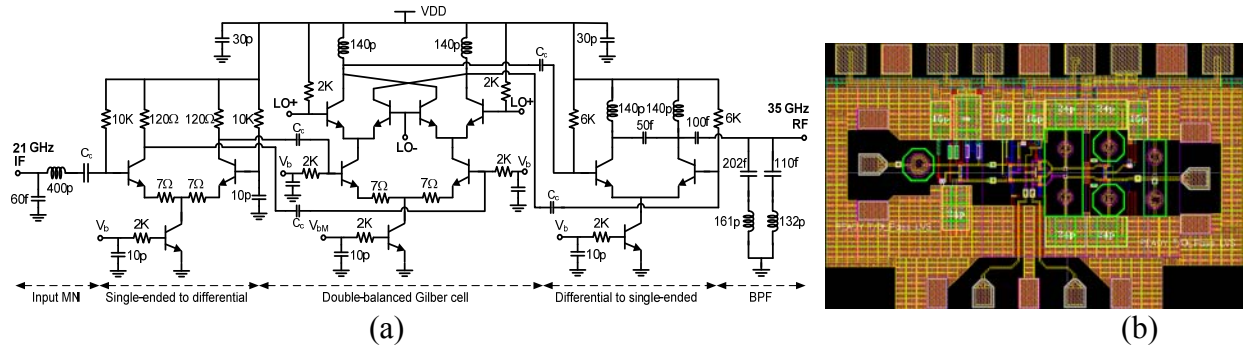


Fig. 6. 35-GHz VGM schematic (a) and layout (b)

Fig. 7 shows the gain, 35-GHz output power, IF-to-RF isolation, LO-to-RF isolation, low-sideband rejection, and output signal spectrum. The 35-GHz VGM exhibits a maximum gain of 27.1 dB, $P_{out,1dB}$ of 2.3 dBm, noise figure of 6.75 dB, low-sideband rejection of 42.8 dB, IF-RF isolation higher than 13 dB, LO-RF isolation higher than 35.7 dB, and good input and output matching. The performance of the 35-GHz VGM is summarized in the Table 3. The VGM output signal spectrum in the Fig. 6(b) shows the 35-GHz tone with power of 0.56 dBm and the harmonic and inter-modulation product suppression of more than 26 dBc. By changing the bias voltage V_{bM} from 0.78 V to 1.3 V the gain of the VGM changes from -14 dB to +27.1 dB.

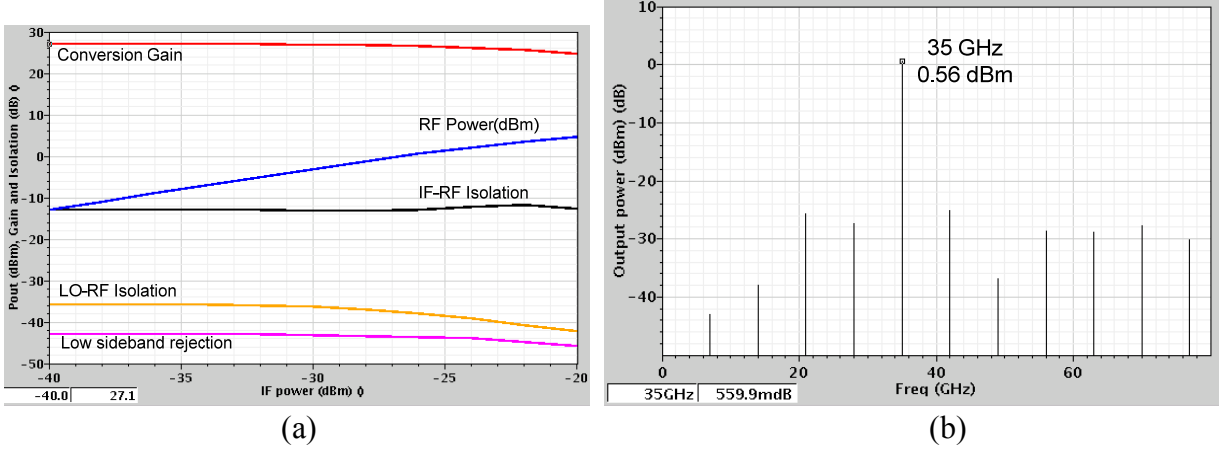


Fig. 7. Performance of the 35-GHz VGM.

Table 3 - 35-GHz VGM performance

Gain (dB)	Low-sideband Rejection (dB)	IF-RF Isolation (dB)	LO-RF Isolation (dB)	P _{out,1dB} (dBm)	P _{in,1dB} (dBm)	NF (dB)	IF Return Loss (dB)	RF Return Loss (dB)
27.1	>42.8	> 13	>35.7	+2.3	-23.8	6.75	13	8

2.4 High-Isolation Switches

2.4.1 35-GHz Switch

Fig. 8 shows the 35-GHz RF switch that consists of two identical SPST switches, an active balun and input and output matching networks. The switch was designed and fabricated using Jazz 0.18- μm BiCMOS process. It occupies a chip area of $450 \times 500 \mu\text{m}^2$. The two identical switches are named “Off-SPST” switch, always operating in the off-mode, and “Core-SPST” switch operating as a normal switch (on/off). The Off-SPST and Core-SPST switches are implemented using a simple conventional switch structure employing a series and a shunt deep-n-well transistor. Three inverters in the Off- and Core-SPST are used to produce complementary control impulses and sharpen the rising and falling edges of these impulses. The active balun functioning as a differential amplifier is used to amplify the RF pulses and suppress the RF leakage. Hence, the 35-GHz switch exhibits gain when it is on and extremely high isolation when it is off.

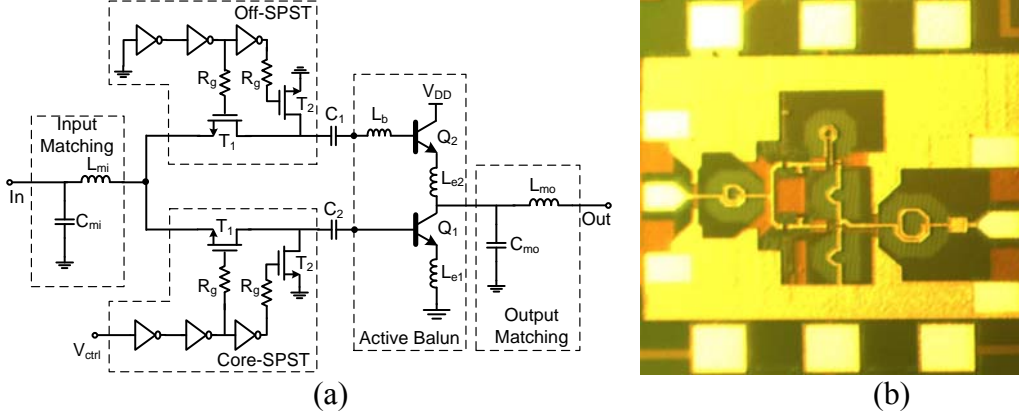


Fig. 8. Simplified schematic of the 35-GHz switch (a) and its microphotograph (b).

The RF pulses are formed by gating the Core-SPST switch using the control impulses applied to the V_{ctrl} pin of the Core-SPST. A small switching time for the switch is obtained by using a small gate resistor for the transistors in the Core- and Off-SPST switch. In order to get small switching time in the order of 200ps, the gate resistor is chosen to be 400 Ω . When the Core-SPST is off, the leakage RF signal from its output will be canceled by the same RF leakage signal from the output of the Off-SPST in the active balun.

2.4.1.1 Core-SPST and Off-SPST Switch Design

The performance of the Core- and Off-SPST affects the overall performance of the RF-pulse former. Using small gate resistors provides a small switching time for the Core- and Off-SPST switch, hence RF-pulse former, but significantly increases the insertion loss of these switches. In addition, at millimeter-wave frequencies, the insertion loss and isolation of these SPST switches are mainly limited by the transistors' parasitic capacitors and deep-n-well parasitic capacitors - all of which are proportional to the transistor size. This requires an analysis to find the optimum sizes for both series and shunt transistor for a given design target of insertion loss or isolation. The integrated inverters used to sharpen the rising and falling edges for the gating impulses are designed to have a very small delay between the input and output, so that they do not affect the switching process of the RF-switch.

2.4.1.2 Active Balun Design

The two HBT transistors Q_1 and Q_2 in the active balun have the same size with an emitter area of $2 \times 10.16 \mu\text{m}^2$ and are biased at a DC current of 7.3 mA. The bases of Q_1 and Q_2 are biased at 1.1 V and 1.8 V, respectively, through large resistors which do not affect the balun's RF operation. The collector of Q_2 is connected to V_{DD} of 1.8 V. The values of inductors L_{e1} , L_{e2} and L_b are calculated as 95 pH, 95 pH and 120 pH, respectively.

2.4.1.3 Performance of 35-GHz Switch

Fig. 9 shows the simulated and measured insertion loss/gain, input and output return losses, and isolation of the 35-GHz switch under small signal conditions. The measured results show that the switch exhibits an ultra-high isolation around the design frequency, hence extremely low RF

leakage, while consuming a DC current of only 7.3 mA from a 1.8-V source. From 31 to 37.1 GHz, the loss/gain is from -1.9 dB (loss) to 1.1 dB (gain), the input return loss is from 14.5 to 30 dB. The output return loss is higher than 10 dB from 33 to 35.9 GHz. From 30 to 40 GHz the isolation is higher 40 dB and especially at 34 GHz the isolation reaches 70 dB, which is the measurement limit of the vector network analyzer, along with a gain of 1.1 dB. While the measured and simulation results of the insertion loss/gain, reverse isolation (S12), and input and output return losses are in good agreement from 10 to 40 GHz, the simulated isolation result shows more than 10-dB difference with the measured one, except in the narrow frequency range of 33-35 GHz. The difference in isolation is mainly due to the imbalance of the fabricated active balun and the inaccuracy of the models for the passive elements and active devices. The input 1-dB compression point was measured to be -6 dBm.

The 35-GHz is used to form a 35-GHz pulse. A 35-GHz CW signal is applied to the switch and gated by an impulse applied to the control pin of the switch. The control impulse has adjustable duration from 100 ps to 10 ns and rising and falling times of 45 ps and 110 ps, respectively. The integrated inverters sharpen the rising and falling edges of the impulse which may be expanded when travelling through the measurement cables, bonding-wires and on-chip interconnects before reaching the gate of the transistors. This helps eliminate external effects to the switching speed of the 35-GHz switch which is mainly determined by the gate-biased resistor and gate-source capacitor of the MOSFETs. Fig. 10 shows the measured 35-GHz RF pulses having pulse widths of 200 ps, 300 ps and 5 ns, from which rising/falling time and pulse width can be determined. For instance, for the 300-ps 35-GHz pulse, the 10%-90% rising time, and 90%-10% falling time are 136 ps and 50 ps, respectively.

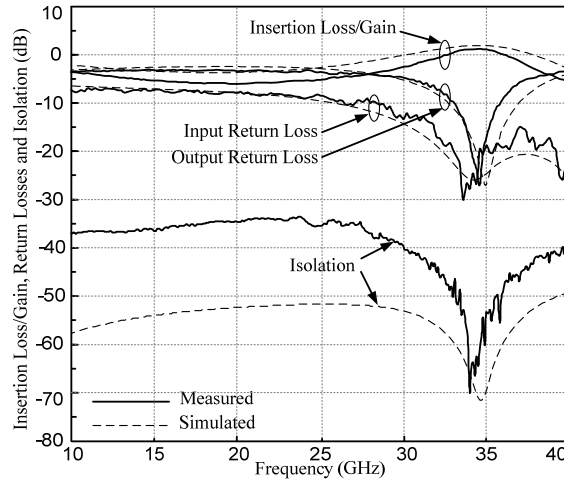


Fig. 9. Simulated and measured insertion loss/gain, return losses and isolation.

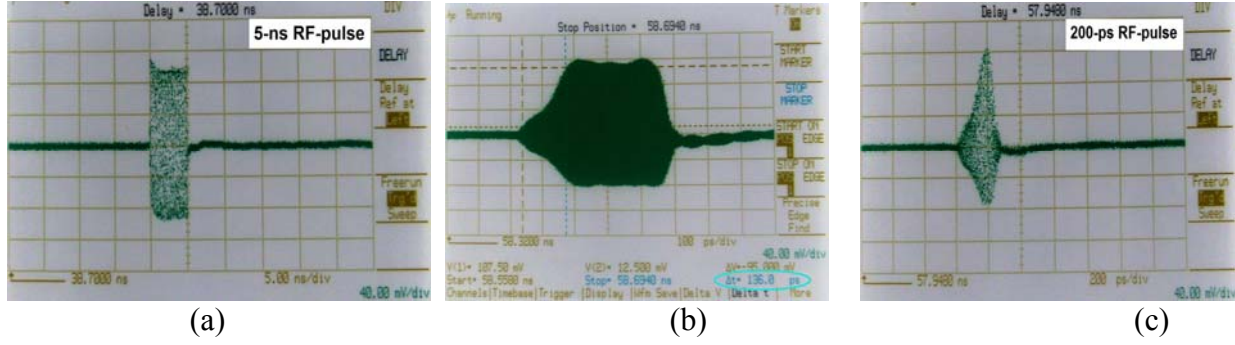


Fig. 10. Measured 35-GHz RF-pulses having pulse width of 5ns (a), 300 ps (b) and 200 ps (c).

2.4.2 24.5-GHz Switch

The design of the 24.5-GHz switch is similar to that of the 35-GHz switch. Fig. 11 shows the microphotograph and measurement results of the 24.5-GHz switch. The measured results show that the switch exhibits insertion loss of 1.55 dB, input return loss of 34 dB, output return loss of 22 dB and isolation of 46 dB at 24.5-GHz. The measured and simulated results agree well.

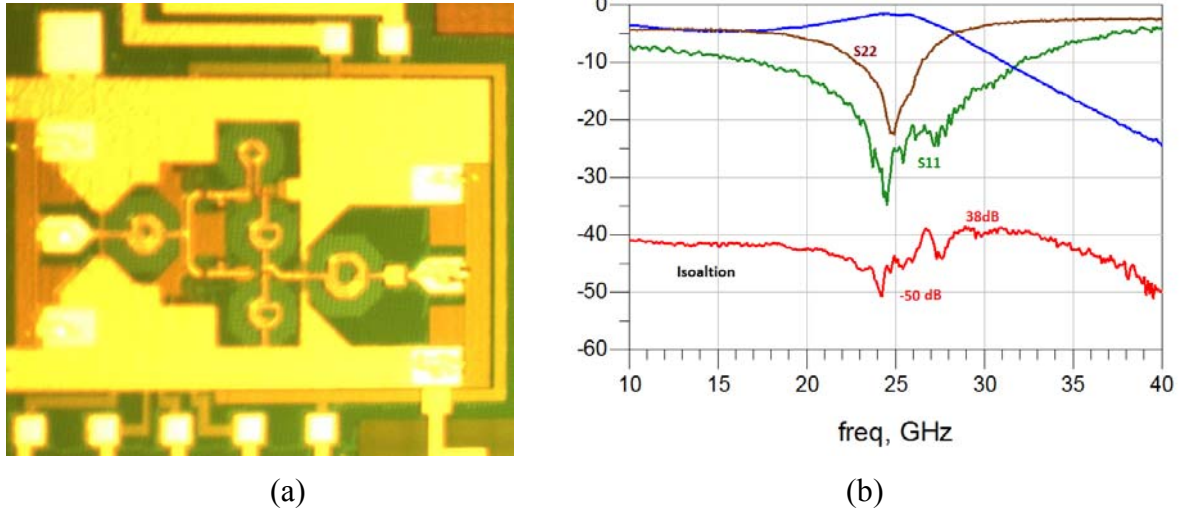


Fig. 11. Microphotograph (a) and measured results (b) of the 24.5-GHz switch.

2.5 Concurrent Dual-Band Power Amplifier

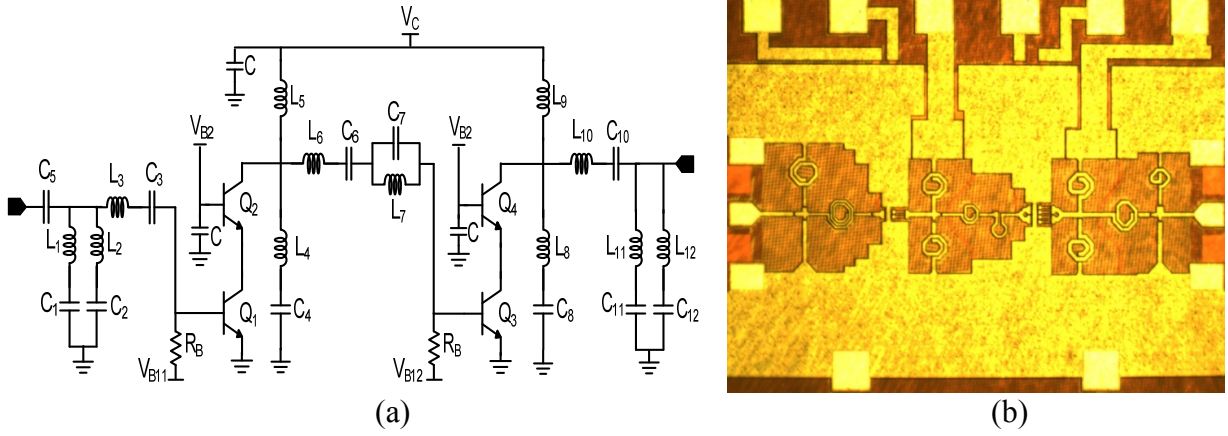


Fig. 12. Schematic (a) and photograph (b) of the dual-band power amplifier.

Fig. 12 shows the schematic and microphotograph of the concurrent dual-band power amplifier (PA). The PA has two cascode stages. The last stage is designed to give the highest power efficiency while the first stage is designed to provide the maximum output power. In order to provide high output power, multiple transistor cells with two emitter, three base and two collector contacts and emitter area of $0.15 \times 20.32 \mu\text{m}^2$ are used. In the last stage, the common emitter transistor Q3 and common base transistor Q4 consist of four transistor cells, while in the first stage the common emitter transistor Q1 and common base transistor Q2 consist of two transistor cells. All transistors are biased at the current density of $10 \text{ mA}/\mu\text{m}^2$ for the maximum f_{max} of 180 GHz. The dual-band matching networks used at the output, central and input stages provide matching as well as harmonic and inter-modulation tone suppression, resulting in optimum performance at two frequencies concurrently.

Fig. 13 shows the measured results of the PA. As seen in Fig. 13(a), at 25.5 and 37 GHz, the PA exhibits gain of 21.4 and 17 dB, input return loss of 14.8 and 9 dB, and output return loss of 12.5 and 15 dB, respectively. The measured results in Figs. 13 (b) and (c) show that, in the single-band mode, the PA has maximum output power of 15.94 and 12.4 dBm at 25.5 and 37 GHz, respectively, whereas, in the concurrent dual-band mode, it provides maximum output power of 12.3 and 12.4 dBm at 25.5 and 37 GHz, respectively. The results are summarized in Table 4.

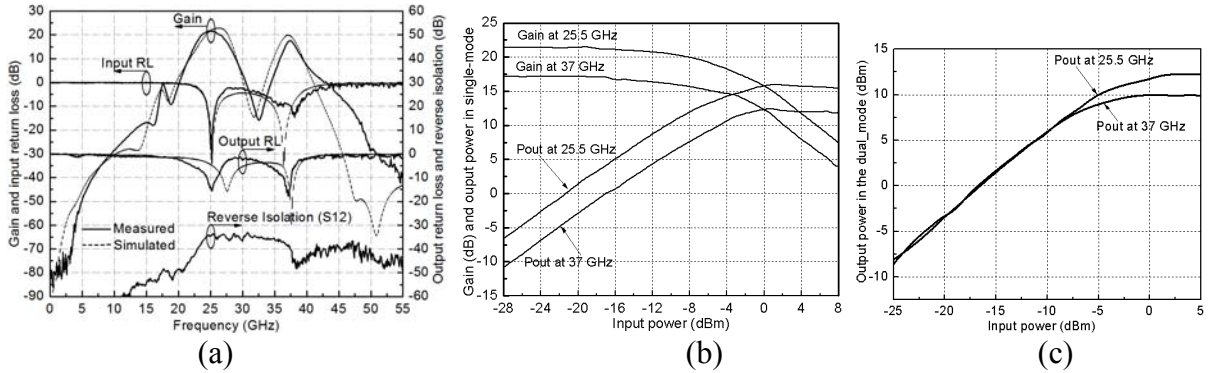


Fig. 13. Measured and simulated gain and return loss (a), and measured output power in single-mode (b) and dual-mode (c).

Table 4 – Performance summary of the concurrent dual-band power amplifier

Parameter/Freq.	25.5 GHz		37 GHz	
VCC (V)	3		3	
Current (mA)	120		120	
Gain (dB)	21.4		17	
S11 (dB)	14.8		9	
S22 (dB)	12.5		15	
	Single-Mode	Dual-Mode	Single-Mode	Dual-Mode
P _{1dB-out} (dBm)	11.24	10.1	6.06	5.5
P _{out-max} (dBm)	15.94	12.3	12.4	10
PAE (%)	10.9	10.7	10.8	2.8

2.6 Transmitter Design and Integration

Fig. 14 shows the layout of the complete concurrent dual-band 24.5/35 GHz transmitter (TX), that integrates the individual circuits presented in the previous sections, according to the transmitter architecture shown in Fig. 2. The TX has a single-ended IF input at 21GHz, two differential LO inputs at 3.5 and 14 GHz, and one single-ended RF output at 24.5 and 35 GHz. It is optimized to have high gain, high output power, and high harmonic/inter-modulation product suppression. The entire TX was designed and fabricated using Jazz 0.18- μ m BiCMOS process.

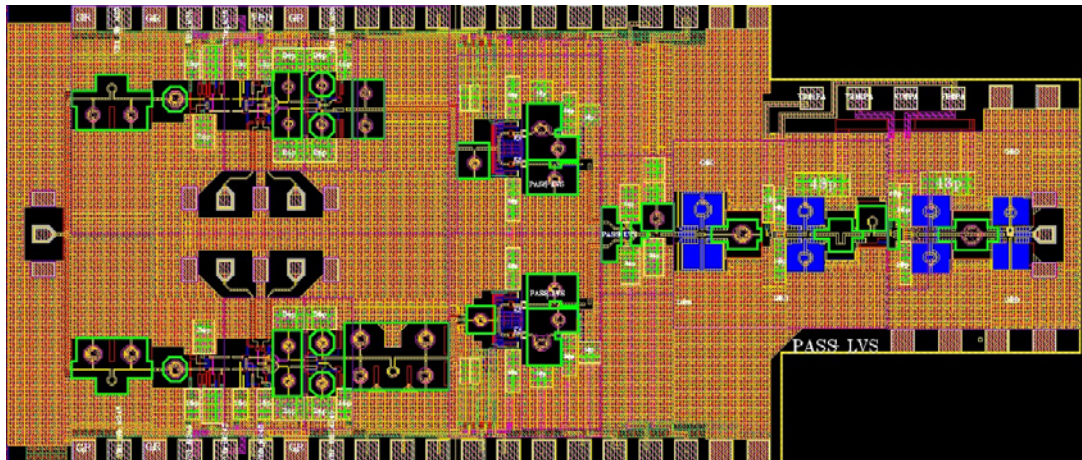


Fig. 14. Layout of the concurrent dual-band 24.5/35 GHz transmitter. Size: 2mmx4.5mm.

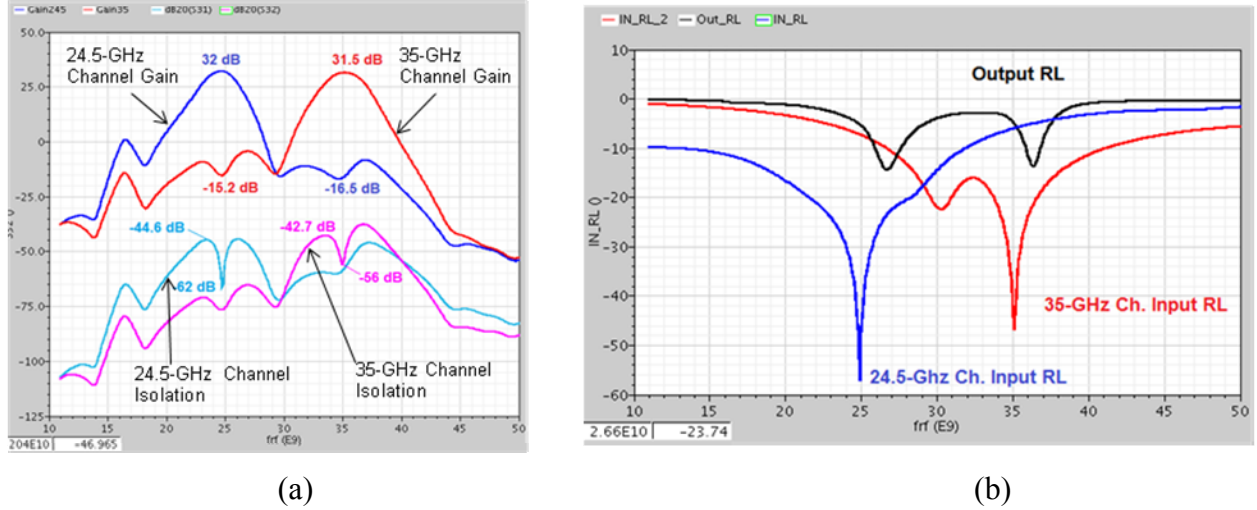


Fig. 15. Gain and isolation of the 24.5-GHz and 35-GHz channels (a) and input and output return losses (b).

Fig. 15 shows the simulated small-signal gain, isolation, and return losses of the TX. In the on-state, the 24.5-GHz channel exhibits a gain of 32 dB at 24.5 GHz and cross-channel suppression of 16.5 dB at 35 GHz, whereas the 35-GHz channel exhibits a gain of 31.5 dB at 35 GHz and cross-channel suppression of 15.2 dB at 24.5 GHz. In the off-state, the TX exhibits a high isolation of 62 and 56 dB at 24.5 and 35 GHz, respectively. The TX has a good matching at the input and output ports.

The gains and output powers of the 24.5- and 35-GHz channels for all working modes, including single and dual modes, and on and off conditions are simulated. The 3.5- and 14-GHz LO powers are fixed at -2 dBm. The two channels' on- and off-state are controlled by two control signals. The 21-GHz IF input power is swept during the simulations. Another two control voltages are used to change the gain of the mixers. The channel gains are defined as

$$\text{24.5-GHz channel gain} = \frac{\text{24.5_GHz output power}}{\text{21_GHz input power}}$$

$$\text{35-GHz channel gain} = \frac{\text{35_GHz output power}}{\text{21_GHz input power}}$$

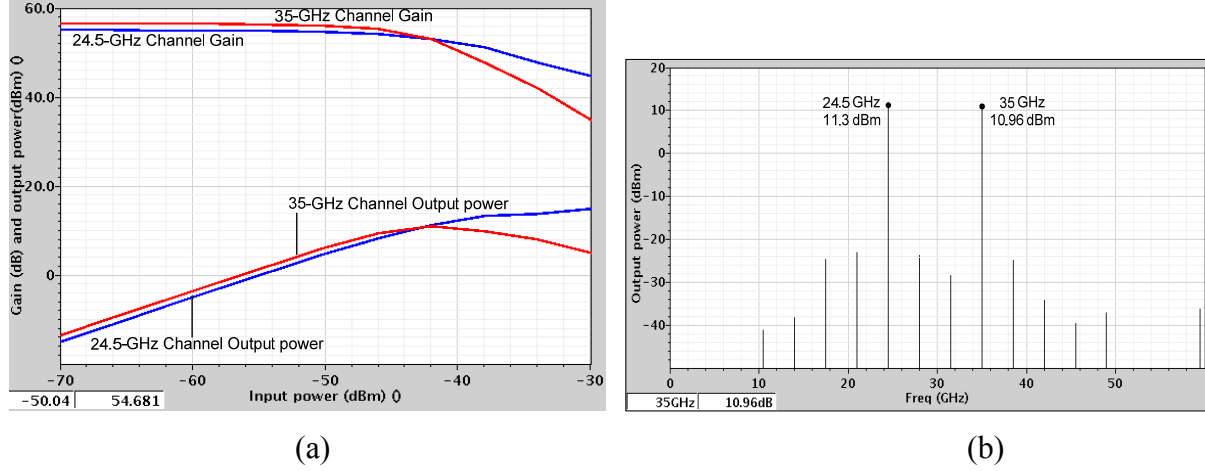


Fig. 16. TX performance with both channels on: gain and output power (a) and output spectrum (b)

Fig. 16 shows the gains and output powers of the two channels. When both channels are on, the simulation results in Fig. 16(a) show that the TX exhibits a gain of 55.5 dB, $P_{\text{out_1dB}}$ of 12.6 dBm and $P_{\text{out_max}}$ of 11.3 dBm on the 24.5-GHz channel, and gain of 57 dB, $P_{\text{out_1dB}}$ of 12.6 dBm and $P_{\text{out_max}}$ of 10.96 dBm on the 35-GHz channel. The spectrum of the TX output signal in Fig. 19(b) shows that all the harmonics and inter-modulation products are 34 dBc lower than the main tones.

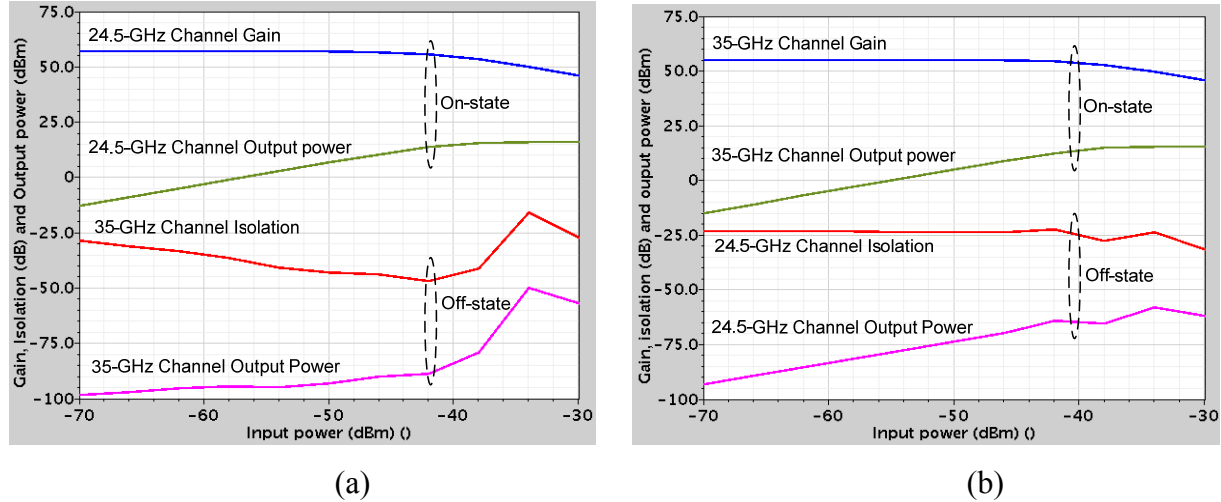


Fig. 17. TX performance with 24.5-GHz channel on and 35-GHz channel off (a), and 24.5-GHz channel off and 35-GHz channel on (b).

Fig. 17(a) shows that, when the 24.5-GHz channel is on and the 35-GHz channel is off, the TX exhibits a gain of 55.5 dB, $P_{\text{out_1dB}}$ of 12.7 dBm and $P_{\text{out_max}}$ of 15.6 dBm for the 24.5-GHz channel, and an isolation higher than 28.4 dB for the 35-GHz channel. Fig. 17(b) shows that, when the 24.5-GHz channel is off and the 35-GHz channel is on, the TX exhibits a gain of 56 dB,

P_{out_1dB} of 12.6 dBm and P_{out_max} of 16.1 dBm for the 35-GHz channel, and an isolation higher than 23.5 dB for the 24.5-GHz channel.

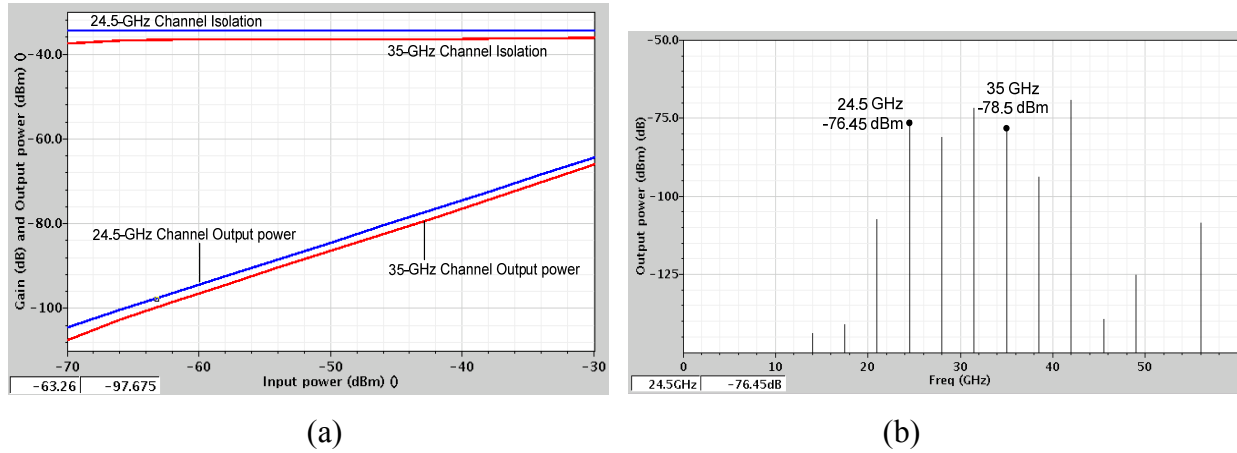


Fig. 18 TX performance with both channel off: gain and output power (a) and output spectrum (b)

Fig. 18(a) shows that, when both 24.5- and 35-GHz channels are off, the TX exhibits an isolation higher than 34.5 dB and 36.5 dB for the 24.5-GHz channel and 35-GHz channel, respectively. The spectrum of the TX output signal in Fig. 18(b) shows extremely low RF powers of -76.45 and -78.5 dBm at 24.5 and 35 GHz corresponding to the input power of -42 dBm.

Table 5 summarizes the performance of the whole TX in all working modes.

Table 5 - TX performance

Condition		24.5-GHz Channel			35-GHz Channel		
24.5-GHz Channel	35-GHz Channel	Gain/ Isolation (dB)	P_{out_1dB}	P_{out_max}	Gain/ Isolation	P_{out_1dB}	P_{out_max}
ON	ON	55	8.7	13	56.4	8.6	10.94
ON	OFF	55	15.6	12.7	-28.4	-	-
OFF	ON	-23.5	-	-	56.4	12.6	16.1
OFF	OFF	-34.5	-	-	-36.5	-	-

3. RECEIVER

Summary of Performance: The architecture and specifications for the concurrent dual-band multi-channel 24.5/35 GHz receiver (RX) have been developed and analyzed. Several components of the RX have been developed with very good performance. A concurrent dual-

band 24.5/35 GHz RX has been designed using Jazz 0.18- μm SiGe BiCMOS process and scheduled for fabrication. This RX, once developed, is the first ever-developed millimeter-wave concurrent multi-channel dual-band RX on SiGe BiCMOS.

3.1 Receiver Architecture

The receiver (RX) architecture is shown in Fig. 1 as part of the system. It is a complex RX consisting of many channels, with each channel having two sub-channels: one for vertical and one for horizontal polarizations. Design of the RX and its components are described in the following sections.

3.2 Wide-band LNA and Concurrent Dual-band LNA

3.2.1 Wide-Band LNA

Figure 19 shows the layout of the 18-40 GHz wide-band LNA covering the entire K- and Ka-band designed using Jazz's 0.18 μm BiCMOS process. The purpose of this wide-band LNA is to generate a LNA prototype from which the concurrent dual-band LNA operating in the 24.5 and 35 GHz bands can be developed.

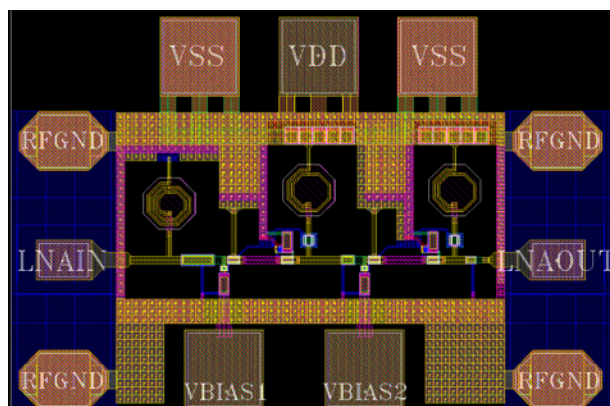


Figure 19. Layout of the 18-40 GHz wide-band LNA.

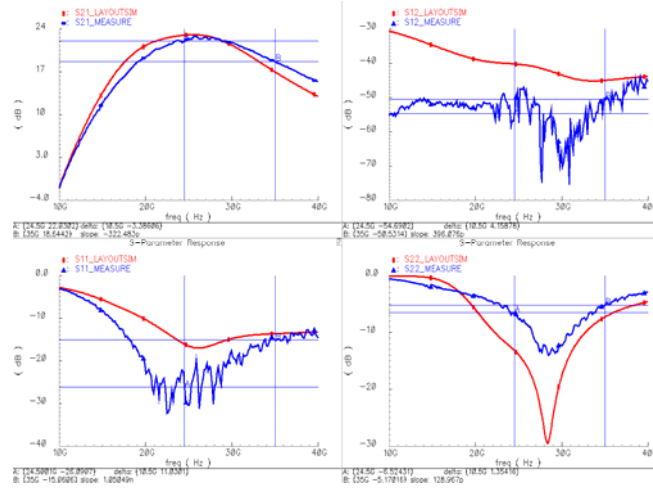


Figure 20. Simulation (red) and measurement (blue) results of the wide-band LNA.

Figure 20 shows the measurement and simulated results of the 18-40 GHz wide-band LNA. The LNA achieves power gain of 22/18.6 dB at 24.5/35 GHz, respectively. The gain drops at the upper band due to the limited f_T of the employed BiCMOS process. Both the gain and the input/output matching agree well with the simulation results. Table 6 summarizes the simulation and measurement results.

Table 6 - Summary of simulation and measurement results of the 18-40 GHz wide-band LNA

Parameter	Target Spec.	Schematic Simulation	Layout Simulation	Measure	Schematic Simulation	Layout Simulation	Measure	Unit
Frequency	24.5 / 35	24.5			35			GHz
Gain	> 15	23	23	22.03	19.7	17	18.64	dB
NF	< 8	4.77	4.96	-	6.51	6.82	-	dB
S11	< -10	-15.8	-17.4	-26	-15.2	-12.6	-15	dB
S22	< -10	-11.3	-13.6	-6.5	-8.5	-7.6	-5.1	dB
IIP3	> -10	-6.3	N/C	-	-4.8	N/C	-	dBm
IP1dB	> -20	-18.8	N/C	-	-16.1	N/C	-	dBm
Current Consumption	25	23.3	22.2	22	23.3	22.2	22	mA
Supply Voltage	1.8	1.8			1.8			V

3.2.2 Concurrent Dual-Band LNAs

Figure 21 shows the layout of the 24.5/35 GHz dual-band LNA designed using Jazz's 0.18 μm BiCMOS process. The LNA employs active notch filters to generate dual-band around 24.5 and 35 GHz. The measurement and simulated results are shown in Fig. 22. The dual-band LNA exhibits a power gain of 22/16.3 dB at 24.5/35 GHz, respectively. The gain drop also occurs at the high-band due to the limited f_T of the process. The measured gain and the input/output matching agree well with the simulation results. Table 7 summarizes the simulation and measurement results.

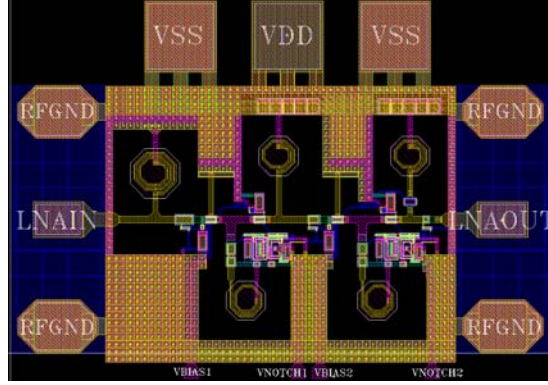


Figure 21. Layout of the concurrent 24.5/35 GHz dual-band LNA.

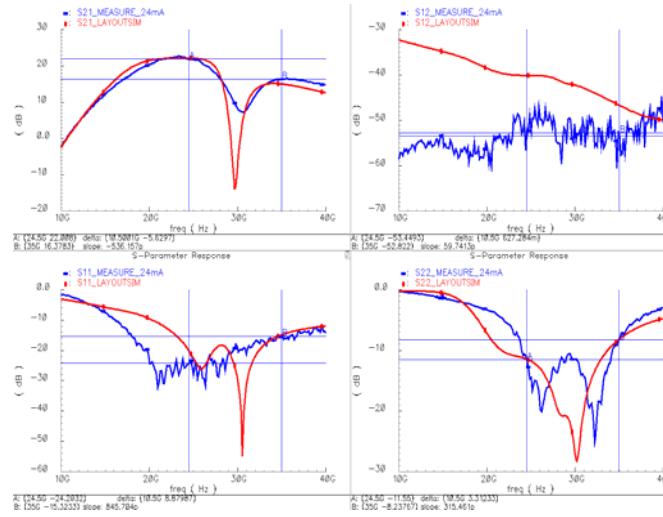


Figure 22. Simulation (red) and measurement (blue) results of the dual-band LNA.

Table 7 - Summary of simulation and measurement results of the dual-band LNA

Parameter	Target Spec.	Schematic Simulation	Layout Simulation	Measure	Schematic Simulation	Layout Simulation	Measure	Unit
Frequency	24.5 / 35	24.5			35			GHz
Gain	> 15	23	22.1	22	19.7	15	16.37	dB
NF	< 8	5.7	6.04	-	6.51	7.36	-	dB
S11	< -10	-16.9	-20.1	-24.2	-15.2	-14.8	-15.3	dB
S22	< -10	-11.4	-11.4	-11.5	-8.5	-8.1	-8.2	dB
IIP3	> -10	-6.7	N/C	-	-4.8	N/C	-	dBm
IP1dB	> -20	-18	N/C	-	-16.1	N/C	-	dBm
Current Consumption	25	25.8	24.6	24	25.8	24.6	24	mA
Supply Voltage	1.8	1.8			1.8			V

Based on the measured results of the dual-band LNA described above, we designed and fabricated two concurrent dual-band LNAs. The first dual-band LNA uses two active notch filters connected to the collector of the common-emitter (CE) device at each stage as shown in Fig. 23. Since the active notch filter can compensate for the loss of an on-chip inductor by providing negative resistance, the implemented active notch filter achieves very high quality factor compared to the low quality factor of the conventional passive notch filter that we used in the first design. Thus, the concurrent dual-band LNA with active notch filters exhibits high stop-band performance at 29 GHz between the two desired RF bands (24.5 and 35 GHz) as shown in Fig 24. Fig.25 shows the layout of this LNA.

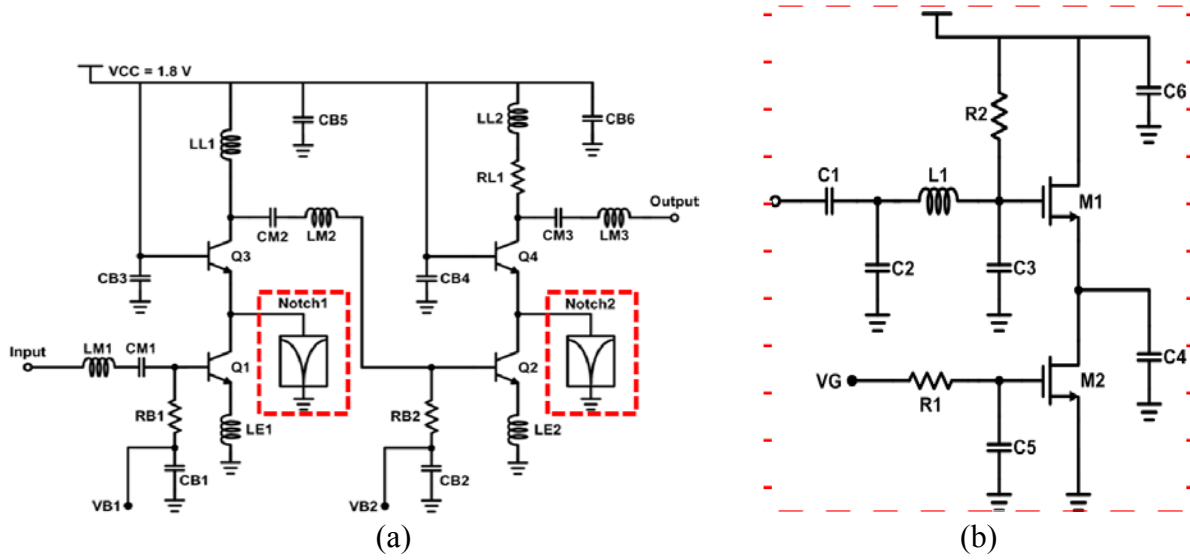


Figure 23. Schematic of the concurrent dual-band LNA (a) with active notch filters (b).

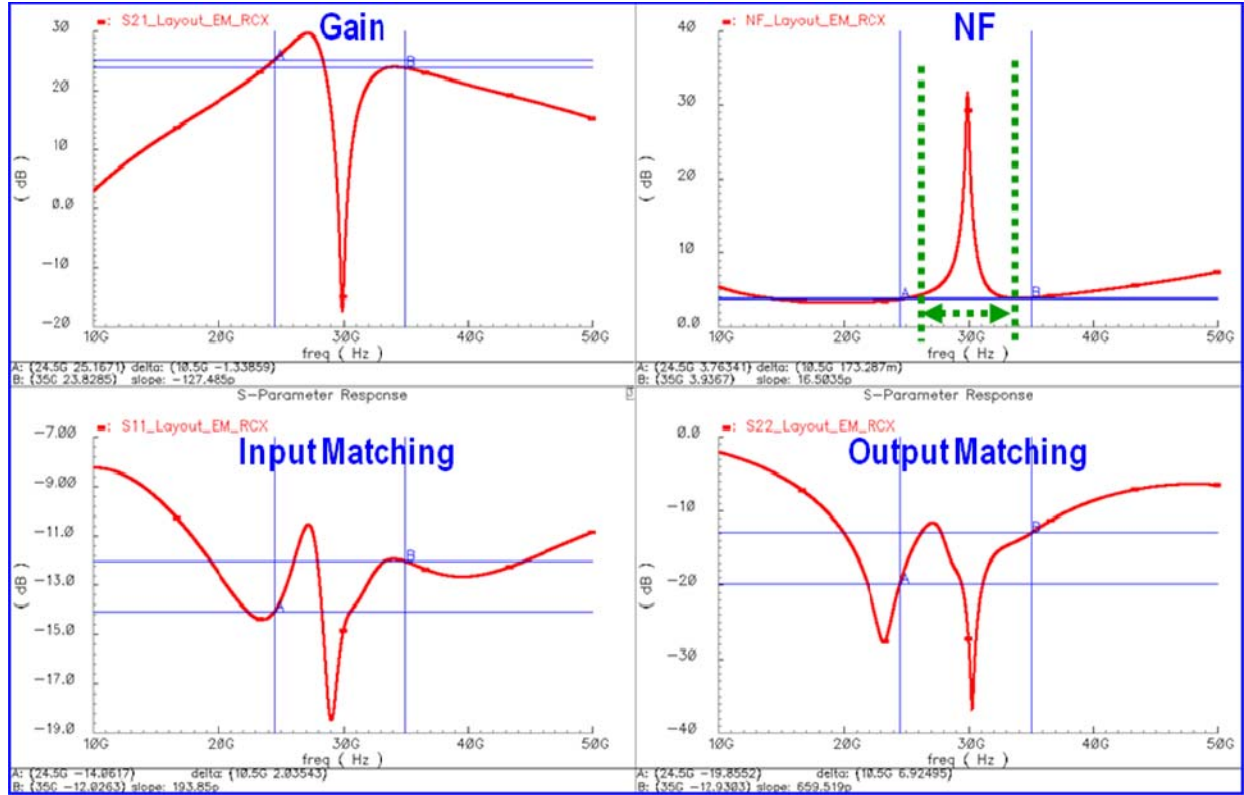


Figure 24. Simulation results of the concurrent dual-band LNA with active notch filters.

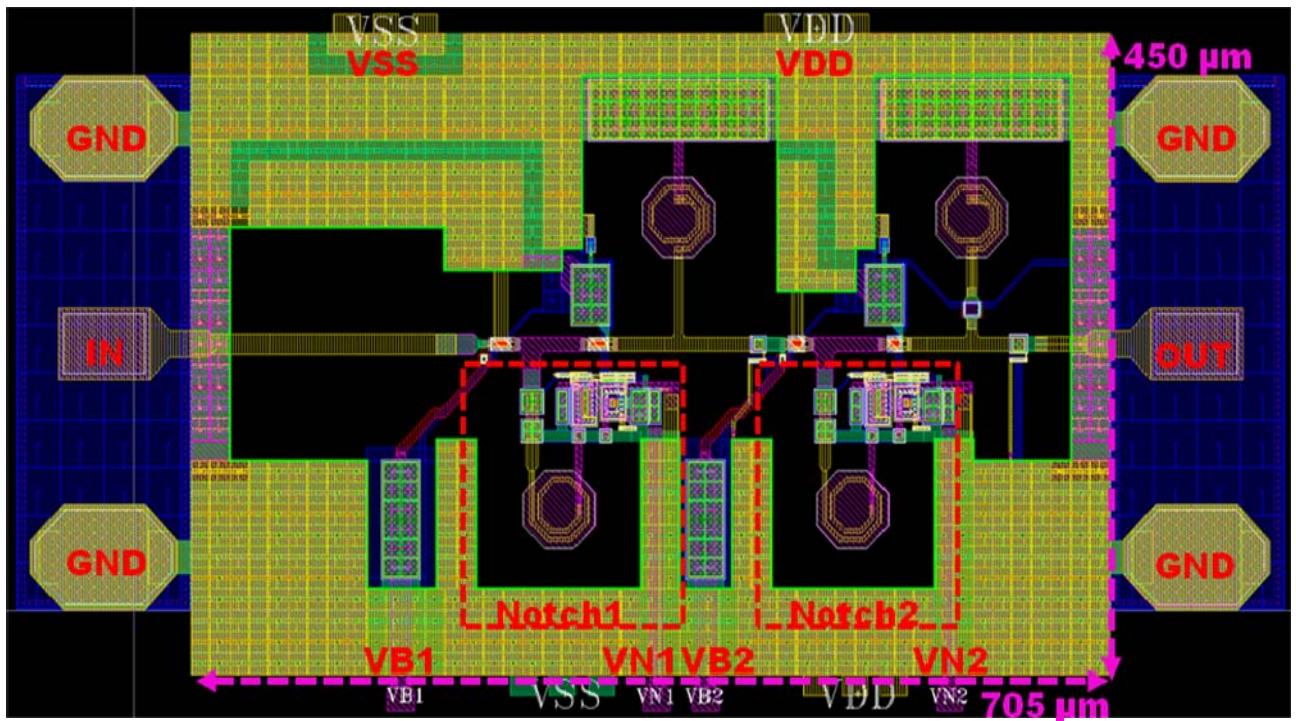


Figure 25. Layout of concurrent dual-band LNA with active notch filters.

For the concurrent dual-band LNA with active notch filters, additional power consumption and increase of noise figure (NF) are unavoidable due to the transistors in the active notch filters. In order to resolve these disadvantages, the second concurrent dual-band LNA is designed by integrating one passive notch with feedback scheme as shown in Fig. 26. The passive notch is fed-back from the collector of CE transistor at the second stage to the tapped inductor load of the first stage. This feedback notch configuration indeed forms a dual-band load network of the first stage, while providing large stop-band attenuation without additional power consumption. Most importantly, the removal of the active notch filter at the first stage results in lower NF performance compared to the concurrent dual-band LNA with active notch filters. The simulation results and layout of this LNA are shown in Figs. 27 and 28, respectively.

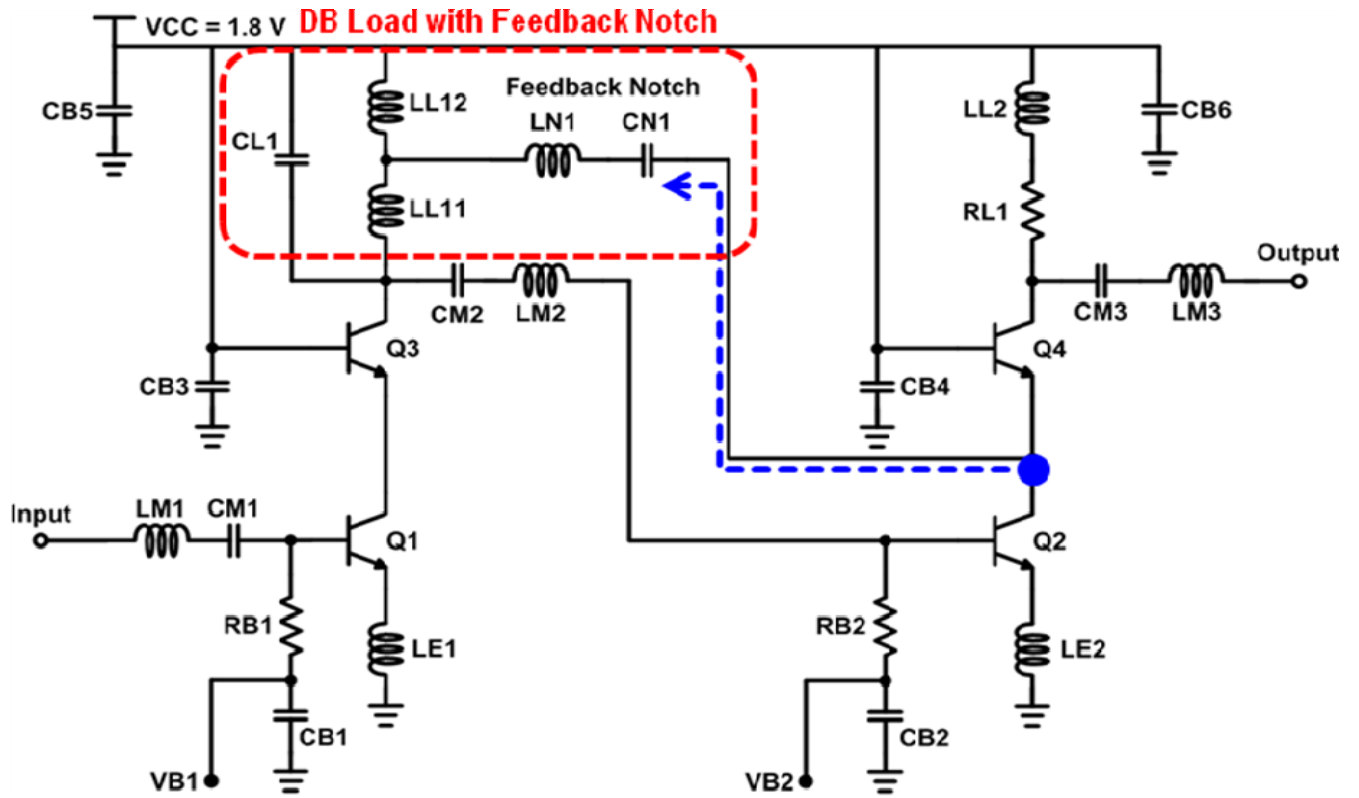


Figure 26. Schematic of the concurrent dual-band LNA with feedback notch filter.

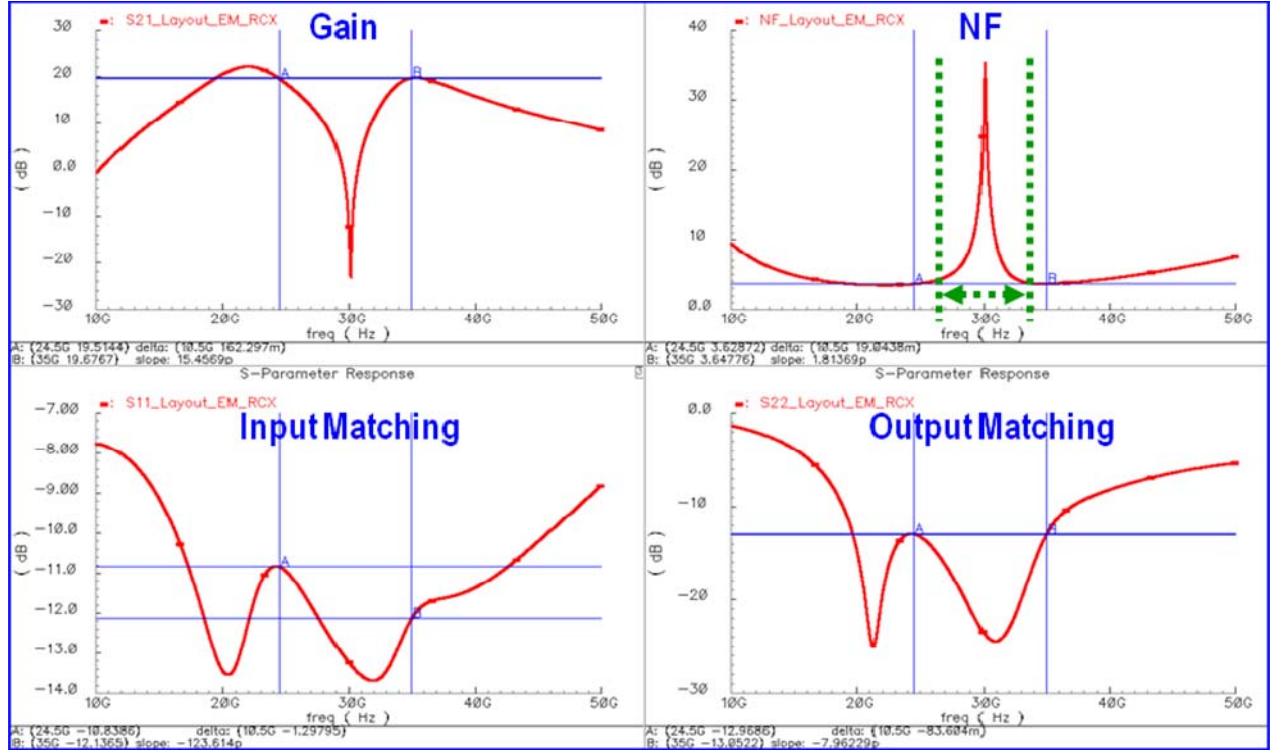


Figure 27. Simulation results of concurrent dual-band LNA with feedback notch filter.

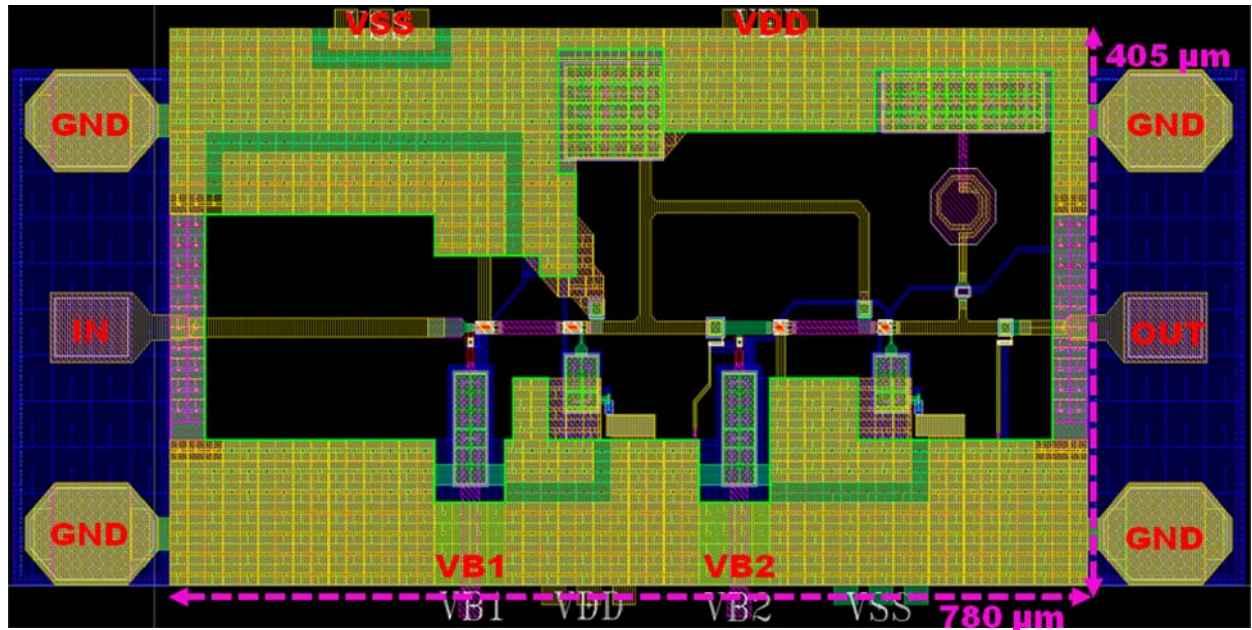


Figure 28. Layout of concurrent dual-band LNA with feedback notch filter.

These concurrent dual-band LNA are designed using a 0.18- μm SiGe BiCMOS process having higher cut-off frequency (f_T) than the fist dual-band LNA shown in Fig. 21. The post-layout simulation results of the concurrent dual-band LNA with active notch filters show a power gain of 25.1/23.8 dB and NF of 3.76/3.93 dB at 24.5/35 GHz, respectively. The power consumption is

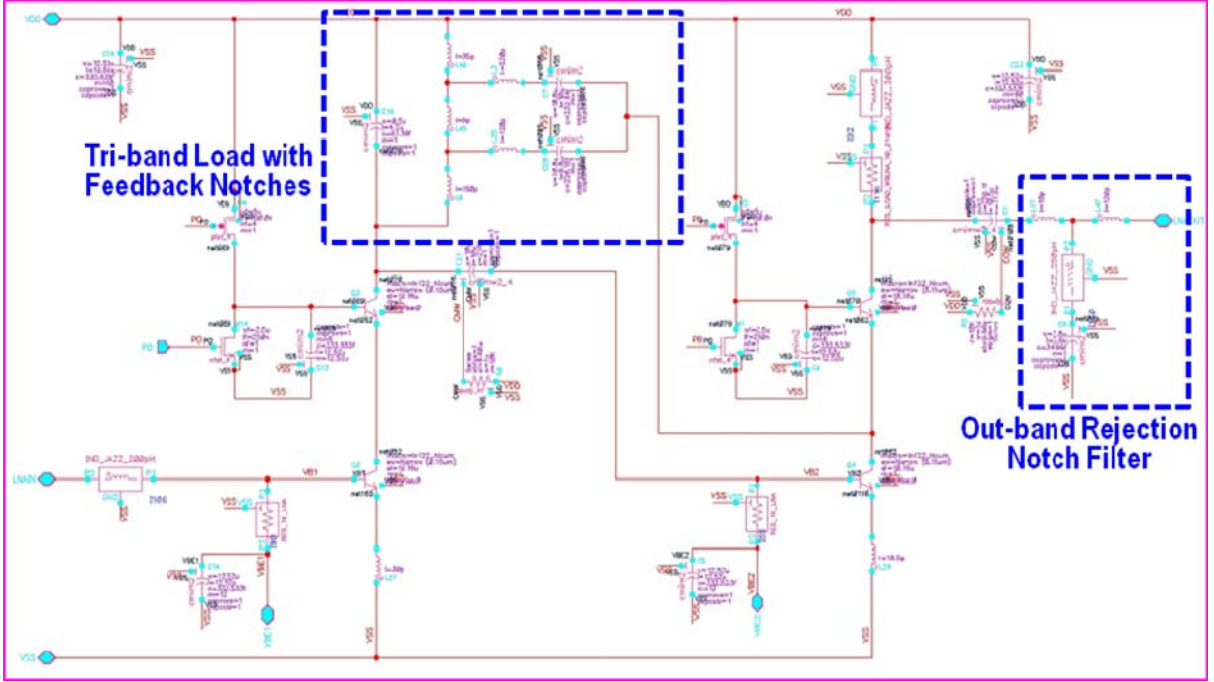
29.5 mW. It occupies an area of $705 \times 450 \mu\text{m}^2$. The concurrent dual-band LNA with feedback notch filter achieves a power gain of 19.6/19.5 dB and NF of 3.62/3.64 dB at 24.5/35 GHz, respectively. The power consumption is 25.2 mW. It occupies $780 \times 405 \mu\text{m}^2$. The input and output return losses of both LNAs are larger than 10 dB over the desired bands. The design results are summarized in Table 8.

Table 8 - Summary of the design results of the dual-band LNAs.

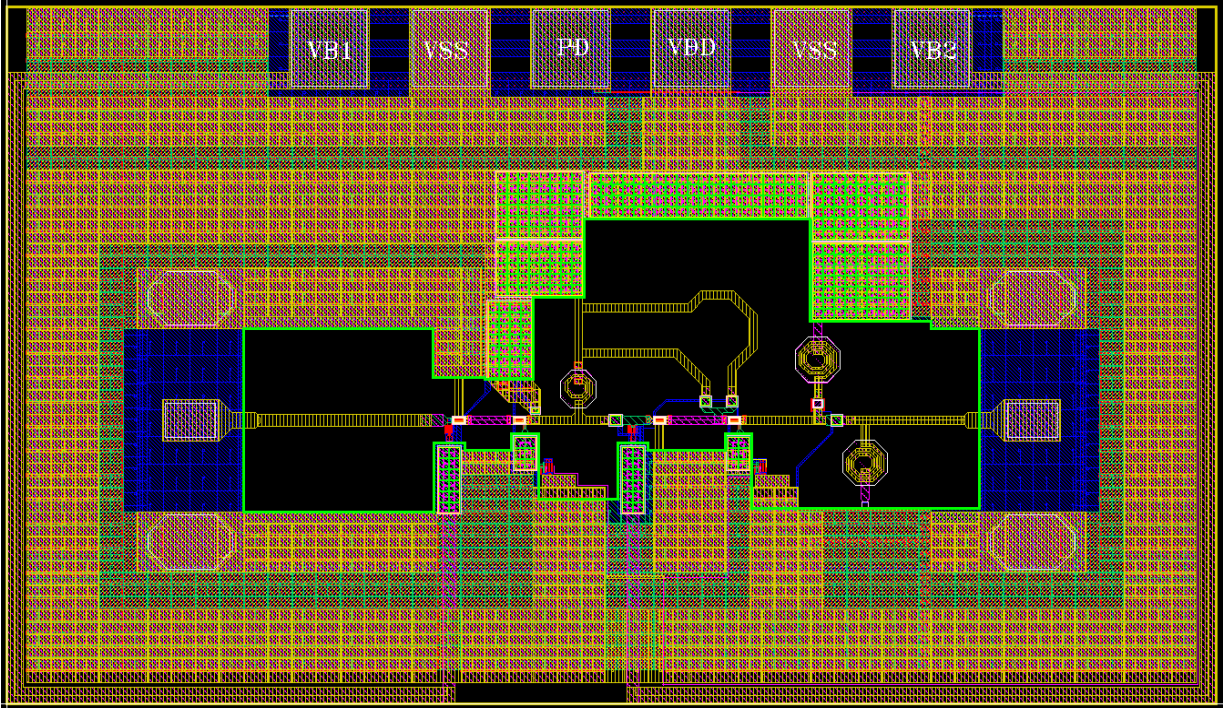
Parameters	Simulation Results		Unit
	DBLNA1	DBLNA2	
Frequency	24.5 / 35	24.5 / 35	GHz
Power Gain	25.1 / 23.8	19.5 / 19.6	dB
Noise Figure	3.76 / 3.93	3.62 / 3.64	dB
S11	-14 / -12	-10.8 / -12.1	dB
S22	-19.8 / -12.9	-12.9 / -13	dB
Input IP3	-12.6 / -12.8	-12 / -8.6	dBm
Input P1dB	-24.8 / -24.5	-23.5 / -21.3	dBm
Current Consumption	16.4	14	mA
VDD	1.8	1.8	V

3.2.3 Concurrent Tri-band LNA

A concurrent tri-band LNA was also designed for Ku-, K-, and Ka-band multiband radar applications and can be used for the dual-band sensor as well. Fig. 29 shows the schematic and layout of the tri-band LNA. The tri-band LNA integrates two feedback notches. The notches are fed-back from the collector of the CE transistor at the second stage to the tapped inductor load of the first stage. This feedback notch configuration forms a tri-band load network for the first stage and provides high quality factor comparable to that of active notch without any additional power consumption. So, high stop-band characteristics and lower NF performance can be achieved simultaneously. Also, in order to reduce the undesired out-band signals higher than Ka-band, a passive notch filter is integrated in the output matching network. The LNA occupies the area of $1505 \times 855 \mu\text{m}^2$ including pads and consumes 45 mW of power. Fig. 30 shows the measurement results. The LNA achieves a power gain of 22.3/24.6/22.2 dB at 13.5/24.5/34.5 GHz, and NF of 3.7/3.3/4.5 dB at 13.5/22.5/33.5 GHz, respectively. Note that the measured NF responses are separated into two parts, one for the low- and mid-band and another for the high-band, due to the different receiver NF of the vector network analyzer at each frequency band.

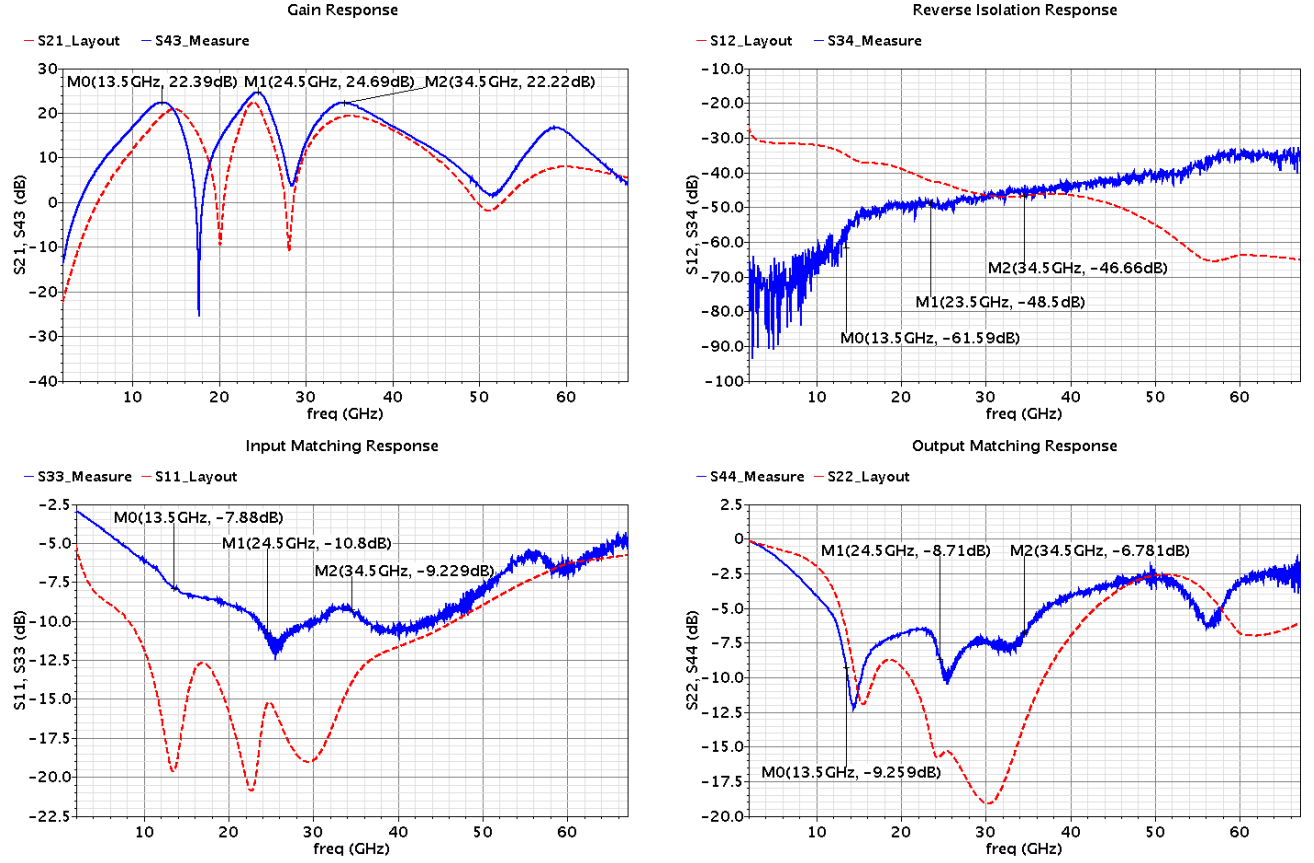


(a)

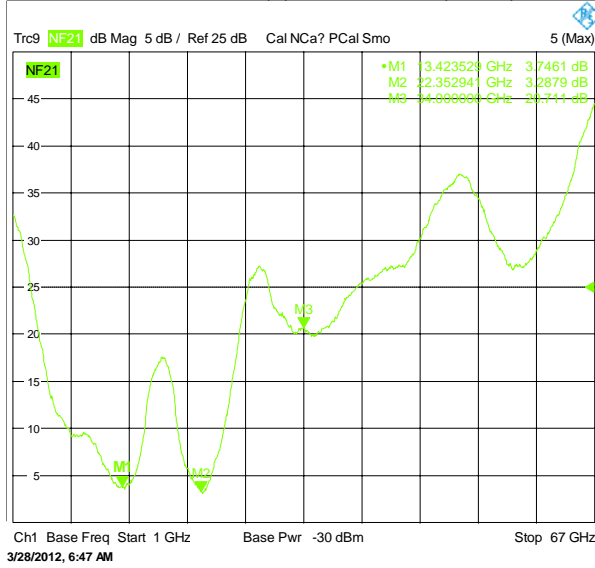


(b)

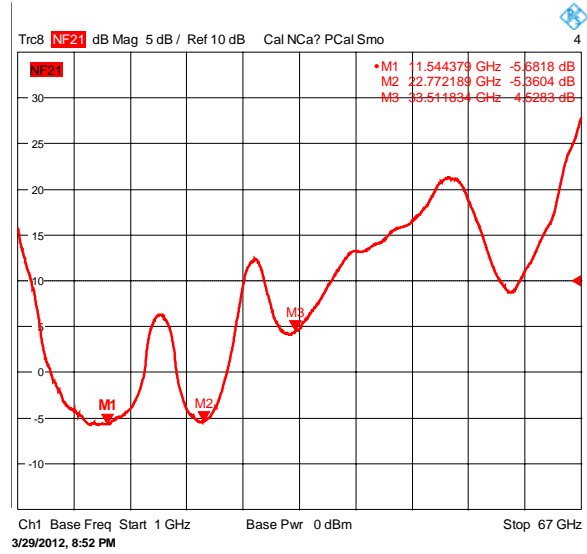
Figure 29. Schematic (a) and layout (b) of the concurrent tri-band LNA.



(a) Measured (solid) and simulated (dashed) S-parameters



(b) NF for low-band and mid-band



(c) NF for high-band

Figure 30. Measurement results of the concurrent tri-band LNA.

3.3 Band-gap Reference Bias

The bias distribution network is important for sensors, particularly large arrays of sensors. Its design needs to be optimized to results in not only optimum performance but also small size for the concurrent 24.5/35 GHz sensor.

The multiband sensor adopts a local bias distribution with each channel having its own precise band-gap reference (BGR) bias (Fig. 31) inside the channel. Such a precise bias network is vital for practical operation of sensors. The BGR output voltage (0.9 V) and current (43 μ A) for each channel are applied to each circuit in the channel. The referred voltage and current to each circuit is then reconfigured or multiplied for individual circuit use. The BGR is designed to provide an accurate biasing current and voltage independent of process, supply voltage, and temperature (PVT) variations. We have designed and fabricated this BGR in SiGe BiCMOS and achieved reference voltage of 0.8984-0.9023 V, which is only 3.95-mV variation over the whole PVT variations. The reference current varies from 36.8 μ A to 51 μ A, which represents 14.2 μ A variation (33 %) over the whole PVT variation while maintaining constant current at each PVT condition. Fig. 31 shows the layout of the designed band-gap reference (BGR) bias network to be integrated within the die of multiband sensor. Fig. 32 shows the performance of the BGR.

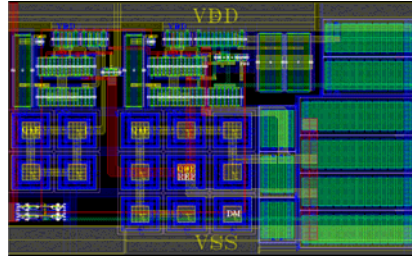
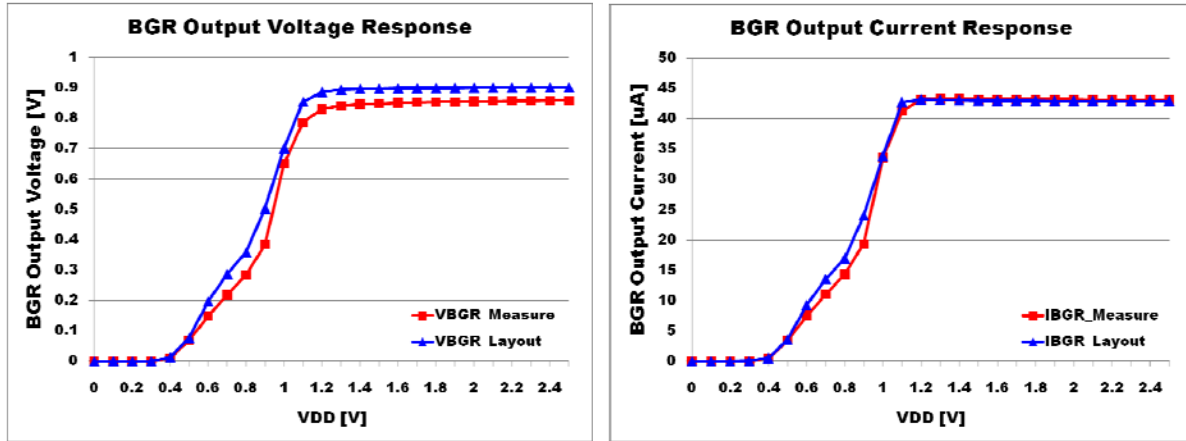


Fig. 31. Layout of the BGR bias network.



(a) BGR output voltage

(b) BGR output current

Figure 32. Simulation and measurement results of the BGR output voltage (a) and current.

3.4 Mixers

There are various mixers needed for the sensors as seen in the system architecture shown in Fig. 1.

3.4.1 Concurrent Dual-band RF Mixer

Fig. 33 shows the schematic of the concurrent dual-band mixer. It has a pseudo differential RF input stage with source-degeneration inductors to enhance the matching and linearity performance. The LO switching stage is composed of a double-balanced Gilbert cell, and a transformer and capacitors used for the differential input matching at 21 GHz. This LO input matching network provides inherently high isolation from RF to LO through the base-emitter resistance of the BJT. The IF output matching circuit consists of parallel and series band-pass resonators for 3.5 GHz and 14 GHz, respectively.

The period static simulation (PSS) results are shown in Fig. 34. When 24.5-GHz and 35-GHz RF tones are applied simultaneously, the RF mixer achieves conversion gain of -0.83/-1.5 dB and input P1dB of -12.08/-12.97 dBm at 24.5/35 GHz, respectively. NF of 8.47/14.26 dB at 24.5/35 GHz is also achieved as shown in Fig. 35.

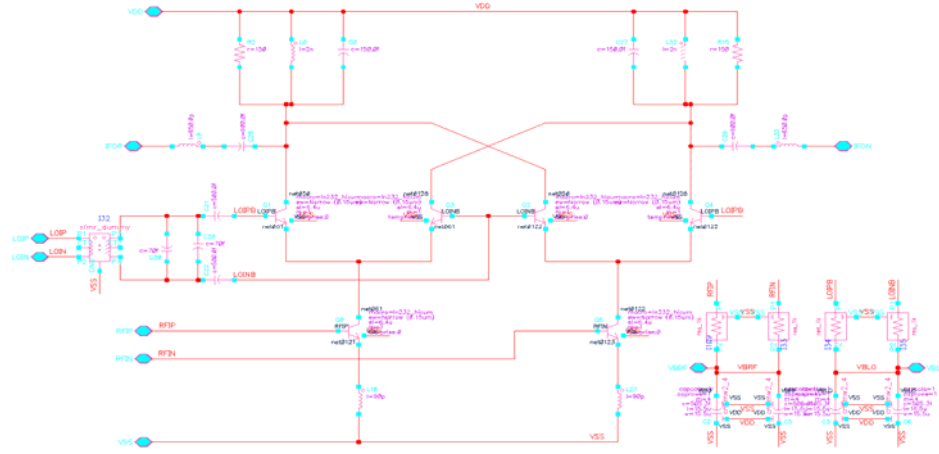


Figure 33. Schematic of the concurrent dual-band RF mixer.

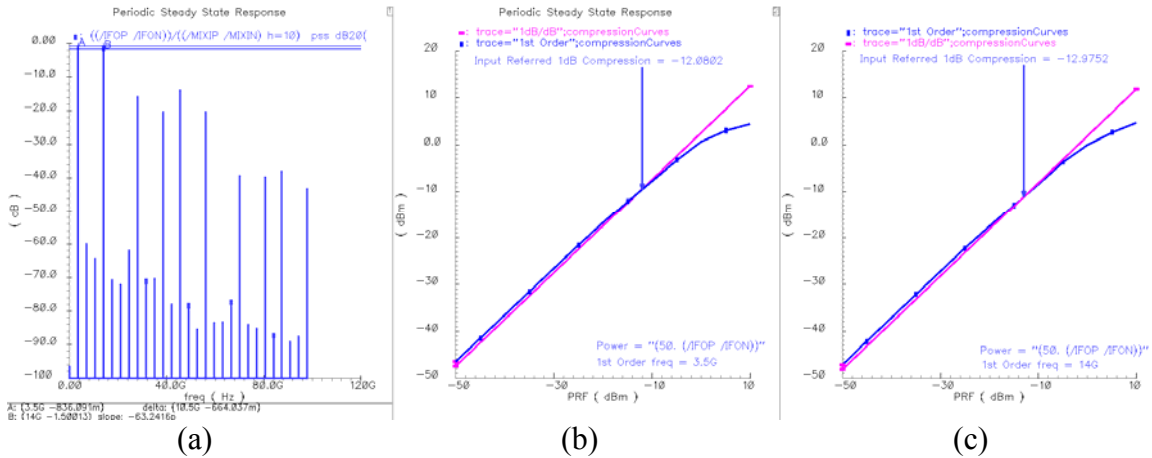


Fig. 34. PSS simulation results of the RF mixer: (a) voltage conversion gain, (b) P1dB for 24.5 GHz RF input, and (c) P1dB for 35 GHz input.

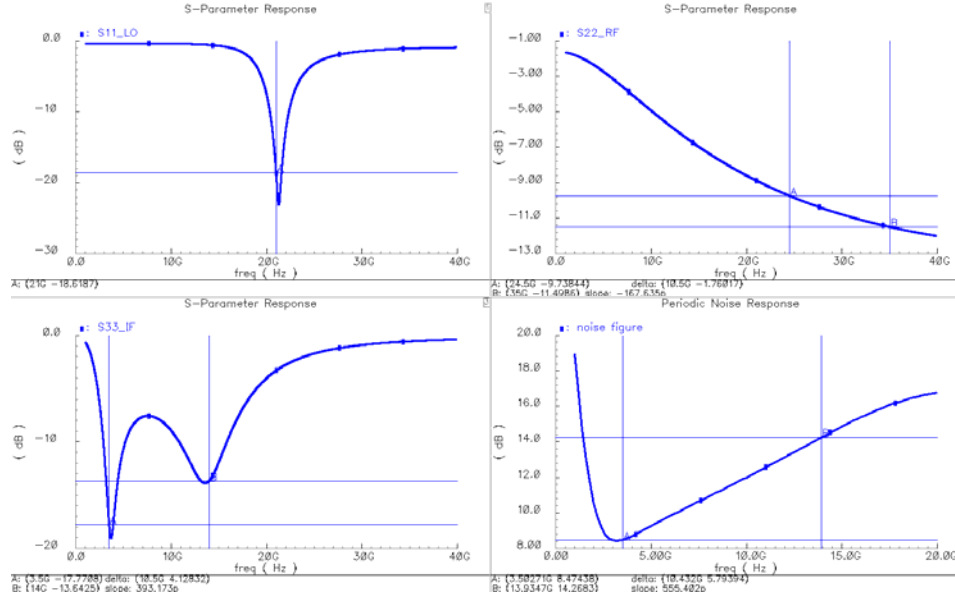
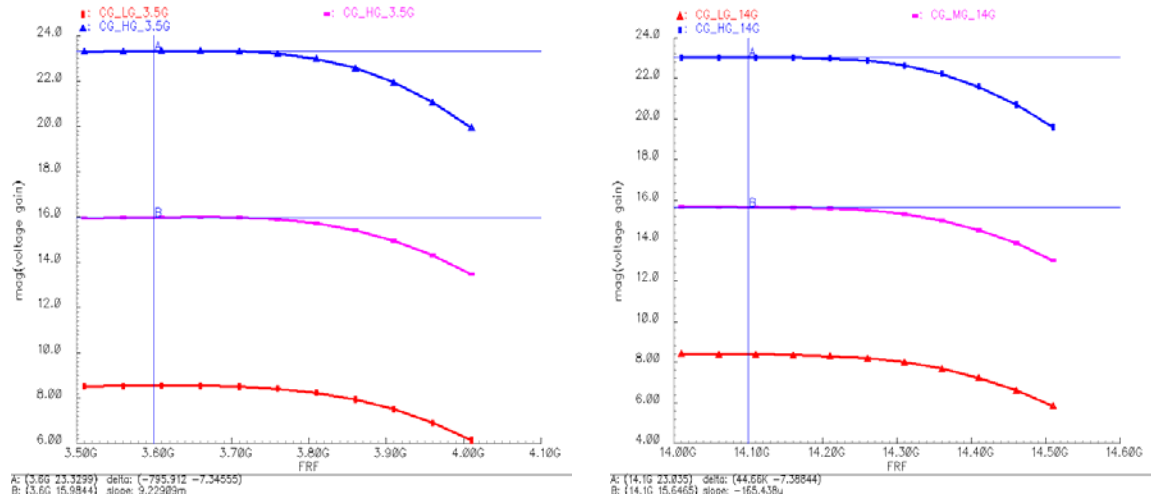


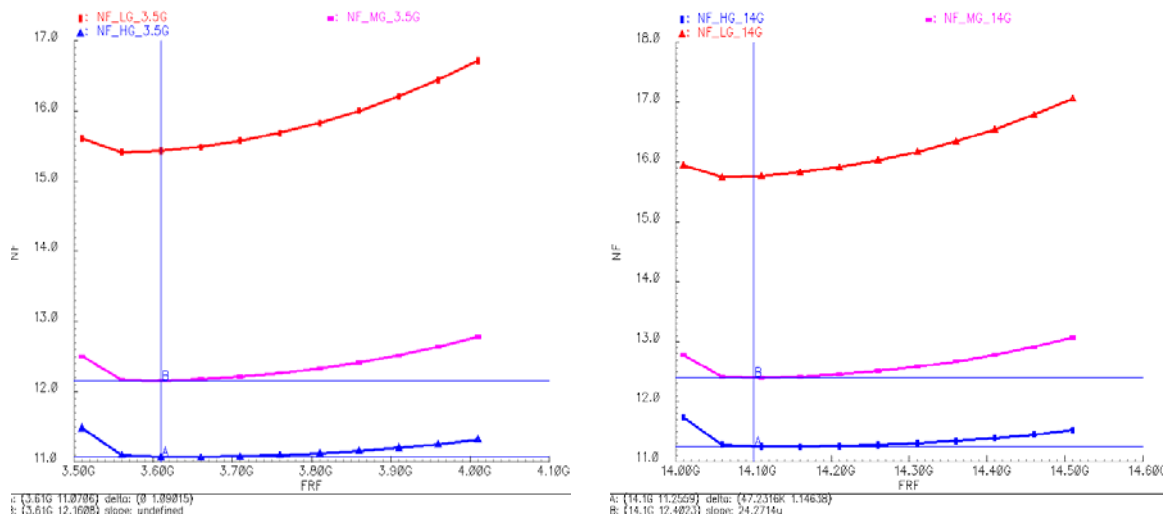
Fig. 35. S-parameter showing the LO (S11), RF (S22) and IF (S22) and NF of the RF mixer.

3.4.2 Intermediate Frequency (IF) Mixer

Figure 36 shows the schematic of the 3.5/14-GHz switchable subharmonic mixer designed for IF to base-band down-conversion. After the first down-conversion from 24.5/35 GHz of the dual-band RF with a 21-GHz local oscillator (LO) signal, two intermediate frequency bands exist at 3.5/14 GHz accordingly. These IF signals can be down-converted to base-band through the second local oscillator signals at 3.5/14 GHz. In order to share the down-conversion path for the dual-band operation, the IF mixer is designed to switch the 3.5/14 GHz LO signals. The fundamental mode (1x) is operated with the 3.5-GHz LO signal and the quadruple subharmonic (4x) mode utilizes the 14-GHz LO signal, whose frequency is four times of 3.5 GHz. Also the IF mixer has three-step variable conversion gain and I/Q gain mismatch compensation functions. The design results are shown in Fig. 37, and the detailed design results are summarized in Table 9.



(b) Conversion gain for 3.5 GHz (left) and 14 GHz (right) IF



(c) Noise figure for 3.5 GHz (left) and 14 GHz (right) IF as a function of conversion gain.

Figure 37. Performance of the of switchable dual-band IF subharmonic mixer.

Table 9. Result summary of the switchable dual-band IF subharmonic mixer

Parameters	Target Spec.	Simulation Results (LB)			Simulation Results (HB)			Unit
Gain Mode	HG/MG/LG	HG	MG	LG	HG	MG	LG	
Frequency	3.5 / 14	3.6			14.1			GHz
Conversion Gain	22/15/8	23.3	15.9	8.5	23	15.6	8.3	dB
Noise Figure (DSB)	13/15/18	11	12.1	15.4	11.2	12.4	15.7	dB
1dB Gain Bandwidth	> 200	380	405	405	375	395	390	MHz
Input IV3	-20	-17.8			-15.4			dBV
Input V1dB	-30	-29.4			-24.9			dBV
IF Return Loss	>10	10.7			12.5			dB
LO Return Loss	> 15	26.4			26.4			dB
IQ Gain Error (at BB = 200 MHz)	< ± 1	0.48			0.2			dB
IQ Phase Error (at BB = 100 MHz)	< ± 5	1.5			5.2			°
Current Consumption	25	22.2			21.8			mA
VDD	1.8	1.8			1.8			V

3.5 IF Low-Pass Filter and VGA

The IF low-pass filter and variable gain amplifier (VGA) are needed for the receiver as seen in the system architecture shown in Fig. 1.

3.5.1 IF Low-Pass Filter

Figure 38 shows the layout of the filter with output buffer. The simulation results for gain, frequency, and quality factor (Q) are given as follows.

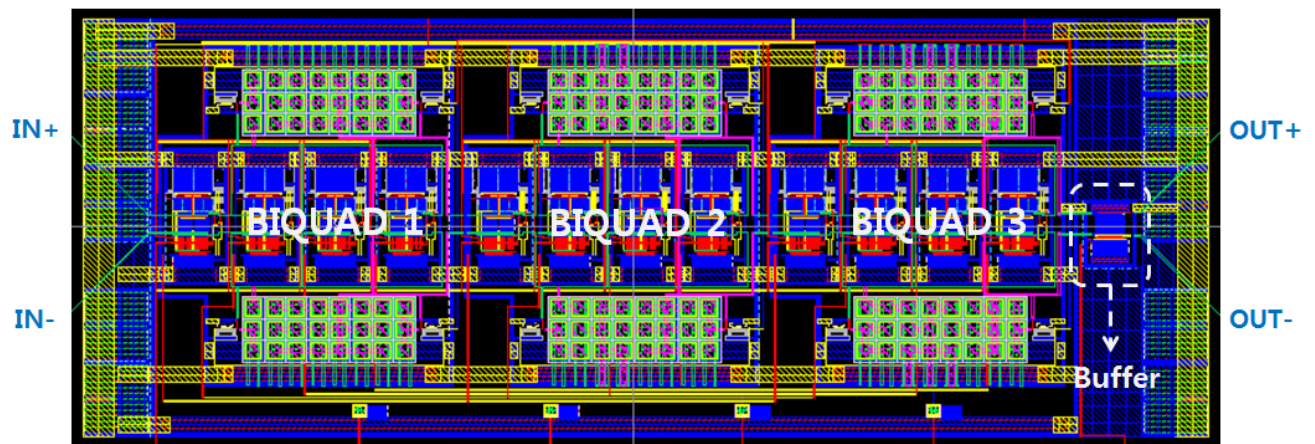


Figure 38. Layout of the low-pass filter.

3.5.1.1 Frequency Tuning

3.5.1.1.1 Coarse Frequency Tuning

Coarse tuning can be achieved by tuning all the 4 tuning variables (V_q , V_{gain} , V_{freq1} , and V_{freq2}) with the same value. Also, by switching the capacitor array, either low or high frequency mode can be selected. Fig. 39 shows the coarse frequency tuning characteristics in both low and high frequency modes. In the low-frequency mode, frequency can be tuned from 200 MHz to 400 MHz while it can be tuned from 360 MHz to 780 MHz in the high-frequency mode. Stopband rejection requirement is satisfied for all the frequency tuning settings.

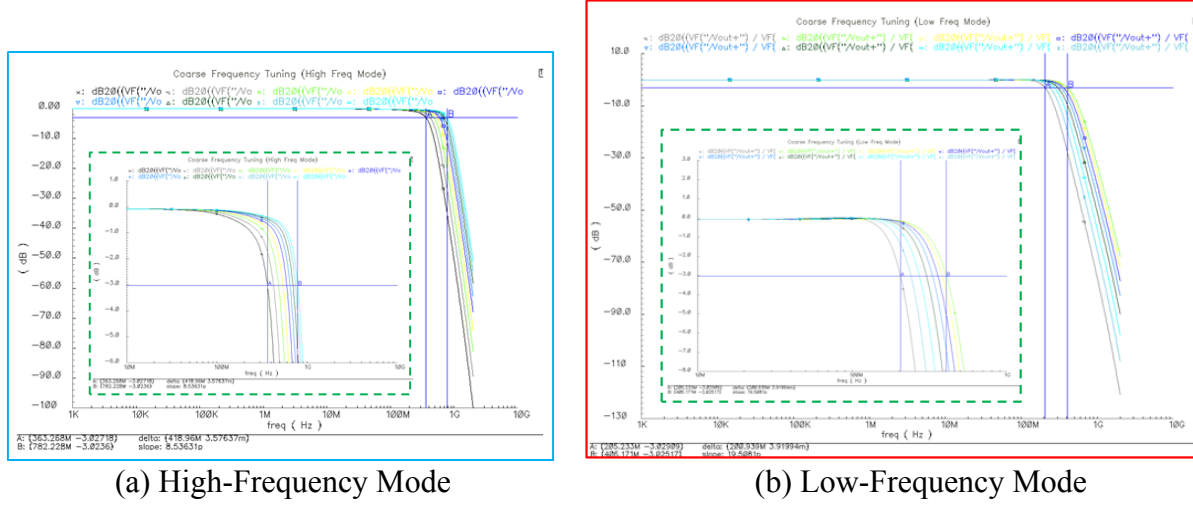


Fig. 39. Coarse frequency tuning.

3.5.1.1.2 Fine Frequency Tuning

Once the coarse frequency tuning is done, fine frequency tuning with less than 10-MHz resolution can be achieved by varying the tuning variable, V_{freq1} . Fig. 40 plots the fine frequency tuning characteristics when the 3-dB cutoff frequency is set to be 594 MHz by coarse tuning. Stop-band rejection requirement is met over 80-MHz fine tuning range.

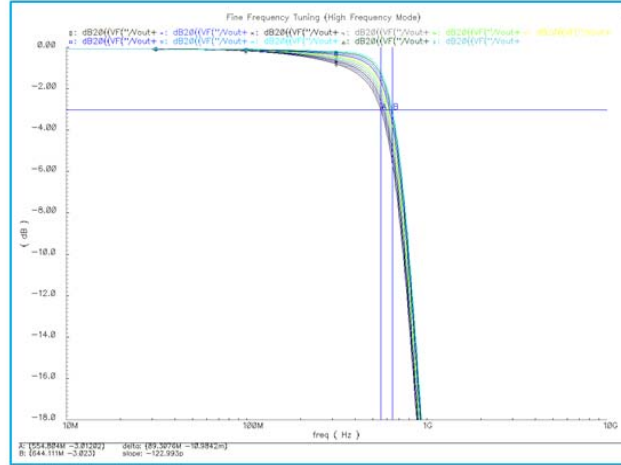


Fig. 40. Fine frequency tuning (for 3-dB frequency of 594 MHz).

3.5.1.2 Gain Tuning

Gain tuning can be achieved by tuning the variable V_{gain} . Fig. 44 shows the gain tuning characteristics when the 3-dB cutoff frequency is set to be 594 MHz by coarse tuning. Gain tuning from -5 dB to 5 dB (10-dB tuning range) can be achieved.

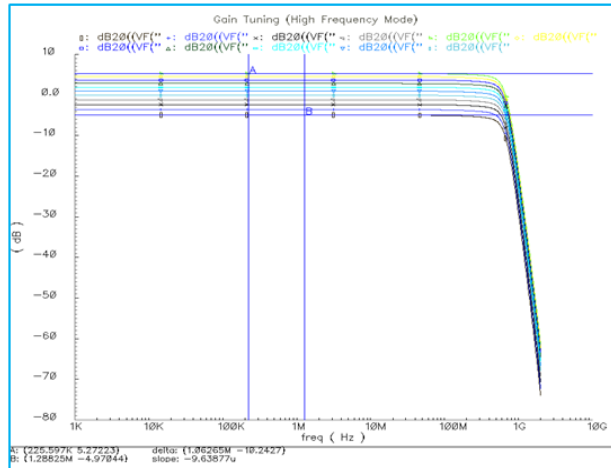


Fig. 41. Gain tuning (for 3-dB frequency of 594 MHz)

3.5.1.3 Q Tuning

Q can be controlled by varying the variable V_q . It is hard to quantify the Q value while the Q tuning effect can be seen from Fig. 42. Note that the 3-dB frequency also slightly changes as Q is tuned while satisfying the stopband rejection requirement.

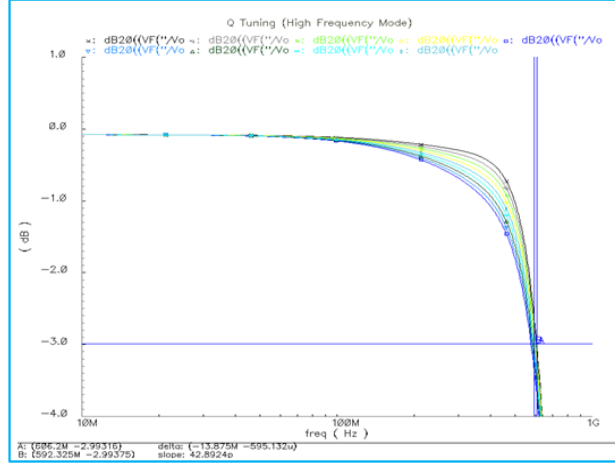


Fig. 42. Q Tuning (for 3-dB frequency of 594 MHz)

3.5.2 IF VGA Design

Figure 43 shows the overall wideband digitally-controlled IF VGA (Variable Gain Amplifier) structure.

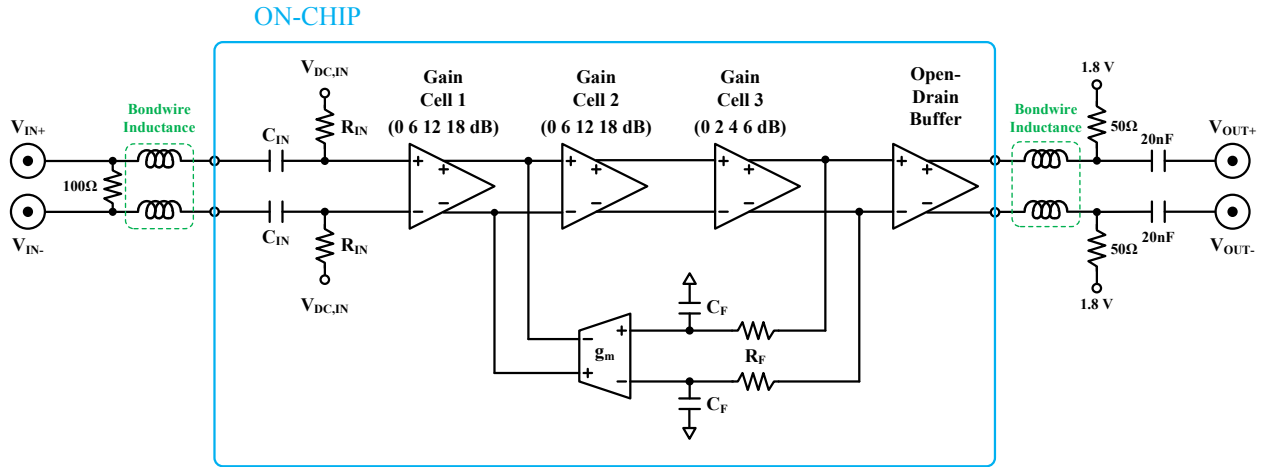


Fig. 43. Overall VGA structure.

VGA consists of 3 cascaded gain cells (two with 6-dB step and one with 2-dB step), input high-pass filter (HPF), and DC offset cancellation loop. Gain tuning from 0 dB to 40 dB with 2-dB step is achieved by 6-bit control to the gain cells (2 bits for each cell). The input HPF blocks any DC offsets coming from the preceding stages such as mixer and low-pass filter. DC offset cancellation loop removes DC offset generated inside VGA due to layout mismatches, etc. Output buffer is added at the output of VGA for measurement. Open-drain buffer is employed for wideband circuit measurement while having loss (around 7 dB).

Gain cell structure is shown in Fig. 44. It is based on fully differential cascode amplifier with degeneration resistor array. For the gain cell with 6-dB step, gain tuning from 0 dB to 18 dB is achieved by switching cascode device as well as degeneration resistor array. For the gain cell

with 2-dB step, only degeneration resistor is switched to achieve gain tuning from 0 dB to 6 dB. Active inductor is added at the output of each gain cell to increase 3-dB bandwidth of each gain cell and hence that of VGA. Each gain cell is controlled by a single 2-to-4 decoder and the overall VGA achieves 40 dB of dynamic range with 2-dB step by using 6-bit control signals.

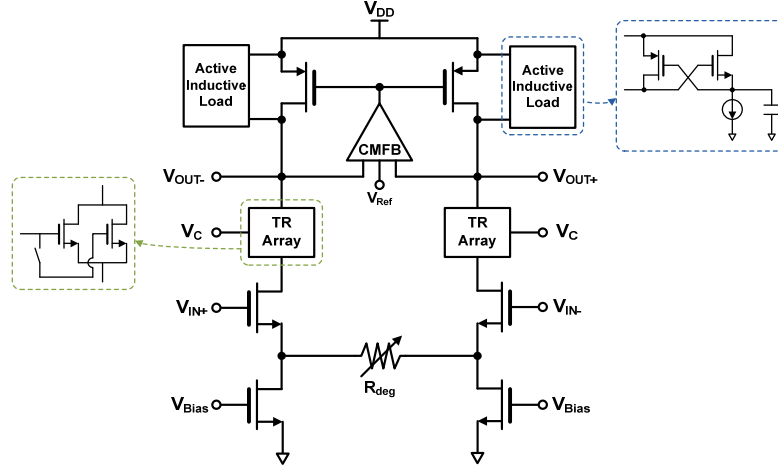


Fig. 44. Gain cell topology

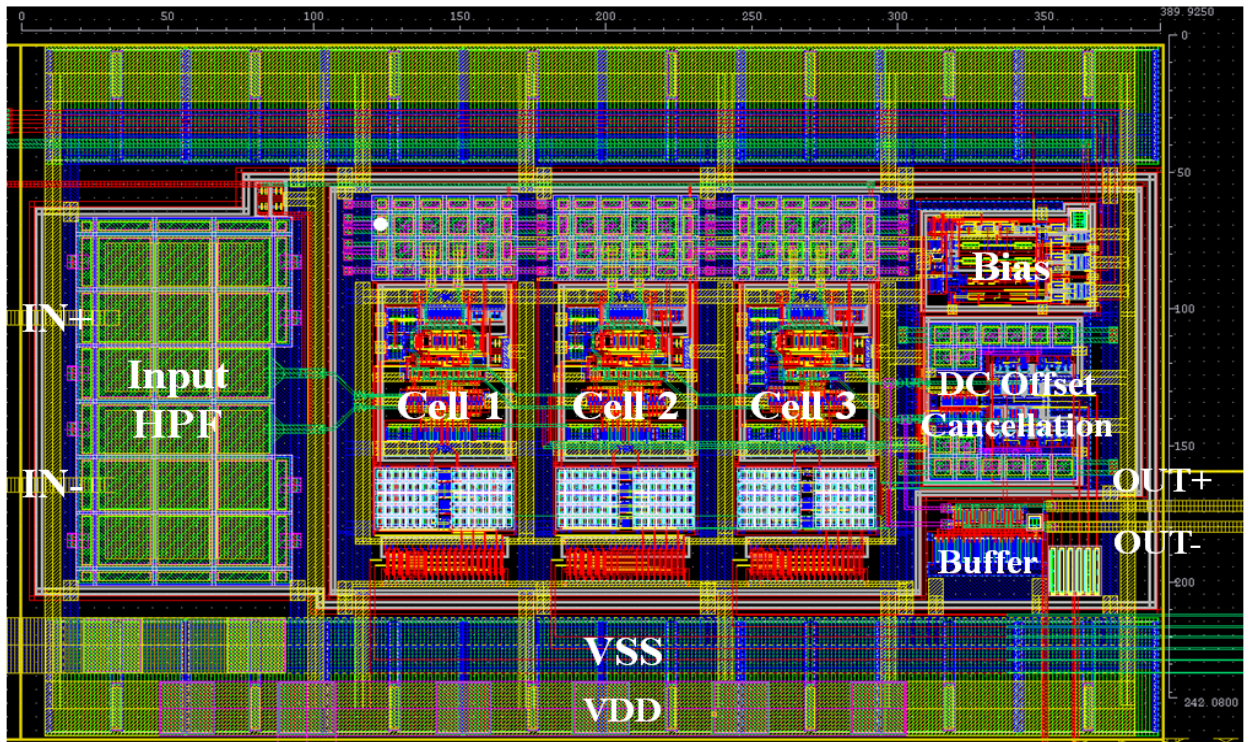


Fig. 45. Layout of overall VGA including output buffer

Fig. 45 shows layout of the VGA including output buffer. Total area including input HPF, output buffer, VDD and VSS is 0.38 mm by 0.25 mm.

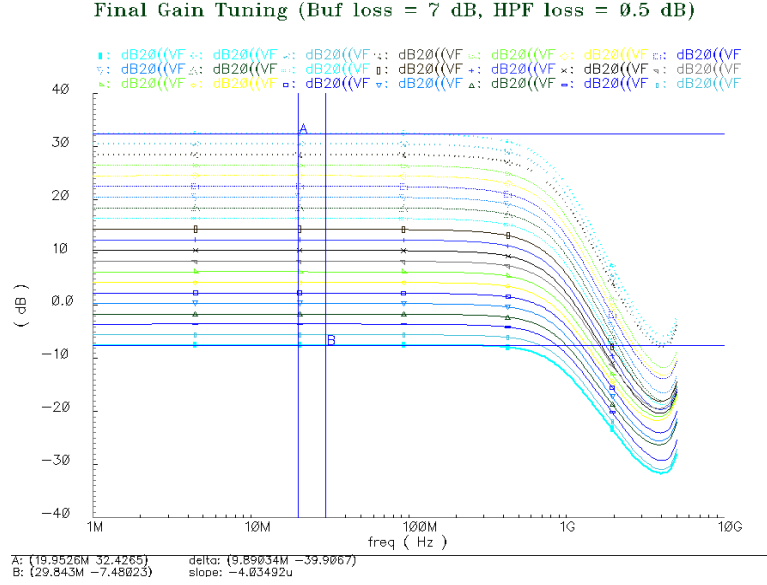


Fig. 46. Gain tuning characteristics of VGA

Fig. 46 shows the AC response of the VGA. The gain can be tuned from -7.5 dB to 32.43 dB including loss of the input HPF (0.5 dB) and gain of the output buffer (7 dB). The maximum gain step error at mid-band (100 MHz) is less than 0.15 dB while that it is less than 0.2 dB at 500 MHz (meaning that the error is less than 10 % of step size). Lower 3-dB cutoff frequency due to input HPF and DC offset cancellation loop is kept below 150 KHz for all gain settings in order not to degrade any signals of interest. Resonance occurs around 10 GHz due to wirebond inductance, but it can be safely ignored since it resides at the frequency far above the 3-dB cutoff frequency of VGA. Fig. 47 shows plots the summary of gain tuning characteristics.

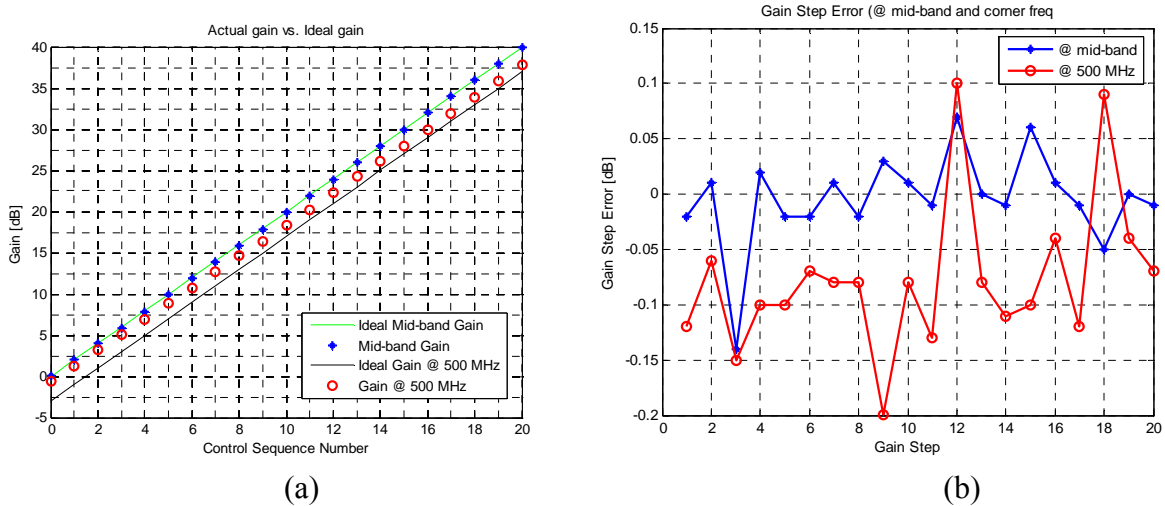


Fig. 47. (a) Deviation of gain from ideal value and (b) gain step errors at mid-band and cutoff frequency.

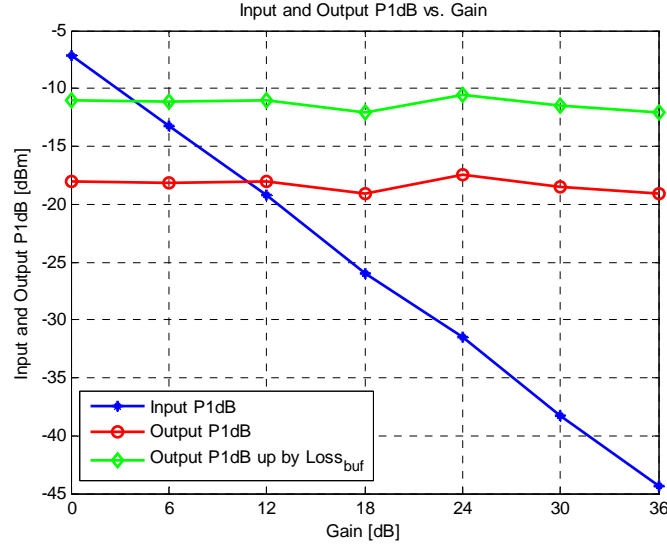
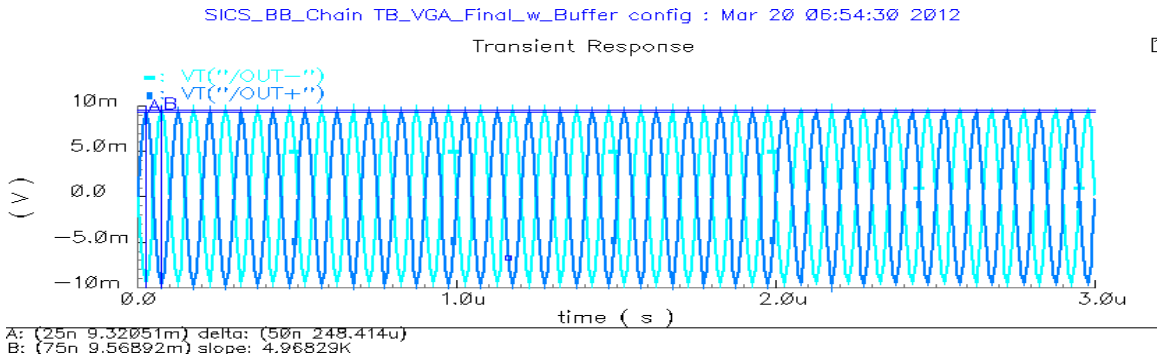


Fig. 48. Input and output P1dB.

For linearity, single-tone test was performed to check the input/output compression points. Fig. 48 plots the input and output P1dB of the VGA (including buffer). Input P1dB varies from -7 dBm to -44 dBm while output P1dB stays almost constant at -18 dBm as gain is tuned from 0 dB to 36 dB with 6-dB step. With consideration of output buffer loss (7 dB), VGA is expected to have output P1dB around -11 dBm.

Finally, the transient simulation was performed in order to check how DC offset cancellation loop corrects offsets generated inside VGA. Fig. 49 plots transient response for 0 dB gain setting. At start-up, DC offset at the output of buffer is about 250 μ V and it is reduced to 11 μ V after a while. The most problematic case is for the highest gain setting since the DC offset is amplified by the gain as well. Fig. 50 plots for the case of 36 dB gain. With the same DC offset at the output of buffer, the offset after settling becomes about 6 μ V. These results ensure that DC offset cancellation loop effectively corrects internally generated DC offset of VGA.



(a)

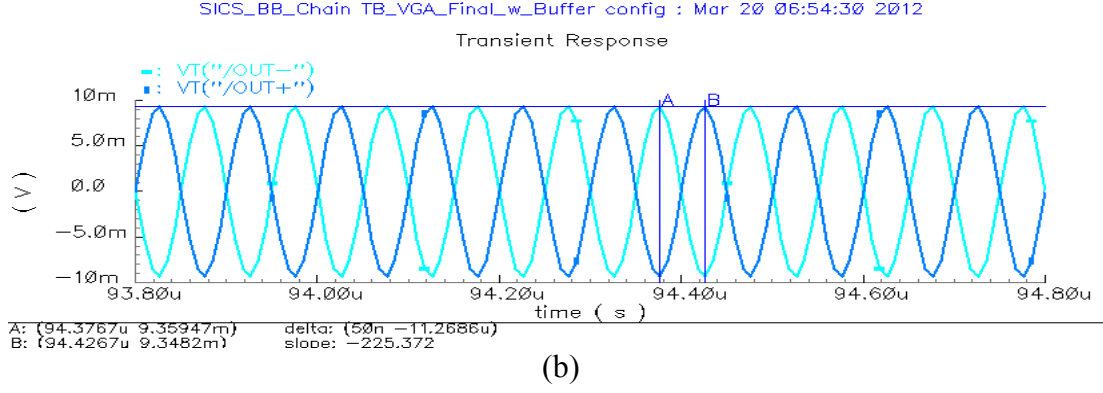


Fig. 49. Transient response for 0 dB: (a) start-up and (b) after settling.

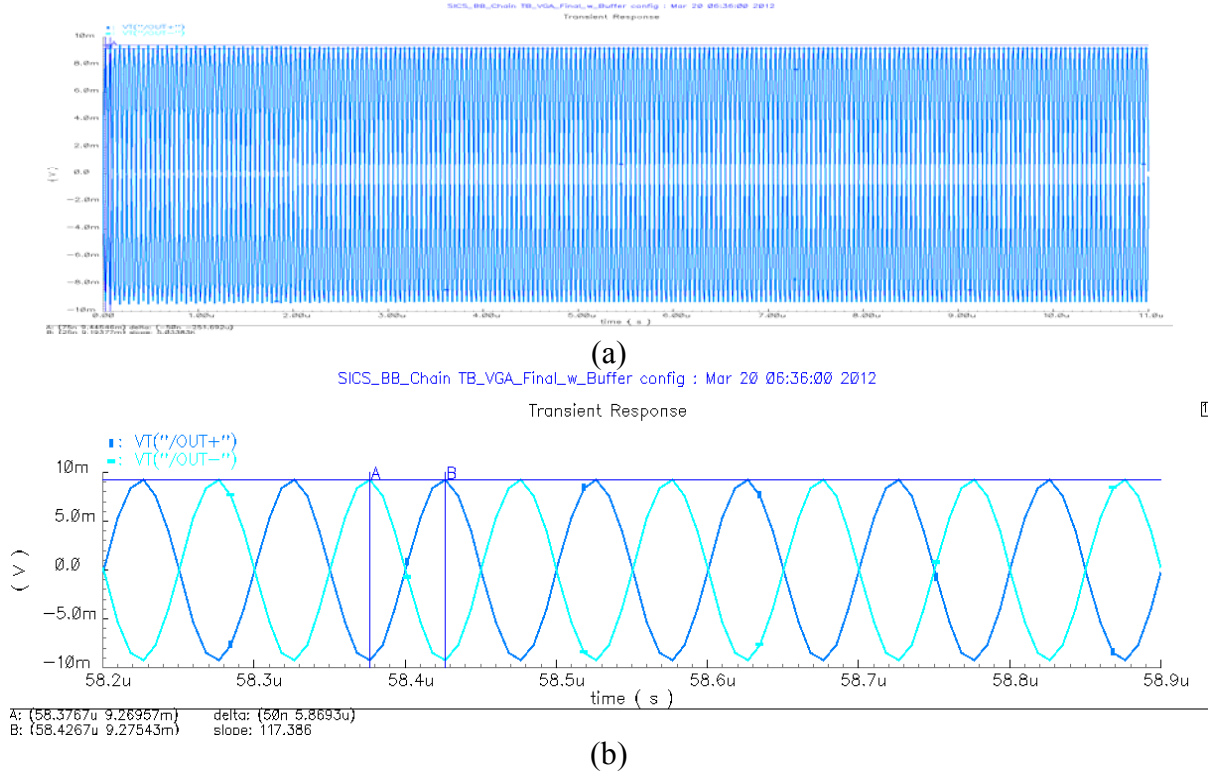


Fig. 50. Transient response for 36 dB: (a) start-up and (b) after settling.

The digitally-controlled wideband VGA is designed using only CMOS transistors in Jazz 0.18- μm BiCMOS process. The 3-dB cutoff frequency is larger than 500 MHz for all gain settings from 0 dB to 40 dB while the gain step error is less than 0.2 dB within the entire desired frequency band (from 200 KHz to 500 MHz). The input P1dB values of the VGA are greater than the desired input signal level for all gain settings, and the output P1dB values are all greater than -11 dBm. The DC offset cancellation effect has also been verified. The overall VGA consumes DC current less than 8 mA (buffer consumes 4 mA) at 1.8 V supply. The results are summarized in Table 10.

Table 10 - Summary of results

3dB Cutoff Frequency	> 500 MHz
Gain Tuning Range	0 dB ~ 40 dB
Tuning Step	2 dB
Max Step Error	< 0.2 dB
Output P1dB	> -16 dBm (100 mVpp)
Current	< 8 mA @ 1.8 V Supply
Size	0.38 mm x 0.25 mm

3.6 Concurrent Dual-band Receiver Front-end Integration and Simulation

Figure 51 shows the simulation model of a single channel of the concurrent dual-band receiver front-end as seen in the system architecture shown in Fig. 1. The RF mixer is reconfigured for I/Q mixer by using I/Q LO at 21 GHz. Fig. 39 shows the polarization selection switch which is designed to have single-ended input and differential output with 6-dB voltage gain and inserted between the concurrent dual-band LNA and RF mixer. The LC tank (L4, C4) under the differential pair replaces a typical current source formed by a transistor. By removing one stack of transistors, this AC coupled-current source increases the linearity further and helps balance the gain shape for each band. Two polarization selection switches share a differential inductor load as shown in Fig. 52. The differential outputs of the switches are combined together through the inductor, and applied to the RF mixer. The dual-band LNA and switch have power on/down control option, so each channel can be enabled and/or disabled independently. When one channel is in operation, another channel is in off-state, and vice versa. This increases the isolation performance by reducing the coupling from another channel. The first down-converted signals after the RF mixer are located at the dual-band IF of 3.5 GHz and 14 GHz. These IF signals are applied to the switchable dual-band IF subharmonic mixer. After the IF mixer, the final down-converted signals from 3.5 GHz and 14 GHz IF are located at the baseband frequency of 250 MHz.

Fig. 53 shows the conversion gain and NF performance of the whole receiver chain (LNA + Switch + RF Mixer + IF Mixer). The designed concurrent dual-band receiver front-end achieves a conversion gain of 62.8/60 dB and noise figure of 3.46/3.35 dB at 24.5/35 GHz, respectively.

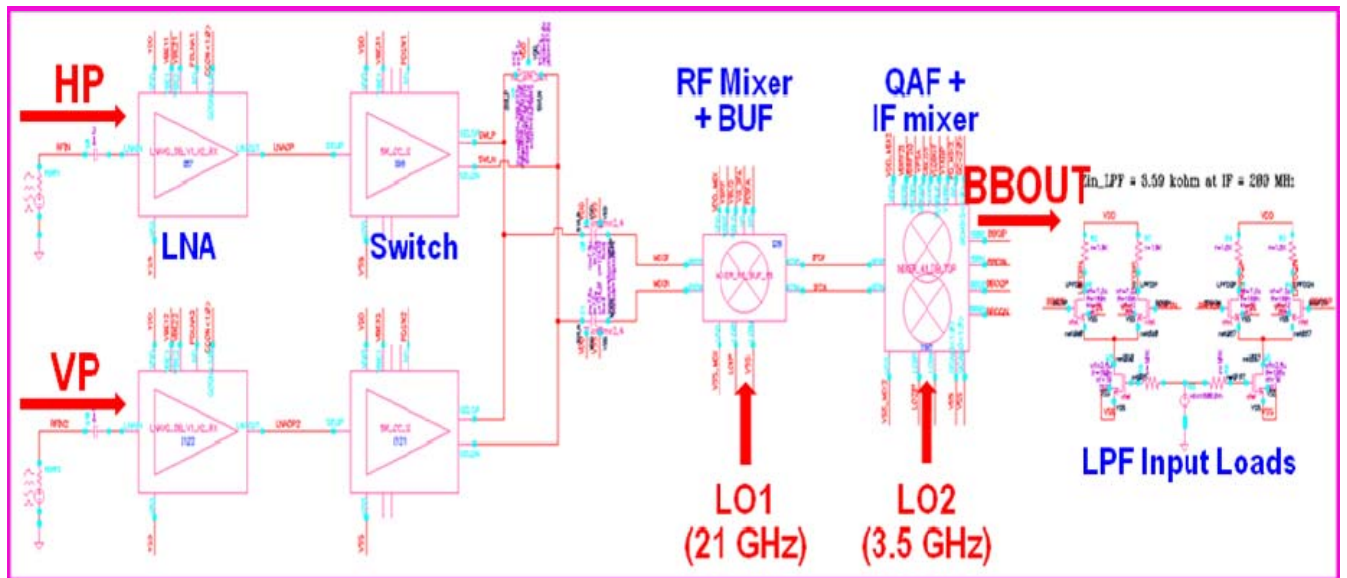


Figure 51. Integrated concurrent dual-band receiver front-end.

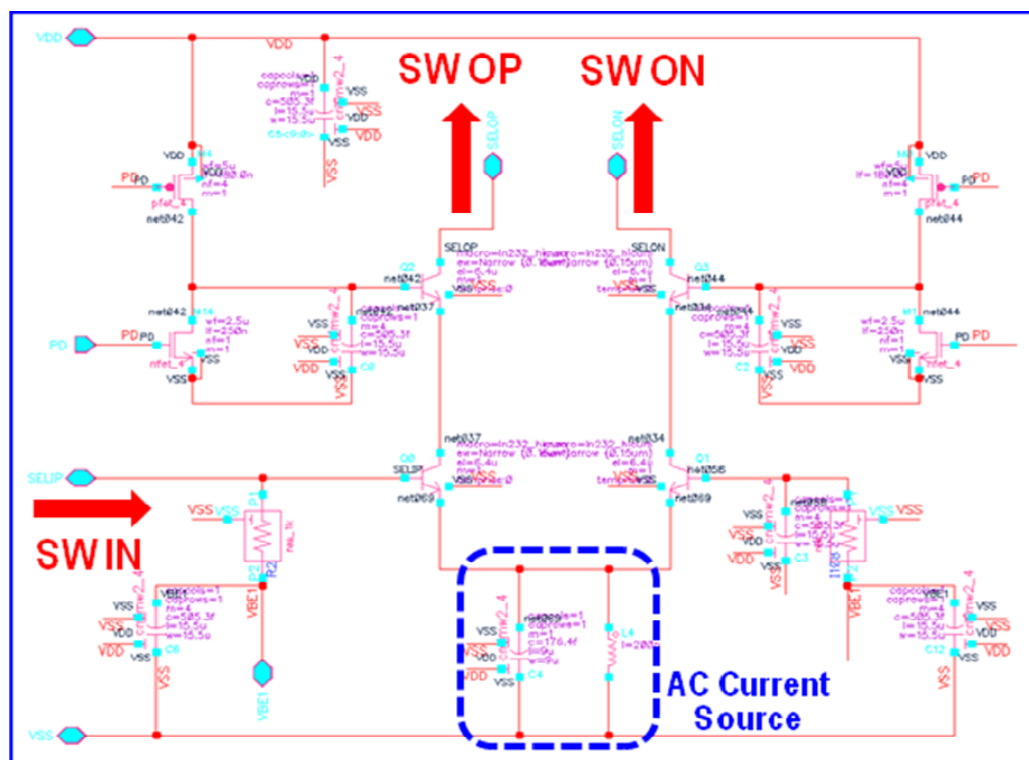


Fig. 52. Schematic of the polarization selection switch.

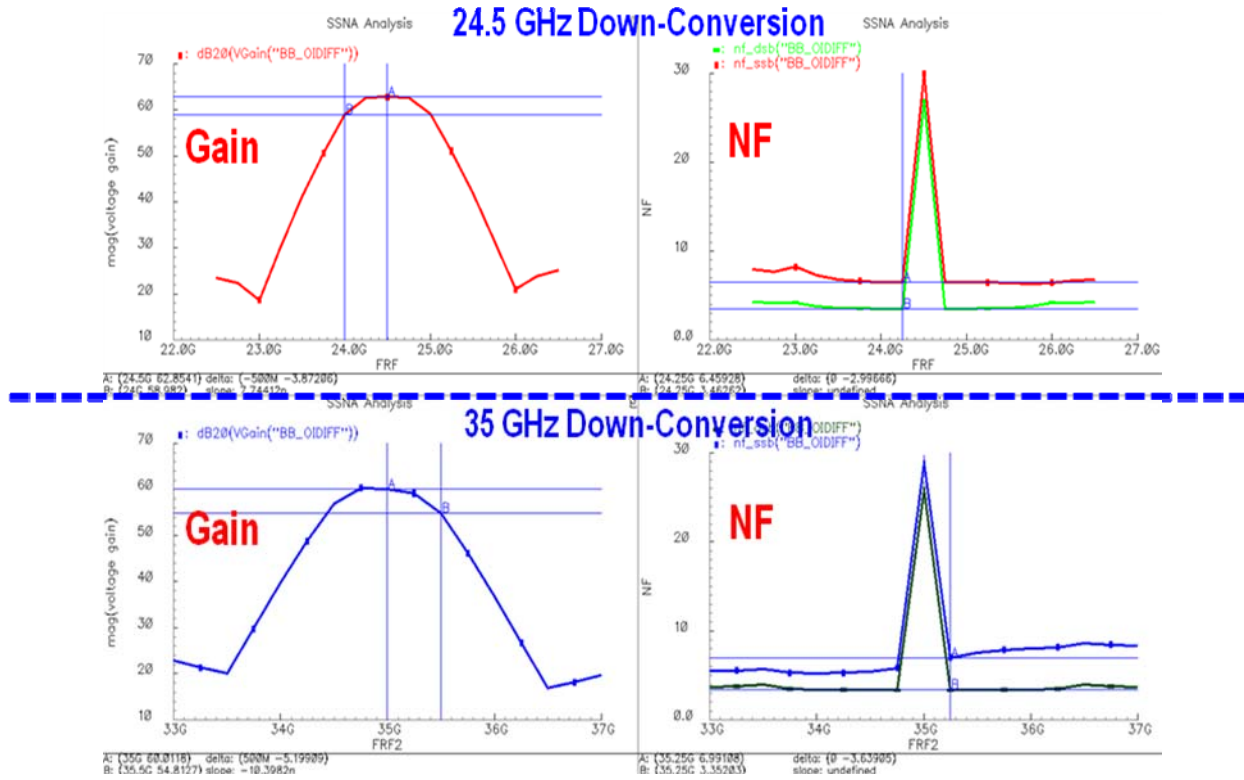


Figure 53. Performance of the integrated single-channel concurrent dual-band receiver front-end.

4. ANTENNA ARRAY

Summary of Performance: The architecture and specifications for the concurrent dual-band dual-polarization 24.5/35 GHz antenna array have been developed and analyzed. Single-element and six-element antenna array have been designed using multi-layer liquid crystal polymer (LCP) substrates and scheduled for fabrication. The total size for the six-element antenna array is estimated to be 5cmx5cm.

4.1 Dual-band Dual-polarization Antenna and Array

Figure 54 shows the dual-band dual-polarization antenna and the Y-array consisting of six antennas. Fig. 55 shows the return loss at the vertical (V) and horizontal (H) polarization ports and the isolation between these ports. The return losses are below 20 dB and the isolation between the two polarization ports is kept under -25 dB at 24.5 ad 35 GHz. Figs. 56 and 57 show the radiation patterns at 24.5 GHz and 35 GHz for the single element and Y-array. The gain of the single antenna element and Y-array are 3 and 10 dBi, respectively at the dual-band of 24.5 ad 35 GHz with good co- and cross-polarization discrimination. Table 11 summarizes the performance.

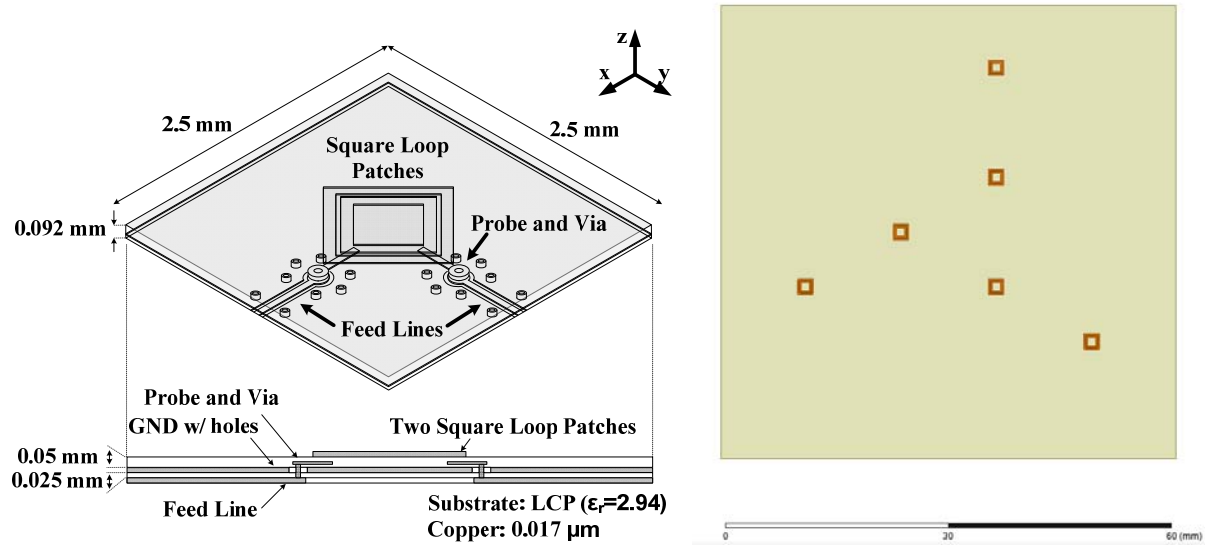


Figure 54. Dual-band dual-polarized antenna and Y-array of 6 elements.

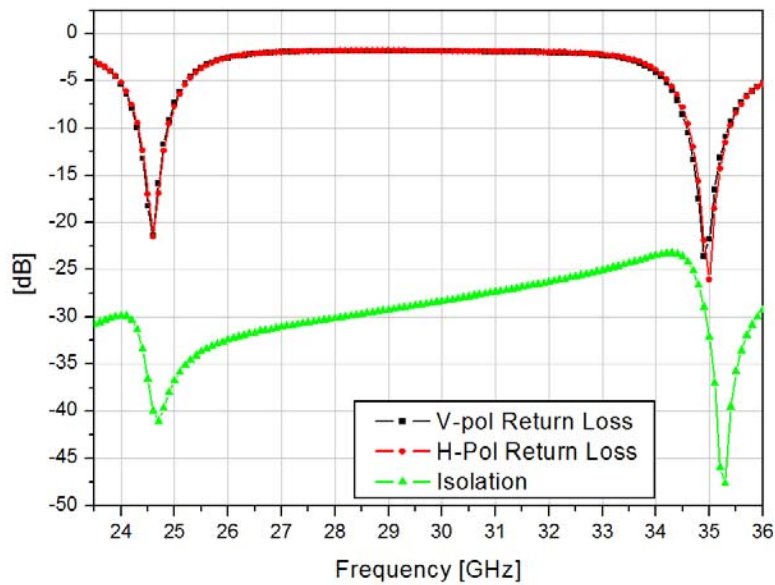
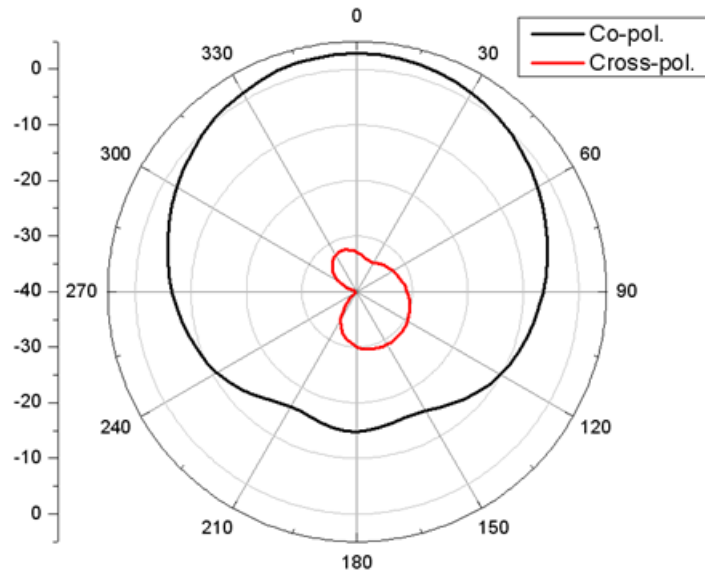
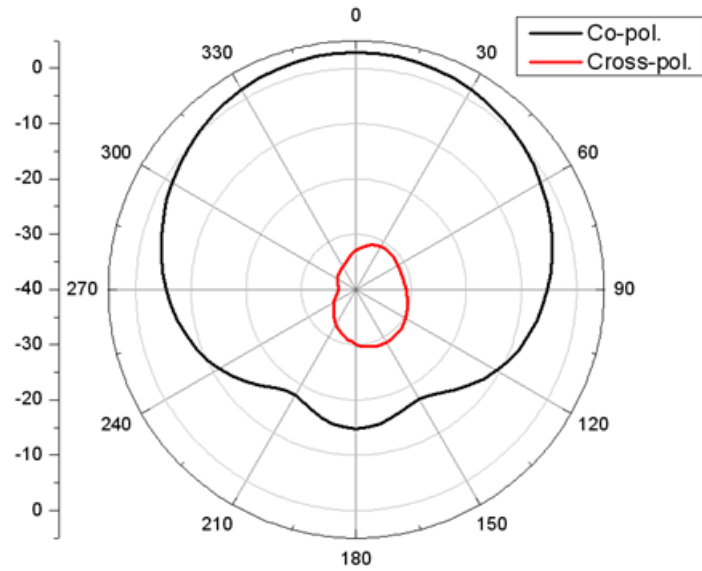


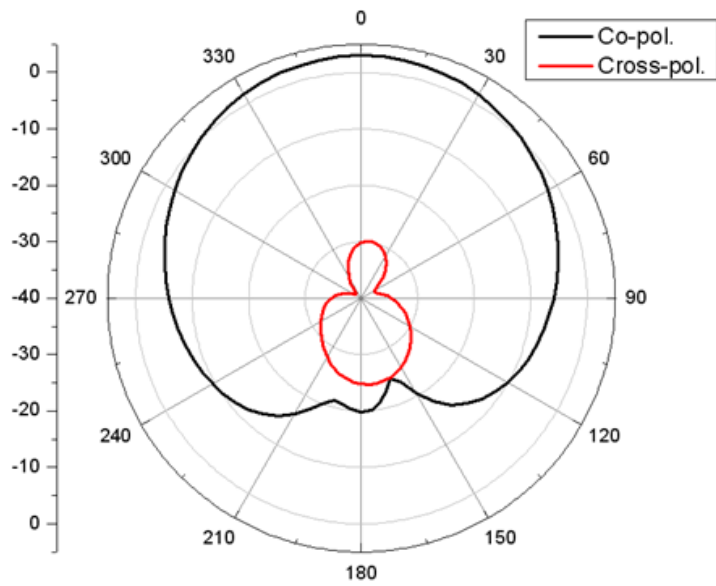
Figure 55. Return loss at V-/H- pol ports and isolation between V- and H- pol ports.



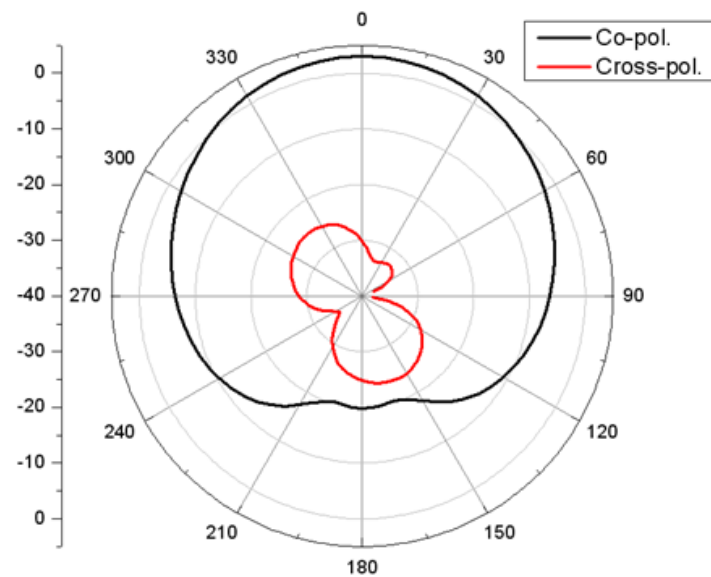
(a) V-pol, E-plane



(b) H-pol, H-plane



(c) V-pol, E-plane



(d) H-pol, H-plane

Figure.55. Radiation patterns at 24.5 GHz (a, b) and 35 GHz (c, d) for the single antenna.

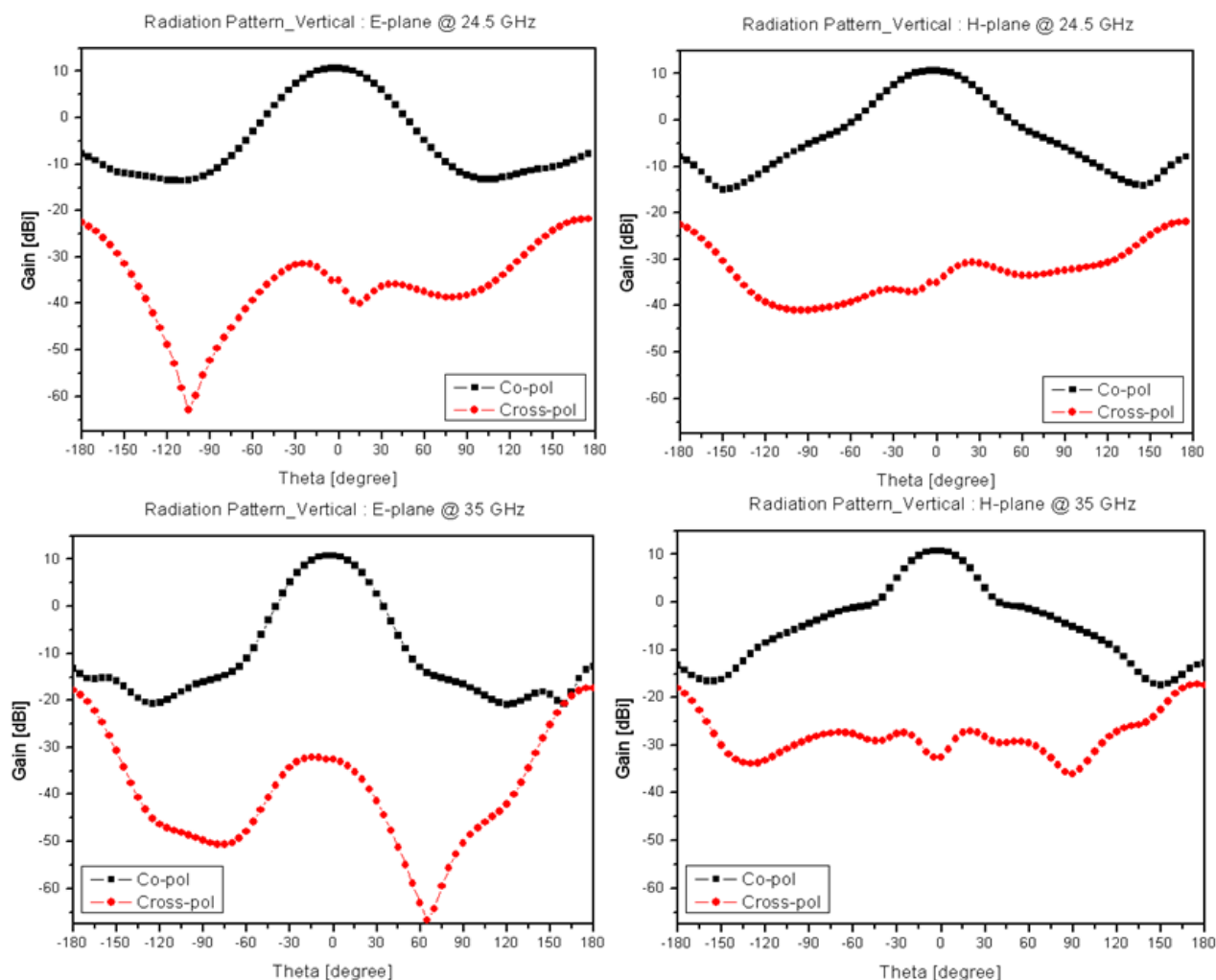


Figure.56. Y-array radiation patterns at 24.5 GHz and 35 GHz

Table 11 - Performance summary of a single antenna and Y-array

Frequency	24.5 GHz	35 GHz	Remarks
Bandwidth	250 MHz	250 MHz	VSWR 2:1
Polarization	Dual-linear polarization	Dual-linear polarization	
Gain(Single/Array)	3.1 / 10.5	3.5 / 11	[dBi]
Front-to-Back Ratio	18	23	[dB]
Isolation	-35	-30	[dB]

Beam Pattern	Broadside	Broadside	
--------------	-----------	-----------	--

5. TR/CAL SWITCH AND SWITCHING ATTENUATOR

Summary of Performance: Two important circuits needed for the system are reported here: a concurrent dual-band dual-polarization transmit-receive/calibration (TR/CAL) switch and a 4-bit attenuator. The TR/CAL switch has been designed using Jazz 0.18- μm SiGe BiCMOS process and scheduled for fabrication. The attenuator across 10-43 GHz has been developed using Jazz 0.18- μm SiGe BiCMOS process and measured with unprecedented performance.

5.1 Concurrent Dual-Band Dual-Polarization TR/CAL Switch

Figure 57 shows the TR/Cal switch, as seen in the system architecture shown in Fig. 1 for the concurrent dual-band dual-polarization operation. It has 7 ports: antenna (AntV, AntH), receiver (RxV, RxH), calibration (CalV, CalH) and transmitter (TxH/TxV) ports.

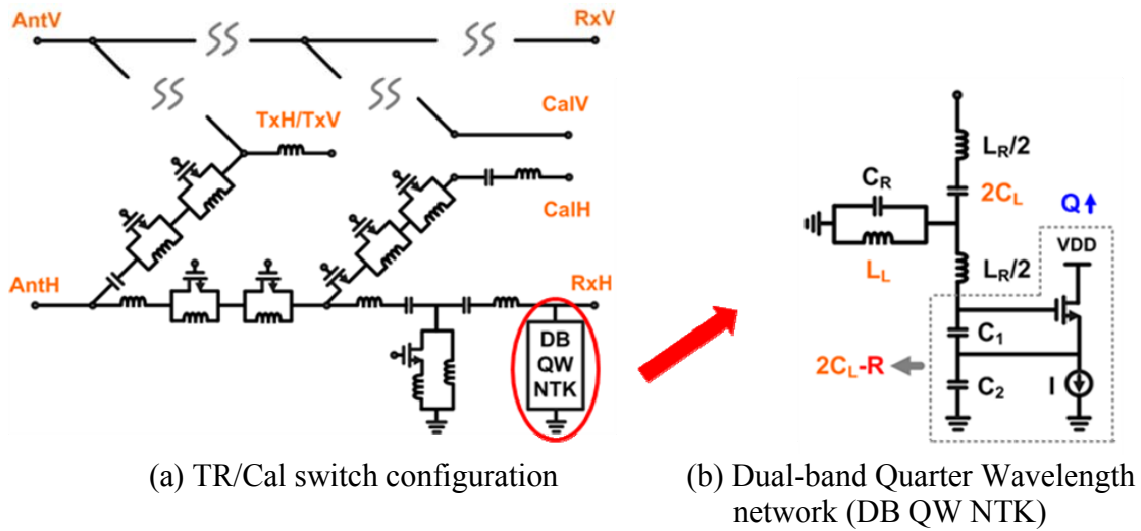


Figure 57. TR/Cal switch for concurrent dual-band dual-mode operation.

Figure 58 shows the S-parameters of the seven-port TR/Cal switch. The RX mode response has a dual-band filtering function and CAL mode response emulates it with an increased insertion loss.

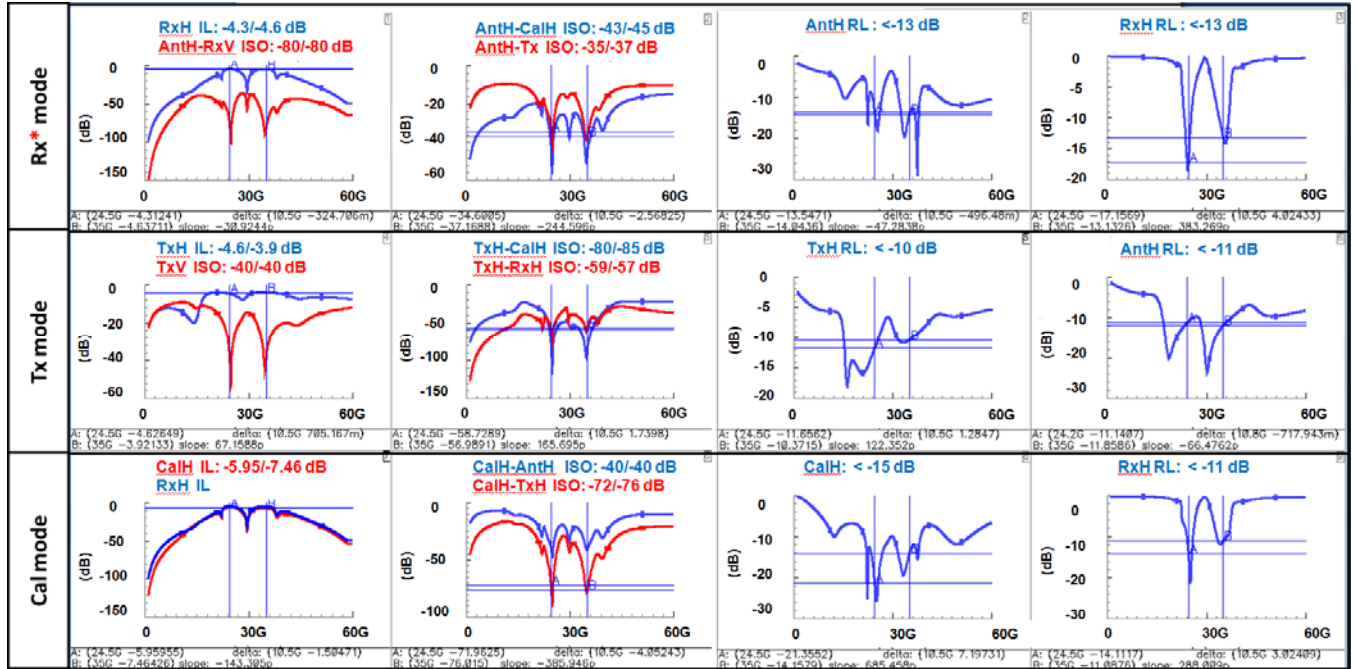
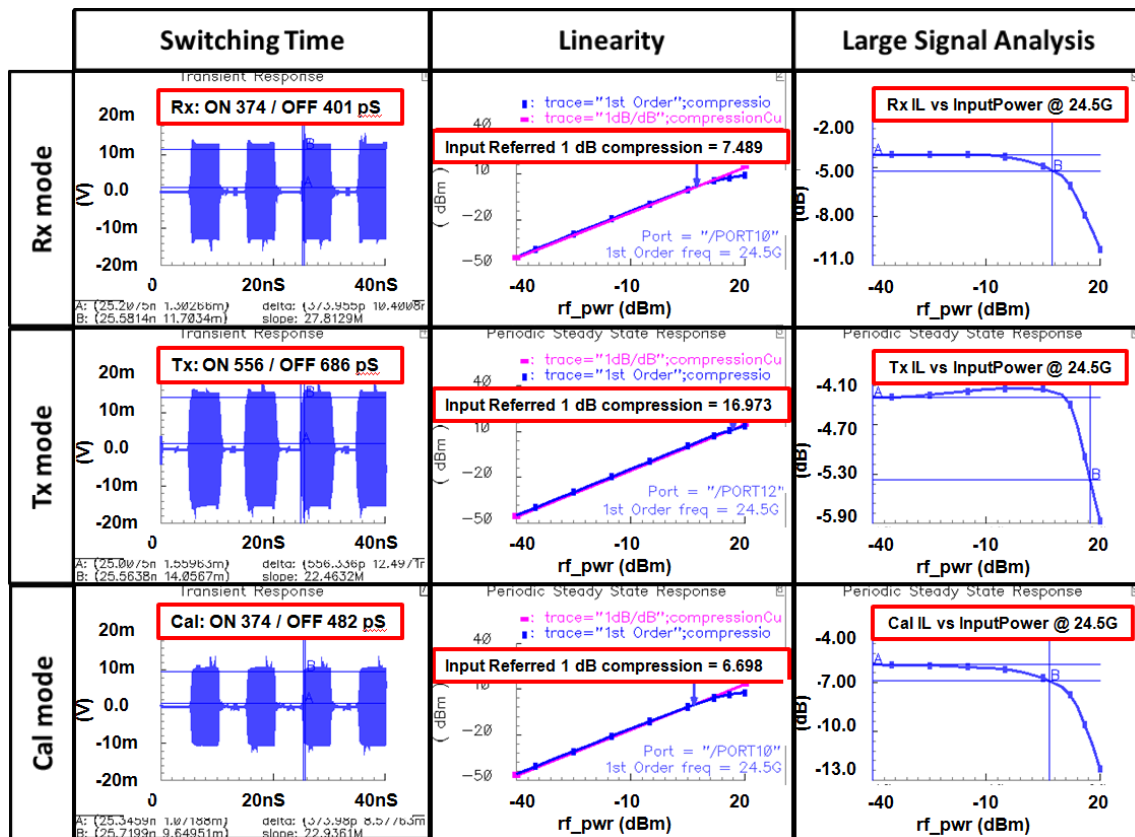
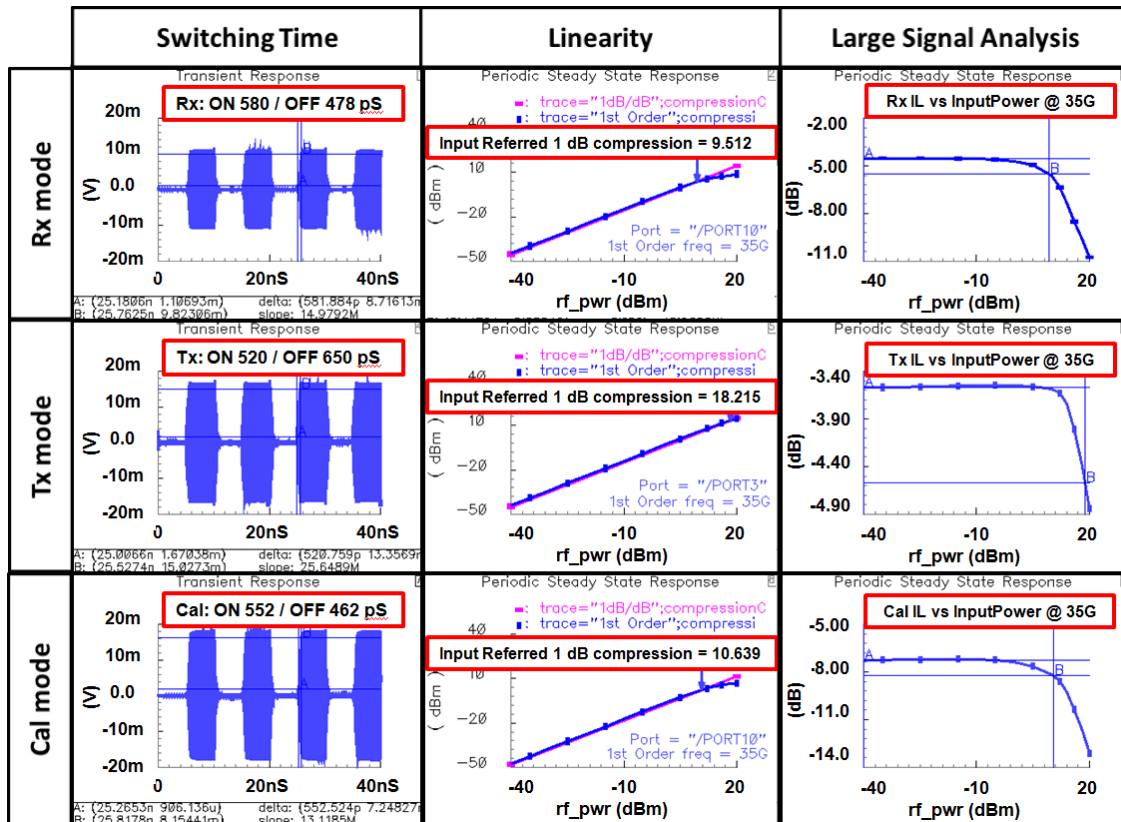


Figure 58. S-parameters of the TR/Cal switch. Both of the V- and H- polarization RX paths are turned on in the Rx mode simulation. All the Rx mode responses for both polarizations are identical. Only H- polarization responses are presented.

Figure 59 shows the switching time, linearity, and large signal analysis for all operation modes at 24.5 and 35 GHz.



(a)



(b)

Figure 59. Switching time, linearity and large signal analysis for the TR/Cal switch at 24.5 GHz (a) and 35 GHz (b).

Table 12 summarizes the results of the TR/Cal switch.

Table 12 – Performance summary for TR/Cal switch.

Parameter	24.5			35			Unit
Frequency							GHz
Mode	Rx*	Tx	Cal	Rx*	Tx	Cal	
Insertion Loss	-4.3	-4.6	-5.95	-4.6	-3.9	-7.46	dB
Isolation**	AntH-RxV: -80 AntH-CalH: -43 AntH-TxH: -	AntH-TxV: -40 TxH-CalH: -80 TxH-RxH: -59	CalH-AntH: -40 CalH-TxH: -72	AntH-RxV: -80 AntH-CalH: -45 AntH-TxH: -37	AntH-TxV: -40 TxH-CalH: -85 TxH-RxH: -57	CalH-AntH: -40 CalH-TxH: -76	dB

	35						
S11	<-13	<-10	<-15	<-13	<-10	<-15	dB
S22	<-13	<-10	<-10	<-13	<-10	<-10	dB
Switching Time ON / OFF	374 / 401	556 / 686	374 / 482	580 / 478	520 / 650	552 / 462	pS
IP1dB	7.5	17	6.7	9.5	18.2	10.6	dBm

- * Both of the V- and H- polarization Rx paths are turned on in the Rx mode simulation.
- ** The notation of H and V are interchangeable since the entire T/R/Cal switch is perfectly symmetrical. The isolation performances given in this table are H polarization perspective.

5.2 Switching Attenuator

Figure 60 shows the layout of the 4-bit attenuator used for the on-chip calibration of the sensor seen in the system architecture as shown in Fig. 1. The attenuator also incorporates the switching function to reduce leakage to the receiver during the duration when the system is not under calibration. It was designed using Jazz 0.18- μm SiGe BiCMOS technology and occupies an area of 2mmx0.64mm.

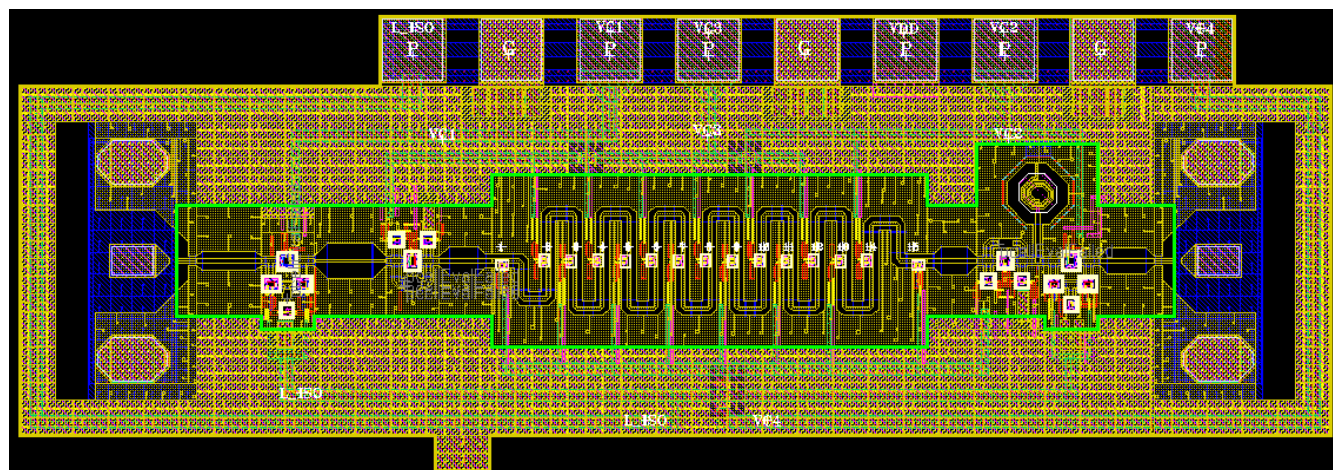


Figure 61. Layout of the 4-bit attenuator.

Figure 61 shows the measured insertion loss, and input return and output return losses for all attenuation states. The amplitude variations at all states are below 3 dB, and the input and output return losses are below 8 dB from 10 to 43 GHz.

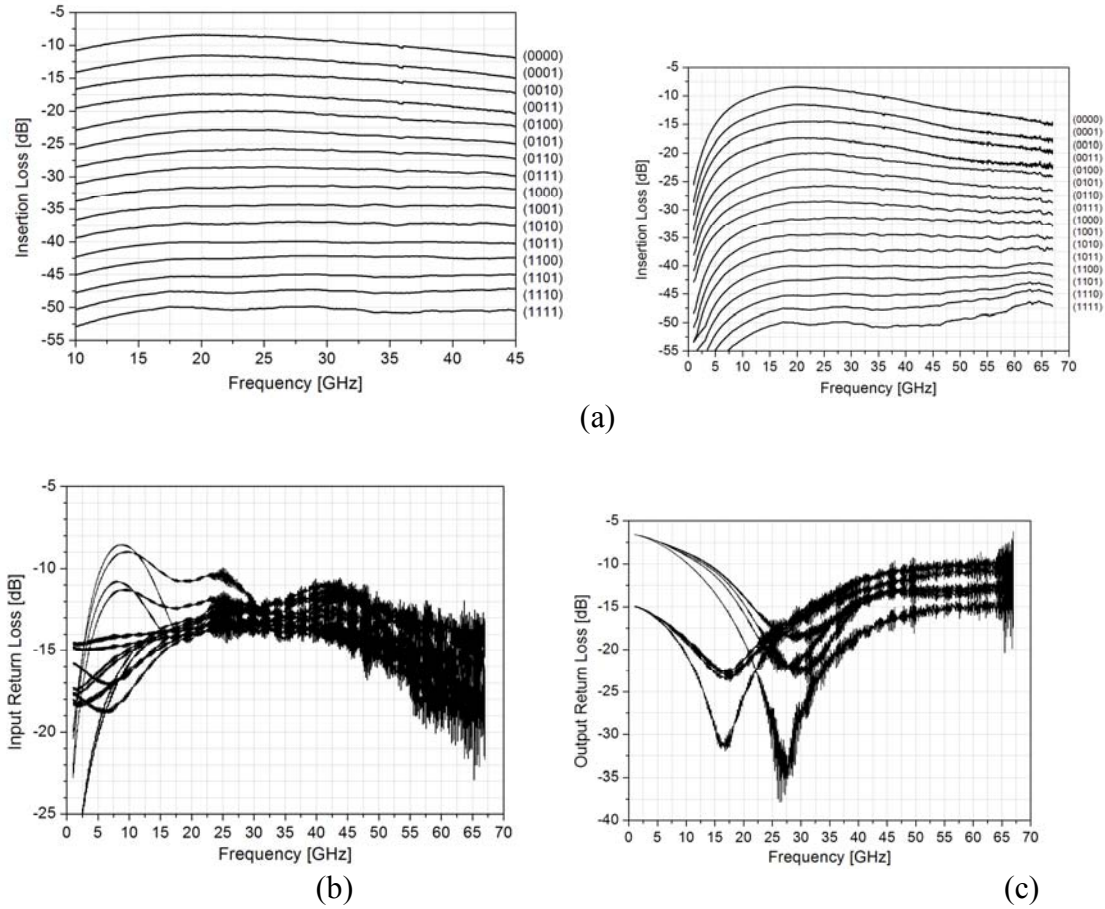


Figure 61. Measured insertion losses (a), input return losses (b) and output return losses (c) of 16 states.

Figure 62 shows the measured return loss (S_{11} , S_{22}) and isolation (S_{12} , S_{21}) in the off state of the attenuator. The isolations are higher than 45 dB over the desired frequency range of 10-43 GHz.

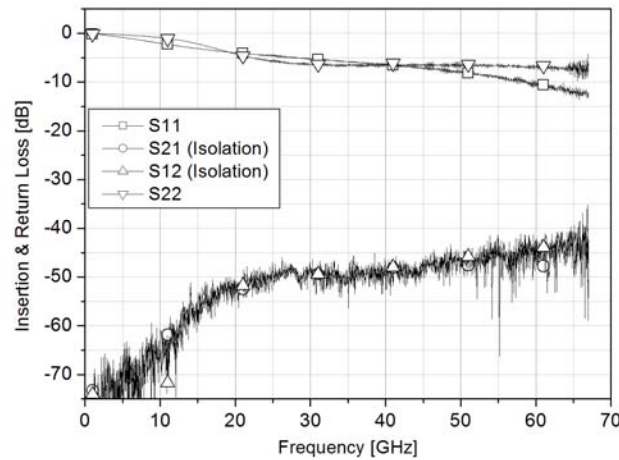


Figure 62. Measured return loss (S_{11} , S_{22}) and isolation (S_{12} , S_{21}) in the off state of the attenuator.

Figure 63 shows the measured input P1dB of the attenuator at 25 GHz and 35 GHz for the 1st, 2nd, 4th, 8th and 16th attenuation state. They are all higher than 15 dBm.

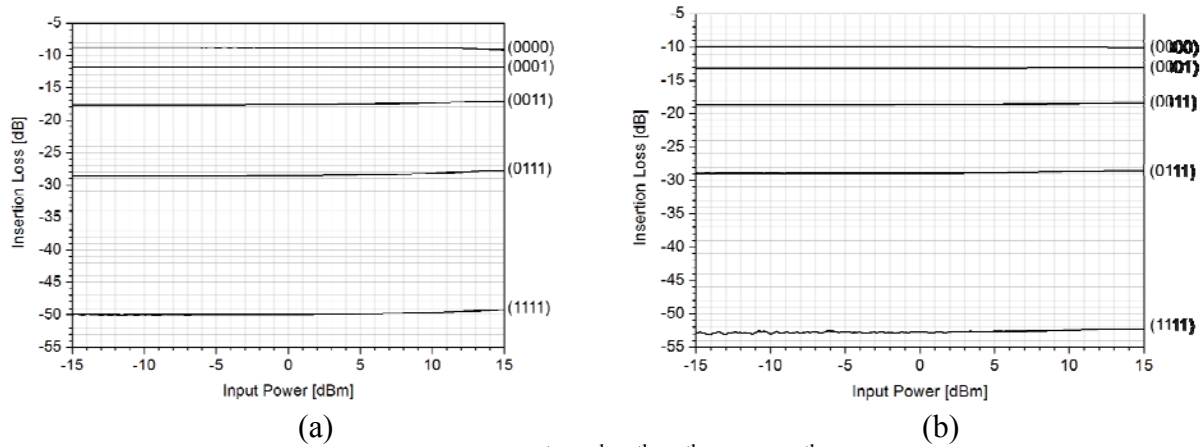


Figure 63. Measured input P1dB for the 1st, 2nd, 4th, 8th, and 16th state of the attenuator at 25 GHz (a) and 35 GHz (b).

Table 13 summarizes the performance of the attenuator.

Table 13 - Performance summary for the attenuator.

	Measured Results		
	10 GHz	26.5 GHz	43 GHz
Insertion Loss (dB)	10.8	8.9	11.5
Input Return Loss (dB)	> 8.7	> 10.8	> 11
Output Return Loss (dB)	> 8.5	> 15	> 11
Isolation in off-state (dB)	62	49.8	49.9
Bandwidth	10 GHz - 43 GHz		
Input P1dB	> 15 dBm		

6. SYNTHESIZER

Summary of Performance: The architecture and specifications for the concurrent tri-band 3.5/7/21 GHz synthesizer have been developed and analyzed. All components of the synthesizer and the complete synthesizer have been developed using Jazz 0.18- μ m CMOS process with very good performance. These components as well the entire synthesizer represent the state of the art with unprecedented performance. The size for this synthesizer is only 1.9mmx0.94mm.

6.1 Synthesizer Architecture

A concurrent multiband synthesizer is needed for the sensor as seen in the system architecture in Fig. 1. This section describes the research and development of the fully integrated concurrent tri-band, tri-output phase-locked loop (PLL) used as the synthesizer with divide-by-3 injection locked frequency divider (ILFD). The architecture of the PLL is shown in Fig. 64.

The PLL is completely realized using 0.18- μm CMOS and employs only one VCO and one frequency divider, resulting in small chip size, low power consumption and less unwanted coupling. A new locking mechanism for the ILFD based on the gain control of the feedback amplifier is utilized to enable tunable and enhanced locking range which facilitates the attainment of stable locking states. The PLL has three concurrent multiband outputs: 3.47-4.313 GHz, 6.94-8.626 GHz and 19.44-21.42-GHz. High second-order harmonic suppression of 62.2 dBc is achieved without using a filter through optimization of the balance between the differential outputs. The PLL consumes 81 mW with supply voltage of 1.8 V and occupies 1.9 mm \times 0.94 mm.

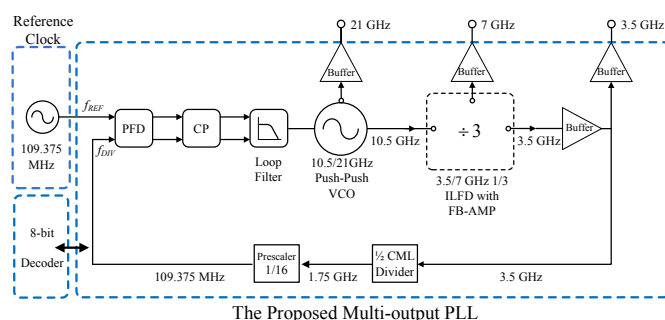


Fig. 64. Architecture of the multi-output PLL integrating all, except the reference clock, on a single chip.

6.2 Limitations of Conventional Calibration Technique for Super-Harmonic-ILFD PLL

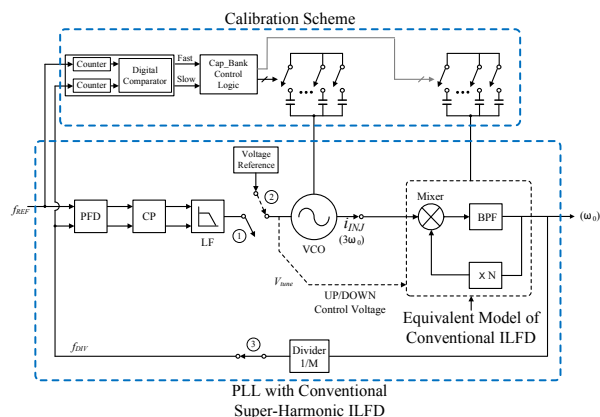


Fig. 65. Block diagram of PLL with conventional super-harmonic ILFD and calibration scheme for VCO frequency at coarse-locking.

Conventional calibration technique has been used for PLL's without ILFD. Implementing this scheme for ILFD PLL's, however, poses several difficulties as described later. Fig. 65 shows a block diagram of a PLL with a conventional super-harmonic ILFD along with the conventional calibration technique for VCO frequency for coarse-locking. An injection signal (i_{INJ}) at frequency of $3\omega_o$ is applied to the mixer. Due to the nonlinearities of the mixer, inter-modulation products are generated between the injection signal ($3\omega_o$) and output signal (ω_o). After passing through the band-pass filter (BPF), only the desired signal (ω_o) can be acquired at the output. Switch 1 is disconnected and switch 3 is connected to the ILFD in order to adjust the frequency using a capacitor bank in the VCO at coarse-locking state (open-loop). Switch 2 is connected to the VCO to provide a fixed dc reference voltage of $0.5V_{DD}$ to the varactor in the VCO to set a certain KVCO. All the operations for switches 2 and 3 are determined in an open-loop state corresponding to the off-switch 1. To obtain a desired free-running frequency for the VCO, the output frequency of the VCO is calculated by counting the number of bits (f_{DIV}) at the output of switch 3 using the corresponding counter in the calibration block. $f_{DIV}=f_{VCO}/M(N+1)$ is under a coarse-locked state, where f_{VCO} is the VCO frequency and M and N are integers. The subsequent comparator then compares f_{DIV} with the reference signal's frequency f_{REF} and decides which one is faster.

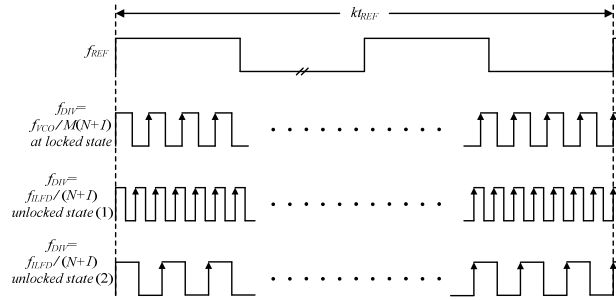


Fig. 66. Timing diagram of the frequency comparison techniques in ILFD PLL

Fig. 66 shows the timing diagram of the frequency comparison technique. It illustrates that f_{DIV} is counted during a time period of kt_{REF} , where $t_{REF}=1/f_{REF}$ and k is the number of the duration t_{REF} executed to achieve $f_{DIV}=f_{REF}$ which implies that a coarse-locked state has been reached. During kt_{REF} , the counter estimates whether f_{DIV} or f_{REF} is faster and controls the capacitor bank of the VCO to adjust f_{DIV} until a coarse-locked state is reached for the PLL. If this method is applied to the ILFD PLL, the VCO loses its coarse-locking. During the coarse-locking, the output frequency of the VCO may be set far away from a desired frequency. The locking range of a conventional ILFD is typically very narrow with small injection power. The output of the ILFD hence does not follow the injection signal under an unlocked state. Possible frequency of the divider (f_{DIV}) that the counter provides during the time duration of kt_{REF} is given by

$$f_{DIV} \begin{cases} = \frac{f_{VCO}}{kM(N+1)}, & \text{locked state} \\ \neq \frac{f_{VCO}}{kM(N+1)}, & \text{unlocked state} \end{cases} \quad (1)$$

which shows that, under the locked state, f_{DIV} follows, and can be used to find, f_{VCO} in coarse-locking state. Under the unlocked state, f_{DIV} does not follow f_{VCO} since the ILFD is not locked with the injection source. Under the unlocked state, f_{DIV} is given by

$$f_{DIV} = \frac{f_{ILFD}}{kM} \quad (2)$$

where f_{ILFD} is the free-running frequency of ILFD, and f_{DIV} can be higher or lower than $f_{VCO}/M(N+1)$ as shown in Fig. 2.

Under the unlocked state, f_{VCO} cannot be recognized when it is out of the boundary of the ILFD's locking range. However, the output counter recognizes the frequency f_{DIV} given in (2), and it simply changes the capacitor bank in the VCO to vary f_{VCO} accordingly. The resultant f_{VCO} , however, may not be the desired frequency within the locking range due to the fact that it cannot be determined from f_{DIV} according to (2). This problem is more serious as the division ratio $(N+1)$ increases for high-order super-harmonic ILFD's due to low harmonic coefficients. Furthermore, if the output power of the VCO (injection signal power) is reduced, the narrow locking range problem becomes severe [9]. The proposed calibration technique and PLL described in Section III achieves enhanced and tunable locking range which helps minimize the problems of the conventional calibration technique.

6.3 Proposed Architecture and Calibration Mechanism for Super-Harmonic-ILFD PLL

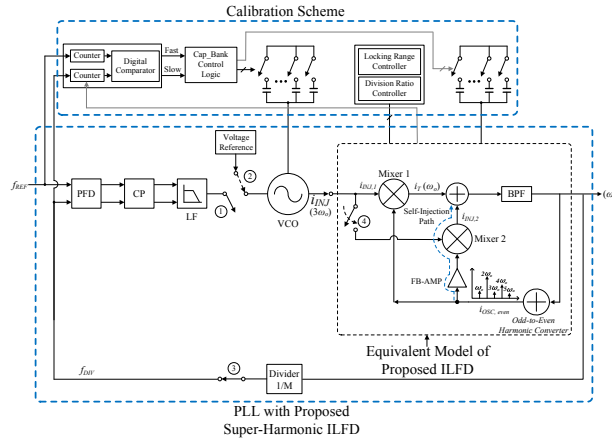


Fig. 67. Block diagram of the proposed ILFD PLL and calibration scheme for VCO frequency at coarse-locking.

Fig. 67 shows the block diagram of the proposed PLL with self-injection signal along with the calibration scheme. To increase the locking range, a self-injection technique is applied with additional power depending on the locking-range control. At the coarse-locking state, switch 1 is off and switches 2, 3 and 4 are on. The injection signal $i_{INJ,2}$ from Mixer 2 is increased per the conversion gain of the mixer, hence helping extend the locking range.

The locking range of an ILFD was derived analytically as

$$\omega_{inj} - \omega_0 = \frac{\omega_0}{2Q_L} \cdot \frac{i_{INJ}}{\sqrt{i_{OSC}^2 - i_{INJ}^2}} \quad (3)$$

where i_{INJ} and i_{OSC} are the injection and oscillation current, respectively. Under a fixed i_{OSC} , the injection current can be adjusted to enhance the locking range until i_{INJ} is less than i_{OSC} and the constructive summation is ensured. However, the injection signal level is limited when it is supplied by an integrated VCO.

With the implemented auxiliary injection technique, the injection signal level can be significantly lower for super-harmonic ILFD due to the boosted injection signal. The injection signal can be defined as

$$i_{INJ} = i_{INJ,1} + i_{INJ,2} \quad (4)$$

where $i_{INJ,1}$ is the injection signal by the VCO and $i_{INJ,2}$ is the auxiliary injected signal. In (4), the injection signal $i_{INJ,1}$ is dependent on the division N of the super-harmonic ILFD. The effective signal strength of the wanted harmonic resulted from the application of $i_{INJ,1}$ is reduced by 1/N in view of the locking range, where N is the division number of the divider. $i_{INJ,2}$ is generated by the auxiliary self-injection with feedback amplifier. The feedback amplifier increases the $i_{INJ,2}$ strength and hence the locking range.

6.4 Design of Concurrent Multiband Multi-Output PLL

Fig. 65 shows the proposed concurrent multi-band multi-output PLL. It consists of a feedback loop, comprised of VCO, 1/3 ILFD, buffer, 1/2 CML divider, 1/16 prescaler (PS), phase-frequency detector (PFD), charge pump (CP), and loop filter (LF), 8-bit decoder, and output buffers – all integrated in a single chip – and an off-chip reference clock. The PLL provides three differential outputs at 21, 7 and 3.5 GHz concurrently utilizing only a single ILFD and VCO. The 21-GHz signal is provided directly by the push-push VCO, whereas those at 7 and 3.5 GHz are obtained via the 1/3 ILFD. The ILFD also provides the 3.5-GHz signal to the feedback loop for close-loop function of the PLL.

A. 10.5/21GHz VCO and 21GHz Buffer

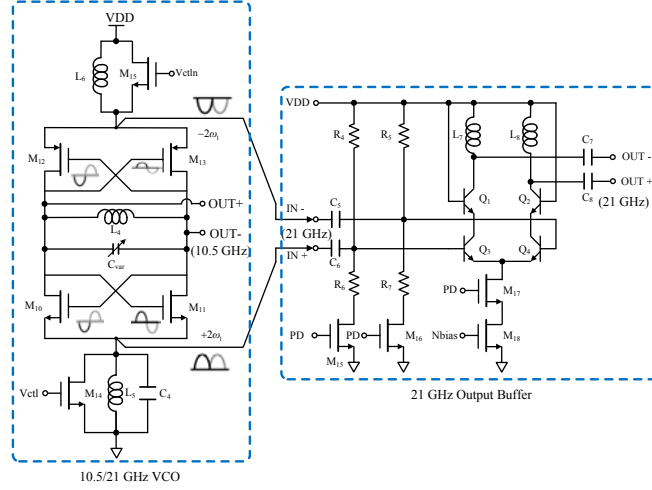


Fig. 68. 10.5/21-GHz push-push VCO and 21-GHz buffer.

Fig. 68 shows the schematic of the 10.5/21GHz VCO along with the 21-GHz output buffer. The VCO is realized using a push-push oscillator architecture based on PMOS and NMOS cross-coupled pairs. The VCO produces two concurrent differential output signals: one at the fundamental frequency of 10.5 GHz and another at the second harmonic of 21 GHz (via the common sources of the cross-coupled pairs). The push-push topology enables both low frequency ($f_0=10.5$ GHz) and high frequency ($2f_0=21$ GHz) to be produced concurrently using transistors having low f_{max} suitable for the low frequency. Generation of signals at high frequencies using transistors with low f_{max} would not be possible if the signals are generated directly using a non-push-push configuration. Potentially higher quality factor Q is also possible since the VCO is designed at the low frequency of $f_0/2$. The 21-GHz buffer is a cascoded amplifier employing BJT (Q_1 - Q_4) instead of MOSFETs as in the other components of the PLL due to the limited f_T of about 40 GHz for the 0.18- μm CMOS.

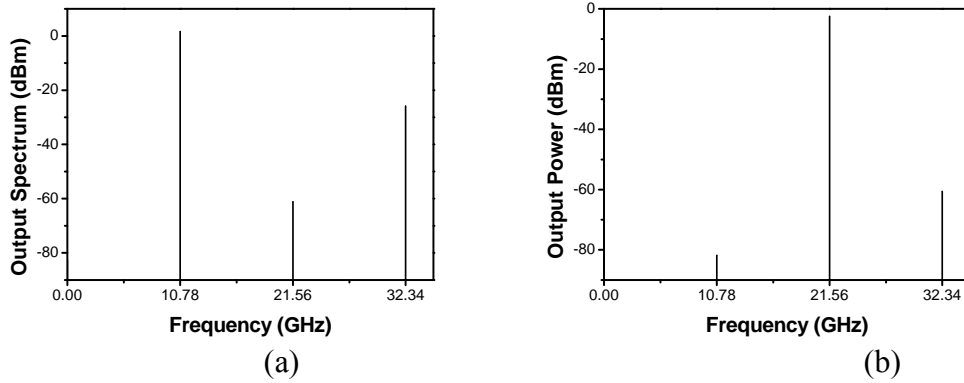


Fig. 69. Simulated output spectrum of the VCO at 10.5-GHz output (a) and 21-GHz output (b) ports.

Fig. 69 shows the simulated results of the spectrums at the 10.5- and 21-GHz output ports. The output powers at 10.5 and 21 GHz are 1.67 and -2.4 dBm, respectively. The harmonic rejections are 59.5 and 25.8 dBc for the 2nd and 3rd harmonic at the 10.5-GHz output port, respectively. At

the 21-GHz output port, the harmonics rejections are 79.37 and 58.1 dBc for the fundamental signal and 3rd harmonic, respectively.

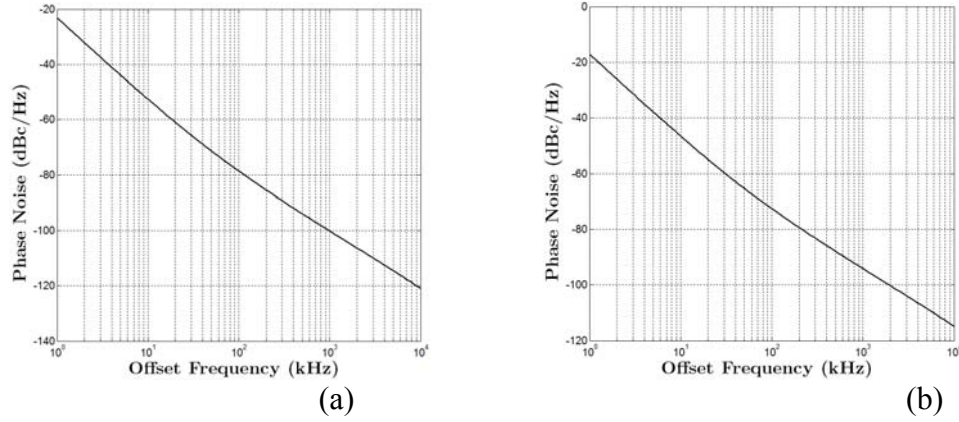


Fig. 70. Simulated phase noise of the VCO at 10.5 GHz output (a) and 21 GHz buffer's output (b).

The simulated phase noise is shown in Fig. 70. The phase noise of the 10.5-GHz signal is -102.05 dBc/Hz at 1-MHz offset, and that of the 21-GHz signal is 3 dB higher. At the common sources of the cross-coupled pairs, the 10.5-GHz fundamental signals are anti-phase, whereas the 21-GHz second-order harmonic signals are in-phase, making it a convenient point to extract the 21-GHz output signal to form a concurrent dual-band along with the 10.5-GHz signal using a single VCO.

B. 1/3 ILFD

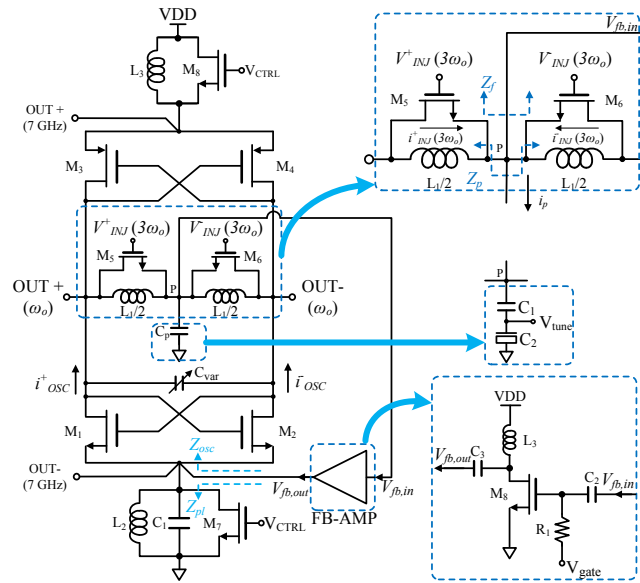


Fig. 71. The schematic of the proposed divide-by-3 ILFD.

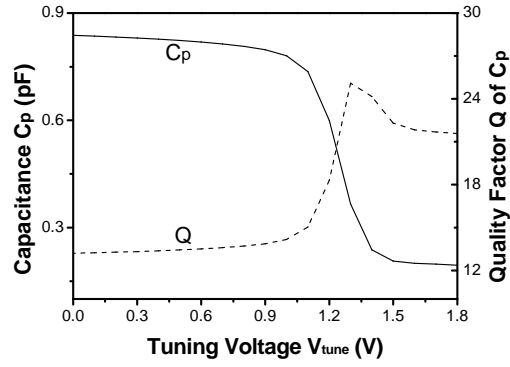


Fig. 73. The capacitance and quality factor of 2nd harmonic at node P.

Fig. 71 shows the schematic of the 1/3 ILFD with an auxiliary self-injection technique that has two concurrent outputs at 3.5 and 7 GHz. Fig. 72 shows the capacitance and quality factor Q of C_p at node P (noted in Fig. 71) implemented using an NMOS active device (C_2) as a function of the tuning voltage V_{tune} . C_p can be tuned from 0.88-0.2-pF while Q can be changed from 12-24. Fig. 73 shows the simulated powers for the fundamental and the 2nd and 3rd harmonics at node P. The fundamental and 3rd harmonic signals are rejected by about 51.5 and 85.6 dBc with respect to the 2nd harmonic, respectively. Fig. 74 displays the simulated spectrums at the 3.5 and 7 GHz output ports of the 1/3 ILFD. The output powers at 3.5 and 7 GHz are -2.5 and -30 dBm, respectively. At the 3.5-GHz output port, the 2nd and 3rd harmonic rejections are 85.6 and 23.3 dBc, respectively. At the 7-GHz output port, the fundamental signal and 3rd harmonic rejections are 49.6 and 100 dBc, respectively.

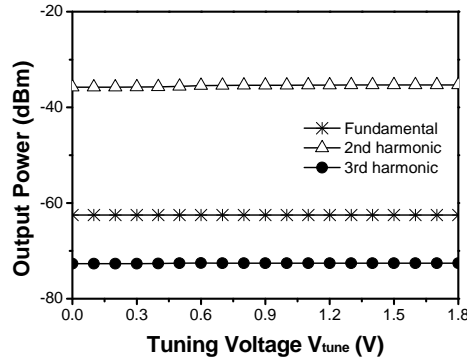
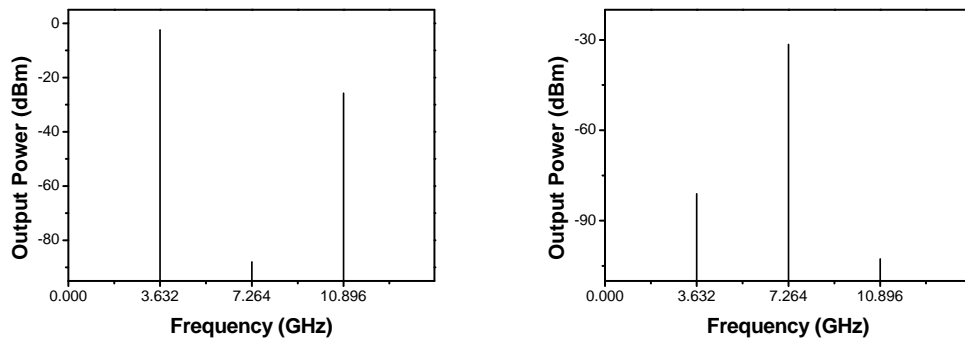


Fig. 73. Simulated output power at node P.



(a)

(b)

Fig. 74. Simulated output spectrum of the 1/3 ILFD at 3.5-GHz (a) and 7-GHz (b) output port.

We now consider the T-network at node P shown in Fig. 71 that consists of $L_1/2$ in parallel with M_5 , $L_1/2$ in parallel with M_6 , and C_p , and let L represent the equivalent inductance of the combined $L_1/2$ and the parasitic capacitance of M_5 (or M_6), and C represent C_p . We can then derive the output frequency under the symmetric condition as

$$\omega_0 = \sqrt{\frac{2LC - C^2 Z_0^4}{L^2 C^2}} \quad (5)$$

where Z_0 is the reference impedance. Since a perfect symmetry for the T-network implies that the outputs OUT+ and OUT- at ω_0 are equal in amplitudes and 180-deg out of phase, we can see from (5) that proper values for L and C can be chosen corresponding to an oscillation at ω_0 that results in differential outputs. In other words, we can optimize the T-network to produce well-behaved differential outputs, which is an interesting and important design information for the 1/3 ILFD.

C. 1/2 CML divider, 1/16 Prescaler, PFD, CP and LF

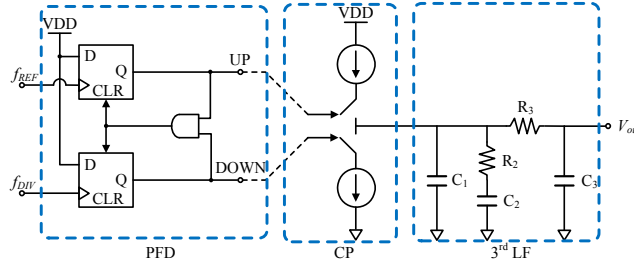


Fig. 75. PFD, CP and 3rd loop-filter.

The 1/2 CML divider, 1/16 prescaler, PFD, CP and LF are based on conventional circuit topologies. As an example, Fig. 76 shows the PFD, CP and LF. The PFD utilizes a three-state phase detection scheme and it operates as a linear system in the locking range. The reference clock is at 109.375 MHz. The CP is the main source for undesired reference spurs due to current and timing mismatch. The reference spurs can be reduced by controlling the loop bandwidth and loop phase error of the LF. The current of CP is controllable from 100 to 200 μ A. The LF is a third-order filter and consists of three capacitors and two poly resistors. The LF's loop bandwidth can be tuned to have either 1 or 2 MHz. The phase margin of the LF is around 56.6 degrees.

D. Latched 8-bit Decoder for Digital Control

Fig. 76 shows the block diagram of the latched 8-bit decoder unit, that has 4-bit address, 8-bit data, 4-bit reset and single clock which provide input signals to the decoder. Each address can be selected from the 4-bit address. Once a path is selected by an address bit, the data is written and stored in the 8-bit registers. The data stored in the registers can be cleared by the 4-bit reset

control. The clock signal is used to write the data while the clock is “high” and to remember the data while the clock is “low”.

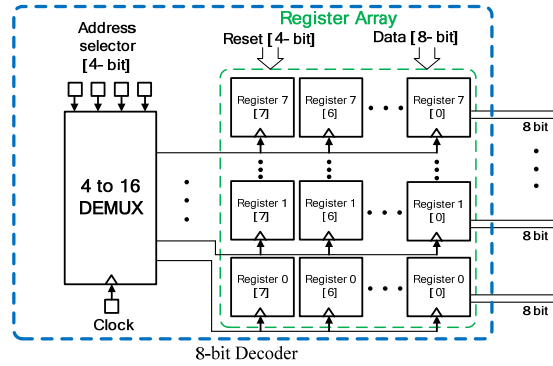


Fig. 76. Block diagram of the 8-bit decoder for digital control pins.

6.5 Performance

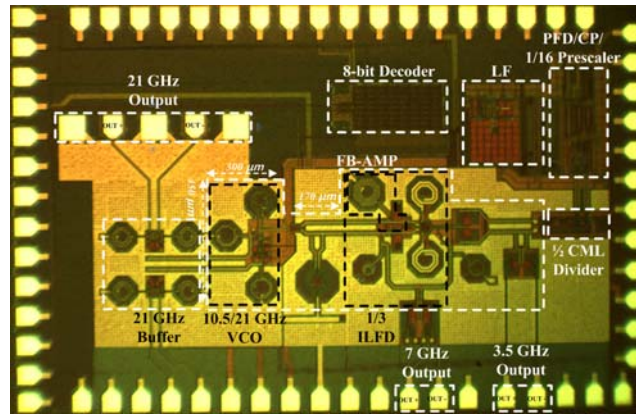


Fig. 77. Die photograph of the fully integrated PLL.

The entire PLL was fabricated using 0.18- μm CMOS, except the 21-GHz buffer, on Jazz 0.18- μm BiCMOS process. Its die photograph is shown in Fig. 77. The chip size is 1.786 mm².

The measured frequency tuning range of the PLL at the 3.5-GHz output port is 3.47-4.313 GHz as shown in Fig. 78. Measured results show that the frequency of the PLL at the 7-GHz and 21-GHz output ports can be tuned from 6.94-8.626 GHz and 19.44-21.42-GHz, respectively. The measured frequency tuning range of the PLL around the 10.5-GHz signal is 9.72-10.71-GHz as shown in Fig. 79.

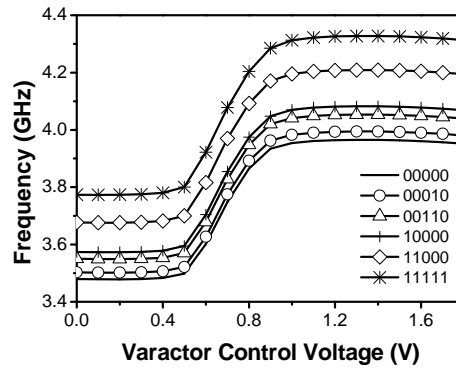


Fig. 78. Measured frequency tuning range of the PLL at the 3.5-GHz output port with 5-bit digital control.

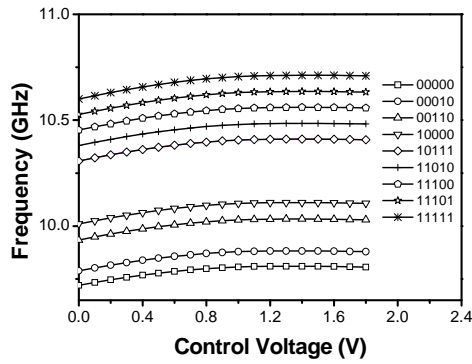


Fig. 79. Measured frequency tuning range of the PLL at the 10.5-GHz output port with 5-bit digital control.

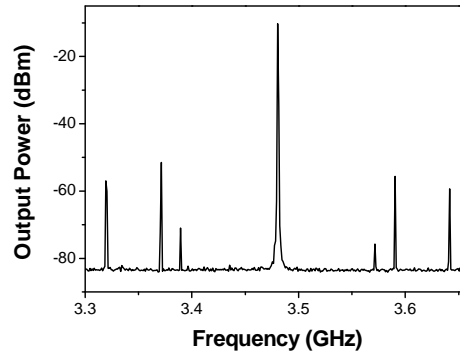


Fig. 80. Measured output spectrum of the PLL at the 3.5 GHz output port. RBW: 100 kHz, VBW: 30 kHz, SPAN: 0.4 GHz, REF: -10 dBm, and ATT: 0, 45.55 dBc at 109.375 MHz, 65.95 dBc at 87 MHz, and 48.9 dBc at 150 MHz

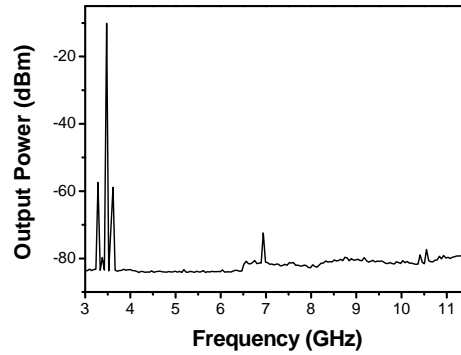


Fig. 81. Measured output spectrum of the PLL at the 3.5 GHz output port. RBW: 100 kHz, VBW: 30 kHz, SPAN: 9 GHz, REF: -10 dBm, and ATT: 0, 2nd harmonic rejection: 62.2 dBc, reference signal rejection: -45.55 dBc.

Fig. 80 shows the measured output spectrum at the 3.5-GHz output port. The suppression of the 109.375-MHz reference spurs is greater than 45.55 dBc. Other spurs come from the buffer of the external clock that is shared between the reference signal and digital control clocking signal. Fig 81 shows that the measured 2nd harmonic suppression is 62.2 dBc. This suppression level is achieved without filter and significantly higher than those reported to date.

It is noted that the locking range of the constituent 1/3 ILFD with the auxiliary self-injection is extended as much as 47.8 %, from 16.4 MHz without the feedback amplifier (FB-AMP) to 24.24 MHz with the FB-AMP using a fixed capacitor bank. The 1/3 ILFD can achieve a locking range about 2.529 GHz with the FB-AMP using a 5-bit capacitor bank and fine-tuning varactor voltage. The 2.529-GHz locking range of this ILFD is more than 2.5 times of the free-running frequency range of 1 GHz (around 10.5 GHz) of the 10.5/21GHz VCO shown in Fig. 79, thus guarantying the finding of the VCO frequency at coarse-locking which, in turn, always results in a locked signal for the PLL.

The measured phase noise of the PLL for different control voltages of the FB-AMP is shown in Fig. 82. As can be seen, the phase noise at 1-MHz offset corresponding to 1.8V control voltage for the FB-AMP is -80.9dBc/Hz at 50-kHz offset, that is 4.4 dB better than that of the PLL with the FB-AMP off. The measured spectrums of the signals at the 7- and 21-GHz output ports of the PLL are shown in Figs. 83 and 84, respectively.

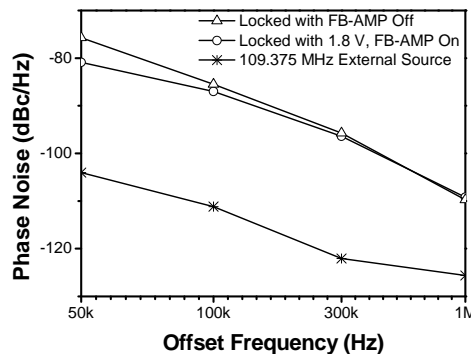


Fig. 82. Measured phase noise of the PLL.

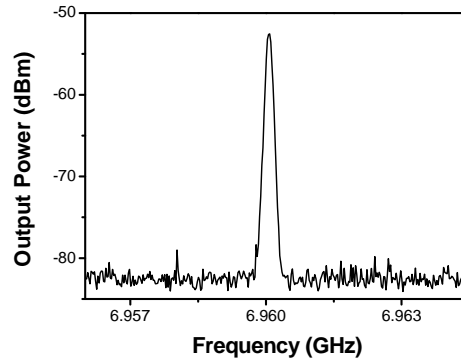


Fig. 83. Measured output spectrum of signal at the 7-GHz port. RBW: 100 kHz, VBW: 30 kHz, SPAN: 10 MHz, REF: -10 dBm, and ATT: 0.

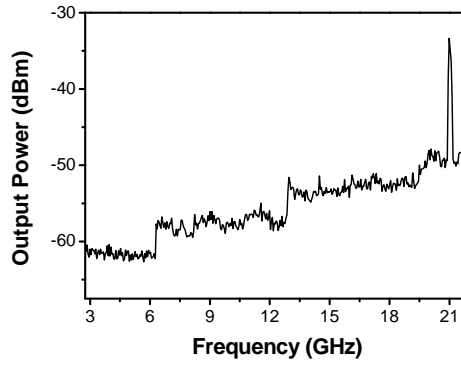


Fig. 84. Measured output spectrum of signal at the 21-GHz port. RBW: 3 MHz, VBW: 1 MHz, SPAN: 19.25 GHz, REF: 0 dBm, and ATT: 0.

Table 14 summarizes the performance of the PLL.

Table 14 - Performance summary for the PLL

Core Active Device		CMOS (ILFD)		CMOS (PLL)
VDD [V]		1.8		1.8
Power [mW]		19.1		81
Area [mm ²]		0.048		1.786
Output Frequency Range [GHz]		3.47-4.313		
		6.94-8.626		
		19.44-21.42		
Number of VCO		1		
Phase Noise [dBc/Hz]	3.5GHz	unlocked	locked	locked
	@ 50k	-54.05	-108	-80.9
	@ 100k	-82.14	-119	-86.98
	@ 300k	-90.67	-123	-96.38
	@ 1M	-105.3	-128	-109.2

Division Ratio		3	96
Locking Range		2.529GHz	300MHz
Spurs rejection	f_{REF}	-45.55	
	2 nd	-62.2	
	others	-48.9	
Architecture		Integer-N, 1/3 ILFD	
Order of LF		3rd for LF 4th type II	

PART B – RESEARCH AND DEVELOPMENT OF SIGNAL PROCESSING AND SOFTWARE

Summary of Performance:

New hardware (HW) software (SW) codesign paradigm was developed for the purposes of adaptive processing of cross-polarization sensor data obtained from multiple sensor modalities aimed at collaborative high-resolution sensing, detection, localization and identification of point-type and distributed targets in urban environments. The unified HW/SW codesign techniques capable to operate in uncertain operational scenarios for a variety of admissible sensor array configurations outperform the existing adaptive radar imaging algorithms both in resolution and convergence rate. The elaborated “Virtual Remote Sensing Laboratory” SW was integrated with the prospective synthesized simulated sensor HW model for demonstration of the superior capabilities of the overall prospective multimode sensor system via extensive simulation studies.

The performed basic research was focused on three subtasks, namely:

- Subtask 2.1: “Research and Development of Efficient Robust Adaptive Methods for Enhancement of Diverse Sensing Capabilities in Real-World Uncertain Operational Scenarios”.
- Subtask 2.2: “Research and Development of Robust Adaptive Techniques for Remote Sensing Search and Discovery Problems with Intelligent Data Fusion”.
- Subtask 2.3: “Elaboration of Integrated Software and Verification of Developed Techniques”.

These tasks are focused on the analytical research and development of efficient methods for (near) real time high-resolution localization of multiple point-type targets remotely sensed with the multimode GeoSTAR-configured array radar as well as for robust adaptive mapping of the distributes large-scale scenes sensed using imaging radar systems based on moving platforms operating in different sensing modes (conventional side looking and fractional aperture synthesis modes), both for the real-world uncertain operational scenarios. Enhancement of diverse remote sensing (RS) capabilities aimed at solving multimode sensing, knowledge-based (KB) search and discovery inverse problems with sensor and method fusion were conceptualized and algorithmically detailed for both the iterative contractive mapping and neural network based computational implementation architectures. The integrated “Virtual Remote Sensing Laboratory” (VRSL) simulations SW for verification of the developed techniques has been elaborated and tested through extensive simulation experiments. The uncertain radar/SAR imaging problems are treated via unification of the minimum risk spectral estimation strategy with the worst case statistical performance optimization-based regularization resulting in the new descriptive experiment design regularization (DEDR) framework. To overcome the processing complexity limitations of the DEDR approach in the aperture synthesis mode aimed at solving the inverse problems of reconstruction of the distributed scene radar images, the new hardware (HW) – software (SW) codesign approach that incorporates the additional convergence enforcing KB regularization into the DEDR framework was developed and algorithmically supported. This task has been performed by combining the KB-inspired variational analysis (VA) image enhancement paradigm with the DEDR framework that parallelizes and further speeds-up the iterative reconstructive image processing procedures. At the final research stage, the VRSL simulations SW has been elaborated and adapted to the synthesized simulation model of the sensor HW under current development by the TAMU HW design team. The VRSL SW was

tested for demonstration of the superior capabilities of the DEDR-VA techniques and particularly, to verify operational effectiveness of the prospective GeoSTAR-configured array sensor system under current development by the TAMU HW design team for a variety of admissible sensor geometries and operational modes in the tests of high-resolution localization of multiple point-type targets. The elaborated SW is accompanied by the detailed data processing and archiving protocols. The reported simulations protocols of multiple target localization are indicative of the considerably superior operational effectiveness provided with the HW/SW codesigned multimode imaging radar system with the DEDR-sparse test data processing.

ROBUST HIGH-RESOLUTION MULTIPLE TARGET LOCALIZATION TECHNIQUES ORIENTED AT IMPLEMENTATION WITH THE DEVELOPED MULTIMODE SENSOR ARRAY SYSTEM

In this section we introduce the adopted coordinate system and specify the geometry for the problem of localization of the point-type targets (TAGs) distributed over the scene plane using the measurement data provided by an arbitrary M -element plane sensor array; we also provide the statistical model of the signals induced by a single TAG and multiple TAGs at the outputs of such M -element sensor array with arbitrary geometry and present the generalization of the signal model for the extended scattering objects (extended targets) distributed over the probing scene. Finally we provide the stochastic model of the random array observation data contaminated with noise for the realistic scenarios with model uncertainties regarding the statistical characteristics of signal and noise necessary for further algorithmic development in the subsequent sections of this part of the report.

A. Coordinate System and Sensor Geometry

65

The origin “0” of the (x, y, z) Cartesian coordinate system coincides with the geometrical center (central sensor) located in the (x, y) array aperture plane (AAP) $P \subset \mathbb{R}^2$, where P defines an aperture support, i.e. bounds the receive array aperture size over which the particular receive sensors may be displaced. All arbitrary points in the AAP characterized by vectors $\mathbf{p} \in P \subset \mathbb{R}^2$, while the phase centers of M particular receive sensors (numbered as $m = 1, 2, \dots, M$) are attributed to the fixed positions

$$\{\mathbf{p}_m \in P; m = 1, 2, \dots, M\} \quad (1.1)$$

in the AAP. For the sake of simplicity, we first, assume omnidirectional identical receive sensors. (More general case of directionally selective sensors with some presumed directional receive patterns can be treated with some proper modifications as well).

Consider first, a single point-type target of interest (TAG) located in some (unknown) point on the scene plane $R \subset \mathbb{R}^2$ characterized by vector

$$\mathbf{r}_T = \mathbf{v} = (x_T, y_T, z_T = h_A)^T \quad (1.2)$$

that we define as the location of the target (LOT) vector parameter (referred to as the parameter of interest) and denote it via $\mathbf{v} = \mathbf{r}_T$ to distinguish with arbitrary points $\mathbf{r} = (x, y, z_T = h_A)^T \in R \subset \mathbb{R}^2$ distributed over the scene plane R . The scene plane is distanced from the AAP along the z coordinate at a fixed (i.e. presumed to be known a priori) height $z_T = h_A$, which is associated with a given (or pre-estimated by some means) elevation of the AAP over the scene plane.

Note that all over the text of this report, we will adopt conventional vector-matrix notations where superscript T denotes transpose when stands with a vector or a matrix; the superscript $*$ denotes complex conjugate, and superscript $+$ denotes the adjoint operator that coincides with Hermitian conjugate when stands with a vector or a matrix.

Any point on the scene plane $\mathbf{r} \in R \subset \mathbb{R}^2$ admits also representation in the conventional polar coordinate system

$$\mathbf{r} = (r, \eta, \varphi); r = \mathbf{r} / |\mathbf{r}| \quad (1.3)$$

where η and φ are the elevation angle and azimuth angle, respectively (see Fig. 1.1), and $r = \mathbf{r} / |\mathbf{r}|$ represents the distance to the scene point \mathbf{r} in the Cartesian coordinate system. If a particular TAG with the information LOT parameter \mathbf{r}_T is considered than the \mathbf{r} coordinate in (1.3) should be replaced by the corresponding $\mathbf{v} = \mathbf{r}_T$ given by (1.2).

Next, we introduce the unit-length directional vector associated with any $\mathbf{r} \in R$ (see Fig. 1.1)

$$\mathbf{g} = \frac{\mathbf{r}}{|\mathbf{r}|} = (\theta_x, \theta_y, \theta_z)^T = (\boldsymbol{\theta}^T, \theta_z)^T; \boldsymbol{\theta} = (\theta_x, \theta_y)^T. \quad (1.4)$$

Following the conventional signal processing (SP) terminology [1] the vector (1.4) is referred to as the direction of arrival (DOA) vector that corresponds to a hypothetical possible tag signal arriving from the scene point \mathbf{r} . Note that if a particular tag with the information LOT parameter \mathbf{r}_T is considered than the \mathbf{r} coordinate in (1.4) should be replaced by the corresponding $\mathbf{v} = \mathbf{r}_T$ given by (1.2).

The DOA vector is a unitary vector, thus has length equal to 1, i.e. $|\mathbf{\vartheta}| = |\mathbf{r}|/|\mathbf{r}| = 1$, and its projections onto the (x, y, z) Cartesian coordinate system axes are equal to the cosines of angles between the DOA and the corresponding axes, i.e.

$$\theta_x = \cos(\mathbf{\vartheta}, \mathbf{x}^\circ); \quad \theta_y = \cos(\mathbf{\vartheta}, \mathbf{y}^\circ); \quad \theta_z = \cos(\mathbf{\vartheta}, \mathbf{z}^\circ), \quad (1.5)$$

where \mathbf{x}° , \mathbf{y}° and \mathbf{z}° denote the orientation vectors along the corresponding axes (x, y, z) normalized to the length one, i.e. $|\mathbf{x}^\circ| = 1$, $|\mathbf{y}^\circ| = 1$, $|\mathbf{z}^\circ| = 1$. These three DOA coordinates (1.5) are also referred to as *directional cosines* [1], [4] related to the DOA vector $\mathbf{\vartheta}$. Using the DOA definition given by (1.4), (1.5), we now express the location of any point \mathbf{r} and the particular TAG location $\mathbf{r}_T = \mathbf{v}$ on the scene plane in the following *directional coordinate system* as

$$\mathbf{r} = (r, \mathbf{\vartheta}) = (r, \theta_x, \theta_y, \theta_z) \quad \text{and} \quad \mathbf{v} = (v, \mathbf{\vartheta}_v) = (v = r_T, \theta_{Tx}, \theta_{Ty}, \theta_{Tz}), \quad (1.6)$$

respectively.

Note that in the considered coordinate system of Fig. 1.1, two principal directional cosines θ_x and θ_y defined by (1.5) explicitly characterize the DOA vector because the third directional cosine θ_z can be calculated from θ_x and θ_y as

$$\theta_z = \sqrt{1 - (\theta_x^2 + \theta_y^2)}. \quad (1.7)$$

From Fig. 1.1, we also can express the elevation angle ϑ and azimuth angle φ via the introduced above DOA parameters as follows,

$$\eta = \arctg\left(\frac{\theta_y}{\theta_x}\right), \quad \varphi = \arcsin\left(\sqrt{\theta_x^2 + \theta_y^2}\right) \quad (1.8.a)$$

and

$$\theta_x = \sin \eta \cos \varphi, \quad \theta_y = \sin \eta \sin \varphi, \quad (1.8.b)$$

respectively.

Next, from the geometry of Fig. 1.1 it follows that any point \mathbf{r} in the scene plane R for a given AAP elevation $z = h_A$ can be explicitly expressed now via only two first directional cosine parameters θ_x and θ_y as

$$\mathbf{r} = (x, y, z)^T \quad \text{with} \quad x = \theta_x \left(\frac{h}{\sqrt{1 - (\theta_x^2 + \theta_y^2)}} \right), \quad y = \theta_y \left(\frac{h}{\sqrt{1 - (\theta_x^2 + \theta_y^2)}} \right), \quad \text{for given } z = h. \quad (1.9)$$

Correspondingly, the LOT Cartesian coordinates (1.2) can be expressed via only two tag DOA parameters θ_{Tx} and θ_{Ty} and the same given AAP elevation h_A as follows,

$$\mathbf{v} = (x_T, y_T, z_T)^T \quad \text{with} \quad x_T = \theta_{Tx} \left(\frac{h}{\sqrt{1 - (\theta_{Tx}^2 + \theta_{Ty}^2)}} \right), \quad y_T = \theta_{Ty} \left(\frac{h}{\sqrt{1 - (\theta_{Tx}^2 + \theta_{Ty}^2)}} \right), \quad z_T = h_A. \quad (1.10)$$

Hence, two-dimensional directional cosine vector $\mathbf{\theta} = \mathbf{\theta}_{xy} = (\theta_x, \theta_y)^T$ composed of *only two* first directional cosines θ_x and θ_y (i.e. the projection of $\mathbf{\vartheta}$ onto the (x, y) AAP, see Fig. 1.1) completely defines (for a given AAP elevation h) the position of point \mathbf{r} in the scene plane

including the desired LOT vector \mathbf{v} defined by (1.10). This enables us, in the sequence, adopt the simplified two dimensional (2-D in our notation) directional cosine format

$$\boldsymbol{\theta} = (\theta_x, \theta_y)^T \text{ with } \theta_x = \cos(\hat{\boldsymbol{\theta}}, \hat{\mathbf{x}}^\circ) \text{ and } \theta_y = \cos(\hat{\boldsymbol{\theta}}, \hat{\mathbf{y}}^\circ) \quad (1.11)$$

for coordinating arbitrary points displaced over the scene plane ($x, y, z = h_A$) with the corresponding LOT explicitly determined via (1.10). The same 2-D coordinate format is eligible for a 3-D scenario with the range coordinate $z \in Z$ sliced within some operational range interval $Z = [range_{min}, range_{max}]$.

B. Transmission System: An Operational Description

According to the SOW, the system under consideration/development is operated at two separate yet concurrent frequencies of 24.5 GHz and 36 GHz with dual polarizations: (V)-vertical and (H)-horizontal. At one instant, radio frequency (RF) pulses of a specified pulse width (PW) are transmitted concurrently at 24.5 and 36 GHz in either V polarization or H polarization. These pulses are “calibrated” to maintain coherency so that their amplitudes and phases are constant for different pulses. The transmitting antenna is switched between the V and H polarizations; i.e., V and H transmitted pulses are delayed by a certain time. For each frequency (24.5 or 36 GHz), transmitted V polarized and H polarized RF pulses are separated by a half of the fixed pulse repetition time (PRT/2). The V polarized RF pulses and H polarized RF pulses are repeated after every PRT. This is illustrated in Figure 1.2, where the transmitted V-pulse envelope is modeled as $a_V(t)$ and the amplitude of the H-pulse is $a_H(t)$.

The multisensor imaging radar (MIR) sensor antenna array is composed of 24 antenna elements. Each element receives signals at V and H polarizations. In every PRT corresponding to one frequency band (24.5 GHz or 36 GHz), 4 multimode measurement row data vectors $\mathbf{U}^T = \{\mathbf{U}_{VV}, \mathbf{U}_{VH}, \mathbf{U}_{HV}, \mathbf{U}_{HH}\}^T$ are provided for further processing. That is, for diverse polarization modes (VV, VH, HV, HH) there is no time delay between receiving antenna elements since they are spaced close to each other, thus one composite data vector \mathbf{U} formed at the outputs of all 24 elements is provided for further processing. Every composite row data vector \mathbf{U}^T is composed of 24 rows ($i = 1, \dots, 24$) collected for $2N$ measurement time instants ($n = 1, \dots, N$).

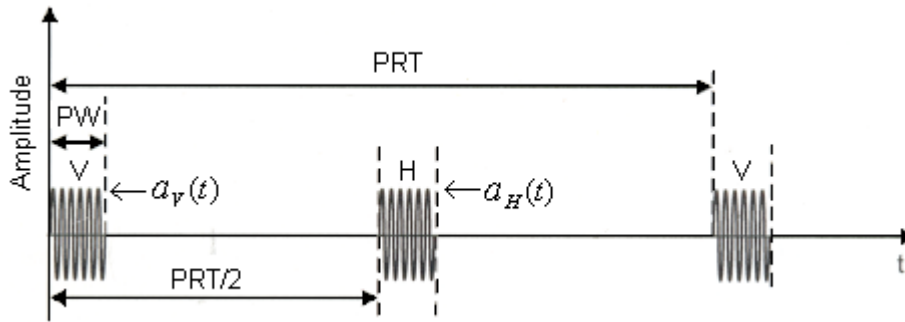


Figure 1.2 Transmitting pulse format.

The format of these data \mathbf{U} vectors is shown below:

$$\mathbf{U}_{VV}^T = \text{row}\{A_{inVV} \cos(\varphi_{inVV}), A_{inVV} \sin(\varphi_{inVV}); i = 1 \rightarrow 24, n = 1 \rightarrow N\} \quad (1.12)$$

$$\mathbf{U}_{\text{vH}}^T = \text{row}\{A_{\text{inVH}} \text{Cos}(\varphi_{\text{inVH}}), A_{\text{inVH}} \text{Sin}(\varphi_{\text{inVH}}); i = 1 \rightarrow 24, n = 1 \rightarrow N\} \quad (1.13)$$

$$\mathbf{U}_{\text{HV}}^T = \text{row}[A_{\text{inHV}} \text{Cos}(\varphi_{\text{inHV}}), A_{\text{inHV}} \text{Sin}(\varphi_{\text{inHV}})] i = 1 \rightarrow 24, n = 1 \rightarrow N \quad (1.14)$$

$$\mathbf{U}_{\text{HH}}^T = \text{row}\{A_{\text{inHH}} \text{Cos}(\varphi_{\text{inHH}}), A_{\text{inHH}} \text{Sin}(\varphi_{\text{inHH}}); i = 1 \rightarrow 24, n = 1 \rightarrow N\} \quad (1.15)$$

The vector formation diagram is shown in Figure 1.3.

1.1.2. Multimode Sensor Array Signal Model

Consider that the array consists of M sensors numbered as $m = 1, 2, \dots, m_0, \dots, M$ located in the AAP R , in which the central sensor (sensor which phase center is located in the array midpoint $\mathbf{p} = \mathbf{0}$) is labeled as m_0 . Each sensor is characterized by its receive pattern response $g_m(\boldsymbol{\theta})$ in the direction $\boldsymbol{\theta}$. A complex bandpass signal at the time instant t within the observation interval T , $t \in T$ induced at the output of the m th sensor of the antenna array that was *reflected/backscattered* by tag TAG located in the point $\mathbf{r} \in R$ can be represented as follows,

$$\dot{s}_m(t, \mathbf{r}) = \dot{s}(t, \mathbf{p} = \mathbf{p}_m; \mathbf{r}) = s_m(t, \mathbf{r}) \exp(i2\pi f_0 t); \quad m = 1, 2, \dots, m_0, \dots, M. \quad (1.16)$$

To distinguish between the bandpass and baseband models, we adopt here the following notational conventions: the point over a symbol (\dot{s}) indicates to the complex *bandpass* signal model [1], [2], while the same symbol without the point (s) represents the complex envelope of the corresponding baseband signal (the analytical baseband model).

The bandpass signal at the output of the central m_0 th element of the array has the following model [1], [2]

$$\dot{s}_{m_0}(t) = \dot{s}(t, \mathbf{p} = \mathbf{0}) = e_v a(t - \tau_v) g_{m_0}(\boldsymbol{\theta}_v) \exp(i2\pi f_0(t - \tau)) \quad (1.17)$$

with the corresponding complex envelope

$$s_{m_0}(t, \mathbf{v}) = e_v a(t - \tau_v) g_{m_0}(\boldsymbol{\theta}_v). \quad (1.18)$$

Here, we adopt the following notations:

- $f_0 \in F_r$ – carrier signal frequency in the waveband F_v allocated for a particular r th TAG;
- $\mathbf{r} \in R$ – tag LOT parameter that defines the exact TAG location on the scene plane R ;
- $\boldsymbol{\theta}_v = (\theta_{v_x}, \theta_{v_y})^T$ – 2-D DOA vector that defines the direction of arrival of the TAG signal wave represented in directional cosines (1.11);
- $g_{m_0}(\boldsymbol{\theta}_v)$ – receive pattern response of the central array sensor (labeled as m_0 th sensor with the phase center located in the array midpoint $\mathbf{p} = \mathbf{0}$) in the direction $\boldsymbol{\theta}_v$;
- e_v – random complex amplitude of the TAG signal located at $\mathbf{v} = \mathbf{r}_T$ induced at the sensor array midpoint; we consider that at the signaling interval T , $t \in T$, the amplitude e_v is a constant random variable;
- $a(t - \tau_v) = a(t - \frac{2|\mathbf{v}|}{c})$ – regular signal complex amplitude specified by the employed

pulse modulation envelope $a(t)$ related to the TAG at distance $|\mathbf{v}|$ from the sensor array midpoint.

The complex amplitude e_v involves all uncertain aspects of the model (1.17), (1.18), in particular: random target reflectivity/scattering factor, wave attenuation factor, random channel distortions factor and non-controlled phase shift due to the propagation delay from the TAG to the array midpoint.

In this report, we consider the case of known (user specified) calibrated transmit signal modulation $a(t)$ calibrated with respect to the normalized L_2 norm (i.e., $\|a(t)\|_{L_2} = 1$) and *unknown random* TAG signal amplitude e_v . Following the maximum entropy channel model considerations [1], [3] we adopt general Gaussian non-stationary (due to the transmitter signal modulation) model for e_v , i.e. the e_v is considered to be a realization of a Gaussian zero-mean random variable with unknown correlation factor

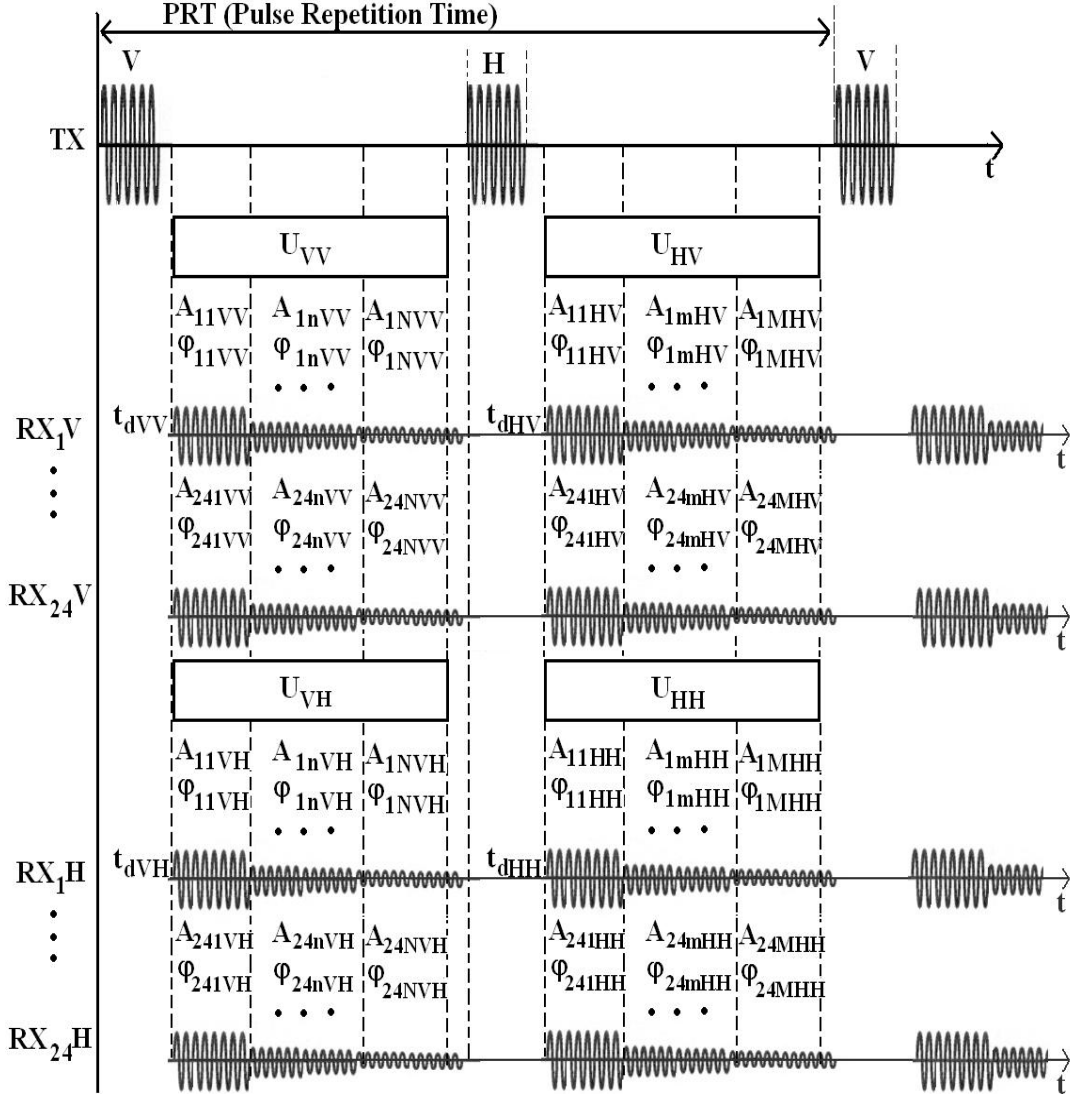


Figure.1.3 Transmitting-receiving signal format.

$$\langle e_v e_v^* \rangle = b_v \quad (1.19)$$

For the zero delay $\tau = 0$, this function relates to the TAG radar cross-section σ_v as [4]

$$\sigma_v = 4\pi |\mathbf{v}|^2 b_v. \quad (1.20)$$

that serves as a conventional measure of power (unknown as well) of the impinging wavefield reflected/scattered by the TAG.

Note that general model (1.17), (1.18) is valid for both continuous-time and discrete-time formats. In the first case (continuous-time), the argument t is associated with a continuous time within the observation interval T . In the second case (discrete-time), the t is associated with the t th snapshot index $\{t = 1, \dots, T\}$ corresponding to the relevant t th discretization time instant, while T represents the number of the recorded discrete signal snapshots.

Next, we have to represent the model of the signals induced at the outputs of all sensors with the phase centers located at points $\mathbf{p}_m \in P$; $m = 1, \dots, M$. Such signals have different radio

frequency (RF) phase shifts (with respect to (1.17)) due to the difference in propagation delays from the tag position \mathbf{v} to a particular sensor position $\mathbf{p}_m \in P$; $m = 1, \dots, M$. To proceed with the derivation of such model, we express the delay of the TAG signal from point \mathbf{v} on the scene plane to point \mathbf{p}_m in the AAP using the geometry of Fig. 1.1,

$$\tau(\mathbf{p}_m, \mathbf{v}) = \frac{d(\mathbf{p}_m, \mathbf{v})}{c} = \frac{|\mathbf{p}_m - \mathbf{v}|}{c} \quad (1.21)$$

where c is the velocity of light, and $d(\mathbf{p}_m, \mathbf{r}_k)$ represents the distance between the end-points of vectors \mathbf{p}_m and \mathbf{r}_v (see Fig. 1.1) defined as a length of the difference vector $d(\mathbf{p}_m, \mathbf{v}) = |\mathbf{p}_m - \mathbf{v}|$. Using the well-known vector form triangular theorem, we can express this distance $d(\mathbf{p}_m, \mathbf{r}_k)$ as

$$d(\mathbf{p}_m, \mathbf{v}) = |\mathbf{p}_m - \mathbf{v}| = \sqrt{p_m^2 + v^2 - 2[\mathbf{p}_m, \mathbf{v}]} = v \sqrt{1 + \frac{p_m^2}{v^2} - 2[\frac{1}{v}\mathbf{p}_m, \boldsymbol{\theta}_v]} \quad (1.22)$$

where $[\cdot, \cdot]$ denotes the vector scalar (inner) product [1], [5], i.e. $[\mathbf{a}, \mathbf{b}] = a_x b_x + a_y b_y$, $r = |\mathbf{r}_v|$ is the distance from the origin of the AAP coordinate system to the TAG; we also expressed the normalized distance $(1/r_k) \mathbf{r}_v$ using the definition (1.4) for the tag DOA vector

$$\boldsymbol{\Theta}_v = (1/v)\mathbf{v} = \boldsymbol{\theta}_v, \quad \boldsymbol{\theta}_v = (\theta_{v_x}, \theta_{v_y})^T \quad (1.23)$$

and used the fact that all vectors $\{\mathbf{p}_m\}$ are orthogonal to the z -component θ_{v_z} of the DOA vector $\boldsymbol{\Theta}_v$, hence we expressed the scalar product in (1.22) as follows, $[\frac{1}{v}\mathbf{p}_m, \boldsymbol{\Theta}_v] = [\frac{1}{v}\mathbf{p}_m, \boldsymbol{\theta}_v]$.

Note that for any real-world sensor system, the quotient $x_m = \frac{p_m}{r_v}$ is a *small* parameter because the sensor aperture size is always much smaller than the distance to the TAG [1]. Hence, we further can approximate the square root at the right hand of (1.22) by preserving only linear (first-order) term in the expansion of the square root (1.22) in power series with respect to this small parameter $x_m = \frac{p_m}{r_v}$, with the corresponding small vector parameter $\mathbf{x}_m = \frac{\mathbf{p}_m}{|\mathbf{v}|}$ that yields

$$d(\mathbf{p}_m, \mathbf{v}) = v \sqrt{1 + x_m^2 - 2[\mathbf{x}_m, \boldsymbol{\theta}_v]} \approx v(1 - [\mathbf{x}_m, \boldsymbol{\theta}_v]) = v \left(1 - \frac{1}{v}[\mathbf{p}_m, \boldsymbol{\theta}_v]\right) = v - [\mathbf{p}_m, \boldsymbol{\theta}_v]. \quad (1.24)$$

The difference of the propagation distances from the TAG position \mathbf{v} to the sensors located at point \mathbf{p}_m and at the array midpoint $\mathbf{0}$ can be expressed as

$$d(\mathbf{p}_m, \mathbf{r}_k) - d(\mathbf{0}, \mathbf{v}) = v - [\mathbf{p}_m, \boldsymbol{\theta}_v] - v = -[\mathbf{p}_m, \boldsymbol{\theta}_v]. \quad (1.25)$$

This difference produces the corresponding RF propagation delay phase shift

$$\tau(\mathbf{p}_m, \mathbf{v}) - \tau(\mathbf{0}, \mathbf{v}) = \frac{d(\mathbf{p}_m, \mathbf{v}) - d(\mathbf{0}, \mathbf{v})}{c} = -\frac{[\mathbf{p}_m, \boldsymbol{\theta}_v]}{c}. \quad (1.26)$$

Using (1.26), we now may write the bandpass model of the random TAG signal $s_m(t; \mathbf{v})$ at the output of the m^{th} sensor as a phase delayed structural generalization of (1.17), i.e.,

$$s_m(t; \mathbf{v}) = s(t, \mathbf{p}_m; \mathbf{v}) = e_v a(t - \tau_v) g_m(\boldsymbol{\theta}_v) \exp\{i2\pi f_0 t - (\tau(\mathbf{p}_m, \mathbf{v}) - \tau(\mathbf{0}, \mathbf{v}))\}$$

$$= e_v(t) a(t - \tau) g_m(\boldsymbol{\theta}_v) \exp(i2\pi f_0 \frac{[\mathbf{p}_m, \boldsymbol{\theta}_v]}{c}) \exp(i2\pi f_0 t) \quad (1.27)$$

where $g_m(\boldsymbol{\theta}_v)$ represents the receive pattern response of the m th array sensor in the TAG direction $\boldsymbol{\theta}_v$ [2], [18].

The corresponding complex envelope of the t th time sampled signal at the m th element of the array (the baseband analytical signal model [2]) now becomes

$$s_m(t; \mathbf{v}) = e_v a(t - \tau_v) g_m(\boldsymbol{\theta}_v) \exp(i2\pi f_0 \frac{[\mathbf{p}_m, \boldsymbol{\theta}_v]}{c}) = e_v a(t - \tau_v) g_m(\boldsymbol{\theta}_v) \exp(i2\pi \frac{1}{\lambda_0} [\mathbf{p}_m, \boldsymbol{\theta}_v]) \quad (1.28)$$

where $\lambda_0 = 1/f_0$ is the carrier signal wavelength, and the random complex TAG signal amplitude e_v incorporates now all uncertain amplitude-phase factors, in particular:

- the random complex TAG reflectivity/scattering factor;
- the random channel propagation distortion factor;
- the unknown/uncontrolled transmitted signal waveform modulation;
- the unknown initial RF phase shift $\exp(-i2\pi f_0 \tau_v)$.

To simplify the sensor signal model (1.24), we next introduce the normalized sensor position vectors (sensor position vectors expressed in the carrier signal wavelengths) [1], [2], [4]

$$\boldsymbol{\rho}_m = \frac{\mathbf{p}_m}{\lambda_0}; \quad m = 1, 2, \dots, M \quad (1.29)$$

and define the regular complex phase modulation signal $S(\mathbf{p}_m, \mathbf{v})$ that we refer to as the regular *unit signal* (referred to also as modulated *steering signal*) [2], [4] in the direction of the TAG

$$S(t, \mathbf{p}_m, \mathbf{v}) = a(t - \tau_v) g_m(\boldsymbol{\theta}_v) \exp(i2\pi [\boldsymbol{\rho}_m, \boldsymbol{\theta}_v]); \quad m = 1, 2, \dots, M \quad (1.30)$$

where $\boldsymbol{\theta}_v$ represents the 2-D target DOA vector expressed via corresponding directional cosines related to the LOT vector \mathbf{v} via (1.23).

These definitions (1.29), (1.30), enable us to express the observation noise-free t th sampled complex bandpass sensor signals (1.28) at the outputs of M sensors positioned in the fixed AAP points $\{\mathbf{p}_m; m = 1, 2, \dots, M\}$ that are induced by the scattering target (labeled as TAG in Fig. 1.1) located on the scene plane in position \mathbf{v} as follows,

$$s(t, \mathbf{p}_m, \mathbf{v}) = e_v S(t, \mathbf{p}_m, \mathbf{v}); \quad m = 1, 2, \dots, M. \quad (1.31)$$

1.1.3. Extended Signal Model Generalization: Distributed Scene Scenario

In this subsection, we provide an expansion of the developed above signal model for the distributed scene imaging scenario. In such a scenario, the scene is considered to be composed of the target(s) spatially distributed over the scene $\mathbf{r} \in R \subset \mathbb{R}^2$ that scatter the random complex zero-mean Gaussian field $e(\mathbf{r})$; $\mathbf{r} \in R \subset \mathbb{R}^2$. Gaussianity follows from the *central limit theorem* [5] that holds due to the integral superposition signal model (we explain this issue further on).

Superposition of all scene scattered signals are available for observations and further processing in some prescribed domain P , $\mathbf{p} \in P$, in the (x, y) array aperture plane (AAP) P

elevated over the scene at a fixed height h . In the 3-D model, $h = r$ corresponds to the particular r th range gate. Every elementary scene domain scattering signal $e(\mathbf{r})d\mathbf{r}$ impinging at the AAP from the direction \mathbf{r} induces in a spatial point $\mathbf{p} \in P$ the corresponding elementary signal $s(t, \mathbf{p}; \mathbf{r})d\mathbf{r}$ that can be expressed using (1.31) via substituting the fixed tag location \mathbf{v} (\mathbf{r}_v) by the spatially distributed scene coordinate \mathbf{r} , and the fixed sensor positions \mathbf{p}_m by an arbitrary observation point \mathbf{p} that yields [1], [4]

$$s(t, \mathbf{p}; \mathbf{r})d\mathbf{r} = e(\mathbf{r})S(t, \mathbf{p}, \mathbf{r})d\mathbf{r}; \quad \mathbf{r} \in R, \mathbf{p} \in P \quad (1.32)$$

with the corresponding unit signal

$$S(t, \mathbf{p}, \mathbf{r}) = a(t - \frac{2|\mathbf{r}|}{c}) \exp(i2\pi [\boldsymbol{\rho}, \boldsymbol{\theta}]) \quad (1.33)$$

$$\text{where } \boldsymbol{\vartheta} = \frac{\mathbf{r}}{|\mathbf{r}|} = (\theta_x, \theta_y, \theta_z)^T = (\boldsymbol{\theta}^T, \theta_z)^T; \quad \boldsymbol{\theta} = (\theta_x, \theta_y)^T, \quad \text{and } \boldsymbol{\rho} = \frac{\mathbf{p}}{\lambda_0}. \quad (1.34)$$

Such unit signal (1.33) is recognized to be a composition of the time modulation envelope with conventional 2-D Fourier transformation kernel with the Fourier mates defined by (1.30).

Next, integral superposition of the induced elementary signal (1.33) over the whole scene $\mathbf{r} \in R$ produces the desired random distributed scene signal field with the complex envelope [1]

$$s(t, \mathbf{p}) = \int_R e(\mathbf{r}) S(t, \mathbf{p}, \mathbf{r})d\mathbf{r}; \quad \mathbf{p} \in P, t \in T \quad (1.35)$$

available for observations and recordings over the aperture points $\mathbf{p} \in P$. Using the definitions (1.32), (1.33), we can also express this integral operator-form distributed scene signal model (1.35) in the normalized (Fourier mate) coordinates $(\boldsymbol{\theta}, \boldsymbol{\rho})$ as

$$s(t, \mathbf{p}) = s(t, \boldsymbol{\rho}) = \int_{\Theta} e(\mathbf{r})a(t - \tau) \exp(i2\pi[\boldsymbol{\rho}, \boldsymbol{\theta}])d\boldsymbol{\theta}; \quad \boldsymbol{\rho} = \frac{\mathbf{p}}{\lambda_0} \in \frac{P}{\lambda_0}, \mathbf{p} \in P, \boldsymbol{\theta} \in \Theta, t \in T \quad (1.36)$$

valid for the adopted uncertain modulation scenario, where the field of view (FOV) Θ bounds the DOA observation sector related to the observation scene domain R .

It is conventional in all remote sensing (RS) and radar imaging (RI) applications [1]–[10], to assume that due to the integral signal formation model (1.34), (1.35), the *central limit theorem* conditions hold, hence the signal fields $e(\mathbf{r})$ can be considered to be the zero-mean complex-valued random Gaussian fields with unknown second-order statistics. Next, since in all RS applications the spatial regions of high correlations of $e(\mathbf{r})$ are always small in comparison with the element of resolution on the probing scene [2], [4], [10], the random complex reflectivity $e(t, \mathbf{r})$ from different directions \mathbf{r}, \mathbf{r}' as a function of different time instances t, t' are assumed to be uncorrelated, i.e. characterized by the correlation function [1]

$$R_e(t, \mathbf{r}; t', \mathbf{r}') = \langle e(t, \mathbf{r})e^*(t', \mathbf{r}') \rangle = K_e(\tau, \mathbf{r})\delta(\mathbf{r} - \mathbf{r}'); \quad \tau = t - t' \quad (1.37)$$

where $\delta(\cdot)$ defines the delta-function, $\langle \cdot \rangle$ is the averaging operator and the asterisk indicates the complex conjugate. The function $K_e(\tau, \mathbf{r})$ in (1.37) characterizes the second-order statistics of the random fluctuating scattering field $e(t, \mathbf{r})$ over the angle-time-delay domain.

The Fourier transform of $K_e(\tau, \mathbf{r})$ over the time delay argument

$$b(f, \mathbf{r}) = \int_{-\infty}^{\infty} K_e(\tau, \mathbf{r}) \exp(-i2\pi f\tau) d\tau \quad (1.38)$$

represents the frequency-angular power spectrum of the scattered wavefield that we refer to as the frequency-variant spatial spectrum pattern (SSP) of the scene. The integration of (1.38) over the frequency argument

$$b(\mathbf{r}) = \int_{-\infty}^{\infty} b(f, \mathbf{r}) df = K_e(0, \mathbf{r}) \quad (1.39)$$

represents the spatial spectrum pattern (SSP) of the scene related to the scene differential radar cross section [6], [7]

$$\sigma(\mathbf{r}) = 4\pi|\mathbf{r}|^2 K_e(0, \mathbf{r}) \quad (1.40)$$

through the normalization factor $4\pi|\mathbf{v}|^2$.

The $b(\mathbf{r})$ as a function over the analysis domain (scene frame) $R \ni \mathbf{r}$ has a statistical meaning of the average spatial power reflectivity and is traditionally referred to (in the RS and radar imaging literature, e.g. [1], [2], [6], [7], [8]) as the *spatial spectrum pattern* (SSP) of the scattering field.

In the considered above case of time independent (at small observation intervals T , $t \in T$) random reflectivity $e(t, \mathbf{r}) = e(\mathbf{r})$, the corresponding SSP is defined via (1.19), i.e.,

$$b(\mathbf{r}) = \langle e(\mathbf{r})e^*(\mathbf{r}) \rangle. \quad (1.41)$$

Representing the spatial distribution of the average power of the random scatterers, the SSP $b(\mathbf{r})$ characterizes in an explicit statistical sense the reflectivity/scattering *brightness* of the scene being observed (for this reason, b is adopted in the notations as an abbreviation from reflectivity/scattering *brightness*). Note that other terms such as spatial power spectrum, power reflectivity or differential radar scattering cross section are sometimes used instead of SSP [3], [5], [9], [12], etc. In this report, we generalize all these definitions by the term SSP.

1.1.4 Noised Data Observations

Consider now once again the point-type TAG(s) model from subsection 1.1.2. In practice, actual measurements of any signal are inevitably contaminated with additive observation noise. Define such noise processes at the outputs of M -sensor array as $\{n_m(t) = n(t, \mathbf{p}_m); m = 1, 2, \dots, M\}$. Following common statistical conventions [2], [53] we adopt for such additive noise the maximum entropy model of the Gaussian locally stationary (at the observation interval T) zero-mean Gaussian process. For the discrete (snapshot) time format, the $n_m(t) = n(t, \mathbf{p}_m)$ represents the t th time sample of the Gaussian zero-mean receiver noise from the m th array sensor [2]. Because of intrinsically random nature, this noise is modeled as a random variable, independent of both the snapshot index t and the sensor index m [1], [4].

The array output data are composed of the signals represented by the model (1.22) and such noise processes $\{n_m(t)\}$, i.e.

$$u_m(t) = s_m(t; \boldsymbol{\theta}_v, e_v) + n_m(t, \mathbf{p}_m) = e_v S(t, \mathbf{p}_m, \boldsymbol{\theta}_v) + n(t, \mathbf{p}_m); m = 1, 2, \dots, M. \quad (1.42)$$

where we used notation “ e_v ” to represent the dependence of the signal component in the observations on the random reflectivity of the TAG with the DOA vector $\boldsymbol{\theta}_v = \frac{\mathbf{v}}{|\mathbf{v}|}$. The previous equation can be put now in the following vectorial form

$$\mathbf{u}(t) = \mathbf{s}(t; \boldsymbol{\theta}_v, e_v) = e_v \mathbf{s}_v(t; \boldsymbol{\theta}_v) + \mathbf{n}(t), \quad t \in T, \quad (1.43)$$

which, in expanded form, is

$$\begin{bmatrix} u_1(t) \\ u_2(t) \\ \vdots \\ u_M(t) \end{bmatrix} = e_v \begin{bmatrix} s_1(t; \boldsymbol{\theta}_v) \\ s_2(t; \boldsymbol{\theta}_v) \\ \vdots \\ s_M(t; \boldsymbol{\theta}_v) \end{bmatrix} + \begin{bmatrix} n_1(t) \\ n_2(t) \\ \vdots \\ n_M(t) \end{bmatrix}, \quad t \in T, \quad (1.44)$$

where the spatial information modulation vector $\mathbf{s}_v(t; \boldsymbol{\theta}_v)$ defined via is referred to as array modulated *steering vector* [2], [4] in the tag direction $\boldsymbol{\theta}_v$. This steering vector is composed of the corresponding spatial modulation factors $\{S(\mathbf{p}_m, \mathbf{v}); m = 1, \dots, M\}$ defined by (1.30). In an expanded form, this modulated steering vector is

$$\mathbf{s}_v = \mathbf{s}(t; \tau_v, \boldsymbol{\theta}_v) = \begin{bmatrix} a(t - \tau_v) s_1(\boldsymbol{\theta}_v) \\ a(t - \tau_v) s_2(\boldsymbol{\theta}_v) \\ \vdots \\ a(t - \tau_v) s_M(\boldsymbol{\theta}_v) \end{bmatrix} = \begin{bmatrix} a(t - \tau_v) g_1(\boldsymbol{\theta}_v) \exp(i2\pi[\boldsymbol{\rho}_1, \boldsymbol{\theta}_v]) \\ a(t - \tau_v) g_2(\boldsymbol{\theta}_v) \exp(i2\pi[\boldsymbol{\rho}_2, \boldsymbol{\theta}_v]) \\ \vdots \\ a(t - \tau_v) g_M(\boldsymbol{\theta}_v) \exp(i2\pi[\boldsymbol{\rho}_M, \boldsymbol{\theta}_v]) \end{bmatrix}; \quad (1.45)$$

$$\boldsymbol{\rho} = \frac{\mathbf{p}}{\lambda_0} \in \frac{P}{\lambda_0}, \quad \mathbf{p} \in P, \quad \boldsymbol{\theta}_v = \frac{\mathbf{v}}{|\mathbf{v}|}, \quad \tau_v = \frac{2|\mathbf{v}|}{c}.$$

For the adopted random zero-mean observation data model,

$$\langle \mathbf{n}(t) \rangle = \mathbf{0}, \quad \langle e_v(t) \rangle = 0, \quad \text{hence} \quad \langle \mathbf{s}(t; \boldsymbol{\theta}_v, e_v) \rangle = \mathbf{0} \quad (1.46)$$

thus, the data vector $\mathbf{u}(t)$ is the zero-mean Gaussian vector, $\langle \mathbf{u}(t) \rangle = \mathbf{0}$. The *spatial* covariance matrix \mathbf{R}_u of such observation vector is defined as [2], [4]

$$\mathbf{R}_u = \langle \mathbf{u}(t) \mathbf{u}^+(t) \rangle = \text{Aver}\{\mathbf{u}(t) \mathbf{u}^+(t)\} \Rightarrow \text{for snapshot format} \Rightarrow \approx \frac{1}{T} \sum_{t=1}^T \mathbf{u}(t) \mathbf{u}^+(t) = \mathbf{Y} \quad (1.47)$$

where superscript $^+$ stands for conjugate transpose (Hermitian transpose, $^+ = \text{T}^*$), and $\text{Aver}\{\cdot\}$ represents the time averaging operator that for the practical discrete (snapshot) registration format is approximately defined by the sum at the right-side hand of (1.47). For the specified above model (1.45), (1.46) with the adopted calibration $\|a(t - \tau_v)\|_{L2} = 1$ of the pulse modulation waveform, the exact covariance matrix is independent on the parameter τ_v and is given by

$$\mathbf{R}_u = b_0 \mathbf{s}_0 \mathbf{s}_0^+ + \mathbf{R}_n. \quad (1.48)$$

where $b_0 = \langle |e_0|^2 \rangle$ is the average TAG signal power as a function of the DOA vector $\boldsymbol{\theta}_v$ (we drop subscript index \mathbf{v} for notational simplicity), $\mathbf{R}_n = \langle \mathbf{n}(t) \mathbf{n}^+(t) \rangle = N_0 \mathbf{I}$ represents the $(M \times M)$ -D spatial covariance matrix of the observation white noise vector, where N_0 is the noise

power (variance), and \mathbf{I} defines the identity matrix, $(M \times M)$ -D for the considered here M -sensor array. In (1.48), the M -D steering vector $\mathbf{s}_\theta = (\mathbf{s}_1(\boldsymbol{\theta}_v), \mathbf{s}_2(\boldsymbol{\theta}_v), \dots, \mathbf{s}_M(\boldsymbol{\theta}_v))^T$ is composed of the elements

$$\{\mathbf{s}_m(\boldsymbol{\theta}_v) = g_m(\boldsymbol{\theta}_v) \exp(i2\pi[\mathbf{p}_m, \boldsymbol{\theta}_v]); m = 1, \dots, M\}. \quad (1.49)$$

Note that the snapshot averaged statistical data correlation model (1.48) excludes the TAG range parameter τ_v . This is acceptable for the adopted above problem model with geometry specified in Fig. 1.1 because vector of two directional cosines $\boldsymbol{\theta}_v$ together with the given distance to the scene plane $z_T = h_A$ uniquely define via (1.9) the TAG location on the scene. In this Part of the report, we adopt such the simplified statistical model (1.48), (1.49) with the corresponding relation to the scene elevation (1.9) for simplicity of the basic model consideration and preliminary algorithmic developments. In the following Parts of this report, we will perform generalization of the data model for arbitrary range gates and observation angles.

1.1.5 Space-Time-Ordered Snapshot Data Model

In this section, we represent the snapshot data vector (1.44) in the expanded vectorial form (as a “long” vector) via ordering all $\{u_m(t); m = 1, \dots, M, t = 1, \dots, T\}$ in (1.44) over the sensor index m and the snapshot index t (first, all $t = 1, \dots, T$ for $m = 1$, next, all $t = 1, \dots, T$ for $m = 2$, and so on up to the last ordering: all $t = 1, \dots, T$ for $m = M$) as follows,

$$\begin{aligned} \mathbf{u} &= \underset{m,t}{\text{vec}}\{u_m(t); m = 1, \dots, M, t = 1, \dots, T\} \\ &= [(u_1(t_1), u_1(t_2), \dots, u_1(T)), (u_2(t_1), u_2(t_2), \dots, u_2(T)), \dots, (u_M(t_1), u_M(t_2), \dots, u_M(T)))]^T. \end{aligned} \quad (1.50)$$

The mt -ordered observation noise vector has the similar representation form,

$$\begin{aligned} \mathbf{n} &= \underset{m,t}{\text{vec}}\{n_m(t); m = 1, \dots, M, t = 1, \dots, T\} \\ &= [(n_1(t_1), n_1(t_2), \dots, n_1(T)), (n_2(t_1), n_2(t_2), \dots, n_2(T)), \dots, (n_M(t_1), n_M(t_2), \dots, n_M(T)))]^T. \end{aligned} \quad (1.51)$$

Using these definitions (1.50) – (1.51) and the original model given by (1.44), we can express the relation of \mathbf{e}_v to the mt -ordered observation data vector \mathbf{u} as

$$\mathbf{u} = \mathbf{s}(\mathbf{v}, e_\theta) + \mathbf{n} \quad (1.52)$$

where the mt -ordered random signal snapshot vector $\mathbf{s}(\mathbf{v}, e_\theta)$ is given by

$$\mathbf{s}(\mathbf{v}, e_\theta) = e_\theta \mathbf{s}_\theta \quad (1.53)$$

with the MT -D modulated steering vector

$$\mathbf{s}_\theta = \begin{bmatrix} s_1(\boldsymbol{\theta}_v) \otimes \mathbf{a}_{(T)}(t - \tau_v) \\ s_2(\boldsymbol{\theta}_v) \otimes \mathbf{a}_{(T)}(t - \tau_v) \\ \vdots \\ s_M(\boldsymbol{\theta}_v) \otimes \mathbf{a}_{(T)}(t - \tau_v) \end{bmatrix}. \quad (1.54)$$

where T -D column vector $\mathbf{a}_{(T)}(t - \tau)$ is composed of the t -sampled modulation envelope $a(t - \tau_v)$ and symbol \otimes defines the Kroneker product.

Last, to preserve the one-to-one correspondence between the mt -ordered vector data model introduced in this section to the original m -ordered model presented in the previous section, the *spatial* correlation operations over the vector \mathbf{u} are defined via the same averaging (1.47), i.e.

$$\mathbf{Y} = \hat{\mathbf{R}}_{\mathbf{u}} = \underset{n}{Aver}\{\mathbf{u}\mathbf{u}^+\} = \frac{1}{N} \sum_{n=1}^T \mathbf{u}(n)\mathbf{u}^+(n) \approx b_0 \mathbf{s}_0 \mathbf{s}_0^+ + \mathbf{R}_n \quad (1.55)$$

where $\mathbf{u}(t)$ represents the original M -D sensor data vector (1.50) for the n th snapshot time instant, and the first term at the right hand side of (1.55) is defined as in (1.48), (1.49), correspondingly.

1.2. Robust Parameter Estimation in Uncertain Scenario: Application to TAG Localization

This section addresses the basic principles of the robust parameter estimation, in particular, the robust maximum likelihood (ML) method, i.e. the ML parameter estimator robust against the operational scenario model uncertainties. The conceptual idea is to derive the robust ML strategy that is invariant to any uncertain data model parameters. In the particular problem of TAG localization, the operational model uncertainties encompass all unknown characteristics of the single tag localization experiment detailed in section 1.1. The goal is to compose the computational structure of the robust ML parameter estimation algorithm for TAG localization with matched multi-beam fan beamformer for such uncertain operational scenario. Finally, we provide useful generalization of the matched spatial filtering (MSF) imaging technique to the Fourier transform-based spatial filtering (FTSF) algorithm.

1.2.1. Problem Formalism

Consider the signal parameter estimation problem of deriving an estimate $\hat{\boldsymbol{\theta}}$ of the desired signal directional vector parameter $\boldsymbol{\theta}$ via processing the recorded data vector \mathbf{u} , i.e.

$$\hat{\boldsymbol{\theta}} = \mathcal{W} \mathbf{u}; \mathcal{W} : \mathbb{U} \rightarrow \Theta \quad (1.56)$$

Here we preserve all notational conventions introduced in the previous sections but omitted subscript \mathbf{v} indicating at the TAG DOA vector, i.e., we denote now $\boldsymbol{\theta}_{\mathbf{v}} = \boldsymbol{\theta}$ to simplify the notations. In (1.56), \mathcal{W} defines a *solution operator* $\mathcal{W} : \mathbb{U} \rightarrow \Theta$, that when operating on the data, $\mathbf{u} \in \mathbb{U}$, produces an estimate $\hat{\mathbf{v}}$ of the desired *information* signal vector (parameter of interest) $\boldsymbol{\theta} \in \Theta$, where Θ domain is associated with the field of view (FOV) in angular directions. Also, in this section, we consider narrow FOV, and associate the scene plane with one particular range gate, in which case the processing is to be performed in two dimensions over the DOA coordinates $\boldsymbol{\theta} \in \Theta$. The general case of 3-D (range-azimuth-elevation) signal processing (SP) will be considered in the next Part of this Report. Thus, here beneath we proceed with basic developments of the SP considerations for robust DOA

estimation in a particular fixed range gate (e.g., over the scene plane distanced from the sensor array at a fixed $z = h_A$ as exemplified in Fig. 1.1).

In contrast to the statistically certain scenario considered in the previous section, now we assume the statistically uncertain scenario. In such a scenario, the space-time-ordered vector-form equation of observation (EO) is defined by (1.52) that we rewrite here as

$$\mathbf{u} = \mathbf{s}(\boldsymbol{\theta}, e_{\theta}) + \mathbf{n} \quad (1.57)$$

where the mt -ordered random signal snapshot vector $\mathbf{s}(\boldsymbol{\theta}, e_{\theta})$ is given by (1.53), (1.54) with the steering vector defined by (1.49).

A. Gaussian observation noise

The measurement noise vector \mathbf{n} in the EO (1.57) is modeled as an unknown random Gaussian L -D complex-valued vector composed of the tm -ordered noise samples with zero mean

$$\mathbf{m}_n = \langle \mathbf{n} \rangle = \mathbf{0},$$

(any non-zero known value \mathbf{m}_n can be simply subtracted from the data vector \mathbf{u}) and general-form (spatial-temporal) $L \times L$ correlation matrix $\mathbf{R}_n = \langle \mathbf{n}\mathbf{n}^+ \rangle$. Such noise vector is explicitly characterized by its pdf [4], [5]:

$$p(\mathbf{n}) = (2\pi)^{-L} \det^{-1} \mathbf{R}_n \exp\{-\mathbf{n}^+ \mathbf{R}_n^{-1} \mathbf{n}\}. \quad (1.58)$$

B. Gaussian uncertain signal

The random signal vector $\mathbf{s}(\boldsymbol{\theta}, e_{\theta})$ defined by (1.53), (1.49) is composed of the tm -ordered samples $\{s_m(t, \boldsymbol{\theta}, e_{\theta}); m = 1, \dots, M, t = 1, \dots, T\}$ of a random zero-mean Gaussian process dependent on the unknown realization e_{θ} of the Gaussian amplitude variable. The latter constitutes the not-of-interest (nuisance) random parameter of the signal model, while the parameter of interest \mathbf{v} is now modeled as a *deterministic* vector because in the particular problem at hand, \mathbf{v} represents the unknown LOT parameter. No statistical a priori distribution information is associated with the deterministic \mathbf{v} , thus the Bayesian minimum risk estimation strategy must be constructed based on the maximum likelihood (ML) inference making rule.

To proceed with derivation of such a rule, we need to define the (conditional) pdf of the tm -ordered data vector \mathbf{u} under the condition of a fixed tm -ordered signal vector $\mathbf{s}(\boldsymbol{\theta}, e_{\theta})$ defined by (1.49) for a fixed information parameter $\boldsymbol{\theta}$ and fixed realization of the nuisance parameter e_{θ} . For the Gaussian observation model, such conditional pdf is the likelihood function [1]

$$p(\mathbf{u}|\mathbf{s}(\mathbf{v}, e_{\mathbf{v}})) = (2\pi)^{-L} \det^{-1} \mathbf{R}_n \exp\{-(\mathbf{u} - \mathbf{s}(\boldsymbol{\theta}, e_{\theta}))^+ \mathbf{R}_n^{-1} (\mathbf{u} - \mathbf{s}(\boldsymbol{\theta}, e_{\theta}))\}. \quad (1.59)$$

viewed as a function of all unknown signal parameters $\boldsymbol{\theta}, e_{\theta}$.

1.2.2 Robust ML Estimation of a Single Information Parameter

Following the basic concepts of the statistical estimation theory [1], [2], [4] the optimal *robust* ML inference making rule must be based on the maximization of some sufficient statistics constructed from the likelihood function independent on the nuisance parameters, i.e.

$$\hat{\boldsymbol{\theta}} = \underset{\boldsymbol{\theta}}{\operatorname{argmax}} \varphi(p(\mathbf{u}|\mathbf{s}(\boldsymbol{\theta}))) \quad (1.60)$$

where as previously, $\varphi(\cdot)$ represents any monotonous nonnegative function of the likelihood function $p(\mathbf{u}|\mathbf{s}(\boldsymbol{\theta}))$ dependent *only* on the information vector (parameter of interest) $\boldsymbol{\theta}$ and *independent* on the not-of-interest parameter $e_{\boldsymbol{\theta}}$.

Two statistically grounded approaches may be followed to proceed with the construction of the robust sufficient statistics [1]. The first one is to exploit the idea of statistical averaging of the likelihood function defined for all unknown parameters $\boldsymbol{\theta}$, $e_{\boldsymbol{\theta}}$ over the Gaussian distribution $p(\mathbf{e}_v)$ of the nuisance vector \mathbf{e}_v , i.e.

$$p(\mathbf{u}|\mathbf{s}(\boldsymbol{\theta})) = \int_{-\infty}^{\infty} p(\mathbf{u}|\mathbf{s}(\boldsymbol{\theta}, e_{\boldsymbol{\theta}})) p(e_{\boldsymbol{\theta}}) d e_{\boldsymbol{\theta}}. \quad (1.61)$$

The crucial point is that in practice, the covariance function of the Gaussian pdf $p(e_{\boldsymbol{\theta}})$ is itself unknown, and moreover, because of the unknown statistics of noise (and clutter), the resulting likelihood function of the information parameter depends also on such unknown statistics, in particular, on the unknown correlation matrix \mathbf{R}_n of the composite noise (receiver noise and clutter). The robust likelihood sufficient statistics can be thus constructed only for the case of *white* observation noise model. We will pursue this approach in the sequence of this section.

The second possible way is an *adaptive* estimation approach that prescribes construction of robust adaptive estimation strategies with the objective to obtain an accurate estimate of the source information parameter by means of data-adaptive spatial filtering and interference rejection. Such an approach is computationally more expensive, and is the matter of further developments in Part II and Part III of this report.

In this section of the report, (following the state of work (SOW) statements), we proceed with the development of the robust single TAG localization technique adopting the practically motivated assumptions of white observation noise and completely unknown (i.e arbitrary) average TAG signal power defined via (1.41) that we rewrite here as

$$b_{\boldsymbol{\theta}} = \langle e_{\boldsymbol{\theta}} e_{\boldsymbol{\theta}}^* \rangle. \quad (1.62)$$

Our goal now is to derive the technically tractable accurate tag localization technique based on the statistically optimal robust ML strategy (1.60). To proceed with this development, we first borrow (from the statistical estimation theory [4]) the formula for the sufficient statistics $\varphi(p(\mathbf{u}|\mathbf{s}(\boldsymbol{\theta})))$ for the information parameter \mathbf{v} of a single signal observed in a white additive noise with an arbitrary spectral intensity (noise variance) N_0 . Such the sufficient statistics is represented by the logarithm of the likelihood ratio [1]

$$\varphi(p(\mathbf{u}|\mathbf{s}(\boldsymbol{\theta}))) = \ln \frac{p(\mathbf{u}|\mathbf{s}(\boldsymbol{\theta}))}{p(\mathbf{u}|\mathbf{s}=\mathbf{0})} = -\ln(1 + \mu_A) + \frac{b_v}{1 + \mu_A} \mathbf{s}_{\boldsymbol{\theta}}^+ \mathbf{Y} \mathbf{s}_{\boldsymbol{\theta}} \quad (1.63)$$

where the array signal-to-noise ratio (SNR) μ_A is defined as

$$\mu_A = b_{\boldsymbol{\theta}} \frac{\|\mathbf{s}_{\boldsymbol{\theta}}\|^2}{N_0}. \quad (1.64)$$

In (1.63), $p(\mathbf{u}|\mathbf{s} = \mathbf{0}) = p(\mathbf{n})$ is the normalizing pdf defined by (1.58) for the data composed of only the noise vector; \mathbf{s}_0 is the array steering vector defined by (1.49) that depends on the information vector $\boldsymbol{\theta} = \boldsymbol{\theta}_v$, and \mathbf{Y} represents the $M \times M$ data statistics matrix defined by (1.55).

The formula (1.63) establishes the desirable robustness properties of the log-likelihood sufficient statistics $\frac{p(\mathbf{u}|\mathbf{s}(\boldsymbol{\theta}))}{p(\mathbf{u}|\mathbf{s} = \mathbf{0})}$. In fact, examining the formula (1.63) one may easily deduce

that neither the bias term, $c = -\ln(1 + \mu_A)$, nor the coefficient $k = \frac{b_0}{1 + \mu_A}$ depend on the

information vector $\boldsymbol{\theta}$, i.e., on the tag DOA vector $\boldsymbol{\theta} = \boldsymbol{\theta}_v$ only. Hence, following the basic rules for construction of the sufficient statistics we derive now the *minimal sufficient statistics* via subtracting the constant c from the log-likelihood ratio (1.63) and normalizing it by the constant k^{-1} , i.e.

$$l(\boldsymbol{\theta}) = k^{-1} \ln p(\mathbf{u}|\boldsymbol{\theta}) - c = \mathbf{s}_0^+ \mathbf{Y} \mathbf{s}_0 \quad (1.65)$$

where we conserved the notation, $l(\boldsymbol{\theta})$, for such minimal sufficient statistics. The argument of the maximum of the original statistics (1.63) is the same as the argument of the maximum of the minimal sufficient statistics $l(\mathbf{v})$, thus the robust ML decision making rule for the single TAG localization becomes

$$\hat{\boldsymbol{\theta}} = \underset{\boldsymbol{\theta}}{\operatorname{argmax}} l(\boldsymbol{\theta}) = \underset{\boldsymbol{\theta}}{\operatorname{argmax}} (\mathbf{s}_0^+ \mathbf{Y} \mathbf{s}_0) . \quad (1.66)$$

The statistics (1.68) is recognized to be a ML estimate of the tag signal power formed applying the matched spatial beamforming method [2], hence the statistical meaning of the estimation rule (1.68) is as follows:

Table 1.1.

To find the coordinate of the maximum of the matched beamformer estimate of the signal power spatial spectrum pattern (SSP) distribution over the scene produced by a single tag signal, i.e. $\hat{\boldsymbol{\theta}} = \underset{\mathbf{v}}{\operatorname{argmax}} \{\text{matched estimate } \mathbf{s}_0^+ \mathbf{Y} \mathbf{s}_0 \text{ of the SSP distribution produced by a single TAG signal}\}.$ (1.67)

Also, in the imaging applications [5], an estimate of the signal power distribution over the scene is interpreted as a source *image*. Hence, the robust ML localization procedure (1.66), (1.67) admits also the following image analysis interpretation:

Table 1.2.

To form the image of the TAG as a function of the spatial scene coordinates $\boldsymbol{\theta} \in \Theta$ in the observation domain (FOV) Θ applying the matched beamforming method, i.e. forming function $l(\boldsymbol{\theta}) = \mathbf{s}_0^+ \mathbf{Y} \mathbf{s}_0$ over the FOV $\boldsymbol{\theta} \in \Theta$ and localize the TAG via finding the coordinate of the image maximum, i.e.

$$\hat{\boldsymbol{\theta}} \Leftarrow \text{coordinate of maximum of the matched image } \mathbf{s}_0^+ \mathbf{Y} \mathbf{s}_0, \text{ of the TAG over the FOV } \boldsymbol{\theta} \in \Theta .$$

Having established the robust ML inference making rule (1.60) interpreted also both in the SSP estimation (1.67) and the image analysis (1.68) statements, we are ready now to proceed with the derivation of the technically easy-to-implement tag localization algorithm.

1.3. Robust ML TAG Localization Algorithm

To simplify the computations prescribed by the ML decision rule (1.68), let us make use of the fact that the averaging procedure (1.55) may be accomplished *after* the spatial data correlation procedure when performing the matched beamforming (1.68), in which case the minimal sufficient statistics (1.65) can be rewritten for a particular fixed range gate as

$$l(\boldsymbol{\theta}) = \mathbf{s}_0^+ \mathbf{Y} \mathbf{s}_0 = \mathbf{s}_0^+ \frac{1}{N} \sum_{n=1}^N \mathbf{u}(n) \mathbf{u}^+(n) \mathbf{s}_0 = \frac{1}{N} \sum_{n=1}^N q_{\boldsymbol{\theta}}^*(n) q_{\boldsymbol{\theta}}(n) = \frac{1}{N} \sum_{n=1}^N |q_{\boldsymbol{\theta}}^*(n)|^2 \quad (1.69)$$

where

$$q_{\boldsymbol{\theta}}^*(n) = \mathbf{u}^+(n) \mathbf{s}_0 = [\mathbf{s}_0, \mathbf{u}(n)] ; \quad n = 1, \dots, N \quad (1.70)$$

represents the conjugate spatial correlation factor between the n th data snapshot and the steering vector \mathbf{s}_0 in the direction $\boldsymbol{\theta} \in \Theta$. Also, the square modulus in (1.69) is invariant to the complex conjugation of (1.70), thus, the sufficient statistics (1.69) can be further transformed into

$$l(\boldsymbol{\theta}) = \frac{1}{N} \sum_{n=1}^N |q_{\boldsymbol{\theta}}^*(t)|^2 = \underset{n}{Aver} \{ |q_{\boldsymbol{\theta}}(t)|^2 \} \quad (1.71)$$

that is essentially, the averaging of the squared modulus of the complex correlation factors

$$q_{\boldsymbol{\theta}}(n) = \mathbf{u}^T(n) \mathbf{s}_0^* = [\mathbf{u}(n), \mathbf{s}_0] \quad (1.72)$$

over all collected data snapshots $t = 1, \dots, T$. Hence, the ML rule (1.68) can be re-defined now as follows,

$$\hat{\boldsymbol{\theta}} = \underset{\boldsymbol{\theta}}{\operatorname{argmax}} l(\boldsymbol{\theta}) = \underset{\boldsymbol{\theta}}{\operatorname{argmax}} \{ \underset{n}{Aver} \{ |q_{\boldsymbol{\theta}}(n)|^2 \} \} \quad (1.73)$$

with the spatial data correlation factors computed via (1.72).

Next, consider the practically motivated discrete (pixel) scene analysis format, in which case the LOT information vector \mathbf{v} may take one of I possible values $\{\mathbf{r}_i; i = 1, \dots, I\}$ in the discrete (pixel-formatted) scene search domain, i.e.

$$\boldsymbol{\theta} \text{ — may take one of the ordered discrete values } \rightarrow \{ \boldsymbol{\theta}_1, \boldsymbol{\theta}_2, \dots, \boldsymbol{\theta}_i, \dots, \boldsymbol{\theta}_I \}. \quad (1.74)$$

For the discrete model of the permissible parameter values (1.74) the sufficient statistic should be computed for these I values $\{ \boldsymbol{\theta}_1, \boldsymbol{\theta}_2, \dots, \boldsymbol{\theta}_i, \dots, \boldsymbol{\theta}_I \}$. Thus, the robust ML signal processing (SP) algorithm implies computing the set of statistics

$$\{ |q_i(n)|^2 = \| [\mathbf{u}(t), \mathbf{s}_{\boldsymbol{\theta}_i}] \|^2 ; \quad i = 1, \dots, I \}, \quad (1.75)$$

for all permissible pixels $\{i = 1, \dots, I\}$, their averaging (1.73) over all collected data snapshots $\{n = 1, \dots, N\}$, comparison of the resulting statistics and making the decision $\hat{\boldsymbol{\theta}} = \boldsymbol{\theta}_j$ in favor of the pixel j , for which the statistics (1.75) takes the maximal value.

Next computational modification of this algorithm can be made via representing the squared modulus in (1.75) as the sum of the corresponding squared real and imaging parts, namely,

$$\begin{aligned} \{|q_i(n)|^2\} &= \{(\text{Re}\{q_i(n)\})^2 + (\text{Im}\{q_i(n)\})^2; i = 1, \dots, I\} \\ &= \{([\mathbf{u}_{\text{Re}}(n), \mathbf{s}_{\text{Re}}(\boldsymbol{\theta}_i)] + [\mathbf{u}_{\text{Im}}(n), \mathbf{s}_{\text{Im}}(\boldsymbol{\theta}_i)])^2 + ([\mathbf{u}_{\text{Im}}(n), \mathbf{s}_{\text{Re}}(\boldsymbol{\theta}_i)] - [\mathbf{u}_{\text{Re}}(n), \mathbf{s}_{\text{Im}}(\boldsymbol{\theta}_i)])^2; i = 1, \dots, I\} \end{aligned} \quad (1.76)$$

where $\mathbf{u}_{\text{Re}}(n) = \text{Re}\{\mathbf{u}(n)\}$ (1.77)

and $\mathbf{u}_{\text{Im}}(n) = \text{Im}\{\mathbf{u}(n)\}$ (1.78)

represent the *in-phase* and *quadrature* components of the actually acquired i th snapshot array data vectors, respectively, while

$$\mathbf{s}_{\text{Re}}(\boldsymbol{\theta}_i) = \text{Re}\{\mathbf{s}_{\boldsymbol{\theta}_i}\} \quad (1.79)$$

and $\mathbf{s}_{\text{Im}}(\boldsymbol{\theta}_i) = \text{Im}\{\mathbf{s}_{\boldsymbol{\theta}_i}\}$ (1.80)

are the real part and the imagery part of the array steering vector $\mathbf{s}_{\boldsymbol{\theta}_i}$ in the direction $\boldsymbol{\theta}_i$. Assuming that the array consists of identical sensors with the identical real-valued receive patterns $g_m(\boldsymbol{\theta}_i)$ in the i th direction (DOA) $\boldsymbol{\theta}_i$, we now specify the element structures of the array steering vectors (1.79), (1.80) as follows,

$$\mathbf{s}_{\text{Re}}(\boldsymbol{\theta}_i) = \begin{bmatrix} s_{1\text{Re}}(\boldsymbol{\theta}_i) \\ s_{2\text{Re}}(\boldsymbol{\theta}_i) \\ \vdots \\ s_{M\text{Re}}(\boldsymbol{\theta}_i) \end{bmatrix} = \begin{bmatrix} g_1(\boldsymbol{\theta}_i) \cos(2\pi[\boldsymbol{\rho}_1, \boldsymbol{\theta}_i]) \\ g_2(\boldsymbol{\theta}_i) \cos(2\pi[\boldsymbol{\rho}_2, \boldsymbol{\theta}_i]) \\ \vdots \\ g_M(\boldsymbol{\theta}_i) \cos(2\pi[\boldsymbol{\rho}_M, \boldsymbol{\theta}_i]) \end{bmatrix}; \quad (1.81)$$

$$\mathbf{s}_{\text{Im}}(\boldsymbol{\theta}_i) = \begin{bmatrix} s_{1\text{Im}}(\boldsymbol{\theta}_i) \\ s_{2\text{Im}}(\boldsymbol{\theta}_i) \\ \vdots \\ s_{M\text{Im}}(\boldsymbol{\theta}_i) \end{bmatrix} = \begin{bmatrix} g_1(\boldsymbol{\theta}_i) \sin(2\pi[\boldsymbol{\rho}_1, \boldsymbol{\theta}_i]) \\ g_2(\boldsymbol{\theta}_i) \sin(2\pi[\boldsymbol{\rho}_2, \boldsymbol{\theta}_i]) \\ \vdots \\ g_M(\boldsymbol{\theta}_i) \sin(2\pi[\boldsymbol{\rho}_M, \boldsymbol{\theta}_i]) \end{bmatrix}, \boldsymbol{\theta}_i = \left(\frac{x_i}{|\mathbf{r}_i|}, \frac{y_i}{|\mathbf{r}_i|} \right)^T, \quad (1.82)$$

respectively. Using these specifications, we finally represent the robust ML tag localization algorithm (1.73) as

Table 1.3.

$$\begin{aligned}
\hat{\boldsymbol{\theta}} &= \underset{i}{\operatorname{argmax}} \{ \underset{n}{\operatorname{Aver}} \{ |q_i(n)|^2 \} \} \\
&= \underset{i}{\operatorname{argmax}} \{ \underset{t}{\operatorname{Aver}} \{ ([\mathbf{u}_{\operatorname{Re}}(n), \mathbf{s}_{\operatorname{Re}}(\boldsymbol{\theta}_i)] + [\mathbf{u}_{\operatorname{Im}}(n), \mathbf{s}_{\operatorname{Im}}(\boldsymbol{\theta}_i)])^2 \\
&\quad + ([\mathbf{u}_{\operatorname{Im}}(n), \mathbf{s}_{\operatorname{Re}}(\boldsymbol{\theta}_i)] - [\mathbf{u}_{\operatorname{Re}}(n), \mathbf{s}_{\operatorname{Im}}(\boldsymbol{\theta}_i)])^2 \} \} \quad (1.83)
\end{aligned}$$

The implementation of such robust ML algorithms presumes the following SP operations to be performed over the collected array in-phase (1.77) and quadrature (1.78) snapshot data signals:

Table 1.4.

First step: For all permissible pixel values $\{\boldsymbol{\theta}_i\}$ (1.74) of the desired DOA parameter, $\boldsymbol{\theta}_i \in \Theta$, compute the in-phase $\mathbf{s}_{\operatorname{Re}}(\boldsymbol{\theta}_i)$ and quadrature $\mathbf{s}_{\operatorname{Im}}(\boldsymbol{\theta}_i)$ components of the steering vectors $\mathbf{s}_{\boldsymbol{\theta}_i}$ specified by (1.81) and (1.82).

Second step: Given the in-phase $\{\mathbf{u}_{\operatorname{Re}}(n)\}$ and quadrature $\{\mathbf{u}_{\operatorname{Im}}(n)\}$ data vector snapshots (acquired from the observations), compute the sufficient statistics

$$\{|q_i(t)|^2; i = 1, \dots, I; n = 1, \dots, N\} \quad \text{specified via (1.76)}$$

for all collected snapshots $\{n = 1, \dots, N\}$ and all permissible values $\{\mathbf{r}_i\}$ of $\mathbf{r} \in V$.

Third step: Compute the sufficient statistics performing the averaging

$$l_i = l(\mathbf{r}_i) = \underset{n}{\operatorname{Aver}} \{ |q_i(n)|^2 \} = \frac{1}{N} \sum_{n=1}^N |q_i(n)|^2 \quad (1.84)$$

of $\{|q_i(t)|^2\}$ over all collected snapshots $\{t = 1, \dots, T\}$ for all permissible values $\{\boldsymbol{\theta}_i\}$ in the FOV $\boldsymbol{\theta} \in \Theta$.

Fourth step: Perform the comparison (I hypothesis testing) of the sufficient statistics (1.94) and make the decision using the rule (1.83) that we now specify as follows,

$$\begin{aligned}
\mathcal{W} : \text{if } l_j > l_i \text{ for all } i = 1, \dots, I; j \neq i &\xrightarrow{W} \hat{H}_j: \hat{\boldsymbol{\theta}} = \boldsymbol{\theta}_j \\
&\Rightarrow \hat{\boldsymbol{\theta}} \text{ is assigned the value } \boldsymbol{\theta}_j.
\end{aligned} \quad (1.85)$$

1.4. Matched Spatial Filtering (MSF) Image Formation and Analysis Algorithm for Robust TAG Localization with Multi-Beam Fan

The developed ML robust tag localization algorithm (1.83) permits also the image analysis interpretation form that we address here as follows.

Table 1.5.

To form the image of the tag $\hat{b}(\theta) = l(\theta)$ as a function of the spatial FOV $\theta \in \Theta$ in the applying the *matched spatial filtering* (MSF) method, i.e.

$$\hat{b}(\theta) = \mathbf{s}_\theta^+ \mathbf{Y} \mathbf{s}_\theta, \quad (1.86)$$

in which the image is formed as an MSF estimate of the SSP distribution over the FOV (over the scene), and localize the TAG via finding the coordinate of the image maximum in the

$\hat{\theta} \leftarrow$ coordinate of the maximum of the tag image (1.86) in the FOV $\theta \in \Theta$, i.e.

$$\hat{\theta} = \underset{\theta}{\operatorname{argmax}} \{ \hat{b}(\theta) \}. \quad (1.87)$$

Table 1.5 provides the imaging interpretation of the ML-optimal TAG localization algorithm specified previously in Table 1.4. This interpretation provides also another fan *imaging* approach for performing the ML-optimal robust TAG localization algorithm specified in the following table.

Table 1.6.

First step: For all M collected sensor outputs

$$\mathbf{u} = \underset{m,n}{\operatorname{vec}} \{ u_m(n); m = 1, \dots, M, n = 1, \dots, N \} \quad \text{defined by (1.50)}$$

compute the estimate \mathbf{Y} of the M -by- M array spatial correlation matrix via performing the averaging over the N snapshots as determined by (1.58), i.e.

$$\mathbf{Y} = \{ \hat{\mathbf{R}}_{\mathbf{u}} \} = \frac{1}{N} \sum_{n=1}^N \mathbf{u}(n) \mathbf{u}^+(n) \quad \text{defined by (1.55)}$$

Second step: For all permissible pixel values $\{\mathbf{r}_i\}$ (1.74) of the desired LOT parameter, $\mathbf{v}_i \in V$, compute the in-phase $\mathbf{s}_{\text{Re}}(\theta_i)$ and quadrature $\mathbf{s}_{\text{Im}}(\theta_i)$ components of the steering vectors $\{\mathbf{s}_{\theta_i}\}$ specified by (1.81) and (1.82) for all beams $\{i = 1, \dots, I\}$ in the fan.

Third step: Compute the MSF estimate of the SSP distribution over the observed scene that is

interpreted as a tag image via performing the MSF beamforming in all search directions in the *parallel mode*, i.e. via generating the *fan of beams* focused in all search directions $\{\boldsymbol{\theta}_i; i = 1, \dots, I\}$ *simultaneously*. In the complex format these operations are defined by (1.86), i.e.

$$\hat{b}(\boldsymbol{\theta}_i) = \mathbf{s}_{\mathbf{0}_i}^+ \mathbf{Y} \mathbf{s}_{\mathbf{0}_i} \text{ in the } \textit{parallel mode} \text{ for all } i = 1, \dots, I \text{ in the fan of } I \text{ beams} \quad (1.88)$$

Fourth step: Perform the comparison (*I* hypothesis testing) of the imaging sufficient statistics (1.88) for every beam $\{i = 1, \dots, I\}$ in the fan and make the ML decision using the rule,

$$\begin{aligned} W: \text{ if } \hat{b}(\boldsymbol{\theta}_j) \hat{b}(\mathbf{r}_j) > \hat{b}(\boldsymbol{\theta}_i) \text{ for all } i = 1, \dots, i; j \neq i \xrightarrow{W} \hat{H}_j: \hat{\boldsymbol{\theta}} = \boldsymbol{\theta}_j \quad (1.89) \\ \Rightarrow \hat{\boldsymbol{\theta}} \text{ is assigned the value } \boldsymbol{\theta}_j. \end{aligned}$$

1.5 Generalization of MSF Imaging Algorithm for Robust TAG Localization: Fourier Transform-Based Spatial Filtering (FTSF) Technique

To proceed with further applications with the particular array geometries, we provide here generalization of the developed above MSF imaging algorithm for the case of distributed scene scenario. First, we invoke the results of the distributed scene signal model generalization considered in details in subsection 1.1.3 conserving all notations from that subsection. Referring to (1.35) and (1.36), the stochastic model of the distributed signal field can be represented via the aggregation of the 1-D filtering over the continuous time argument $t \in T$ and 2-D Fourier transform over the spatial angular argument $\boldsymbol{\theta} \in \Theta$ of the scene SSP phasor $e(\mathbf{r})$ that we rewrite now as follows,

$$s(t, \mathbf{p}) = (\mathcal{S} e(\tau, \boldsymbol{\theta}))(t, \mathbf{p}) = \int_T \int_{\Theta} e(\tau, \boldsymbol{\theta}) a(t - \tau) \exp(i2\pi[\mathbf{p}, \boldsymbol{\theta}]) d\boldsymbol{\theta} d\tau; \quad (1.90)$$

$$t \in T; \mathbf{p} = \frac{\mathbf{p}}{\lambda_0} \in \frac{P}{\lambda_0}; \tau = \frac{2|\mathbf{r}|}{c} \in T = \frac{2R}{c}, |\mathbf{r}| = r \in R; \boldsymbol{\theta} = (\theta_x, \theta_y)^T \boldsymbol{\vartheta} = \begin{pmatrix} \boldsymbol{\theta} \\ \theta_z \end{pmatrix} = \frac{\mathbf{r}}{|\mathbf{r}|} \in \Theta \quad (1.91)$$

where \mathcal{S} represents the linear 3-D signal formation operator (SFO) defined by the integral at the right-hand side of (1.90) and $e(\tau, \boldsymbol{\theta})$ defines the spatial distribution of the SSP over the delay

$(\tau = \frac{2|\mathbf{r}|}{c} \in T)$ and the angular $(\boldsymbol{\vartheta} = \begin{pmatrix} \boldsymbol{\theta} \\ \theta_z \end{pmatrix} = \frac{\mathbf{r}}{|\mathbf{r}|}, \boldsymbol{\theta} = (\theta_x, \theta_y)^T)$ coordinates in the 3-D space

$T \times \Theta$.

An important observation that directly follows from the analysis of (1.90) consists in the factorization (separability) of the integral SFO \mathcal{S} along the time-delay (t, τ) and sensor spacing-

angles $(\mathbf{p}, \mathbf{\theta})$ argument pairs. This constitutes the base for separable space-time processing of the continuous-time data signals $s(t, \mathbf{p})$ aimed at reconstruction of the desired SSP distribution $\hat{e}(\tau, \mathbf{\theta})$ over the scene represented now in the coordinate frame $\{\mathbf{T} \times \mathbf{\Theta}; \tau \in \mathbf{T}, \mathbf{\theta} \in \mathbf{\Theta}\}$. The coordinate transforms (1.91) define the mapping of the processing frame $\mathbf{T} \times \mathbf{\Theta}$ onto the and Cartesian scene coordinate frame.

To establish the robust spatial filtration procedure for reconstruction of the SSP over the angular coordinates $\mathbf{\theta} \in \mathbf{\Theta}$, one has first to perform the time compression processing of the signal (1.90) for all admissible delay intervals (gates) τ_r that we number by index $r = 1, \dots, R$ to stress the relationship with the corresponding range gates. For the considered case of symmetrical (rectangular, Gaussian bell, etc.) non modulated real valued envelope $a(t)$, such compression is the standard matched time filtering (MTF) procedure [1], [10]

$$\{ s_r(\mathbf{p}) = \int_{\mathbf{T}} s(t, \mathbf{p}) a(\tau_r - t) dt \quad \text{for all range gates } r = 1, \dots, R \}. \quad (1.92)$$

Putting the above defined model (1.90) of the data signal $s(t, \mathbf{p})$ into (1.92) yields

$$\{ s_r(\mathbf{p}) = \int_{\mathbf{\Theta}} e_r(\mathbf{\theta}) \exp(i2\pi[\mathbf{p}, \mathbf{\theta}]) d\mathbf{\theta} \quad \text{for all range gates } r = 1, \dots, R \}. \quad (1.93)$$

Here, $e_r(\mathbf{\theta})$ represents the scaled angular *only* SSP distribution

$$e_r(\mathbf{\theta}) = \int_{\mathbf{T}} e(\tau, \mathbf{\theta}) \Psi_r(\tau) d\tau \quad (1.94)$$

where the integration kernel $\Psi_r(\tau)$ represents the range ambiguity function (AF)

$$\Psi_r(\tau) = \Psi(\tau_r - \tau) = \int_{\mathbf{T}} a(\tau_r - t) a(t - \tau) dt. \quad (1.95)$$

The model (1.94), (1.95) defines the MSF-inspired transformation of the 3-D complex reflectivity phasor $e(\tau, \mathbf{\theta})$ distributed over the 3-D coordinate frame $\{\tau \in \mathbf{T}, \mathbf{\theta} \in \mathbf{\Theta}\}$ to the corresponding 2-D angular distribution $e_r(\mathbf{\theta})$ within the FOV $\{\mathbf{\theta} \in \mathbf{\Theta}\}$ for all discrete range gates numbered by $r = 1, \dots, R$. In a particular range gate r , the resulting $e_r(\mathbf{\theta})$ (1.94) is composed from the original reflectivity function $e(\tau, \mathbf{\theta})$ via its integration over the delay coordinate τ with the smoothing AF kernel (1.95) with respect to the reference gate delay τ_r . Such factorization of the range (r) - DOA ($\mathbf{\theta}$) processing coordinates considerably simplifies the overall signal processing (SP) operations because all structurally identical angular processing operations could be performed in a parallel fashion over all corresponding R range gates.

Now, in a particular range gate of analysis r , complex reflectivity $e_r(\mathbf{\theta})$ defined by (1.94) relates to the signal component $s_r(\mathbf{p})$ of the observation data as an inverse spatial Fourier transform given by (1.93). This permits us to define the corresponding set of spatial covariance functions for different spatial observation points \mathbf{p}, \mathbf{p}' for corresponding range gates $r = 1, \dots, R$

$$R_s(\mathbf{p}, \mathbf{p}' | r) = \langle s_r(\mathbf{p}) s_r^*(\mathbf{p}') \rangle$$

$$= \int_{\Theta} \exp\{+i2\pi[\mathbf{p}, \boldsymbol{\theta}]\} \langle |e_r(\boldsymbol{\theta})|^2 \rangle \exp\{-i2\pi[\mathbf{p}', \boldsymbol{\theta}]\} d\boldsymbol{\theta}. \quad (1.96)$$

Using the definition of the SSP given by (1.41) that now is specified for DOV parameter vector $\boldsymbol{\theta}$ over the corresponding range gates, i.e.,

$$b_r(\boldsymbol{\theta}) = \langle |e_r(\boldsymbol{\theta})|^2 \rangle; \quad r = 1, \dots, R \quad (1.97)$$

and using the conjugate symmetry properties of the spatial Fourier kernels,

$$\exp\{+i2\pi[\mathbf{p}, \boldsymbol{\theta}]\} \exp\{-i2\pi[\mathbf{p}', \boldsymbol{\theta}]\} = \exp\{i2\pi[(\mathbf{p} - \mathbf{p}'), \boldsymbol{\theta}]\} = \exp\{i2\pi[\mathbf{p}_{\Delta}, \boldsymbol{\theta}]\}, \quad (1.98)$$

we further simplify (1.96) to

$$R_s(\mathbf{p}_{\Delta}|r) = \mathcal{F}_{(\Theta)}^{-1} \{b_r(\boldsymbol{\theta})\} = \int_{\Theta} b_r(\boldsymbol{\theta}) \exp\{i2\pi[\mathbf{p}_{\Delta}, \boldsymbol{\theta}]\} d\boldsymbol{\theta}. \quad (1.99)$$

where the 2-D spatial inverse Fourier transform operator $\mathcal{F}_{(\Theta)}^{-1}$ is defined by the integral at the right-hand of (1.104), and \mathbf{p}_{Δ} represents the actual *baseline* vector between the aperture points \mathbf{p}, \mathbf{p}' ,

$$\mathbf{p}_{\Delta} = \mathbf{p} - \mathbf{p}'; \quad \mathbf{p}, \mathbf{p}' \in \frac{P}{\lambda_0}. \quad (1.100)$$

The formula (1.99) is recognized to coincide with the celebrated Van Zittert-Zernike theorem from the radio astronomy [1] that establishes the desired relation between the spatial signal correlation function $R_s(\mathbf{p}_{\Delta})$ (referred to as the *visibility* function, in radio astronomy) and the SSP (referred to as the brightness temperature or simply *brightness*, in radio astronomy). Thus, we can drop the range gate index r (for notational simplicity in the rest of this Section) and express (1.99) in terms similar to the Van Zittert-Zernike theorem [1]. Hence, we reformulate the model (1.99) (dropping the range gate index r for notational simplicity) as follows.

Table 1.7.

Reformulation of the correlation signal data model (in terms of Van Zittert-Zernike theorem):

The spatial signal correlation function $R_s(\mathbf{p}_{\Delta})$ (referred to as the *visibility* function, in radio astronomy [1], [11]) is the 2-D inverse Fourier transform

$$R_s(\mathbf{p}_{\Delta}) = \mathcal{F}_{(\Theta)}^{-1} b(\boldsymbol{\theta}) = \int_{\Theta} b(\boldsymbol{\theta}) \exp\{i2\pi[\mathbf{p}_{\Delta}, \boldsymbol{\theta}]\} d\boldsymbol{\theta} \quad (1.101)$$

of the SSP (or *brightness*) distribution $b(\boldsymbol{\theta})$ over the angular observation space $\boldsymbol{\theta} \in \Theta$, where the visibility function argument $\mathbf{p}_{\Delta} = \mathbf{p} - \mathbf{p}'$ represents the *baseline* vector in the *visibility* domain

$$\mathbf{p}, \mathbf{p}' \in \frac{P}{\lambda_0}.$$

This formula establishes the model base used in many imaging applications [1], [5], [11], [12] (radio astronomy, passive RS, radiometry, sonar listening, etc.). The formal *imaging* approach for reconstructing the SSP $b(\boldsymbol{\theta})$ that can be inferred (in the *ad. hoc.* manner) from the Van Zittert-Zernike theorem (1.101) can be interpreted as follows.

Table 1.8.

Fourier Transform-Based Approach to SSP Reconstruction over DOA coordinates:

By measuring the visibility function $R_s(\boldsymbol{\rho}_\Delta)$ (in all range gates) over a range of spacings $\{\boldsymbol{\rho}_\Delta\} \in \frac{P}{\lambda_0}$ one can *potentially* reconstruct, or “synthesize”, an image $\hat{b}(\boldsymbol{\theta})$ by performing the 2-D Fourier Transform-Based Spatial Filtering (FTSF)

$$\hat{b}(\boldsymbol{\theta}) = \mathcal{F}_{(\boldsymbol{\rho}_\Delta)}\{\Pi_{A\{\boldsymbol{\rho}_\Delta\}}R_s(\boldsymbol{\rho}_\Delta)\} = \int_{-\infty}^{\infty} \Pi_{A\{\boldsymbol{\rho}_\Delta\}}R_s(\boldsymbol{\rho}_\Delta)\exp\{-i2\pi[\boldsymbol{\rho}_\Delta, \boldsymbol{\theta}]\}d\boldsymbol{\rho}_\Delta; \{\boldsymbol{\rho}_\Delta\} \in \frac{P}{\lambda_0}; \boldsymbol{\theta} \in \Theta \quad (1.102)$$

of the actually collected measurements

$$\Pi_{A\{\boldsymbol{\rho}_\Delta\}}R_s(\boldsymbol{\rho}_\Delta) \quad (1.103)$$

of the spatial correlation function $R_s(\boldsymbol{\rho}_\Delta)$ collected (for all corresponding range gates) in the visibility domain $\{\boldsymbol{\rho}_\Delta\} \in \frac{P}{\lambda_0}$ where the projector $\Pi_{A\{\boldsymbol{\rho}_\Delta\}}$ determines the aperture $A\{\boldsymbol{\rho}_\Delta\}$ over which the actual data measurements (1.102) are collected. Such a projector $\Pi_{A\{\boldsymbol{\rho}_\Delta\}}$ is specified by the employed registration system, i.e. by the configuration of the particular employed sensor antenna array (AA).

The crucial issue of such an FTSF-inspired approach is the intrinsic systematic error in the reconstructed SSP $\hat{b}(\boldsymbol{\theta})$ because of the finite (incomplete) data recording aperture $A\{\boldsymbol{\rho}_\Delta\} \subset \mathbb{R}^2$ that could be technically realized with any AA. The exact reconstruction (i.e. zero systematic error) could be achieved *potentially* if and only if the aperture $A\{\boldsymbol{\rho}_\Delta\}$ covers the complete observation plain, $A\{\boldsymbol{\rho}_\Delta\} = \mathbb{R}^2$, (i.e. no projection in (1.103), $\Pi_{A\{\boldsymbol{\rho}_\Delta\}} = \mathcal{I}$, an identity operator), in which case according to the Van Zittert-Zernike theorem (1.102), the Fourier transform $\mathcal{F}_{(\boldsymbol{\rho}_\Delta)}$ performed over the hypothetically complete measurements $R_s(\boldsymbol{\rho}_\Delta)$ produces the desired SSP $b(\boldsymbol{\theta})$ [1]. It is obvious that in practice, we are always limited to finite data observation apertures, $A\{\boldsymbol{\rho}_\Delta\} \subset \mathbb{R}^2$, technically realizable with any employed AA, hence *inevitable systematic errors* in the reconstructed SSP $\hat{b}(\boldsymbol{\theta})$.

The second source of error (so-called *fluctuation* or *noise* error [1]) in the FTSF procedure (1.102) is due to the inevitable noise in the observations. This results in the measurements of the *noised* data spatial correlation (visibility) function

$$R_u(\boldsymbol{\rho}_\Delta | r) = R_s(\boldsymbol{\rho}_\Delta | r) + R_n(\boldsymbol{\rho}_\Delta | r) \quad (1.104)$$

instead of the pure signal spatial correlation function $R_s(\mathbf{p}_\Delta | r)$ where

$$R_n(\mathbf{p}_\Delta | r) = R_n(\mathbf{p}, \mathbf{p}' | r) = \langle n_r(\mathbf{p}) n_r^*(\mathbf{p}') \rangle \quad (1.105)$$

represents the correlation function of noise that contaminates the observations, where we recovered the range gate index r to stress the dependence of the noise over the range coordinate.

Thus the technically realizable FTSF approach to imaging of the SSP reconstructed from the available finite aperture measurements $\Pi_{A\{\mathbf{p}_\Delta\}} R_u(\mathbf{p}_\Delta)$ of the noised visibility function $R_u(\mathbf{p}_\Delta)$ can now be formalized as

$$\hat{b}(\boldsymbol{\theta}) = \mathcal{F}_{(\mathbf{p}_\Delta)} \{ \Pi_{A\{\mathbf{p}_\Delta\}} R_u(\mathbf{p}_\Delta) \} = \int_{-\infty}^{\infty} \Pi_{A\{\mathbf{p}_\Delta\}} R_u(\mathbf{p}_\Delta) \exp\{-i2\pi[\mathbf{p}_\Delta, \boldsymbol{\theta}]\} d\mathbf{p}_\Delta ; \{ \mathbf{p}_\Delta \} \in \frac{P}{\lambda_0} ; \boldsymbol{\theta} \in \Theta \quad (1.106)$$

Recall that the problem at hand is the localization of TAGs (or reconstruction of the distributed SSP over the scene plane) via analysis of the reconstructed scene image, the SSP $\hat{b}(\mathbf{r})$. In the case of the point-type TAGs distributed over the scene plane with the one-to-one geometrical correspondence between vectors $\mathbf{r} \in V$ and $\boldsymbol{\theta} = \boldsymbol{\theta}_{xy} = (\theta_x, \theta_y)^T \in \Theta$ given by (1.9) we can formulate the FTSF approach to multiple TAG localization as follows.

Table 1.9.

FTSF-Based Approach to TAG Localization:

To form the image of the TAG $\hat{b}(\mathbf{r})$ as a function of the spatial scene coordinates $\mathbf{r} \in V$ in the scene domain $V = R$ applying the FTSF method, i.e.

$$\hat{b}(\mathbf{r}) = \mathcal{F}_{(\mathbf{p}_\Delta)} \{ \Pi_{A\{\mathbf{p}_\Delta\}} R_u(\mathbf{p}_\Delta) \} = \int_{-\infty}^{\infty} \Pi_{A\{\mathbf{p}_\Delta\}} R_u(\mathbf{p}_\Delta) \exp\{i2\pi[-\mathbf{p}_\Delta, \boldsymbol{\theta}]\} d\mathbf{p}_\Delta ; \{ \mathbf{p}_\Delta \} \in \frac{P}{\lambda_0} ; \boldsymbol{\theta} \in \Theta ; \mathbf{r} \in V \quad (1.107)$$

in which the image is formed as a FTSF estimate of the SSP distribution over the scene, and localize the TAGs via finding the coordinates of the image maximums in the scene plane $\hat{\mathbf{v}} \Leftarrow$ coordinates of the maximum of the multiple TAG image (1.112) in the scene $\mathbf{r} \in V$.

In practice, one should introduce some feasible threshold to discriminate the TAGs of interest against the noise and possible unwanted (nuisance) maximums in the SSP estimate (1.107). We defer consideration of these aspects as well as other regularization issues to the sequent Sections.

1.6 Algorithmic Implementation of Robust MSF and FTSF Image Formation Methods

This Subsection describes the algorithmic implementation of MSF and FTFS methods for three different configurations (geometries) of *multi-sensor imaging radar* (MIR). It examines the particular preferable geometry of the antenna array (AA), the Y-shaped geometry called *Synthetic Thinned Aperture Radiometer* (STAR) configuration [11], [12], as well as the circular and cross shaped array configurations. We present the FTFS algorithmic structure for the data processing technique for these test geometries, as well as comparative analysis of the MSF and FTFS algorithms.

1.6.1 AA Geometries

This section provide a brief introduction to the array imaging technique recently proposed by A. B Tanner et al. [11], [12] that, in fact, implements a version of the method mentioned and developed in the previous Section – the FTFS imaging technique particularly adapted for the MIR-Y specific geometry called GeoSTAR (Geostationary STAR) (see [11], [12] for details).

GeoSTAR was initially introduced as a concept to provide imaging via passive probe with high spatial resolution of scenes in the microwave bands. 2-D images are synthesized by Fourier transform of the data collected by a correlation interferometer with the GeoSTAR Y-configured sensor array.

The array consists of $M = 24$ receiving sensors configured in a Y-shaped geometry with eight elements in each arm. This geometry is structurally similar for any admissible interelement spacing (normalized with respect to the wavelength λ_0 , e.g., a half lambda distance between sensor elements, $d_{A(1)} = 0.5 \lambda_0$). The other two configurations (circular O-shaped and cross or X-shaped) are composed of 24 elements each, in the case of cross array is conformed for 6 evenly spaced elements by arm each and the circular array is conformed with 24 elements, which are configured in a circle.

Figure 1.5, shows the GeoSTAR Y geometry with an interelement spacing $d_{A(1)} = 0.5 \lambda_0$ (equal to half of the wavelength related to the operation frequency). Figure 1.6, shows the MIR - X geometry, and Figure 1.7 shows the MIR - O coordinates (referred to the so-called visibility domain coordinate system) $\mathcal{U} = x / \lambda_0$, $\mathcal{V} = y / \lambda_0$.

The individual antennas in the array are identical and share the same *field of view* (FOV). The IF signals collected by all receivers for R corresponding range gates are simultaneously cross-correlated against one another in a digital subsystem. Thus, each correlated antenna pair forms an interferometer which measures a particular value of the data spatial correlation (visibility) function that corresponds to a spatial scene brightness harmonic across the FOV. When expressed as a function of antenna spacing (or “*baselines*”) $\{\mathbf{p}_\Delta\} \in P/\lambda_0$ with dimensions “ \mathcal{U} ” and “ \mathcal{V} ” (by conventions [12]), i.e.

$$\mathcal{U} = \rho_{\Delta x}, \mathcal{V} = \rho_{\Delta y} ; \mathbf{p}_\Delta = (\rho_{\Delta x}, \rho_{\Delta y})^T = (\mathcal{U}, \mathcal{V})^T \quad (1.108)$$

in the (x, y) observation plane. The complex cross-correlation measurements

$$R_u(\mathcal{U}, \mathcal{V}) = R_u(\mathbf{p}_\Delta) = R_s(\mathcal{U}, \mathcal{V}) + R_n(\mathcal{U}, \mathcal{V}); \quad \{\mathbf{p}_\Delta\} \in \frac{P}{\lambda_0} \quad (1.109)$$

compose the *visibility* function.

The Y-shaped array that we adopt from [11], [12] provides the visibility measurement samples $R_u(\mathcal{U}, \mathcal{V})$ using a *minimum number* of antennas with a fixed geometry that compose the so-called *thinned* array. As illustrated in Figures 1.5, 1.6 and 1.7, the spacings between the various antenna pairs yield a uniform hexagonal grid of visibility samples in the $(\mathcal{U}, \mathcal{V})$ plane. Such, grids are uniform in the sense that the measurements (1.109) provide the uniform hexagonal grid of visibility functions available for further processing. There are 8 elements in each arm of the array, and these yield 64 unique spacings between arms 1, 2 and 3 (see Fig. 1.5).

Another 64 conjugate-symmetric samples are derived by subtracting arm 2 from arm 1. In all, the 24-element array produces $6 \times 64 = 384$ $(\mathcal{U}, \mathcal{V})$ samples to be employed in the FTSF image reconstruction algorithm (1.107) for every particular range gate. Likewise, for the X-shaped array, we have $(36 \times 4) + (11 \times 4) = 188$ \mathcal{U}, \mathcal{V} samples and for the O-shaped array we measure 288 \mathcal{U}, \mathcal{V} samples, correspondingly. It is worth mentioning that following the GeoSTAR array design all the \mathcal{U}, \mathcal{V} samples are shaped by elements of different Y arms, not by elements of the same arm. According to [11], [12], this scheme simplifies the electrical and mechanical design. We will examine in the simulation experiment that such *sparse* correlations employed in the FTSF algorithm produce more fine shape of the resulting point spread function (PSF) than the complete correlation mode employed in the MSF imaging method.

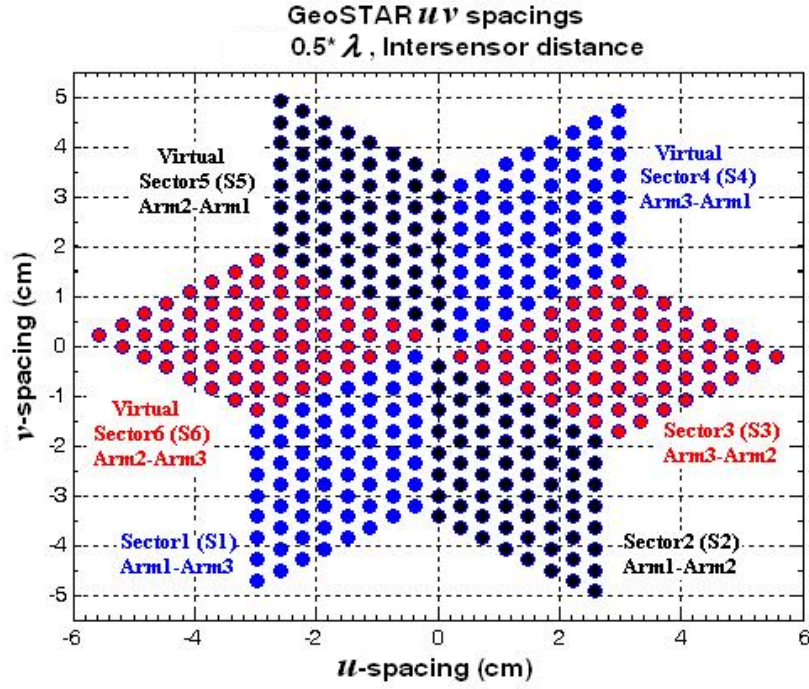
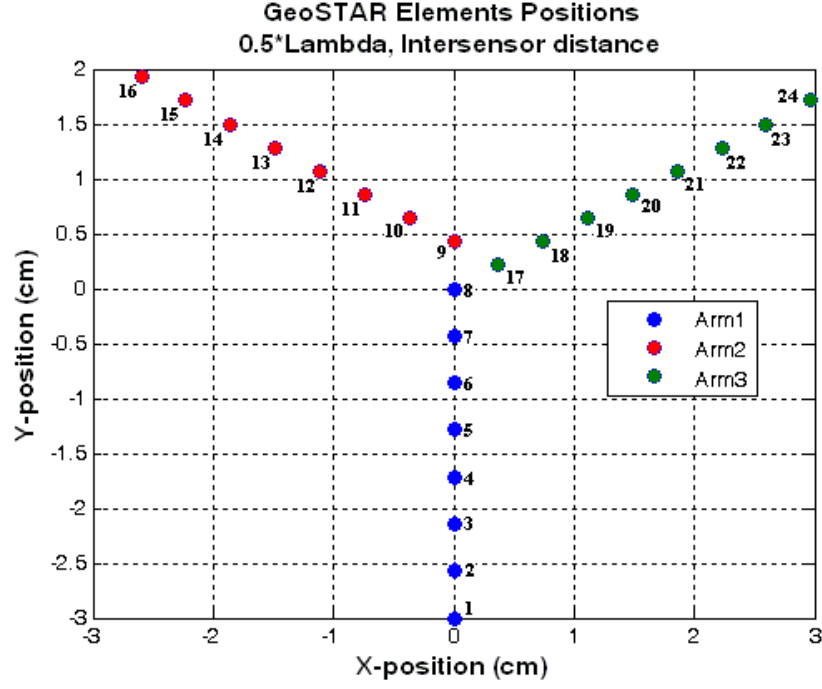
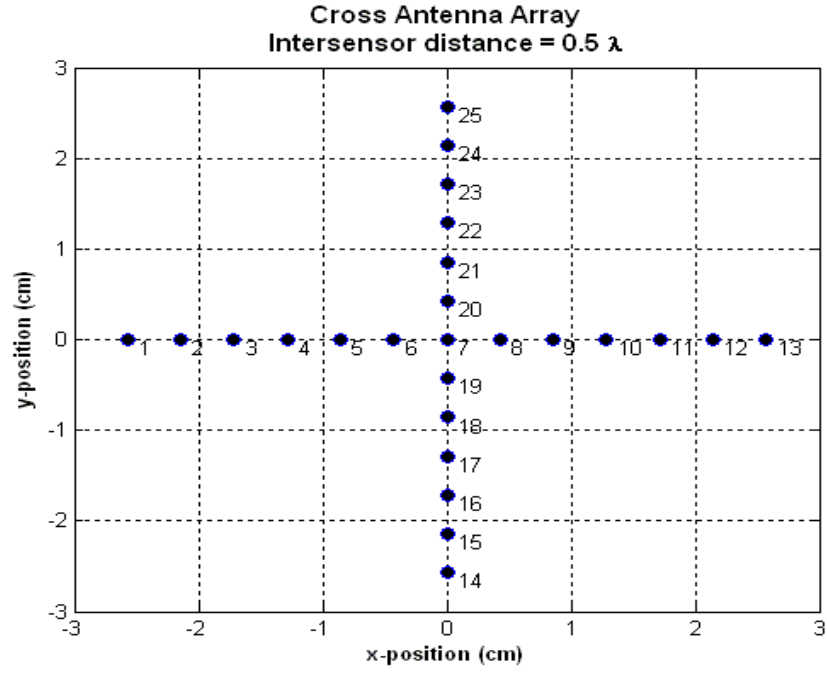
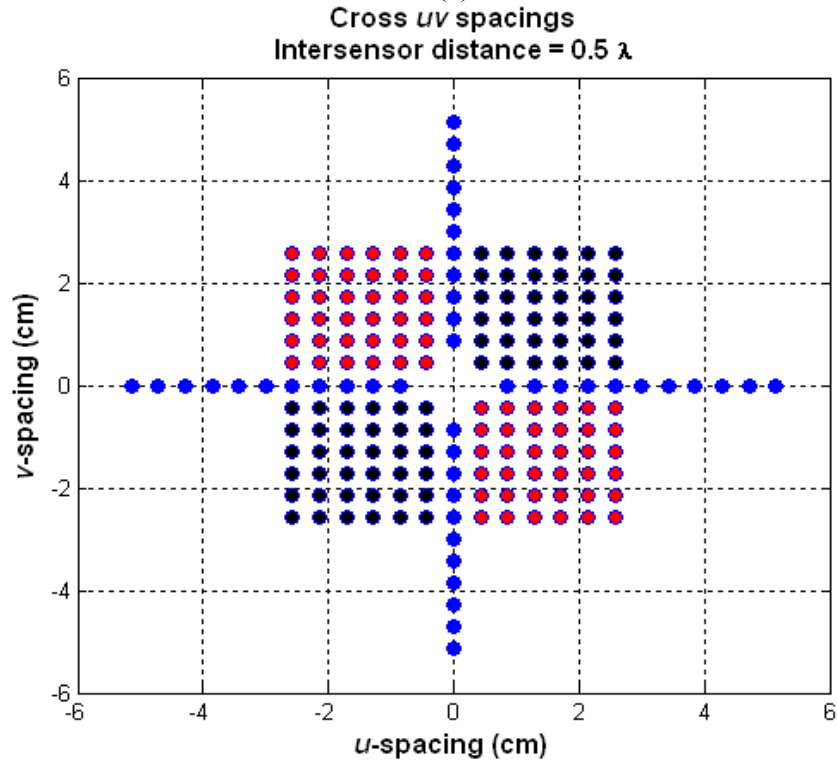


Figure 1.5 (a) *Layout* for the Y-shaped AA with an interelement spacing $d_{\Lambda(1)} = 0.5 \lambda_0$;
(b) corresponding $\mathcal{U}\mathcal{V}$ samples.



(a)



(b)

Figure 1.6 (a) *Layout* for the X-shaped AA with an interelement spacing of $d_{\Lambda(1)} = 0.5 \lambda_0$;
(b) corresponding $\mathcal{U} \mathcal{V}$ samples.

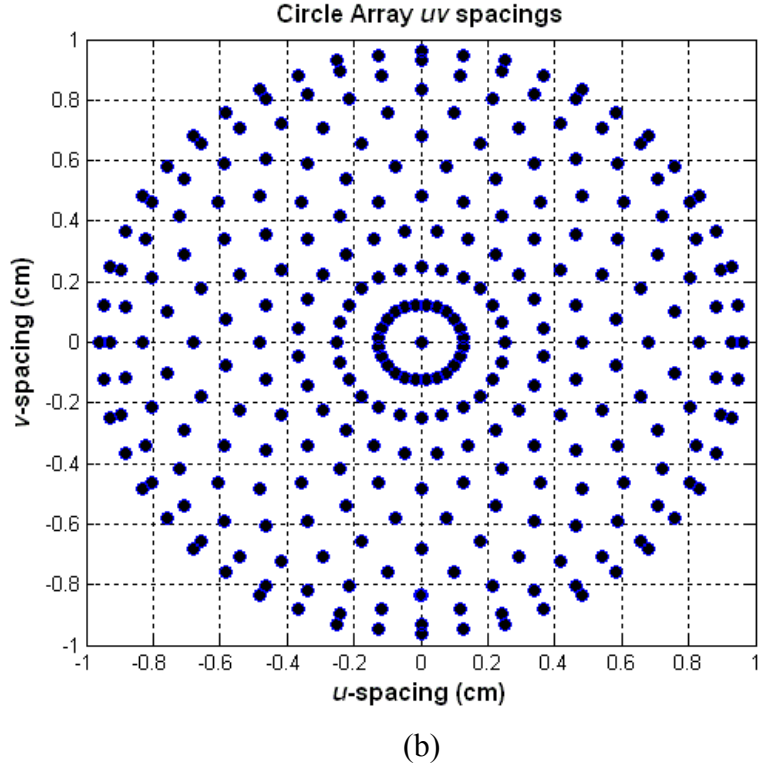
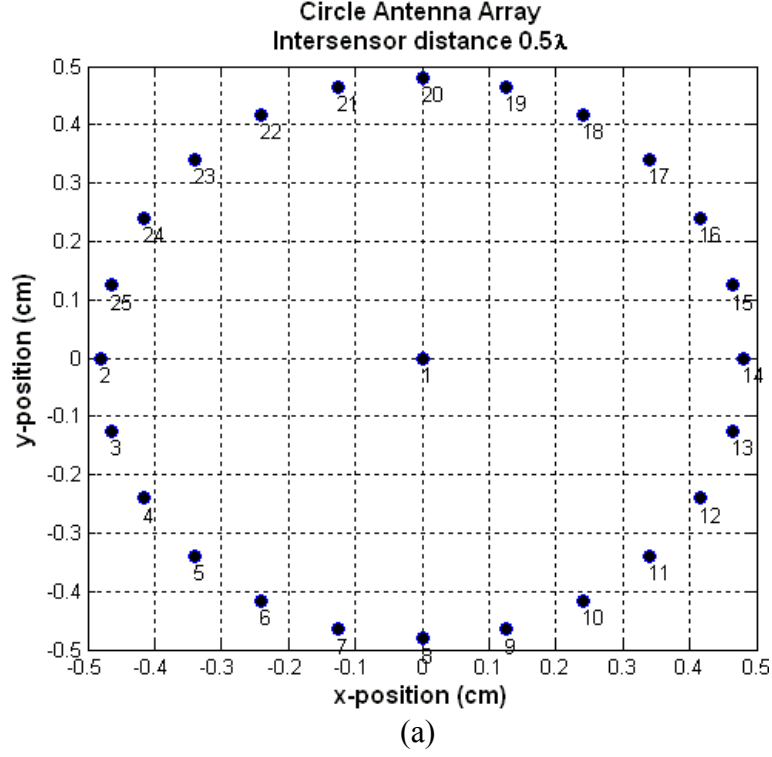


Figure 1.7 (a) *Layout* for the O-shaped AA with an interelement spacing of $d_{A(1)} = 0.5 \lambda_0$;
(b) corresponding $\mathcal{U} \mathcal{V}$ samples.

1.6.2. FTSF Algorithm for the MIR Data Processing

According to the FTSF inspired algorithm (1.106), in the case of *noise-free* observations (i.e. $R_u(\mathcal{U}, \mathcal{V}) = R_s(\mathcal{U}, \mathcal{V})$; $R_n(\mathcal{U}, \mathcal{V}) = 0$), the signal component of the visibility function is the 2-D inverse Fourier transform of the brightness (or SSP) distribution $b(\boldsymbol{\theta})$ over the angular observation space $\boldsymbol{\theta} \in \Theta$. (Recall that we consider a single particular range gate and drop the corresponding range gate index r for notational simplicity because the SP algorithm over the angular DOA coordinates $\boldsymbol{\theta}$ is identical for all R range gates). In the notational conventions of [11], [12], the angular argument $\boldsymbol{\theta}$ is represented by its x - y projections, i.e. the directional cosines defined by (1.11) that we rewrite here for convenience as

$$\boldsymbol{\theta} = (\theta_x, \theta_y)^T \text{ with } \theta_x = \cos(\hat{\boldsymbol{\theta}}, \hat{\mathbf{x}}^\circ) \text{ and } \theta_y = \cos(\hat{\boldsymbol{\theta}}, \hat{\mathbf{y}}^\circ). \quad (1.110)$$

Now, in the $(\mathcal{U}, \mathcal{V})$ and $\boldsymbol{\theta} = (\theta_x, \theta_y)^T$ DOA coordinates, the spatial Fourier transform (1.102) can be rewritten as follows.

Fourier transform relations in the $(\mathcal{U}, \mathcal{V})$ and (θ_x, θ_y) coordinates:

The *noise-free* visibility function $R_s(\mathcal{U}, \mathcal{V})$ is the 2-D inverse Fourier transform

$$R_s(\mathcal{U}, \mathcal{V}) = \mathcal{F}_{(\boldsymbol{\theta})}^{-1} \{ b(\theta_x, \theta_y) \} = \int_{\Theta} b(\theta_x, \theta_y) \exp \{ i2\pi(\mathcal{U}\theta_x + \mathcal{V}\theta_y) \} d\theta_x d\theta_y \quad (1.111)$$

of the SSP (or *brightness*) distribution $b(\theta_x, \theta_y)$ over the 2-D angular observation space $(\theta_x, \theta_y) \in \Theta$ (in a particular range gate of interest), where the visibility function arguments $(\mathcal{U}, \mathcal{V})$ represent the x - y projections of the normalized *baseline* vector in the *visibility* domain $(\mathcal{U}, \mathcal{V}) \in \frac{P}{\lambda_0}$.

Thus, collecting sufficient measurements of the visibility function over a range of spacings $(\mathcal{U}, \mathcal{V}) \in \frac{P}{\lambda_0}$ the FTSF-inspired method for SSP reconstruction is as follows.

FTSF-Based Approach to SSP Reconstruction in the $(\mathcal{U}, \mathcal{V})$ and (θ_x, θ_y) coordinates:

By measuring the observed *noised* visibility function $R_u(\mathcal{U}, \mathcal{V})$ over a range of normalized spacings $(\mathcal{U}, \mathcal{V}) \in \frac{P}{\lambda_0}$ one can *potentially* reconstruct, or “synthesize”, a 2-D image $\hat{b}(\theta_x, \theta_y)$ by performing the 2-D Fourier Transform-based Spatial Filtering (FTSF)

$$\hat{b}(\theta_x, \theta_y) = \mathcal{F}_{(\mathcal{U}, \mathcal{V})} \{ \Pi_{A(\mathcal{U}, \mathcal{V})} R_u(\mathcal{U}, \mathcal{V}) \}$$

$$= \int_{-\infty}^{\infty} \Pi_{A\{\mathcal{U}, \mathcal{V}\}} R_s(\mathcal{U}, \mathcal{V}) \exp\{-i2\pi(\mathcal{U}\theta_x + \mathcal{V}\theta_y)\} d\mathcal{U} d\mathcal{V}; (\mathcal{U}, \mathcal{V}) \in \frac{P}{\lambda_0}; (\theta_x, \theta_y) \in \Theta \quad (1.112)$$

of the actually collected measurements

$$\Pi_{A\{\mathcal{U}, \mathcal{V}\}} R_u(\mathcal{U}, \mathcal{V}) \quad (1.113)$$

of the spatial data correlation function $R_u(\mathcal{U}, \mathcal{V})$ collected in the visibility domain

$(\mathcal{U}, \mathcal{V}) \in \frac{P}{\lambda_0}$ where the projector $\Pi_{A\{\mathcal{U}, \mathcal{V}\}}$ determines the aperture $A\{\mathcal{U}, \mathcal{V}\}$ over which

the actual data correlation measurements (1.113) are collected. Such a projector $\Pi_{A\{\mathcal{U}, \mathcal{V}\}}$ is specified by the employed registration system, i.e. by the configuration (geometry) of the particular employed sensor antenna array (AA).

Note that the way in which the measurements of the visibility function are collected constitutes a degree of freedom of such general FTSF-based approach to SSP reconstruction.

Now, we analyze the number of measurement samples of visibility for the case of Y-shaped array geometry. Note that for the above mentioned case of notational simplicity, only one range gate is considered. The algorithmic structure is similar for all R range gates. The collected visibility measurements compose $6 \times 64 = 384$ $(\mathcal{U}, \mathcal{V})$ -samples. Note that only a half, i.e. $(3 \times 64) = 192$ $(\mathcal{U}, \mathcal{V})$ -sample measurements correspond to the *unique* baselines. These correlation measurements

$$\tilde{Y}(m, m') = \hat{R}_u(\mathcal{U}\{m - m'\}, \mathcal{V}\{m - m'\}) = \hat{R}_u(m, m') = \underset{n}{Aver}\{u_m(n)u_{m'}^*(n)\} \quad (1.114)$$

that correspond to unique $(3 \times 64) = 192$ baselines $\{m - m'\}$ between arms A–B, A–C and B–C are collected in sectors $S1$, $S2$, and $S3$, respectively, as shown in Figure 1.5(b). In (1.114) the averaging is performed over independent N pulses reflected from the particular $\{r \in R\}$ range gate of interest. Thus N independent samples with the fixed PRT are collected in each range gate and averaged to form the sufficient statistics (1.114). In the same manner, the second half of $(\mathcal{U}, \mathcal{V})$ -sample measurements are composed of 192 conjugate-symmetric copies of the original set of (1.114), i.e.

$$\begin{aligned} \tilde{Y}(m', m) &= \hat{R}_u(\mathcal{U}\{m' - m\}, \mathcal{V}\{m' - m\}) = \hat{R}_u(m', m) \\ &= \underset{n}{Aver}\{u_{m'}(n)u_m^*(n)\} = \hat{R}_u^*(m, m') \end{aligned} \quad (1.115)$$

that correspond to $(3 \times 64) = 192$ symmetrical *virtual* baselines $\{m' - m\}$. These are collected in sectors $S4$, $S5$, and $S6$, respectively. All the measured visibilities, i.e. (1.114) and (1.115) are grouped into 6 sectors ($S1, S2, \dots, S6$). These grouped visibilities compose the data

$$\{\hat{R}_u(m, m')\}_{S1}; \{\hat{R}_u(m, m')\}_{S2}; \dots, \{\hat{R}_u(m, m')\}_{S6} \quad (1.116)$$

available for further numerical processing. Last, these grouped visibilities (1.116) are transformed into the image $\hat{b}(\theta_x, \theta_y)$ using the FTSF algorithm (1.112). It is important to note, that the pattern of all antenna element must be identical and precisely characterized by a single model, $g_m(\boldsymbol{\theta}) = g(\boldsymbol{\theta}) \forall m = 1, \dots, M$.

The specific “Y” configuration of the GeoSTAR array is motivated by the need to measure a complete set of visibility samples with a *minimum* number of antennas. The “Y” array is one of the best in terms of efficient use of antennas and in terms of the simplicity of the structure [11], [12]. In Section 3, we will demonstrate how the Y-shaped GeoSTAR AA outperforms the corresponding MIR-X and the MIR-O architectures.

The next figure shows the implementation of the proposed system in a very simple diagram. The outputs of sensors are coupled to the corresponding HW blocks that provide acquisition of the multimode measurement row data vectors specified by (1.12) –(1.15). The sufficient statistics for all observation range gates is formed using the statistical averaging procedure (1.115), (1.116). These are processed next employing the FTSF algorithm (1.112) that we specify in Figure 1.8. via $\mathcal{W}_{\text{FTSF}}$, through of which, the signals are obtained employing the format described in the chapter 4, subtopic 3. The signals received by the system will be processed later using the \mathcal{W}_{opt} algorithm defined by (1.118). Figure 1.8 shows the MIR-Y shaped, but it can be equally applied to the MIR-X and MIR-O with the same number of sensors.

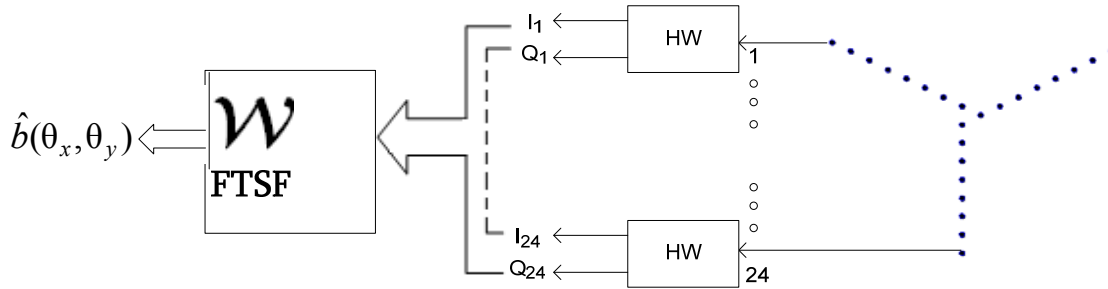


Figure 1.8 Data flow diagram for implementation of the FTSF algorithm.

1.6.3. Relationship Between Robust MSF and FTST Algorithms

In this Subection, we establish the relationship between the robust MSF image formation algorithm (1.86) and the FTST-MIR imaging algorithm (1.112).

First, let us form a spatial correlation matrix $\tilde{\mathbf{Y}}$ that can be composed of all grouped measured visibilities (1.113), which is structurally similar to the spatial data correlation matrix \mathbf{Y} defined by (1.55), i.e.,

$$\tilde{\mathbf{Y}} = \text{matrix } \{ \{ \hat{R}_u(m, m') \} \text{ for all baselines } \{m - m'\}, \{m' - m\} \}. \quad (1.117)$$

where $m, m' = 1, \dots, M$, and the elements of the matrix are composed of two conjugate sets:

$$\{\tilde{\mathbf{Y}}\}_{m, m'} = \tilde{Y}(m, m') = \underset{n}{Aver} \{ u_m(n) u_{m'}^*(n) \} \quad (1.118)$$

for unique $(3 \times 64) = 192$ baselines $\{m - m'\}$ between arms A–B A–C and B–C; and

$$\{\tilde{\mathbf{Y}}\}_{m', m} = \tilde{Y}(m', m) = \underset{n}{Aver} \{ u_{m'}(n) u_m^*(n) \} = \tilde{Y}^*(m, m') \quad (1.119)$$

for 192 symmetrical (*virtual*) baselines $\{m' - m\}$ between arms B–A, C–A and C–B.

We must take into account the difference between the two considered imaging techniques:

- MSF imaging algorithm involves into the processing all $(24 \times 24) = 576$ spatial correlations (complete array spatial correlation matrix \mathbf{Y} given by (1.55))
- FTSF imaging algorithm uses in the processing $(6 \times 64) = 384$ i.e. *sparse* $(\mathcal{U}, \mathcal{V})$ -sample measurements of the visibilities (for the MIR-Y), 188 for the MIR-X and 289 for the MIR-O (visibility data matrix $\tilde{\mathbf{Y}}$ specified by (1.117)).

To complete the analysis, let us demonstrate how the MSF algorithm can be “transformed” into the FTSF-MIR imaging algorithm via excluding $(576 - 384) = 192$ spatial correlations in the MSF algorithm (1.86). In the analysis, we consider that the pattern of every antenna element is identical and precisely characterized by a single model $g_m(\boldsymbol{\theta}) = g(\boldsymbol{\theta}) \forall m = 1, \dots, M$ [11], [12]. We also consider the identical processing over all R range gates and drop index r for notational simplicity. Thus, for the considered here angular argument $\boldsymbol{\theta} \in \Theta$ and the *steering* vector specified by (1.81), (1.82), the MSF algorithm (1.86) for a particular range gate becomes

$$\begin{aligned} \hat{b}_{MSF}(\boldsymbol{\theta}) &= \mathbf{s}_0^+ \mathbf{Y} \mathbf{s}_0 = |g(\boldsymbol{\theta})|^2 \sum_{m, m'=1}^{M, M} s_m^*(\boldsymbol{\theta}) Y_{mm'} s_{m'}(\boldsymbol{\theta}) = \\ &= |g(\boldsymbol{\theta})|^2 \sum_{m, m'=1}^{M, M} Y_{mm'} \exp \{ -i2\pi [(\boldsymbol{\rho}_m - \boldsymbol{\rho}_{m'}), \boldsymbol{\theta}] \} \end{aligned} \quad (1.120)$$

where $\{Y_{mm'}\}$ compose a set of *all* 576 elements of the complete measured spatial array data correlation matrix \mathbf{Y} formed for the considered particular range gate.

This MSF algorithm (1.120) is recognized to be the Fourier transform of the *complete* data correlation matrix $\mathbf{Y} = \mathbf{Y}_r$ composed of all 576 collected correlations $\{Y_{mm'}\}$ between all possible sensors $\{m, m' = 1, \dots, M = 24\}$ formed for a particular range gate r . Last, the factor $|g(\boldsymbol{\theta})|^2$ incorporated in (1.120) provides the selection of the desired FOV according to the directional pattern of a single sensor.

Next, via cancelling $(576 - 384) = 192$ elements in the complete correlation matrix \mathbf{Y} that correspond to the correlations between arms A–A, B–B and C–C (with the corresponding

complex-conjugate pairs) that are *not* collected by the GeoSTAR system, the algorithm (1.120) is transformed into

$$\hat{b}_{FTSF}(\boldsymbol{\theta}) = |g(\boldsymbol{\theta})|^2 \sum_{m,m'=1}^{M,M} \tilde{Y}_{mm'} \exp\{-i2\pi[(\mathbf{p}_m - \mathbf{p}_{m'}), \boldsymbol{\theta}]\}, \quad (1.121)$$

that is recognize to be the FTSF algorithm of the previous subtopic for the adopted identical array elements precisely characterized by a single model of their receive patterns $g_m(\boldsymbol{\theta}) = g(\boldsymbol{\theta}) \forall m = 1, \dots, M$ as it is required for the GeoSTAR system [11], [12].

1.6.4 Specifications of Quality Metrics for Simulation Experiments

Now, let us specify quality metrics for simulation experiments that we run for testing the *potential* quality of the images that can be formed employing the presented above robust MSF beamforming algorithm (1.120), and the alternative FTSF method (1.121).

We compose the first test simulation experiment for imaging a single TAG located in the origin of the x - y Cartesian coordinate system on the scene plane (i.e. $\mathbf{v} = \mathbf{v}_0$: $x = 0, y = 0, z = h_A$) as illustrated in Figure 1.9.

The *potentially/asymptotically best* image $\hat{b}(\mathbf{r} : \mathbf{v} = \mathbf{v}_0)$ of a single point-type target (TAG) located in the origin of the scene coordinate system, (\mathbf{v}_0 : $x = 0, y = 0, z = h_A$), is referred to as the imaging system *power ambiguity function* (the term borrowed from the imaging radar applications [6], [7]) or system *point spread function* (PSF, the term borrowed from the image science [1], [5]), both represented in the same way as

$$\Psi_{(method)}^2(\mathbf{r}) = C_\Psi \hat{b}_{(method)}(\mathbf{r} : \mathbf{v} = \mathbf{v}_0) \quad (1.122)$$

with the normalization factor

$$C_\Psi = \frac{1}{\max\{\hat{b}_{(method)}(\mathbf{r} : \mathbf{v} = \mathbf{v}_0)\}}. \quad (1.123)$$

Note that the *asymptotically best* image is associated with the one produced for a hypothetical case of a complete \mathbf{R}_s or sparse $\tilde{\mathbf{R}}_s$ signal model correlation matrix employed in the particular tested image formation algorithms, not the measured data correlation matrix \mathbf{Y} or the sparse data correlation matrix $\tilde{\mathbf{Y}}$, both degraded by the noise components and low-rank measurements. Also, the amplitude scaling (1.123) of the PSF ($\Psi_{(method)}^2(\mathbf{r} = \mathbf{v}_0) = 1$) makes this function representative only of the *shape* of the point-type TAG image irresponsable of the particular target power. That is why, the PSF is referred to as a common measure of a *potential quality* of the image shape. The wider is the PSF at some fixed image level the worse is the spatial

resolution that can be provided by the particular employed system/method. The standard characterization of the resolution cell is associated with the cross-section of the PSF at -3 dB level, i.e. at a half of the maximum of the PSF. Note that different array geometries and different employed image formation methods affect also the sidelobes of the resulting PSF associated with the so-called image *artifacts*, as great sidelobes degrade the point-type image shape.

In the indoor operational scenarios the reflected/scattered signals may have the coordinates that coincide with the sidelobe position of the true TAG image that will result in masking the TAG and incorrect decision making regarding the TAG location. That is why, the preferable (desirable) shape of the PSF is a *unimodal* symmetrical function, i.e., a function with one dominant sharpest possible main beam and minimal possible level of the sidelobes. This is associated with the desired imaging system/method that provides the best possible spatial resolution (sharp main beam) with minimal possible image artifacts (low sidelobes).

To distinguish between different geometries and different employed algorithms, that was used to composed image (MSF or FTSF), we are specifying the PSF in the definition (1.122) with subscript *method* .

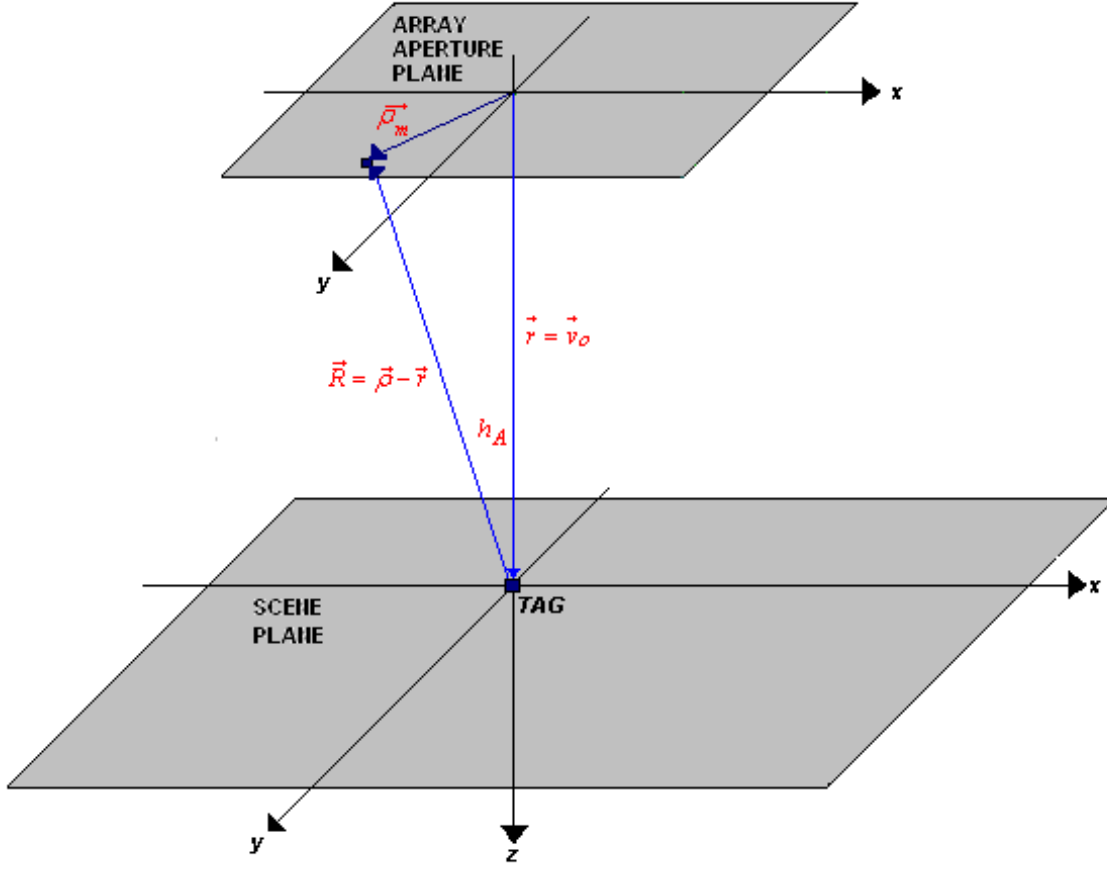


Figure 1.9 Geometry of the simulation experiment for modeling the system PSF.

Continuing the experiment specifications, first, define the model signal correlation matrix \mathbf{R}_s that corresponds to the TAG signal in the origin of the scene coordinate system (\mathbf{v}_0 : $x = 0$, $y = 0$, $z = h_A$). Using the model definition given by (1.55), we directly compute such signal correlation matrix \mathbf{R}_s that is recognized to be the rank-one (i.e. ill-posed [6]) matrix of the following structure

$$\mathbf{R}_s = P_0 \mathbf{s}_{\mathbf{v}_0} \mathbf{s}_{\mathbf{v}_0}^+ = P_0 \mathbf{1}_{(M \times M)} \quad (1.124)$$

where $P_0 = b_{\mathbf{v}_0}$ represents the TAG power and

$$\mathbf{1}_{(M \times M)} = \mathbf{s}_{\mathbf{v}_0} \mathbf{s}_{\mathbf{v}_0}^+ = \begin{bmatrix} 1 & \dots & \dots & 1 \\ \vdots & \ddots & \ddots & \vdots \\ \vdots & \ddots & \ddots & \vdots \\ 1 & \dots & \dots & 1 \end{bmatrix} \quad (1.125)$$

is the $(M \times M)$ rank-one matrix composed of only ones.

Using these definitions, we first, compose the MSF algorithm (1.120) to compute the FTSF defined by (1.121) for all three tested geometries of the AA,

$$\Psi_{MSF(X)}^2(\mathbf{r}) = C_\Psi \mathbf{s}_{(X|d_A)}^+(\mathbf{v}) \begin{bmatrix} 1 & \cdots & \cdots & 1 \\ \vdots & \ddots & \ddots & \vdots \\ \vdots & \ddots & \ddots & \vdots \\ 1 & \cdots & \cdots & 1 \end{bmatrix} \mathbf{s}_{(X|d_A)}(\mathbf{v}), \quad (1.126)$$

$$\Psi_{MSF(O)}^2(\mathbf{r}) = C_\Psi \mathbf{s}_{(O|d_A)}^+(\mathbf{v}) \begin{bmatrix} 1 & \cdots & \cdots & 1 \\ \vdots & \ddots & \ddots & \vdots \\ \vdots & \ddots & \ddots & \vdots \\ 1 & \cdots & \cdots & 1 \end{bmatrix} \mathbf{s}_{(O|d_A)}(\mathbf{v}), \quad (1.127)$$

and

$$\Psi_{MSF(Y)}^2(\mathbf{r}) = C_\Psi \mathbf{s}_{(Y|d_A)}^+(\mathbf{v}) \begin{bmatrix} 1 & \cdots & \cdots & 1 \\ \vdots & \ddots & \ddots & \vdots \\ \vdots & \ddots & \ddots & \vdots \\ 1 & \cdots & \cdots & 1 \end{bmatrix} \mathbf{s}_{(Y|d_A)}(\mathbf{v}), \quad (1.128)$$

respectively. The corresponding Cartesian (x, y, z) scene coordinates are computed via (1.9), i.e.

$$\mathbf{r} = (x, y, z)^T \text{ with } x = \theta_x \left(\frac{h}{\sqrt{1 - (\theta_x^2 + \theta_y^2)}} \right), \quad y = \theta_y \left(\frac{h}{\sqrt{1 - (\theta_x^2 + \theta_y^2)}} \right), \text{ for given } z = h_A. \quad (1.129)$$

The difference between the PSF (1.126)– (1.128) is in the particular structure of the *steering* vectors.

$$\mathbf{s}_{(X|d_A)}(\boldsymbol{\theta}) = g(\boldsymbol{\theta}) \begin{bmatrix} \exp(i2\pi[\boldsymbol{\rho}_{(X|d_A)1}, \boldsymbol{\theta}]) \\ \exp(i2\pi[\boldsymbol{\rho}_{(X|d_A)2}, \boldsymbol{\theta}]) \\ \vdots \\ \exp(i2\pi[\boldsymbol{\rho}_{(X|d_A)M}, \boldsymbol{\theta}]) \end{bmatrix} \quad (1.130)$$

$$\mathbf{s}_{(O|d_A)}(\boldsymbol{\theta}) = g(\boldsymbol{\theta}) \begin{bmatrix} \exp(i2\pi[\boldsymbol{\rho}_{(O|d_A)1}, \boldsymbol{\theta}]) \\ \exp(i2\pi[\boldsymbol{\rho}_{(O|d_A)2}, \boldsymbol{\theta}]) \\ \vdots \\ \exp(i2\pi[\boldsymbol{\rho}_{(O|d_A)M}, \boldsymbol{\theta}]) \end{bmatrix} \quad (1.131)$$

and

$$\mathbf{s}_{(Y|d_A)}(\boldsymbol{\theta}) = g(\boldsymbol{\theta}) \begin{bmatrix} \exp(i2\pi[\mathbf{p}_{(Y|d_A)1}, \boldsymbol{\theta}]) \\ \exp(i2\pi[\mathbf{p}_{(Y|d_A)2}, \boldsymbol{\theta}]) \\ \vdots \\ \exp(i2\pi[\mathbf{p}_{(Y|d_A)M}, \boldsymbol{\theta}]) \end{bmatrix}. \quad (1.132)$$

Next, the FTSF method (1.121) produces the PSF that is computed by the formula similar to (1.122), in which the sparse signal correlation matrix

$$\tilde{\mathbf{R}}_s = P_0 \tilde{\mathbf{I}}_{(M \times M)} = P_0 \begin{bmatrix} \mathbf{0}_{(8 \times 8)} & \mathbf{1}_{(8 \times 8)} & \mathbf{1}_{(8 \times 8)} \\ \mathbf{1}_{(8 \times 8)} & \mathbf{0}_{(8 \times 8)} & \mathbf{1}_{(8 \times 8)} \\ \mathbf{1}_{(8 \times 8)} & \mathbf{1}_{(8 \times 8)} & \mathbf{0}_{(8 \times 8)} \end{bmatrix} \quad (1.133)$$

must be used instead of the complete signal correlation matrix (1.55).

This sparse signal model correlation matrix (1.133) is composed of six identical blocks $\mathbf{1}_{(8 \times 8)}$ of 8-by-8 matrices of ones and three diagonal blocks $\mathbf{0}_{(8 \times 8)}$ composed of zeros. Three upper blocks of ones $\mathbf{1}_{(8 \times 8)}$ in (1.133) relate to the sectors S1, S2 and S3), and the three lower blocks of ones $\mathbf{1}_{(8 \times 8)}$ in (1.133) correspond to the symmetrical (virtual) baselines. Last, three zero blocks $\mathbf{0}_{(8 \times 8)}$ located along the principal diagonal of the matrix correspond to the baselines between arms A-A, B-B and C-C that are not incorporated in the processing algorithm. Thus, the FTSF algorithm produces the PSF employing the following SP formula

$$\Psi_{FTSF}^2(\mathbf{r}) = C_\Psi \mathbf{s}_{(Y|d_A)}^+(\mathbf{v}) \tilde{\mathbf{R}}_s \mathbf{s}_{(Y|d_A)}(\mathbf{v}); \quad (1.134)$$

for the *steering* vector $\mathbf{s}_{(Y|d_A)}(\mathbf{v})$ defined by (1.132). For other two configurations, the corresponding steering vectors are defined by (1.130), (1.131), respectively.

1.7 Analysis of Computational Complexity

In this section, we provide the comparison of the computational complexities of the developed MSF algorithm (1.120) and the FTSF algorithm (1.121). As we examined above, both these algorithms reconstruct the scene image via performing the 2-D spatial Fourier transform of the collected measurements of spatial correlations between different antenna elements in the MIR sensor system.

For any of the three MIR AA configurations, the MSF method requires $24 \times 24 = 576 + 1$ complex multiplications and 576 complex summations for every search direction $(\theta_x, \theta_y) \in \Theta$ associated with the particular beam (θ_x, θ_y) in the fan of beams (labeled as Θ).

Consider now, for example, very “dense” fan of 256-by-256 beams $(\theta_x, \theta_y) \in \Theta$ in the angular sector (FOV) of $[-60^\circ, +60^\circ]$, i.e. two beams in the fan for every one angular degree, 1° . Then, the computational complexities of the MSF and the FTSF algorithm can be estimated as follows.

Computational complexities (in required number of operations) of the MSF algorithm and the FTSF algorithm

- **MSF imaging algorithm performed in the Fourier transform mode (1.120) requires:**

$$\begin{aligned} (576+1) \times 256^2 &= 37,814,272 && \leq \text{complex multiplications} \\ &\text{and} \\ 576 \times 256^2 &= 37,748,736 && \leq \text{complex summations} \end{aligned}$$

to compose the discrete scene image via beamforming the 256-by-256 fan of beams that cover the FOV of $[-60^\circ, +60^\circ]$ over both θ_x and θ_y angular directions.

- **FTSF imaging algorithm (1.121) for the MIR-GeoSTAR configuration requires:**

$$\begin{aligned} (384+1) \times 256^2 &= 25,231,360 && \leq \text{complex multiplications} \\ &\text{and} \\ 384 \times 256^2 &= 25,165,824 && \leq \text{complex summations} \end{aligned}$$

- **FTSF imaging algorithm (1.121) for the MIR-X configuration requires:**

$$\begin{aligned} (188+1) \times 256^2 &= 12,386,304 && \leq \text{complex multiplications} \\ &\text{and} \\ 188 \times 256^2 &= 12,320,768 && \leq \text{complex summations} \end{aligned}$$

- **FTSF imaging algorithm (1.121) for the MIR-O configuration requires:**

$$(289+1) \times 256^2 = 19,005,440 \quad \leq \text{complex multiplications}$$

and

$$289 \times 256^2 = 18,939,904 \quad \leq \text{complex summations}$$

to compose the discrete scene image via beamforming the 256-by-256 fan of beams that cover the FOV of $[-60^\circ, +60^\circ]$ over both θ_x and θ_y angular directions.

The above analysis establishes that if realized in the same spatial 2-D Fourier transform fashion, the robust MSF algorithm (1.120) requires approximately 33.17% more operations (both in complex multiplications and complex summations) than the FTSF imaging algorithm (1.121). The crucial aspect is that to perform the MSF algorithm, the 2-D Fourier transform mode (1.120) is not necessarily required. Much less computationally consuming mode is to perform the MSF algorithm in the alternative spatial fan beamforming mode that we rewrite here for the angular arguments as follows.

$$\begin{aligned} \hat{\theta}_v &= \operatorname{argmax}_i \{ \operatorname{Aver}_t \{ |q_i(t)|^2 \} \} \\ &= \operatorname{argmax}_i \{ \operatorname{Aver}_n \{ \{ ([\mathbf{u}_{\text{Re}}(n), \mathbf{s}_{\text{Re}}(\theta_i)] + [\mathbf{u}_{\text{Im}}(n), \mathbf{s}_{\text{Im}}(\theta_i)])^2 \\ &\quad + ([\mathbf{u}_{\text{Im}}(n), \mathbf{s}_{\text{Re}}(\theta_i)] - [\mathbf{u}_{\text{Re}}(n), \mathbf{s}_{\text{Im}}(\theta_i)])^2 \} \} \end{aligned} \quad (1.135)$$

The crucial aspect is that the number of the spatial processing operations required to perform the algorithm (1.135) is drastically less than in (1.120) and (1.121). The computational complexities of the spatial fan beamforming MSF algorithm (1.135) and the FTSF algorithm (1.121) can be estimated as follows.

Computational complexities (in required number of operations) of the MSF algorithm performed in the spatial fan beamforming mode and the FTSF-GeoSTAR algorithm

- **MSF imaging algorithm performed in the spatial fan beamforming mode (1.135) requires:**

$$(24+1) \times 256^2 = 1,638,400 \quad \leq \text{complex multiplications}$$

and

$$24 \times 256^2 = 1,572,864 \quad \leq \text{complex summations}$$

to compose the discrete scene image via beamforming the 256-by-256 fan of beams that cover

the FOV of $[-60^\circ, +60^\circ]$ over both θ_x and θ_y angular directions.

- **FTSF imaging algorithm (1.121) for the MIR-GeoSTAR configuration requires:**

$$\begin{array}{ll} (384+1) \times 256^2 = 25,231,360 & \leq \text{complex multiplications} \\ \text{and} & \\ 384 \times 256^2 = 25,165,824 & \leq \text{complex summations} \end{array}$$

- **FTSF imaging algorithm (1.121) for the MIR-X configuration requires:**

$$\begin{array}{ll} (188+1) \times 256^2 = 12,386,304 & \leq \text{complex multiplications} \\ \text{and} & \\ 188 \times 256^2 = 12,320,768 & \leq \text{complex summations} \end{array}$$

- **FTSF imaging algorithm (1.121) for the MIR-O configuration requires:**

$$\begin{array}{ll} (289+1) \times 256^2 = 19,005,440 & \leq \text{complex multiplications} \\ \text{and} & \\ 289 \times 256^2 = 18,939,904 & \leq \text{complex summations} \end{array}$$

to compose the discrete scene image via beamforming the 256-by-256 fan of beams that cover the FOV of $[-60^\circ, +60^\circ]$ over both θ_x and θ_y angular directions.

The above results establishes that if realized in the conventional fan beamforming fashion (i.e. different from the 2-D Fourier transform, the robust MSF algorithm (1.135) requires approximately **16 times less** computational operations (both in complex multiplications and complex summations) than the FTSF (1.121). This may be considered as a cost one has to pay for the suppressed grating sidelobes level, hence better performances gained with the FTSF method.

1.8 Virtual Remote Sensing Laboratory (VRSL) Simulations SW

This Subsection aims to introduce the Virtual Remote Sensing Laboratory (VRSL) software (SW) that was elaborated according to the Statement of Work (SOW) as Subtask 2.3: Elaboration of Integrated Software for Simulation and Verification of Developed Techniques. The goal of this subtask is to verify, evaluate, and demonstrate the capabilities of the RS signal and image processing with problem-oriented extraction of remote sensing signatures (RSS) and their knowledge based (KB) intelligent analysis, multiple target detection and scene-zones localization via development of sophisticated end-user-oriented software that we refer to as “Virtual Remote Sensing Laboratory” (VRSL). The purpose of the VRSL software is to implement computationally all the RS reconstruction/enhancement/post-processing/detection/localization tasks. The elaborated VRSL SW aggregates interactive computational tools that offer the user different options for acquisition and processing of any real-world single or multi-sensor, multi-spectral, multi-polarization RS images, application of different system-level effects of image degradation with a particular simulated RS system, simulation of random channel turbulence and noisy effects, and different RS system model mismatch/uncertainty effects. Various enhancement/reconstruction/post-processing/target detection tasks can be simulated in an interactive mode applying different collaborative DEDR-based algorithms to the degraded noisy images, and the quantitative performance enhancement characteristics attained with every particularly simulated method can then be evaluated. The user has options to display on the computer screen different simulated processed scene images and RSS along with corresponding protocols of analysis of different task performance quality metrics. All the qualitative and quantitative results obtained at different simulation stages could be saved for further administration. The VRSL is capable of performing the computer-aided analysis of the corresponding stages of the RS data acquisition, noising, resolution degradation, image formation, RSS extraction, enhancement, reconstruction, method fusion, KB post-processing, target detection and distributed zones localization tasks. The VRSL has been elaborated employing the GUIDE platform (Graphical User Interface Development Environment) for MATLAB ® to produce a user-oriented SW system.

In this Subsection, we first, specify the capabilities of the VRSL SW for performing a variety of simulations studies of the TAG localization algorithms. Figure 1.10 shows the VRSL interface. On the right hand side of the interface, there is a control panel with which a user has capabilities to specify the MIR AA configuration, the operating frequency(ies) the interelement spacing, the number of point-type TAGs in a particular tested range gate, and finally the algorithm to be employed for . Four windows are available to display the simulation results.

The user must perform the following activities to work with the VRSL SW. First, he must specify one of three available MIR AA configurations developed above. This is illustrated in Figure 1.11. In the case presented in this Subsection, we specify the Y-shaped AA configuration.

Next, the user has to select the frequency and range gates for testing the sensor system operation performances as specified in Section 2.2, namely: frequencies – 24 GHz or 36 GHz, and test range gates – 30 m or 100 m, respectively. This is illustrated in Figures 1.12 and 1.13.

With respect to the interelement spacing, it is important to note, that these vary with the wavelength of the operating frequency, i.e., are normalized in λ_0 . 10 different spacings were tested in the particular reported simulations:

$$\begin{aligned} d_{A(1)} &= 0.5 \lambda_0 . & d_{A(3)} &= 1 \lambda_0 . \\ d_{A(2)} &= 0.8 \lambda_0 . & d_{A(4)} &= 1.5 \lambda_0 . \end{aligned}$$

$$d_{\Lambda(5)} = 1.8 \lambda_0 .$$

$$d_{\Lambda(8)} = 3 \lambda_0 .$$

$$d_{\Lambda(6)} = 2 \lambda_0 .$$

$$d_{\Lambda(9)} = 3.5 \lambda_0 .$$

$$d_{\Lambda(7)} = 2.5 \lambda_0 .$$

$$d_{\Lambda(10)} = 4 \lambda_0 .$$

and the specifications are performed using the interface shown in Figure 1.14.

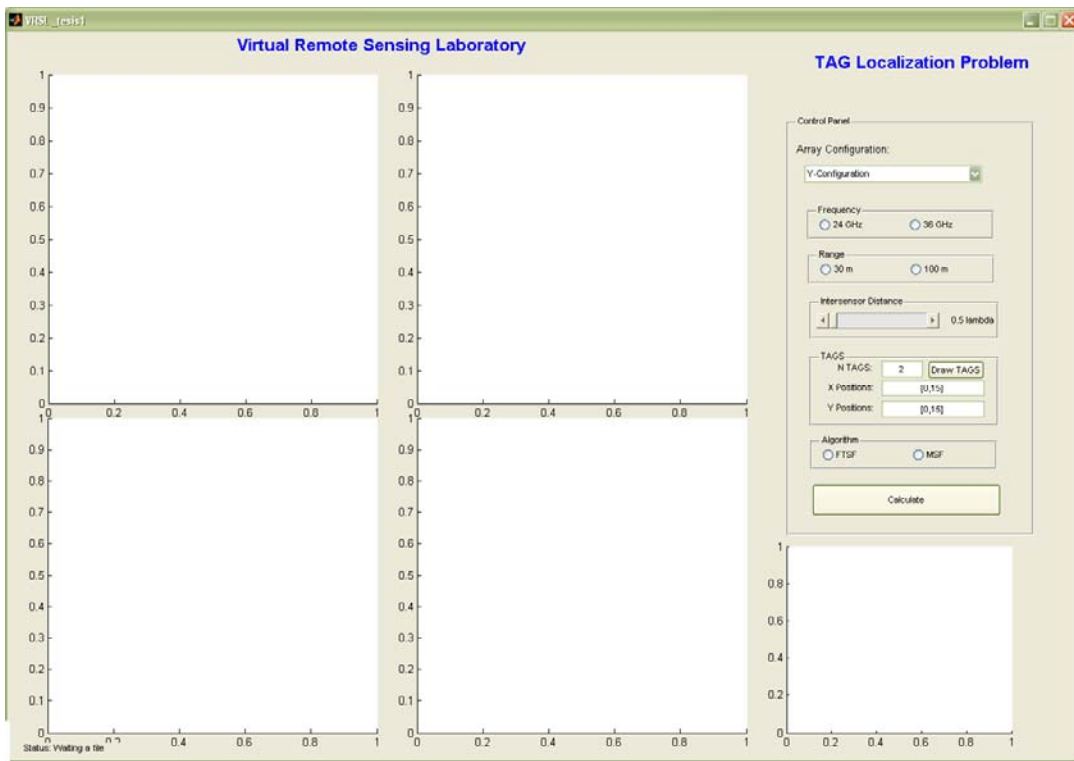


Figure 1.10 Graphic interface of the Virtual Laboratory developed to solve the direct problem employing the GUIDE of MATLAB® platform, called VRSL (*Virtual Remote Sensing Laboratory*).

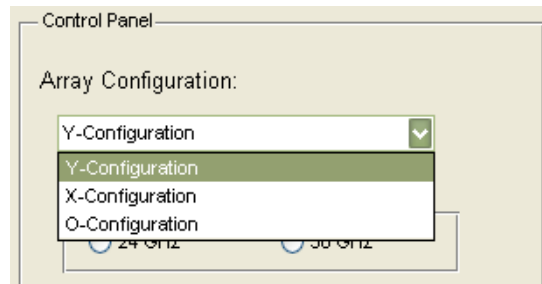


Figure 1.11 Interactive interface for specifying the antenna array configuration.

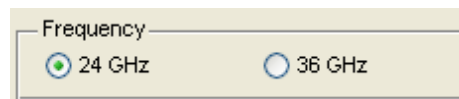


Figure 1.12 Interactive interface for specifying the operating frequency.

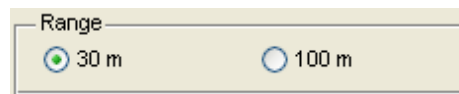


Figure 1.13 Interactive interface for specifying the test range gate.

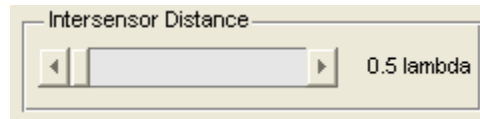


Figure 1.14 Interactive interface for specifying the interelement spacing.

The next step consists in specifying the number of point-type TAGs and their location in x - y coordinates (in meters) in the particular test range gate. This is performed in writing using MATLAB syntax in three fields as shown in Figure 1.15. The positions of TAGs are then entered in a vector format. Figure 1.16 illustrates the TAGs with the coordinates specified in the windows of the interface box presented in Figure 1.15.

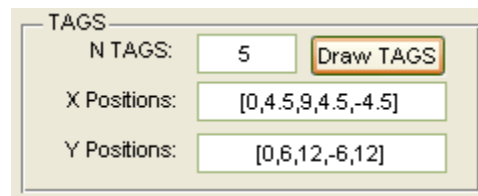


Figure 1.15 Interactive interface to specify the positions of TAGs.

After the TAGs positioning has been specified, the user must press '*Draw TAGS*' button (Figure 1.15), and the SW automatically stores and displays the TAGs in an x - y plane in the specified range gate, see Figure 1.16.

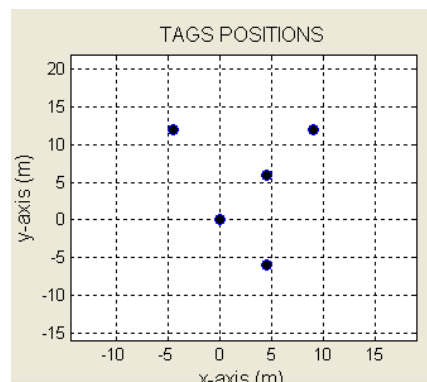


Figure 1.16. Positions of the TAGs in x - y plane (for pre-specified test range gate).

Finally, the user must specify (select) the TAG localization algorithm to be simulated, i.e., the MSF algorithm (1.120) or the FTSF algorithm (1.121). This is illustrated in Figure 1.17. To run the simulations experiment, the user has only to press the '*Calculate*' button on the SW interface.

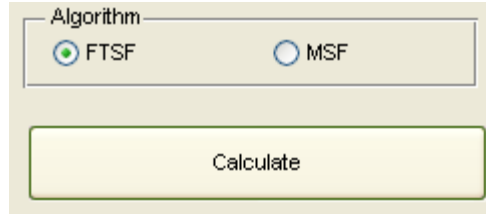


Figure 1.17 Interactive interface for specifying the algorithm and to run the simulations.

One example of the simulations protocols displayed on the interface of the VRSL is presented in Figure 1.18. This is illustrative of the capabilities of the elaborated SW. The VRSL system has four fields to present the simulations protocols. In the top left window, the configuration and layout of the specified tested AA is displayed, in this case, the Y-shaped GeoSTAR configured AA. In the top right window, the spacing related to the visibility function is presented in $U-V$ coordinates. The left bottom window displays the PSF related to the particular specified AA configuration. The right bottom window displays the image of the scene in the pre-specified test range gate obtained with the specified imaging technique, i.e., the MSF algorithm (1.120) or the FTSF algorithm (1.121), correspondingly.

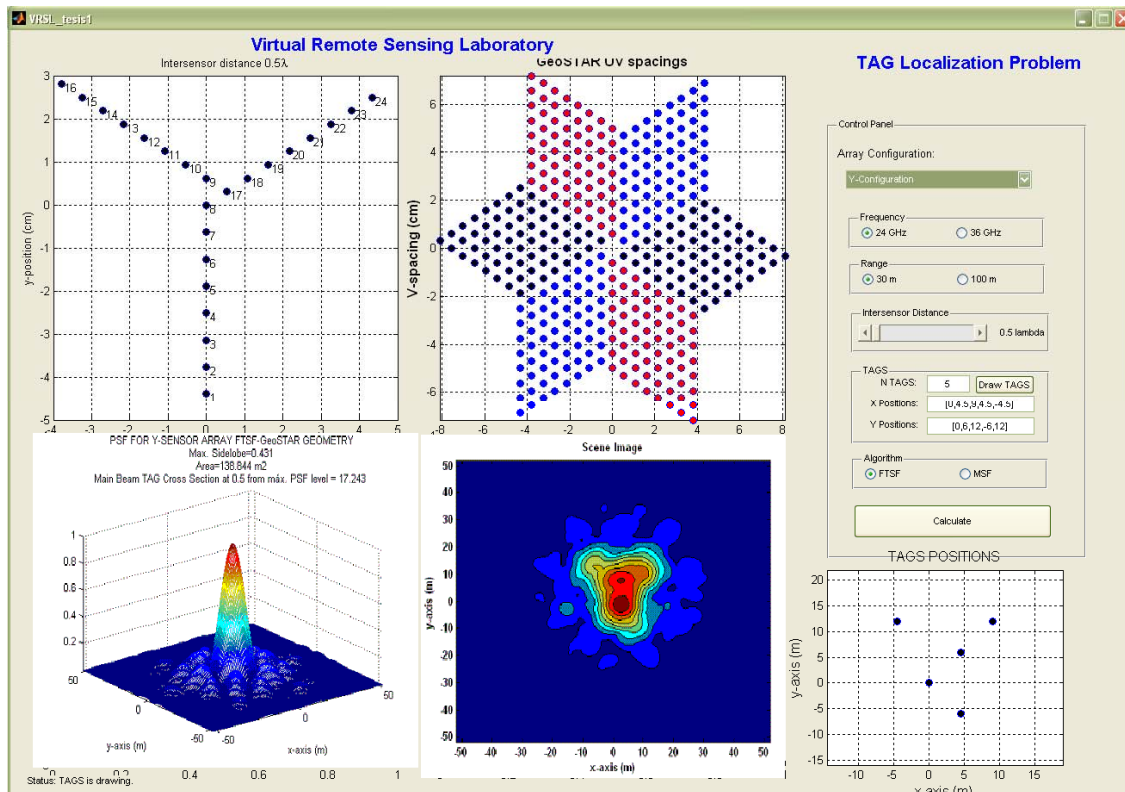


Figure 1.18. Example of interface information displayed after performing the simulations experiment. All the simulation data is next archived in corresponding protocol formats. The developed SP and data archiving protocols are detailed and analyzed in Part III of this Report.

1.9. Summary of Part I

In this Part of the Report, we provided the foundations, basic methodological and algorithmic developments related to the new (HW) software (SW) codesign paradigm developed for the purposes of robust high-resolution processing of cross-polarization sensor data obtained from multiple sensor modalities aimed at high-resolution sensing, detection and localization of point-type targets in uncertain remote sensing (RS) environment. Approaching these goals, we have performed the following research & development tasks.

- Specified the coordinate system and geometry for the problem of localization of the point type TAGs on the scene plane using the measurement data provided by an arbitrary plane M -element sensor array;
- Provide the necessary statistical model of the signals induced by the TAGs at the outputs of the M -element sensor array;
- Performed generalization of the signal model for the distributed scene scenario;
- Provided the robust stochastic model of the random array observation data contaminated with noise for the realistic scenario with model uncertainties regarding the statistical characteristics of signal and noise;
- Composed and detailed the robust ML algorithm for TAGs localization in uncertain operational scenario;
- Revealed the relationship between the robust parametric ML and nonparametric robust beamforming methods for spatial spectrum pattern (SSP) characterization;
- Provided generalization of the ML-based matched spatial filtering (MSF) technique to the Fourier transform-based spatial filtering (FTSF) algorithm for TAGs localization via formation and analysis of the scene images;
- Revealed the structural similarity of the robust MSF and FTST algorithms for the particular problem of multiple TAG localization with the GeoSTAR geometry in uncertain operational scenario;
- Perform the comparative analysis of computational complexities of the robust MSF and FTST algorithms for the employed GeoSTAR geometry;
- Provided computational recipes for composing the simulations experiment;
- Presented a summary of the elaborated VRSL software for simulation studies of the developed techniques.

The presented preliminary simulation results are indicative of the potential performances, operational gains/loses and processing restrictions related to the HW-SW codesign of the overall multimode sensor system that can employs different available sensor array configurations, namely: the X-shaoed, the O-shaped and the Y-shaped array (GeoSTAR geometry) composed of **omnidirectional** elements. The reported preliminary results verify that the Y-shaped array (virtual synthetic GeoSTAR-configured array) provides the best operational performances in the sense of the compromise between the resulting resolution cell cross-section and artifacts due to the sidelobes and grating lobes levels in the resulting point spread function. The issues related to optimization of the Y-shaped array geometry via adjusting the interelement spacing and employing the directional sensors array are to be reported in details in Part III of the present Report.

PART II

DESCRIPTIVE EXPERIMENT DESIGN REGULARIZATION PARADIGM AND RELATED TECHNIQUES FOR ROBUST ADAPTIVE SENSING AND IMAGE FUSION IN THE APERTURE ARRAY SYNTHESIS MODE

In this Part of the Report, we present the results of the methodological and algorithmic developments of the descriptive experiment design regularization (DEDR) method that next is integrated with the variational analysis (VA) approach for adaptive multimode high-resolution sensing into a new unified DEDR-VA framework that puts in a single optimization frame collaborative sensor array/SAR data acquisition, despeckling, dynamic scene imaging in the uncertain operational scenarios for a variety of admissible sensor array configurations, and method/sensor fusion that outperform the existing adaptive radar imaging techniques both in resolution and convergence rate. We also report a summary of the development of the integrated “Virtual Remote Sensing Laboratory” (VRSL) software (SW) elaborated for verification, evaluation, and demonstration of the capabilities of the adaptive DEDR-VA-related multimode remote sensing and array radar/SAR imaging techniques.

According to the SOW, these developments are focused on the analytical research and development of efficient methods for (near) real time adaptive mapping of the distributed large-scale scenes remotely sensed with the multimode imaging array radar/SAR sensor systems in the real-world uncertain operational scenarios, enhancement of diverse remote sensing (RS) – sensor network (SN) capabilities for solving multimode sensing, knowledge-based (KB) search and discovery inverse problems, and elaboration of the integrated “Virtual Remote Sensing Laboratory” (VRSL) simulations software for verification of the developed techniques through the diverse problem oriented simulation experiments. The operational uncertainties are attributed to inevitable random signal perturbations in inhomogeneous propagation medium with unknown statistics, possible imperfect array sensor calibration and uncontrolled SAR carrier trajectory deviations. During the previous year, such uncertain radar/SAR imaging problems were treated via unification of the minimum risk spectral estimation strategy with the worst case statistical performance (WCSP) optimization-based regularization resulting in the descriptive experiment design regularization (DEDR) method. Although the DEDR framework offers considerable flexibility in designing the adaptive techniques robust against the operational uncertainties, their implementation requires rather complex signal processing operations ruled by the slowly converging nonlinear fixed-point iterative processes. To overcome such processing limitations, during the second year we have developed a new hardware (HW) – software (SW) codesign approach that incorporates the additional convergence enforcing regularization into the DEDR framework. We perform this task by combining the variational analysis (VA) image enhancement paradigm with the descriptive regularization via projections onto convex solution sets (POCS) that parallelizes and further speeds-up the reconstructive image processing procedures. We have designed a family of such significantly speeded-up POCS-regularized DEDR-VA-related algorithms employing the proposed HW/SW codesign, and performed the extended simulations using the elaborated VRSL software to verify their operational effectiveness in adaptive imaging and mapping of the remote sensing signatures (RSS), in particular, despeckling, superresolution and convergence rate, for a variety of admissible

imaging array sensor geometries and SAR operational modes. Last, the DEDR-VA framework is aggregated with the neural network (NN) adapted method for adaptive high resolution multimode sensor data fusion. We have designed a family of such significantly speeded-up DEDR-VA-related algorithms, and performed the simulations to illustrate the effectiveness of the proposed high-resolution DEDR-VA-NN-based image enhancement/fusion approach particularly adapted to the robust fractional aperture synthesis modes.

2.1. Problem Formalism

A. Continuous-Form Problem Model

The general mathematical formalism of the problem at hand is similar in notation and structural framework to that described in [6]–[8], [16]–[20] and some crucial elements are repeated for convenience to the reader. Following [7], [17], [19] we define the model of the observation RS wavefield u by specifying the stochastic equation of observation (EO) of an operator form

$$u = \mathcal{S}e + n ; \quad \mathcal{S}: \mathbb{E}(R) \rightarrow \mathbb{U}(P) \quad (2.1)$$

where $e = e(\mathbf{r})$, represents the complex scattering function over the probing surface $R \ni \mathbf{r}$, n is the additive noise, $u = u(\mathbf{p})$, is the observation field, $\mathbf{p} = (t, \boldsymbol{\rho})$ defines the time (t) – space ($\boldsymbol{\rho}$) points in the temporal-spatial observation domain $\mathbf{p} \in P = T \times P$ ($t \in T$, $\boldsymbol{\rho} \in P$) (in the SAR case, $\boldsymbol{\rho} = \boldsymbol{\rho}(t)$ specifies the carrier trajectory [7]), and the kernel-type integral signal formation operator (SFO) $\mathcal{S}: \mathbb{E}(R) \rightarrow \mathbb{U}(P)$ defines a mapping of the source signal space $\mathbb{E}(R)$ onto the observation signal space $\mathbb{U}(P)$. The metrics structures in the corresponding Hilbert signal spaces $\mathbb{U}(P)$, $\mathbb{E}(R)$ are imposed by scalar products, $[u, u']_{\mathbb{U}} = \int_P u(\mathbf{p}) u'^*(\mathbf{p}) d\mathbf{p}$, $[e, e']_{\mathbb{E}} = \int_R e(\mathbf{r}) e'^*(\mathbf{r}) d\mathbf{r}$, respectively [6].

The functional kernel $S(\mathbf{p}, \mathbf{r})$ of the SFO \mathcal{S} is referred to as the *unit signal* [6] determined by the time-space modulation employed in a particular RS system. In the case of uncertain operational scenarios, the SFO is randomly perturbed [19], i.e. $\tilde{\mathcal{S}} = \mathcal{S} + \Delta$ where Δ pertains to the random uncontrolled perturbations, usually with *unknown* statistics. The fields e, n, u are assumed to be zero-mean complex valued Gaussian random fields [6], [7]. Next, since in all RS applications the regions of high correlation of $e(\mathbf{r})$ are always small in comparison with the resolution element on the probing scene [1]–[3], the signals $e(\mathbf{r})$ scattered from different directions $\mathbf{r}, \mathbf{r}' \in R$ of the remotely sensed scene R are assumed to be uncorrelated with the correlation function $R_e(\mathbf{r}, \mathbf{r}') = \langle e(\mathbf{r}) e^*(\mathbf{r}') \rangle = b(\mathbf{r}) \delta(\mathbf{r} - \mathbf{r}')$; $\mathbf{r}, \mathbf{r}' \in R$ where $b(\mathbf{r}) = \langle e(\mathbf{r}) e^*(\mathbf{r}) \rangle = \langle |e(\mathbf{r})|^2 \rangle$; $\mathbf{r} \in R$ represents the power spatial spectrum pattern (SSP) of the scattered field [7]. The problem of enhanced RS imaging is to develop a signal processing method for performing the high efficient estimation of the SSP $b(\mathbf{r})$ by processing the available finite dimensional array radar measurements of the data wavefield $u(\mathbf{p})$. Such the estimate $\hat{b}(\mathbf{x})$ of the SSP $b(\mathbf{x})$ is referred to as the desired reconstructed RS image of the remotely sensed scene.

The problem of high-resolution RS imaging is to develop a framework and related method(s) that perform optimal estimation of the SSP $b(\mathbf{r})$ (referred to as a scene image) from the available

radar/SAR data measurements. Note that we are going to develop and follow the unified DEDR-VA-NN framework.

B. Discrete-Form Problem Model

Now we proceed from the stochastic integral-form EO (2.1) to its finite-dimensional approximation (vector) form

$$\mathbf{u} = \tilde{\mathbf{S}}\mathbf{e} + \mathbf{n} = \mathbf{S}\mathbf{e} + \Delta\mathbf{e} + \mathbf{n}, \quad (2.2)$$

in which the disturbed SFO matrix

$$\tilde{\mathbf{S}} = \mathbf{S} + \Delta \quad (2.3)$$

is the discrete-form approximation of the integral SFO defined for the uncertain operational scenario by the EO (2.1), and \mathbf{e} , \mathbf{n} , \mathbf{u} represent zero-mean vectors composed of the decomposition coefficients e_k , n_m , and u_m , respectively. These vectors are characterized by the correlation matrices: $\mathbf{R}_e = \mathbf{D} = \mathbf{D}(\mathbf{b}) = \text{diag}(\mathbf{b})$ (a diagonal matrix with vector \mathbf{b} at its principal diagonal), \mathbf{R}_n , and $\mathbf{R}_u = \langle \tilde{\mathbf{S}}\mathbf{R}_e\tilde{\mathbf{S}}^+ \rangle_{p(\Delta)} + \mathbf{R}_n$, respectively, where $\langle \cdot \rangle_{p(\Delta)}$ defines the averaging performed over the randomness of Δ characterized by the *unknown* probability density function $p(\Delta)$, and superscript $+$ stands for Hermitian conjugate. Vector \mathbf{b} is composed of the elements, $b_k = \mathcal{B}(e_k) = \langle e_k e_k^* \rangle = \langle |e_k|^2 \rangle$; $k = 1, \dots, K$, and is referred to as a K -D vector-form representation of the SSP, where \mathcal{B} represents the second-order statistical ensemble averaging operator [6]. The SSP vector \mathbf{b} is associated with the so-called lexicographically ordered image pixels [13]. The corresponding conventional $K_y \times K_x$ rectangular frame ordered scene image $\mathbf{B} = \{b(k_x, k_y); k_x = 1, \dots, K_x; k_y = 1, \dots, K_y\}$ relates to its lexicographically ordered vector-form representation $\mathbf{b} = \{b(k); k = 1, \dots, K = K_y \times K_x\}$ via the standard row by row concatenation (so-called lexicographical reordering) procedure, $\mathbf{B} = L\{\mathbf{b}\}$ [20]. Note that in the simple case of certain operational scenario [10], [17], the discrete-form (i.e. matrix-form) SFO \mathbf{S} is assumed to be deterministic, i.e. the random perturbation term in (2.3) is irrelevant, $\Delta = \mathbf{0}$.

The digital enhanced RS imaging problem is stated mathematically as follows: to map the scene pixel frame image $\hat{\mathbf{B}}$ via lexicographical reordering $\hat{\mathbf{B}} = L\{\hat{\mathbf{b}}\}$ of the SSP vector estimate $\hat{\mathbf{b}}$ reconstructed from whatever available measurements of independent realizations of the recorded data vector \mathbf{u} . The reconstructed SSP vector $\hat{\mathbf{b}}$ is an estimate of the second-order statistics of the scattering vector \mathbf{e} observed through the perturbed SFO (2.3) and contaminated with noise \mathbf{n} ; hence, the imaging problem at hand must be qualified and treated as a statistical nonlinear *inverse* problem [10]. The high-resolution imaging implies solution of such an inverse problem in some optimal way. Recall that in this project we intend to follow and unify the DEDR and FBR methodologies originally proposed in our previous studies [6], [10], [16].

2.2 Unified DEDR Method

A. DEDR Strategy for Certain Operational Scenario

In the descriptive statistical formalism, the desired SSP vector $\hat{\mathbf{b}}$ is recognized to be the vector of a principal diagonal of the estimate of the correlation matrix $\mathbf{R}_e(\mathbf{b})$, i.e. $\hat{\mathbf{b}} = \{\hat{\mathbf{R}}_e\}_{\text{diag}}$.

Following the DEDR optimization approach [10] [17], we seek to estimate $\hat{\mathbf{b}} = \{\hat{\mathbf{R}}_e\}_{\text{diag}}$ given the data matrix \mathbf{Y} formed via averaging $J \geq 1$ outer products of the recorded data vector snapshots $\{\mathbf{u}_{(j)}\}$, i.e.,

$$\mathbf{Y} = \hat{\mathbf{R}}_u = \frac{1}{J} \sum_{j=1}^J \mathbf{u}_{(j)} \mathbf{u}_{(j)}^+, \quad (2.4)$$

(the outer product $\mathbf{Y} = \mathbf{u}\mathbf{u}^+$ of a single recorded trajectory signal realization in the case of a single-look SAR, $J = 1$, [10], [13]) by determining the solution operator (SO) \mathbf{F} such that

$$\hat{\mathbf{b}} = \{\hat{\mathbf{R}}_e\}_{\text{diag}} = \{\mathbf{F}\mathbf{Y}\mathbf{F}^+\}_{\text{diag}} \quad (2.5)$$

where $\{\cdot\}_{\text{diag}}$ defines the vector composed of the principal diagonal of the embraced matrix.

To optimize the search for \mathbf{F} in the *certain* operational scenario we follow the DEDR strategy

$$\mathbf{F} \rightarrow \min_{\mathbf{F}} \{\mathcal{R}(\mathbf{F})\}, \quad (2.6)$$

$$\mathcal{R}(\mathbf{F}) = \text{trace}\{(\mathbf{F}\mathbf{S} - \mathbf{I})\mathbf{A}(\mathbf{F}\mathbf{S} - \mathbf{I})^+\} + \alpha \text{trace}\{\mathbf{F}\mathbf{R}_n\mathbf{F}^+\} \quad (2.7)$$

The DEDR strategy (2.6) implies the minimization of the weighted sum (2.7) of the systematic and fluctuation errors in the desired estimate where the selection (adjustment) of the regularization parameter α and the weight matrix \mathbf{A} provide the additional experiment design degrees of freedom incorporating any descriptive properties of a solution if those are known a priori [10], [17]. It is easy to recognize that the strategy (2.6) is a structural extension of the statistical Bayesian minimum risk estimation strategy [17] for the nonlinear spectral estimation problem at hand because in both cases the balance between the gained spatial resolution and the noise suppression in the resulting estimate is optimized.

B. Extended DEDR Strategy for Uncertain Scenario

To optimize the search for the desired SO \mathbf{F} in the *uncertain* operational scenario with the randomly perturbed SFO (2.3), we propose the following *extended DEDR* strategy

$$\mathbf{F} = \arg \min_{\mathbf{F}} \max_{\langle \|\Delta\|^2 \rangle_{p(\Delta)} \leq \delta} \{\mathcal{R}_{\text{ext}}(\mathbf{F})\} \quad (2.8)$$

$$\text{subject to } \langle \|\Delta\|^2 \rangle_{p(\Delta)} \leq \delta \quad (2.9)$$

where the conditioning term (2.9) represents the worst-case statistical performance (WCSP) regularizing constraint imposed on the unknown second-order statistics $\langle \|\Delta\|^2 \rangle_{p(\Delta)}$ of the random distortion component Δ of the SFO matrix (2.3), and the DEDR “extended risk” is defined by

$$\mathcal{R}_{\text{ext}}(\mathbf{F}) = \text{tr}\{\langle (\mathbf{F}\tilde{\mathbf{S}} - \mathbf{I})\mathbf{A}(\mathbf{F}\tilde{\mathbf{S}} - \mathbf{I})^+ \rangle_{p(\Delta)}\} + \alpha \text{tr}\{\mathbf{F}\mathbf{R}_n\mathbf{F}^+\}. \quad (2.10)$$

where the regularization parameter α and the weight matrix \mathbf{A} compose the processing level “degrees of freedom” of the extended DEDR method.

To proceed with the derivation of the robust SO (2.8), the risk function (2.10) can next be decomposed and evaluated for its maximum value applying the Cauchy-Schwarz inequality and Loewner ordering [17] of the weight matrix $\mathbf{A} \leq \gamma \mathbf{I}$ with the scaled Loewner ordering factor $\gamma =$

$\min\{\hat{\gamma} : \mathbf{A} \leq \hat{\gamma}\mathbf{I}\} = 1$. With these robustifications, the extended DEDR problem (2.8) is transformed into the following optimization problem

$$\mathbf{F} \rightarrow \min_{\mathbf{F}} \{ \mathcal{R}_{\Sigma}(\mathbf{F}) \} \quad (2.11)$$

with the *aggregated* DEDR risk function

$$\mathcal{R}_{\Sigma}(\mathbf{F}) = \text{tr}\{(\mathbf{F}\mathbf{S} - \mathbf{I})\mathbf{A}(\mathbf{F}\mathbf{S} - \mathbf{I})^+\} + \alpha \text{tr}\{\mathbf{F}\mathbf{R}_{\Sigma}\mathbf{F}^+\}, \quad (2.12)$$

$$\text{where} \quad \mathbf{R}_{\Sigma} = \mathbf{R}_{\Sigma}(\beta) = (\mathbf{R}_{\mathbf{n}} + \beta\mathbf{I}); \quad \beta = \delta/\alpha \geq 0. \quad (2.13)$$

C. DEDR-Optimal Solution Operators

Examining the DEDR strategies (2.6) and (2.11) one can deduce that those both are structurally similar and differ only by the definition of the second (i.e. noise) risk component terms in (2.7) and (2.12). In the certain operational scenario [10], [17], the trace $\text{tr}\{\mathbf{F}\mathbf{R}_{\mathbf{n}}\mathbf{F}^+\}$ for the noise error measure is used, while in the uncertain scenario [13], the augmented measure $\text{tr}\{\mathbf{F}\mathbf{R}_{\Sigma}\mathbf{F}^+\}$ is employed with the diagonal loaded extension (2.13) of the composite noise correlation matrix \mathbf{R}_{Σ} . The established structural similarity (the so-called problem model homomorphism [8]) of two DEDR problems (2.6) and (2.11) makes it possible to unify the solutions for both scenarios. Doing so, we specify the SOs for both considered operational scenarios, namely:

1) *SO for certain operational scenario* follows directly from the solution to the optimization problem (2.6) found in our previous study [10] that results in

$$\mathbf{F} = \mathbf{K}\mathbf{S}^+\mathbf{R}_{\mathbf{n}}^{-1}, \quad (2.14)$$

$$\text{where} \quad \mathbf{K} = (\mathbf{S}^+\mathbf{R}_{\mathbf{n}}^{-1}\mathbf{S} + \alpha\mathbf{A}^{-1})^{-1} \quad (2.15)$$

represents the so-called regularized reconstruction operator [10] and the adjoint (i.e. Hermitian transpose) SFO \mathbf{S}^+ defines the matched spatial filter in the conventional signal processing terminology [6], [10];

2) *SO for uncertain operational scenario* follows as structural extension of (2.14) for the augmented (diagonal loaded) \mathbf{R}_{Σ} that yields

$$\mathbf{F} = \mathbf{K}_{\Sigma}\mathbf{S}^+\mathbf{R}_{\Sigma}^{-1}, \quad (2.16)$$

$$\text{where} \quad \mathbf{K}_{\Sigma} = (\mathbf{S}^+\mathbf{R}_{\Sigma}^{-1}\mathbf{S} + \alpha\mathbf{A}^{-1})^{-1} \quad (2.17)$$

represents the robustified reconstruction operator for the *uncertain* scenario.

D. DEDR-Related Imaging Techniques

Here we exemplify three practically motivated DEDR-related imaging techniques, namely, the conventional matched spatial filtering (MSF) method, and two high-resolution reconstructive imaging techniques: (i) the robust spatial filtering (RSF) method, and (ii) the robust adaptive spatial filtering (RASf) method.

1) *MSF*: The MSF algorithm is a member of the DEDR-related family [10] specified for $\alpha \gg \|\mathbf{S}^+\mathbf{S}\|$, i.e. the case of a dominating priority of suppression of noise over the systematic error

in the optimization problem (2.6). In this case, the SO (2.14) is approximated by the matched spatial filter (MSF):

$$\mathbf{F}_{MSF} = \mathbf{F}^{(1)} \approx \mathbf{S}^+. \quad (2.18)$$

2) *RSF*: The RSF method implies no preference to any prior model information (i.e., $\mathbf{A} = \mathbf{I}$) and balanced minimization of the systematic and noise error measures in (8), (11) by adjusting the regularization parameter α to the inverse of the signal-to-noise ratio (SNR). In that case the SO becomes the Tikhonov-type robust spatial filter (RSF):

$$\mathbf{F}_{RSF} = \mathbf{F}^{(2)} = (\mathbf{S}^+ \mathbf{S} + \alpha_{RSF} \mathbf{I})^{-1} \mathbf{S}^+, \quad (2.19)$$

in which the regularization parameter α_{RSF} is adjusted to a particular operational scenario model, namely, $\alpha_{RSF} = (N_0/b_0)$ for the case of a certain operational scenario [10], and $\alpha_{RSF} = (N_\Sigma/b_0)$ in the uncertain operational scenario case [8], respectively, where N_0 represents the white observation noise power density, b_0 is the average a priori SSP value, and $N_\Sigma = N_0 + \beta$ corresponds to the augmented noise power density in the correlation matrix specified by (2.13).

3) *RASF*: In the Bayesian statistically optimal problem treatment, α and \mathbf{A} are adjusted in an adaptive fashion following the FBR minimum risk strategy [6], i.e. $\alpha \mathbf{A}^{-1} = \hat{\mathbf{D}} = \text{diag}(\hat{\mathbf{b}})$, the diagonal matrix with the estimate $\hat{\mathbf{b}}$ at its principal diagonal, in which case the SOs (2.14), (2.16) become itself solution-dependent operators that result in the following robust adaptive spatial filters (RASFs):

$$\mathbf{F}_{RASF} = \mathbf{F}^{(3)} = (\mathbf{S}^+ \mathbf{R}_n^{-1} \mathbf{S} + \hat{\mathbf{D}}^{-1})^{-1} \mathbf{S}^+ \mathbf{R}_n^{-1} \quad (2.20)$$

for the certain operational scenario, and

$$\mathbf{F}_{RASF\Sigma} = \mathbf{F}^{(4)} = (\mathbf{S}^+ \mathbf{R}_\Sigma^{-1} \mathbf{S} + \hat{\mathbf{D}}^{-1})^{-1} \mathbf{S}^+ \mathbf{R}_\Sigma^{-1} \quad (2.21)$$

for the uncertain operational scenario, respectively. Next, in all practical RS scenarios [6]–[10] (and specifically, in SAR uncertain imaging applications [13], [8]), it is a common practice to accept the robust white additive noise model, i.e. $\mathbf{R}_n = N_0 \mathbf{I}$, attributing the unknown correlated noise component as well as multiplicative speckle noise to the composite uncertain noise term $\Delta \mathbf{e}$ in (2), in which case $\mathbf{R}_\Sigma = N_\Sigma \mathbf{I}$ with the composite noise power density $N_\Sigma = N_0 + \beta$, the initial observation noise variance N_0 augmented by the loading factor β specified by (2.13).

Using the defined above SOs, the DEDR-related data processing techniques for high-resolution SSP reconstruction and RS imaging in the conventional pixel-frame format can be unified now as follows

$$\hat{\mathbf{B}} = L \{ \hat{\mathbf{b}} \} = L \{ \{ \mathbf{F}^{(p)} \mathbf{Y} \mathbf{F}^{(p)+} \}_{\text{diag}} \}; \quad p = 1, 2, 3, 4 \quad (2.22)$$

with $\mathbf{F}^{(1)} = \mathbf{F}_{MSF}$, $\mathbf{F}^{(2)} = \mathbf{F}_{RSF}$, and $\mathbf{F}^{(3)} = \mathbf{F}_{RASF}$, $\mathbf{F}^{(4)} = \mathbf{F}_{RASF\Sigma}$, respectively. Any other feasible adjustments of the DEDR degrees of freedom (two regularization parameters α , β , and the weight matrix \mathbf{A}) provide other possible DEDR-related SSP reconstruction techniques.

2.3. POCS-Regularized DEDR Method

Because of the extremely high dimension $(K \times K) = (K_y \times K_x) \times (K_y \times K_x) \sim 10^{12}$ of the operator inversions required to form the corresponding SOs specified by (2.20), (2.21), it is questionable to recommend the general-form DEDR-related family (2.22) as practical enhanced RS imaging techniques realizable in (near) real computational time. Hence, one has to proceed from the conventional-form $(K_y \times K_x) \times (K_y \times K_x)$ -dimensional RSF and RASF algorithms (that require cumbersome operator inversions (2.20), (2.21)) to more computationally efficient *iterative* techniques that do *not* involve the large-scale operator inversions and incorporate the convergence enforcement regularization into the DEDR procedure via constructing the proper projections onto convex sets (POCS) in the solution domain. In the considered here RS imaging applications, such POCS is aimed at performing the factorization of the overall procedures over the orthogonal range (y) – azimuth (x) coordinates in the scene frame making also an optimal use of the sparseness properties of the employed radar/SAR modulation format. Thus, the innovative idea is to perform the POCS regularization in an aggregated multi-level fashion. In particular, we propose to aggregate the positivity and range-azimuth orthogonalization projectors constructed previously in [13] with the point spread function (PSF) sparseness enforcing sliding window projectors acting in parallel over both range and azimuth image frames that set the corresponding PSF pixel values to zeroes outside their specified support regions. In this project, we address such a unified multi-level POCS-regularized iterative DEDR method as an extension of the previously proposed DEDR-POCS [8] that we have developed in two stages.

A. First Stage: Fixed-Point Iterative DEDR Algorithm

The first stage is a structural extension of the fixed-point method considered by us in [17], the extension being done for the case of the unified SOs specified now by (2.14) and (2.16). Thus, following the fixed-point algorithm design scheme of [5, Section 6], we first, specify a sequence of the iterative DEDR-POCS estimates

$$\hat{\mathbf{b}}_{[n+1]} = \mathcal{T}_{[n]}(\hat{\mathbf{b}}_{[n]}; \mathbf{Y}) = \mathcal{P}\{\mathbf{K}_{[n]} \mathbf{S}^+ \mathbf{Y} \mathbf{S} \mathbf{K}_{[n]}\}_{\text{diag}}, \quad (2.23)$$

$n = 0, 1, \dots$, where \mathcal{P} is a convergence enforcing projector (i.e., the POCS-regularizing operator) that we next construct at the second design stage (clarified in the next subsection). In (2.23),

$$\mathbf{K}_{[n]} = \mathbf{K}(\hat{\mathbf{b}}_{[n]}) = (\mathbf{\Psi} + N_{\Sigma} \mathbf{D}^{-1}(\hat{\mathbf{b}}_{[n]}))^{-1} \quad (2.24)$$

represents the self-adjoint reconstruction operator at the n th iteration step, $n = 0, 1, \dots$, and

$$\mathbf{\Psi} = \mathbf{S}^+ \mathbf{S} \quad (2.25)$$

is the nominal system point spread function (PSF) operator (a $K \times K$ matrix). Applying routinely the fixed-point technique [8] to the equation (2.23), we derive the desired extended POCS-regularized iterative SSP estimation algorithm

$$\hat{\mathbf{b}}_{[n+1]} = \mathcal{P}\hat{\mathbf{b}}_{[0]} + \mathcal{P}\mathbf{T}_{[n]}\hat{\mathbf{b}}_{[n]}; \quad n = 0, 1, \dots \quad (2.26)$$

Here,

$$\mathbf{T}_{[n]} = 2\text{diag}(\{\mathbf{W}_{[n]}(\hat{\mathbf{b}}_{[n]})\}_{\text{diag}}) - \mathbf{H}_{[n]}(\hat{\mathbf{b}}_{[n]}); \quad n = 0, 1, \dots \quad (2.27)$$

represents the solution-dependent matrix-form iteration operator, in which

$$\mathbf{W}_{[n]}(\hat{\mathbf{b}}_{[n]}) = \mathbf{I} - \mathbf{\Psi} - N_{\Sigma}\mathbf{D}^{-1}(\hat{\mathbf{b}}_{[n]}) ; \quad (2.28)$$

$$\mathbf{H}_{[n]}(\hat{\mathbf{b}}_{[n]}) = \mathbf{W}_{[n]}(\hat{\mathbf{b}}_{[n]}) \circ \mathbf{W}_{[n]}(\hat{\mathbf{b}}_{[n]}) ; \quad (2.29)$$

\circ denotes the Shur-Hadamard (element-by-element) matrix product, and the zero-step iteration

$$\hat{\mathbf{b}}_{[0]} = \hat{\mathbf{b}}_{MSF} = \{\mathbf{S}^+\mathbf{Y}\mathbf{S}\}_{\text{diag}} \quad (2.30)$$

is formed as an outcome of the MSF algorithm from the DEDR family (2.22) specified for the adjoint SFO solution operator \mathbf{S}^+ .

B. Second Stage: Multi-Level POCS Regularization

Next, to specify the regularizing POCS projector operator \mathcal{P} in the fixed-point algorithm (2.26) we make the use of factorization of the PSM (2.25) over the azimuth (x) and range (y) coordinates valid for all existing imaging radar/SAR systems [1], [6], [10]. Such factorization is illustrated in Figure 1. We formalize this stage by introducing the range-azimuth factorization operator $\mathcal{P}_{a\perp r}$,

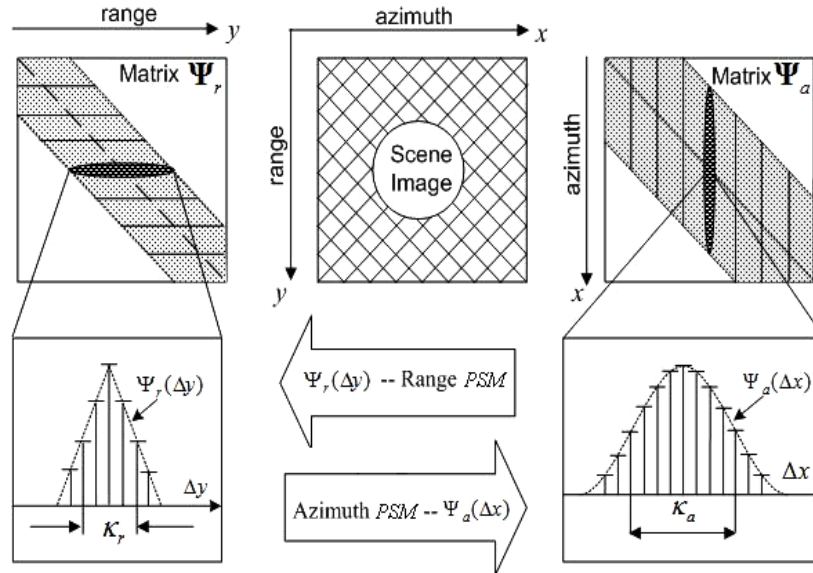


Figure 2.1. Illustration of the scene image degradations over the range and azimuth directions with factorized PSMs.

the same one as in the POCS regularization constructed by us in [17]. Next, to make a use of the intrinsic sparseness properties of the SAR point spread functions over the range and azimuth

frames, we propose to incorporate the new POCS regularization stage via constructing the x - y factorized projection operator (algorithm) $\mathcal{P}_{\kappa_a \perp \kappa_r}$ that acts as a composition of the orthogonal sliding windows [17] with the window apertures adjusted to the PSM widths: (i) $2\kappa_a$ specifies the azimuth window frame adjusted to the effective pixel width of the non-zero strip $\Psi_a(x)$ of the azimuth PSM Ψ_a along the x axis; (ii) $2\kappa_r$ specifies the range window frame adjusted to the effective pixel width of the non-zero strip $\Psi_r(y)$ of the range PSM Ψ_r along the y axis, respectively, as illustrated in Figure 1. Such the sliding window projector $\mathcal{P}_{\kappa_a \perp \kappa_r}$ is an easy-to-implement numerical algorithm that simply sets the pixels values to zero outside the support regions $2\kappa_a \subset K_x$ and $2\kappa_r \subset K_y$ around every particular pixel $\hat{B}_{[i](k_x, k_y)}$; $k_x = 1, \dots, K_x$; $k_y = 1, \dots, K_y$ in the rectangular image frame $\hat{\mathbf{b}}_{[n]} = L\{\hat{\mathbf{b}}_{[n]}\}$ separately reconstructed via (2.26) along the corresponding x and y axes, respectively. Last, to enforce prior knowledge on the intrinsic positivity of the SSP we impose, in addition to $\mathcal{P}_{a \perp r}$ and $\mathcal{P}_{\kappa_a \perp \kappa_r}$, the positivity operator (algorithm) \mathcal{P}_+ that has the effect of clipping off all negative values [5]. The defined above orthogonal projecting window $\mathcal{P}_{\kappa_a \perp \kappa_r}$ and positivity operator \mathcal{P}_+ are projectors onto convex sets, i.e. POCS operators [17], thus a composition

$$\mathcal{P} = \mathcal{P}_+ \mathcal{P}_{\kappa_a \perp \kappa_r} \mathcal{P}_{a \perp r} \quad (2.31)$$

is a POCS operator as well. While this definition in the terms of the proposed aggregated projections sounds complicated, the algorithmic meaning of (2.31) is very simple and is easily established in the algorithmic form familiar to the signal processing and RS communities. Acting on a $\hat{\mathbf{b}}_{[n]}$ (that may be not a member of the convex set at a particular iteration n), the \mathcal{P} applied to $\hat{\mathbf{b}}_{[n]}$ produces the member of the convex cone set composed of non-negative elements that is nearest to $\hat{\mathbf{b}}_{[n]}$ in the sense of minimization of the L_2 norm $\|\mathcal{P}\hat{\mathbf{b}}_{[n]} - \hat{\mathbf{b}}_{[n]}\|$ [5, Section 6].

Now, the application of the \mathcal{P} constructed by (2.31) to the iteration process (2.26) yields the desired resulting POCS-regularized fixed-point update rule

$$\hat{\mathbf{b}}_{[n+1]} = \mathcal{P}\{\hat{\mathbf{b}}_{[0]}\} + \mathcal{P}\{\mathbf{T}_{[n]}\hat{\mathbf{b}}_{[n]}\}; \quad n = 0, 1, \dots, \quad (2.32)$$

in which the zero-step iteration $\hat{\mathbf{b}}_{[0]}$ is formed using the conventional (i.e. low-resolution) MSF imaging algorithm (2.30), the aggregated convergence enforcing POCS regularizing operator is constructed by (2.31), and the matrix-form fixed-point iteration operator $\mathbf{T}_{[n]}$ is specified by (2.27).

We address such POCS-regularized DEDR technique (2.32) as the unified DEDR-POCS method. Its general framework is presented in Figure 2. Note that the fixed-point process (2.32) does *not* involve the cumbersome operator inversions (in contrast to the initial DEDR techniques defined by (2.5), (2.22) and, moreover, it is performed separately along the range (y) and azimuth (x) directions making an optimal use of the PSM sparseness properties ($\kappa_a \ll K_x$, $\kappa_r \ll K_y$). These features of the POCS-regularized RSF and RASF algorithms generalized by (2.32) result in the

drastically decreased algorithmic computational complexity (e.g., $(K_x/\kappa_a) \times (K_x/\kappa_a) \sim 10^3$ times at each fixed-point iteration for the typical large-scale SAR image formats [10], [17]).

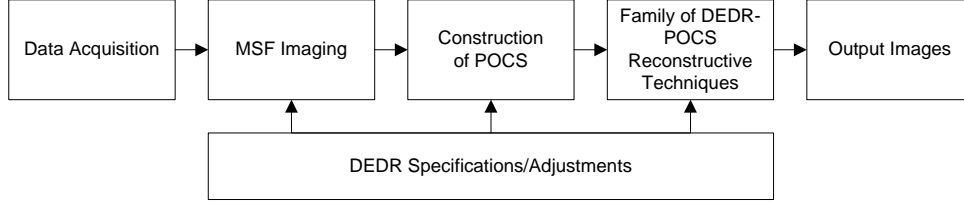


Figure 2.2 General framework of the unified DEDR-POCS method.

2.4 Adaptation of Convex Optimization Techniques for Array Sensor/SAR Imaging

We now perform an extension of the recently proposed high-resolution maximum likelihood (ML) based amplitude phase estimator (APES), i.e. ML-APES method, to the SSP reconstructive problem via its convex optimization-based modification adapted to the imaging of distributed RS scenes. Having analyzed the operational and computational performances of the ML-APES technique, as well as other convex optimization-based ML-related imaging approaches, we establish their inconsistency in the cases of “short” data observations (small number of snapshots) and particularly, in the case of a single look SAR mode with only one realization of the trajectory signal available for further processing. We next have analytically found that to overcome such inconsistency, the adaptive kernel windowing operators should be employed into convex optimization to guarantee the consistent convergent high-resolution imaging procedures.

A. High-Resolution ML-APES Imaging Algorithm.

In the considered low snapshot sample case (e.g., one recorded SAR trajectory data signal), the sample data covariance matrix $\mathbf{Y} = (1/J) \sum_{j=1}^J \mathbf{u}_{(j)} \mathbf{u}_{(j)}^+$ is rank deficient (rank-1 in the single radar snapshot and single look SAR modes, $J = 1$). The convex optimization problem of minimization of the negative likelihood function $-\ln \det\{\mathbf{R}_u\} + \text{tr}\{\mathbf{R}_u^{-1} \mathbf{Y}\}$ with respect to the SSP vector \mathbf{b} subject to the convexity guaranteed non-negativity constraint results in the nonlinear ML-APES estimator [17]

$$\hat{b}_k = \frac{\mathbf{s}_k^+ \mathbf{R}_u^{-1} \mathbf{Y} \mathbf{R}_u^{-1} \mathbf{s}_k}{(\mathbf{s}_k^+ \mathbf{R}_u^{-1} \mathbf{s}_k)^2} ; \quad k = 1, \dots, K. \quad (2.33)$$

In the APES terminology (as well as in the minimum variance distortionless response (MVDR) and other ML-related approaches [6], [8], etc.), \mathbf{s}_k represents the so-called *steering* vector in the k th look direction, which in our notational conventions is essentially the k th column vector of the SFO matrix \mathbf{S} . The numerical implementation of the ML-APES algorithm (2.33) assumes application of an iterative fixed-point technique by building the model-based estimate $\hat{\mathbf{R}}_u = \mathbf{R}_u(\hat{\mathbf{b}}_{[i]})$ of the unknown covariance \mathbf{R}_u from the latest (i th) iterative SSP estimate $\hat{\mathbf{b}}_{[i]}$ with the zero step initialization $\hat{\mathbf{b}}_{[0]} = \hat{\mathbf{b}}_{MSF}$ computed applying the conventional MSF estimator [10].

We have adapted the algorithm (2.33) to the considered single snapshot/single look mode ($J = 1$) substituting \mathbf{Y} by $\mathbf{u}\mathbf{u}^+$, taking into account the properties of the convergent MVDR estimates of the SSP, and making the use of a fixed-point nature of the algorithm (2.33) according to which the ML-APES estimates in the vector form $\hat{\mathbf{b}} = \text{vec}_k\{\hat{\mathbf{b}}_k; k=1, \dots, K\}$ are to be found as a numerical solution to the nonlinear matrix-vector equation

$$\hat{\mathbf{b}}_{\text{ML-APES}} = \hat{\mathbf{b}}^{(1)} = \{\mathbf{F}^{(1)}\mathbf{u}\mathbf{u}^+\mathbf{F}^{(1)+}\}_{\text{diag}} = (\mathbf{F}^{(1)}\mathbf{u}) \odot (\mathbf{F}^{(1)}\mathbf{u})^*, \quad (2.34)$$

where \odot defines the Shur-Hadamard (element wise) vector/matrix product $\mathbf{F}_{\text{APES}} = \mathbf{F}^{(1)} = \hat{\mathbf{D}}\mathbf{S}^+\mathbf{R}_u^{-1}(\hat{\mathbf{b}})$ represents the ML-APES matrix-form solution operator (SO), in which

$$\hat{\mathbf{D}} = \mathbf{D}(\hat{\mathbf{b}}) = \text{diag}(\hat{\mathbf{b}}) \quad \text{and} \quad \mathbf{R}_u^{-1}(\hat{\mathbf{b}}) = (\mathbf{S}\hat{\mathbf{D}}\mathbf{S}^+ + \mathbf{R}_n)^{-1} \quad (2.35)$$

where operator $\{\cdot\}_{\text{diag}}$ returns the vector of a principal diagonal of the embraced matrix. The algorithmic structure of the nonlinear (i.e., solution-dependent) ML-APES estimator (2.34) guarantees positivity but does not guarantee the consistency. Therefore, we next propose to employ the DEDR-VA-based convergence enforcing regularization via performing projections onto convex solution sets (POCS) at each iteration step to guarantee the convergence in the considered real-world deficient-rank operational scenarios.

2.5. Unified DEDR-VA Framework for High-Resolution Array Sensor/SAR Imaging

The proposed unified DEDR-VA regularization framework can be viewed as a problem-oriented formalization of the requirements to the signal/image processing/post-processing codesign aimed at satisfying the desirable properties of the reconstructed RS images, namely: (i) convex optimization-based maximization of spatial resolution balanced with noise suppression, (ii) consistency, (iii) positivity, (iv) continuity and agreement with the data [5], [8]. Within the DEDR-VA framework, all these aspects are formalized via codesign of the convex optimization-based balanced resolution-enhancement-over-noise-suppression SSP estimation techniques unified with the POCS regularization. Thus, the proposed unified DEDR-VA framework puts in a single optimization frame, adaptive GeoSTAR-configured sensor focusing, speckle reduction and dynamic scene image enhancement in the real-world uncertain operational scenarios. We have established that due to the VA nature of the resulting POCS-regularized adaptive enhanced imaging techniques the DEDR-VA-related algorithms are well adapted for parallelized numerical implementation using systolic-based neural network (NN) computational procedures. This paves a way for approaching the task of (near) real time implementation of the DEDR-VA-related algorithms via HW/SW codesign oriented at the Field Programmable Gate Array (FPGA) digital processing.

A. DEDR-VA Approach.

The DEDR-VA-optimal SSP estimate $\hat{\mathbf{b}}$ is to be found as the POCS-regularized solution to the nonlinear equation [17]

$$\hat{\mathbf{b}}_{\text{DEED}} = \mathcal{P}\{\mathbf{F}_{\text{DEED}}\mathbf{u}\mathbf{u}^+\mathbf{F}_{\text{DEED}}^+\}_{\text{diag}} = \mathcal{P}\{\mathbf{D}(\hat{\mathbf{b}}_{\text{DEED}})\}_{\text{diag}}, \quad (2.36)$$

where \mathbf{F}_{DEED} represents the adaptive (i.e., dependent on the SSP estimate $\hat{\mathbf{b}}$) matrix-form DEDR solution operator and \mathcal{P} is the VA-related POCS regularization operator. Two fundamental issues constitute the benchmarks of the modified DEDR-VA estimator (3.4) that distinguish it from both the previously developed kernel SSP reconstruction algorithm [7], the DEDR method [6] and the detailed above new ML-APES technique (2.34). First, the strategy for determining the DEED solution operator \mathbf{F}_{DEED} in (2.36) is reformulated in the minimum risk (MR)-inspired worst case statistical performance (WCSP) convex optimization setting, i.e., as the MR-WCSP constrained DEDR convex optimization problem to provide robustness of the SSP vector estimates against possible model uncertainties. The second issue relates to the VA inspired problem-oriented codesign of the POCS regularization operator \mathcal{P} in (2.36). Such codesign (which we report in the next Section) is aimed at satisfying intrinsic and desirable properties of the solution such as positivity, consistency, model agreement (e.g., adaptive despeckling with edge preservation), and convergence [15], [17]. The solution to the MR-WCSP conditioned optimization problem (Eq.(2.8) and Eq. (2.11)) derived in the previous Section yields the DEDR-optimal solution operator (SO)

$$\mathbf{F}_{\text{DEED}} = \mathbf{F}^{(2)} = \mathbf{K}\mathbf{S}^+\mathbf{R}_{\Sigma}^{-1} \quad (2.37)$$

where $\mathbf{K} = (\mathbf{S}^+\mathbf{R}_{\Sigma}^{-1}\mathbf{S} + \alpha\mathbf{A}^{-1})^{-1}$ defines the so-called reconstruction operator (with the regularization parameter α and stabilizer \mathbf{A}), and \mathbf{R}_{Σ}^{-1} is the inverse of the diagonal loaded noise correlation matrix $\mathbf{R}_{\Sigma} = N_{\Sigma}\mathbf{I}$; $N_{\Sigma} = N_0 + \beta$ with the composite noise power density $N_{\Sigma} = N_0 + \beta$, the additive observation noise power density N_0 augmented by the loading factor $\beta = \gamma\eta/\alpha \geq 0$ adjusted to the regularization parameter α , the Loewner ordering factor $\gamma > 0$ of the SFO \mathbf{S} and the uncertainty bound η imposed by the MR-WCSP conditional maximization (see [8] for details). For these operational specifications, the robust DEDR-related SO becomes

$$\mathbf{F}_{\text{DEED}} = \mathbf{F}^{(3)} = (\mathbf{\Psi} + \alpha N_{\Sigma}\mathbf{A}^{-1})^{-1}\mathbf{S}^+ = \mathbf{K}\mathbf{S}^+, \quad (2.38)$$

i.e., a composition of the MSF operator \mathbf{S}^+ and the self adjoint reconstruction operator $\mathbf{K} = (\mathbf{\Psi} + \alpha N_{\Sigma}\mathbf{A}^{-1})^{-1}$ recognized to be a regularized inverse of the discrete-form ambiguity function (AF) matrix operator

$$\mathbf{\Psi} = \mathbf{S}^+\mathbf{S}. \quad (2.39)$$

Note that other feasible adjustments of the processing-level degrees of freedom $\{\alpha, N_{\Sigma}, \mathbf{A}\}$ summarized in previous chapter and in [8] specify the family of relevant POCS-regularized DEDR-related (DEDR-POCS) techniques (3.4) represented in the general form as follows

$$\hat{\mathbf{b}}^{(p)} = \mathcal{P}\{\mathbf{D}(\hat{\mathbf{b}}^{(p)})\}_{\text{diag}} = \mathcal{P}\{\mathbf{F}^{(p)}\mathbf{u}\mathbf{u}^+\mathbf{F}^{(p)+}\}_{\text{diag}} = \mathcal{P}\{\mathbf{K}^{(p)}\mathbf{Q}\mathbf{K}^{(p)+}\}_{\text{diag}}; \quad p = 2, 3, \dots, P \quad (2.40)$$

where $\mathbf{Q} = \mathbf{S}^+\mathbf{u}\mathbf{u}^+\mathbf{S}$ defines the measurement statistics matrix independent on the solution $\hat{\mathbf{b}}$, and different reconstruction operators $\{\mathbf{K}^{(p)}; p = 1, \dots, P\}$ specified for different feasible assignments

to the processing degrees of freedom $\{\alpha, N_\Sigma, \mathbf{A}\}$ define the corresponding DEDR-POCS estimators (2.40) with the relevant SO's $\{\mathbf{F}^{(p)} = \mathbf{K}^{(p)}\mathbf{S}^+; p = 1, \dots, P\}$.

B. Convergence Guaranties.

Following the VA regularization formalism [5], [13], the POCS regularization operator \mathcal{P} in (3.4) could be constructed as a composition of projectors \mathcal{P}_n onto convex sets \mathbb{C}_n ; $n = 1, \dots, N$ with not empty intersection, in which case the (3.8) is guaranteed to converge to a point in the intersection of the sets $\{\mathbb{C}_n\}$ regardless of the initialization $\hat{\mathbf{b}}_{[0]}$ that is a direct sequence of the fundamental theorem of POCS. Also, any operator that acts in the same convex set, e.g., kernel-type windowing operator (WO) can be incorporated into such composite regularization operator \mathcal{P} [5]. Our technical task is to make the use of the presented POCS regularization paradigm (6) employing the practical GeoSTAR-configured array sensor/SAR-motivated considerations.

C. VA-based POCS Regularization.

To attain the superresolution performances in the resulting SSP estimates (3.4), we propose the VA inspired approach [13], [14] to specify the POCS regularization that yields the required composite VA-level regularizing operator

$$\mathcal{P} = \mathcal{P}_2 \mathcal{P}_1. \quad (2.41)$$

The \mathcal{P}_2 in (2.41) represents the convergence guaranteed projector onto the nonnegative convex solution set $\mathcal{P}_2 = \mathcal{P}_+$ defined as the positivity operator that has the effect of clipping off all the negative values [17], and \mathcal{P}_1 is the anisotropic WO that we adjust to the metrics inducing matrix \mathbf{M} , i.e.,

$$\mathcal{P}_1 = \mathbf{M} = m^{(0)}\mathbf{I} + m^{(1)}\nabla^2 \quad (2.42)$$

that specifies the desired metrics structure in the K -D vector solution/image space $\mathbb{B}_{(K)} \ni \mathbf{b}$ given by [14]

$$\|\mathbf{b}\|_{\mathbb{B}_{(K)}}^2 = [\mathbf{b}, \mathbf{M}\mathbf{b}] = m^{(0)} \sum_{k_x, k_y=1}^{K_x, K_y} \left(b(k_x, k_y) \right)^2 + m^{(1)} \sum_{k_x, k_y=1}^{K_x, K_y} \left(b(k_x, k_y) - \frac{1}{4} \left(b(k_x-1, k_y) + b(k_x+1, k_y) + b(k_x, k_y-1) + b(k_x, k_y+1) \right) \right)^2. \quad (2.43)$$

The second sum on the right hand side of (2.43) is recognized to be a 4-nearest-neighbors difference-form approximation of the Laplacian operator ∇^2 , while $m^{(0)}$ and $m^{(1)}$ represent the nonnegative real-valued scalars that control the balance between two metrics measures. In the VA equibalanced case, $m^{(0)} = m^{(1)} = 1$, the same importance is assigned to the both metrics measures, in which case (2.42) specifies the discrete-form approximation to the Sobolev metrics inducing operator \mathcal{M} in the relevant continuous-form solution space $\mathbb{B}(R) \ni \mathbf{b}(\mathbf{r})$ [17]. Incorporation of such \mathcal{M} as the WO into the general-form DEDR-VA-optimal technique

(2.40), i.e., specifying in (2.41) $\mathcal{P}_1 = \mathcal{M}$, results in the consistency guaranteed anisotropic kernel-type windowing because it controls not only the SSP (image) discrepancy measure but also its gradient flow over the scene in the Sobolev-type image/solution space $\mathbb{B}(R) \ni b(\mathbf{r})$. We have established that due to the gradient-dependent anisotropy, such regularizing VA-based processing is aimed at edge preservation in the scene regions with high gradient contrast while performing anisotropic smooth windowing over the homogeneous image zones corrupted by speckle.

D. DEDR-VA-optimal Dynamic SSP Reconstruction.

The transformation of (3.4) into the contractive progressive iterative mapping format yields

$$\hat{\mathbf{b}}_{[i+1]} = \hat{\mathbf{b}}_{[i]} + \tau \mathcal{P}_+ \{ \mathbf{M} \mathbf{q} - \mathbf{M} \Phi_{\mathbf{D}[i]} \hat{\mathbf{b}}_{[i]} \} ; \quad i = 0, 1, 2, \dots \quad (2.44)$$

initialized by the conventional MSF image

$$\hat{\mathbf{b}}_{[0]} = \mathbf{q} = \{ \mathbf{Q} \}_{\text{diag}} = \{ \mathbf{S}^+ \mathbf{Y} \mathbf{S} \}_{\text{diag}}, \quad (2.45)$$

with the relaxation parameter τ and the solution-depended point spread function (PSF) matrix operator

$$\Phi_{\mathbf{D}} = \Phi_{\mathbf{D}}(\hat{\mathbf{b}}) = (\Psi + N_{\Sigma} \mathbf{D}^{-1}(\hat{\mathbf{b}})) \odot (\Psi + N_{\Sigma} \mathbf{D}^{-1}(\hat{\mathbf{b}}))^*, \quad (2.46)$$

constructed from the diagonal loaded AF matrix (10) via the Shur-Hadamard product \odot .

Associating in (3.12) the iterations $i + 1 \rightarrow t + \Delta t; i \rightarrow t; \tau \rightarrow \Delta t$, with “evolution time”, ($\Delta t \rightarrow dt; t + \Delta t \rightarrow t + dt$) and considering the continuous 2-D rectangular scene frame $R \ni \mathbf{r} = (x, y)$ with the corresponding initial MSF scene image $q(\mathbf{r}) = \hat{b}(\mathbf{r}; 0)$ and the “evolutionary” enhanced SSP estimate $\hat{b}(\mathbf{r}; t)$, respectively, we proceed from (15) to the equivalent asymptotic dynamic scheme

$$\frac{\partial \hat{b}(\mathbf{r}; t)}{\partial t} = \mathcal{P}_+ \{ \mathcal{M} \{ (q(\mathbf{r})) \} \} - \mathcal{M} \left\{ \int_R \Phi_{\hat{b}}(\mathbf{r}, \mathbf{r}'; t) \hat{b}(\mathbf{r}', t) d^2 \mathbf{r}' \right\}, \quad (2.47)$$

where $\Phi_{\hat{b}}(\mathbf{r}, \mathbf{r}'; t)$ represents the kernel PSF in evolution time t corresponding to the continuous-form dynamic generalization of the PSF matrix $\Phi_{\mathbf{D}[i]}$ in (2.46), and \mathcal{M} defines the metrics inducing operator.

Three practically inspired dynamic versions of (2.47) relate to three feasible assignments to such metrics inducing operator. These are as follows.

(1) $\mathcal{M}=\mathcal{I}$ specifies the conventional Lebesgue metrics [14], in which case the evolution process (2.47) does not involve control of the image gradient flow over the scene.

(2) $\mathcal{M}=\nabla_{\mathbf{r}}^2$, i.e. the Laplacian with respect to the space variable $\mathbf{r}=(x,y)$ specifies the Dirichlet variational metrics inducing operator [6], in which case, the right-hand side of (2.47) depends on the discrepancy between the corresponding Laplacian edge maps producing anisotropic gain. For short evaluation time intervals, such anisotropic gain term induces significant changes dominantly around the regions of sharp contrast resulting in edge enhancement [14], [17].

(3) $\mathcal{M}=m^{(0)}\mathcal{I}+m^{(1)}\nabla_{\mathbf{r}}^2$ combines the Lebesgue and the Dirichlet metrics, in which case the (2.47) is transformed into the VA dynamic process defined by the partial differential equation (PDE)

$$\frac{\partial \hat{b}(\mathbf{r};t)}{\partial t} = \mathcal{P}_+ \{c_0[q(\mathbf{r}) - \int_R \Phi(\mathbf{r}, \mathbf{r}';t) \hat{b}(\mathbf{r}';t) d\mathbf{r}'] + c_1 \nabla_{\mathbf{r}}^2 \{q(\mathbf{r})\} - c_2 \nabla_{\mathbf{r}}^2 \{ \int_R \Phi(\mathbf{r}, \mathbf{r}';t) \hat{b}(\mathbf{r}';t) d\mathbf{r}' \} \}. \quad (2.48)$$

For the purpose of generality, instead of two balancing coefficients $m^{(0)}$ and $m^{(1)}$ we incorporated into the PDE (2.48) three “conduction” factors c_0 , c_1 and c_2 , respectively, viewed as VA-level user-controlled degrees of freedom to compete between smoothing and edge enhancement.

E. Family of Numerical DEDR-VA Techniques for SSP Reconstruction.

The discrete-form approximation of the PDE (3.16) in “iterative time” $\{i = 0, 1, 2, \dots\}$ yields the iterative numerical procedure

$$\mathbf{b}_{[i+1]} = \hat{\mathbf{b}}_{[i]} + \mathcal{P}_+ \{c_0(\mathbf{q} - \Phi_{\mathbf{d}[i]} \hat{\mathbf{b}}_{[i]}) + c_1 \nabla^2 \{\mathbf{q}\} - c_2 \nabla^2 \{\Phi_{\mathbf{d}[i]} \hat{\mathbf{b}}_{[i]}\} \}; \quad i = 0, 1, 2, \dots, \quad (2.49)$$

with the same MSF initialization $\hat{\mathbf{b}}_{[0]} = \mathbf{q}$, where we have attributed the relaxation parameter τ to the corresponding conduction factors, for simplicity. Different feasible assignments to these degrees of freedom specify a family of different DEDR-VA-related reconstruction techniques. Here beneath we exemplify the following ones.

(i) The simplest case relates to the specifications: $c_0 = 0$, $c_1 = 0$, $c_2 = \text{const} = -c$, $c > 0$, and $\Phi(\mathbf{r}, \mathbf{r}';t) = \delta(\mathbf{r} - \mathbf{r}')$ with excluded projector \mathcal{P}_+ . In this case, the PDE (2.48) reduces to the *isotropic diffusion* (so-called heat diffusion) equation $\partial \hat{b}(\mathbf{r};t)/\partial t = c \nabla_{\mathbf{r}}^2 \hat{b}(\mathbf{r};t)$. We reject the isotropic diffusion because of its resolution deteriorating nature.

(ii) The previous assignments but with the anisotropic factor, $-c_2 = c(\mathbf{r}; t) \geq 0$ specified as a monotonically decreasing function of the magnitude of the image gradient distribution, i.e., a function $c(\mathbf{r}; |\nabla_{\mathbf{r}} \cdot \hat{b}(\mathbf{r};t)|) \geq 0$, transforms the (2.48) into the celebrated Perona-Malik *anisotropic diffusion* (AD) method, $\partial \hat{b}(\mathbf{r};t)/\partial t = c(\mathbf{r}; |\nabla_{\mathbf{r}} \hat{b}(\mathbf{r};t)|) \nabla_{\mathbf{r}}^2 \hat{b}(\mathbf{r};t)$ that sharpens the edge map on the low-resolution MSF images.

(iii) For the Lebesgue metrics specification $c_0 = 1$ with $c_1 = c_2 = 0$, the PDE (3.16) involves only the first term at the right hand side resulting in the locally selective *robust adaptive spatial filtering* (RASf) approach investigated in details in our previous studies [10]).

(iv) The alternative assignments $c_0 = 0$ with $c_1 = c_2 = 1$ combine the isotropic diffusion with the anisotropic gain controlled by the Laplacian edge map. This approach is addressed as a *selective information fusion* method that manifests almost the same performances as the DEDR-related RASf method developed in our previous Section 2.2.

(v) The VA-based approach that we address here as the unified DEDR-VA method involves all three terms at the right hand side of the PDE (3.16) with the equibalanced $c_0 = c_1 = c_2 = \text{const}$ (one for simplicity), hence, it combines the isotropic diffusion (specified by the second term at the right hand side of (2.49)) with the composite anisotropic gain dependent both on the evolution of the synthesized SSP frame and its Laplacian edge map. This produces a balanced compromise between the anisotropic reconstruction-fusion and locally selective image despeckling with adaptive edge preservation.

All exemplified above algorithms with different feasible specifications of the user-controllable degrees of freedom compose a family of the DEDR-VA-related iterative techniques for SSP reconstruction/post processing. The general-form DEDR-VA framework is presented in Figure 2.2 in the previous Section. Note that as in the case of the previously addressed iterative fixed-point DEDR-POCS regularization approach (Section 2.4), the progressive contractive mapping procedure (2.49) does *not* involve the cumbersome operator inversions (in contrast to the initial DEDR techniques defined by (2.5), (2.22) and, moreover, it is performed separately along the range (y) and azimuth (x) directions making an optimal use of the PSF sparseness properties. These features of the POCS-regularized DEDR-VA-related algorithms generalized by (2.49) result in the drastically decreased algorithmic computational complexity (e.g, $\sim 10^3$ times for the typical large-scale SAR image formats, that we verified in the simulations reported in Subsection 3.7).

2.6. DEDR-VA Unified With the KB Paradigm for Collaborative Multimode Data Fusion

The methodological and algorithmic design problems related to high-resolution multimode sensor imaging and knowledge-based (KB) collaborative RS-SN data processing were reconsidered in the framework of the developed unified DEDR-VA approach aggregated with the POCS regularization properly adapted to the distributed collaborative RS-SN processing. Following the developed unified DEDR-VA framework, we have performed the maximum entropy (ME) information theoretic formalization of a priori information regarding the four cross-polarization observation modes (HH, VV, HV and VH) of the scattered wavefield SSPs and incorporated it in a new unified multipolarization multimode imaging/fusion inverse problem for the SSP reconstruction and the related remote sensing signatures (RSS) fusion algorithm design. Figure 2.3 presents the block-diagram that summarizes the addressed intelligent DEDR-VA approach for the KB multimode sensor data fusion. The aggregated KB-DEDR-VA data fusion methodology enables the observer to form the atlas of the desired super-high resolution RSS maps extracted from the collaboratively processed multimode RS imagery,

and also to perform their problem-oriented analysis in an intelligent KB fashion to solve the relevant search and discovery problems.

A. Fusion Problem Formalism

We have employed the DEDR-VA framework as a methodology for the KB multimode data/method fusion that unifies the family of the developed robust nonparametric high-resolution RS imaging techniques. Such unified formalism allows involving into the DEDR-VA approach different convex regularization and neural computing paradigms [3], [20] that enables the user to modify the existing high-resolution imaging techniques via incorporation of additional controllable KB-level “degrees of freedom” as well as design a variety of efficient aggregated/fused data/image DEDR-VA-related collaborative post-processing methods.

Consider the set of equations

$$\mathbf{q}^{(p)} = \mathbf{\Phi}^{(p)} \mathbf{b} + \mathbf{v}^{(p)} ; p = 1, \dots, P , \quad (2.50)$$

which model the data $\{\mathbf{q}^{(p)}\}$ acquired by P RS imaging systems that employ the image formation methods from the DEDR-VA-related family specified in the previous Section. In (2.50), \mathbf{b} represents the original K -D image vector, $\{\mathbf{\Phi}^{(p)}\}$ are the RS image formation operators referred to as the point spread function (PSF) operators of the corresponding DEDR-VA-related imaging systems (or methods) where we have omitted the sub index \mathbf{b} for notational simplicity , and $\{\mathbf{v}^{(p)}\}$ represent the system noise with further assumption that these are uncorrelated from system to system.

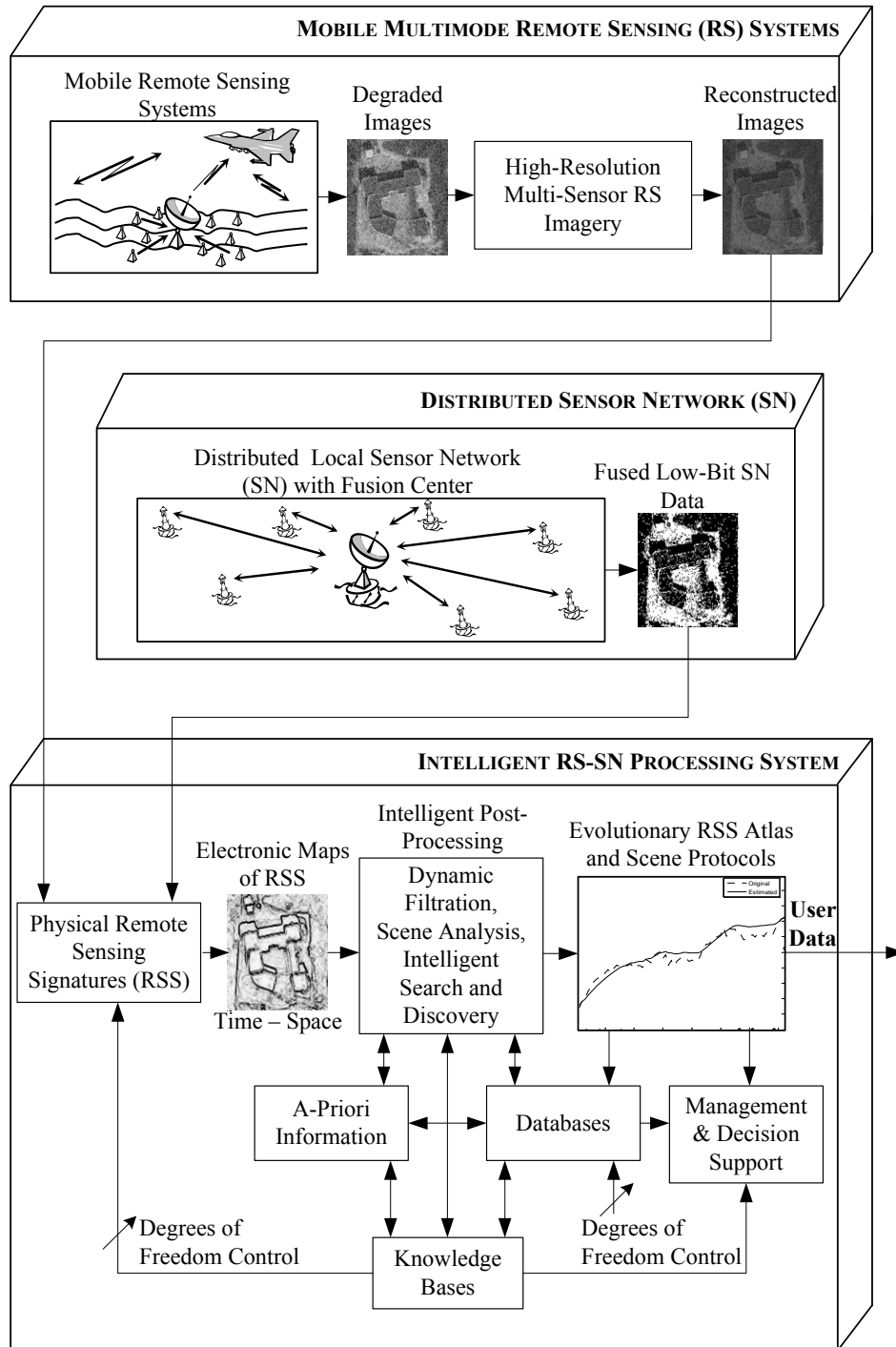


Fig. 2.3. Block-diagram of the proposed KB intelligent DEDR-VA approach for the KB multimode sensor data fusion.

Define the discrepancies between the actually formed images $\{\mathbf{q}^{(p)}\}$ and the true original image \mathbf{b} as the l_2 squared norms, $J_p(\mathbf{b}) = \|\mathbf{q}^{(p)} - \Phi^{(p)} \mathbf{b}\|^2$; $p = 1, \dots, P$. Let's next adopt the VA inspired proposition [10] that the smoothness properties of the desired image are controlled by the second order Tikhonov stabilizer, $J_{P+1}(\mathbf{b}) = \mathbf{b}^T \mathcal{P}_1 \mathbf{b}$, where $\mathcal{P}_1 = \mathbf{M} = m^{(0)} \mathbf{I} + m^{(1)} \nabla^2$ is the VA-based metrics inducing (regularizing) operator specified previously by (9). We further define the image entropy as

$$H(\mathbf{b}) = -\sum_{k=1}^K b_k \ln b_k. \quad (2.51)$$

Then the contrivance for aggregating the imaging systems (methods), when solving the fusion problem, is the formation of the augmented objective (or augmented ME cost) function

$$E(\mathbf{b}|\boldsymbol{\lambda}) = -H(\mathbf{b}) + (1/2) \sum_{p=1}^P \lambda_p J_p(\mathbf{b}) + (1/2) \lambda_{P+1} J_{P+1}(\mathbf{b}), \quad (2.52)$$

and seeking for a fused restored image $\hat{\mathbf{b}}$ that minimizes the objective function (19), in which $\boldsymbol{\lambda} = (\lambda_1 \dots \lambda_P, \lambda_{P+1})^T$ represents the vector of weight parameters, commonly referred to as the fusion *regularization* parameters [10]. Hence, in the frame of the aggregate regularization approach to decentralized fusion [3], [20], the restored image is to be found as a solution of the convex optimization problem

$$\hat{\mathbf{b}} = \underset{\mathbf{b}}{\operatorname{argmin}} E(\mathbf{b}|\boldsymbol{\lambda}) \quad (2.53)$$

for the assigned values of the regularization parameters $\boldsymbol{\lambda}$. A proper selection of $\boldsymbol{\lambda}$ is next associated with parametrical optimization [20] of such the aggregated fusion process.

B. NN-Adapted Fusion Algorithm

The Hopfield-type dynamical NN, which we propose to employ to solve the fusion problem (20) is an NN based on an expansion of the maximum entropy neural network (MENN) proposed in our previous study [3]. We consider the multistate Hopfield-type (i.e., dynamic) NN [10], [11] with the K -D state vector \mathbf{x} and K -D output vector $\mathbf{z} = \operatorname{sgn}(\mathbf{W}\mathbf{x} + \boldsymbol{\theta})$, where \mathbf{W} and $\boldsymbol{\theta}$ are the matrix of synaptic weights and the vector of the corresponding bias inputs of the NN, respectively. The energy function of such the NN is expressed as [20]

$$E(\mathbf{x}) = E(\mathbf{x}; \mathbf{W}, \boldsymbol{\theta}) = - (1/2) \mathbf{x}^T \mathbf{W} \mathbf{x} - \boldsymbol{\theta}^T \mathbf{x} = - (1/2) \sum_{k=1}^K \sum_{m=1}^K W_{km} x_k x_m - \sum_{k=1}^K \theta_k x_k. \quad (2.54)$$

The proposed here idea for solving the RS system/method fusion problem (20) using the dynamical NN is based on extension of the following cognitive processing proposition invoked from [20]. If the energy function of the NN represents the function of a mathematical minimization problem over a parameter space, then the state of the NN would represent the parameters and the stationary point of the network would represent a local minimum of the original minimization problem. Hence, utilizing the concept of the dynamical net, we may translate our image reconstruction/enhancement problem with RS system/method fusion to the correspondent problem of minimization of the energy function (2.54) of the related MENN. Therefore, we define the parameters of the MENN in such a fashion that to aggregate the corresponding parameters of the RS systems/methods to be fused, i.e.,

$$W_{ki} = -\sum_{p=1}^P [\hat{\lambda}_p \sum_{j=1}^K \Phi_{jk}^{(p)} \Phi_{ji}^{(p)}] - \lambda_{P+1} M_{ki}, \quad (2.55)$$

$$\theta_k = -\ln x_k + \sum_{p=1}^P [\hat{\lambda}_p \sum_{j=1}^K \Phi_{jk}^{(p)} y_j^{(p)}] \quad (2.56)$$

$\forall k, i = 1, \dots, K$, where we redefined $\{x_k = b_k\}$ and ignored the constant term E_{const} in $E(\mathbf{x})$ that does not involve the state vector \mathbf{x} . The regularization parameters $\{\hat{\lambda}_p\}$ in (2.55), (2.56) should be specified by an observer or pre-estimated invoking, for example, the VA inspired resolution-over-noise-suppression balancing method developed in [17, Sect. 3]. In the latter case, the result of the enhancement-fusion becomes a balanced tradeoff between the gained spatial resolution and noise suppression in the resulting fused enhanced image with the POCS-based regularizing stabilizer.

Next, we propose to find a minimum of the energy function (2.54) as follows. The states of the network should be updated as $\mathbf{x}'' = \mathbf{x}' + \Delta \mathbf{x}$ using the properly designed update rule $\mathfrak{R}(\mathbf{z})$ for computing a change $\Delta \mathbf{x}$ of the state vector \mathbf{x} , where the superscripts ' and '' correspond to the state values before and after network state updating (at each iteration), respectively. To simplify the design of such the state update rule, we assume that all $x_k \gg 1$, which enables us to approximate the change of the energy function after state updating as [20]

$$\Delta E \approx -(\sum_{i=1}^K W_{ki} x'_i + \theta'_k - 1) \Delta x_k - (1/2) W_{kk} (\Delta x_k)^2. \quad (2.57)$$

We now redefine the outputs of neurons as $\{z_k = \text{sgn}(\sum_{i=1}^K W_{ki} x'_i + \theta'_k - 1) \mid \forall k = 1, \dots, K\}$. Using these definitions, and adopting the equilibrated fusion regularization weights, $\lambda_p = 1 \mid \forall p = 1, \dots, P$, we next, design the desired state update rule $\mathfrak{R}(\mathbf{z})$ which guarantees nonpositive values of the energy changes ΔE at each updating step as follows,

$$\Delta x_k = \mathfrak{R}(z_k) = \begin{cases} 0 & \text{if } z_k = 0, \\ \Delta & \text{if } z_k > 0, \\ -\Delta & \text{if } z_k < 0, \end{cases} \quad (2.58)$$

where Δ is the pre-assigned step-size parameter. If no changes of $\Delta E(\Delta \mathbf{x})$ are examined while approaching to the stationary point of the network, then the step-size parameter Δ may be decreased, which enables one to monitor the updating process as it progresses setting a compromise between the desired accuracy of finding the NN's stationary point and computational complexity [3]. To satisfy the condition $x_k \gg 1$ some constant x^0 may be added to the gray level of every original image pixel and after restoration the same constant should be deducted from the gray level of every restored image pixel, hence, the selection of a particular value of x^0 is not critical [3]. Consequently, the restored image $\hat{\mathbf{b}}$ corresponds to the state vector $\hat{\mathbf{x}}$ of the NN in its stationary point as, $\hat{\mathbf{b}} = \hat{\mathbf{x}} - x^0 \mathbf{1}$, where $\mathbf{1} = (1 \ 1 \ \dots \ 1)^T \in R^K$ is the $K \times 1$ vector composed with units. The computational structures of such the MENN and its single neuron are presented in Figures 2.4 and 2.5, respectively.

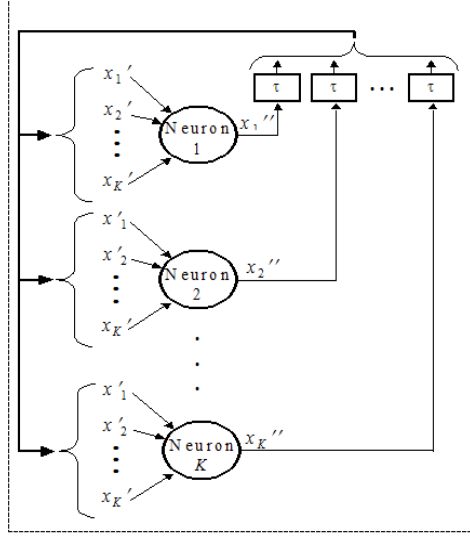


Figure 2.4. Computational structure of the multi-state MENN for sensor/image fusion.

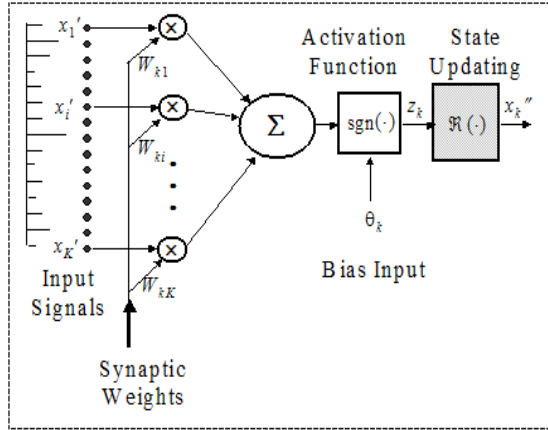


Figure 2.5. Computational structure of a single neuron in the MENN.

C. Generalization for NN-Adapted Multimode Data Fusion

The data/image fusion and post-processing (e.g., search and discovery) tasks that could be next performed employing the KB-DEDR-VA framework are mathematically formalized in the terms of the VA-extended DEDR convex optimization problem

$$\hat{\mathbf{v}} = \arg \min_{\mathbf{v}} E(\mathbf{v}|\boldsymbol{\lambda}) \quad (2.59)$$

of minimization of the aggregated ME-DEDR-VA objective (cost) function

$$E(\mathbf{v}|\boldsymbol{\lambda}) = -H(\mathbf{v}) + (1/2) \sum_{p=1}^P \lambda_p J_p(\mathbf{v}) + (1/2) \lambda_{P+1} J_{P+1}(\mathbf{v}) \quad (2.60)$$

with respect to some desired K -D non-negative *feature/RSS* vector \mathbf{v} for the assigned (or adjusted) values of $P+1$ regularization parameters $\{\lambda_p\}$ that compose a vector $\boldsymbol{\lambda}$ of the controllable KB-level “degrees of freedom”, where $H(\mathbf{v}) = - \sum_{k=1}^K v_k \ln v_k$ is the generalization of

the image entropy defined by (2.51), $\{J_p(\mathbf{v})\}$ ($p = 1, \dots, P$) compose a set of particular DEDR-VA objective (cost) functions incorporated into the post-processing optimization/fusion (e.g., ML-APES, AD, DEDR-related RSF, RASF, AD, DEDR-VA, etc.), and $J_{p+1}(\mathbf{v}) = \mathbf{v}^T \mathcal{P}_1 \mathbf{v}$ represents the VA regularizing stabilizer specified as a direct generalization of $J_{p+1}(\mathbf{b})$ in (2.52) for the considered feature/RSS vector \mathbf{v} . In every particular KB fusion method, the proper selection of $\{\lambda_p\}$ is associated with the parametric-level adjustment of the KB-DEDR-VA optimization procedure (2.50). The multimode data fusion model is defined by the set of equations, $\hat{\mathbf{b}}^{(p)} = \mathbf{Z}^{(p)} \mathbf{v} + \mathbf{v}^{(p)}$ for P system modes/methods to be aggregated/fused, i.e. $p = 1, \dots, P$, where $\mathbf{Z}^{(p)}$ represent the RSS formation or related feature extraction operator for the p th mode/method to be fused, and vectors $\mathbf{v}^{(p)}$ represent composite uncompensated mode noises (usually with unknown statistics) in the actually acquired data/image mode vectors, $\hat{\mathbf{b}}^{(p)}$, respectively. Different KB-DEDR-VA fusion methods incorporate different definitions for corresponding employed objective (cost) functions $\{J_p(\mathbf{v})\}$. The unified KB-DEDR-VA paradigm is able to incorporate into the aggregated optimization problem (2.50), (2.60) different DEDR-VA-related techniques specified by (2.22), (2.49) and also other statistical methods, among them are: the rough conventional matched spatial filtering (MSF) approach [14]; the descriptive maximum entropy (ME) technique [6]; the robust spatial filtering (RSF) and the robust adaptive spatial filtering (RASF) methods (Section 2.3), the fused Bayesian-DEDR regularization (FBR) method [6], the AD approach [14], the ML-APES method (Section 2.2), the unified DEDR-VA-optimal dynamic technique (2.49), etc. All such methods involve particular specifications of the corresponding $\{J_p(\mathbf{v})\}$ and $\{\mathbf{Z}^{(p)}\}$ into the KB-DEDR-VA optimization procedure (2.59), (2.60). Note that due to the non-linearity of the objective function (2.60) the solution of the parametrically controlled fusion-optimization problem (2.59) will require extremely complex (NP-complex [8]) algorithms and result in the technically intractable computational schemes if solve these problems employing the standard direct minimization techniques [4]. For this reason, at this research stage, we employed the POCS-regularized DEDR-VA-related techniques (2.49) implemented using the lattice-adapted neural network (NN) computing architecture presented in Figures 2.4, 2.5 for solving the unified ME-DEDR-VA fusion problem (2.59), (2.60) via KB adjustments of the lattice nodes and the related lattice arcs that enable such the NN to perform the fusion task in a near-real time computational fashion exemplified for the image fusion applications via the MENN algorithm developed in the previous Subsection 2.6.B.

2.7. Virtual Remote Sensing Laboratory Simulations SW and Examples of Simulation Protocols

A. Summary of the Elaborated Integrated VRSL Software for Simulations of the Developed Enhanced Techniques for Extended Scene Imaging/Fusion

Having developed a manifold of the DEDR-POCS-VA-related computational techniques, the next research goal of this project is to computationally implement, verify, and demonstrate the capabilities of the collaborative RS signal and image processing for RSS extraction, KB intelligent scene analysis, multiple target detection and scene zones localization via development of the sophisticated end-user-oriented software that we refer to as “Virtual remote sensing laboratory” (VRSL). The purpose of the VRSL software is to implement computationally all considered DEDR-related methods (MSF, CLS, WCLS, ME, RSF, RASF, FBR, etc) and to

perform the RS image formation/ reconstruction/enhancement tasks with or without method and/or sensor system fusion. The VRSL software (elaborated in the MATLAB V.7 computational environment) aggregates interactive computational tools offering to the user different options of acquisition and processing of any image in the JPEG, TIFF, BMP and PNG formats as test input images, application of different system-level effects of image degradation with a particular simulated RS system and simulation of random noising effects with different noise intensities and distributions. Next, various RS image enhancement/fusion/reconstruction/post-processing tasks can be simulated in an interactive mode applying different DEDR-related algorithms to the degraded noised images, and the quantitative performance enhancement characteristics attained in every particular simulated scenario can then be computed and archived. The user has options to display on the screen all simulated processed scene images and RSS along with the corresponding protocols of analysis of different performance quality metrics (see the illustrative RS image reconstruction examples displayed in the user interface presented in Fig. 2.6).

The goal of the simulation study is to verify, evaluate, and demonstrate the capabilities of the DEDR-VA-based signal and image processing with the problem-oriented extraction of different RSS, and their KB intelligent analysis, multiple target detection and scene-zones localization via elaboration of the end-user-oriented VRSL software using the MATLAB programming tools. The RS imaging algorithms were modeled for a variety of admissible sensor array architectures that range from the conventional circular and cross-type equidistant arrays to the prominent GeoSTAR Y-shaped quasi-synthetic array geometries admitting different number of sensors and different sensor interspacing. The elaborated VRSL interactive simulation tools offer the options for modeling the processes of data acquisition, formation of the RS images/maps employing different DEDR-VA-related techniques summarized by (2.22), (2.49), and application of different KB multimode data fusion procedures specified by (2.59), (2.60).

B. Specifications of the Simulation Experiments and Quality Metrics

We simulated fractional side-looking imaging SAR operating in uncertain scenario [7]. We adopted a triangular shape of such imaging SAR range ambiguity function (AF) and a Gaussian shape of the corresponding azimuth AF [1], [10]. Simulation results are presented in the next Subsection. To qualify the effectiveness of different simulated methods, we employ

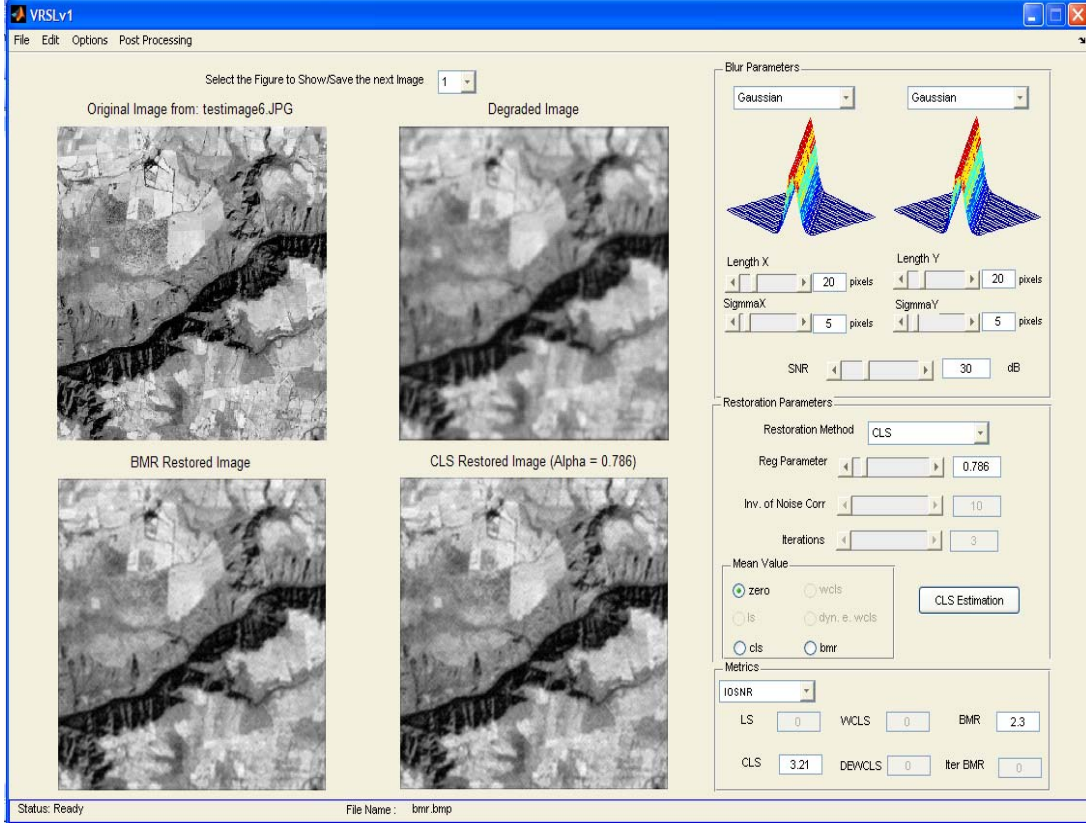


Fig.2.6. Graphical user interface of the elaborated VRSL.

two quality metrics for performance assessment of the reconstructive methods developed in this paper. The traditional quantitative quality metric [5] for RS images is the so-called improvement in the output signal-to-noise ratio (IOSNR), which provides the metrics for performance gains attained with different employed estimators in dB scale

$$IOSNR(\text{dB}) = 10 \cdot \log_{10} \left(\frac{\sum_{k=1}^K \left(\left\| \hat{b}_k^{(MSF)} - b_k \right\|^2 \right)}{\sum_{k=1}^K \left(\left\| \hat{b}_k^{(p)} - b_k \right\|^2 \right)} \right), p = 1, \dots, P, \quad (2.62)$$

where b_k represents the value of the k -th element (pixel) of the original SSP, $\hat{b}_k^{(MSF)}$ represents the value of the k -th element (pixel) of the rough SSP estimate formed applying the conventional low-resolution matched spatial filtering (MSF) technique (12), and $\hat{b}_k^{(p)}$ represents the value of the k -th element (pixel) of the enhanced SSP estimate formed applying the p th enhanced imaging method ($p = 1, \dots, P$), correspondingly. Recall that we consider and compare here five (i.e., $P = 5$) RS image enhancement/reconstruction methods, in which case $p = 1$ corresponds to the Lee's local statistics-based adaptive despeckling technique [2], $p = 2$ corresponds to the Perona-Malik AD method [13], $p = 3$ corresponds to the DEDR-related locally selective RASF technique [10], $p = 4$ corresponds to the APES method [17], and $p = 5$ corresponds to the fused RSF and DEDR-VA methods, respectively. The fusion was performed using the MENN algorithm detailed in Subsection 2.6.B.

The second employed quality metric is the l_1 total mean absolute error (MAE) metric [5]

$$MAE = \frac{1}{K} \sum_{k=1}^K \left| \hat{b}_k^{(p)} - b_k \right|, \quad p = 1, \dots, P. \quad (2.63)$$

The quality metrics specified by (2.62) and (2.63) allow us to quantify the performance of the developed DEDR-VA-related high-resolution reconstructive methods (enumerated above by $p = 1, \dots, P = 5$) and, also, the NN fusion quality.

C. Examples of Simulations Protocols and Concluding Remarks

Simulation results are presented in Figures 2.7 and 2.8. The figure captions specify each particular simulated image formation/enhancement method ($p = 1, \dots, P = 5$). Aggregation of the locally selective robust spatial filtering (RSF) technique [10] with the DEDR-VA-optimal algorithm (2.49) were considered in the simulations of the NN-based fused enhancement mode. Next, Figure 2.9 reports the convergence rates for three most prominent VA-related enhanced RS imaging approaches: the APES [6], the DEDR and the developed NN-adapted fused RSF and DEDR-VA methods, respectively. The fusion was performed using the MENN algorithm detailed in Subsection 2.6.B.

The quantitative measures of the image enhancement/reconstruction performance gains achieved with the particular employed DEDR-RSF method [10], the APES algorithm [17] and DEDR-VA-NN technique (16) for different SNRs evaluated with two different quality metrics (26), (27) are reported in Table 1 and Table 2, respectively. The numerical simulations verify that the MENN implemented DEDR-VA method outperforms the most prominent existing competing high-resolution RS imaging techniques [4]–[14] (both without fusion and in the fused version) in the attainable resolution enhancement as well as in the convergence rates.

The reported simulations reveal that with the NN-adapted POCS-regularized DEDR-VA techniques, the overall RS imaging performances are improved if compared with those obtained using separately the most prominent in the literature despeckling, anisotropic diffusion or locally selective RS image reconstruction methods that do not unify the DEDR, the VA and the NN-adapted method fusion considerations. Therefore, the developed unified DEDR-VA-NN framework puts in a single optimization frame, radar/SAR image formation, speckle reduction and adaptive dynamic scene image enhancement/fusion performed in the rapidly convergent NN-adapted computational fashion.

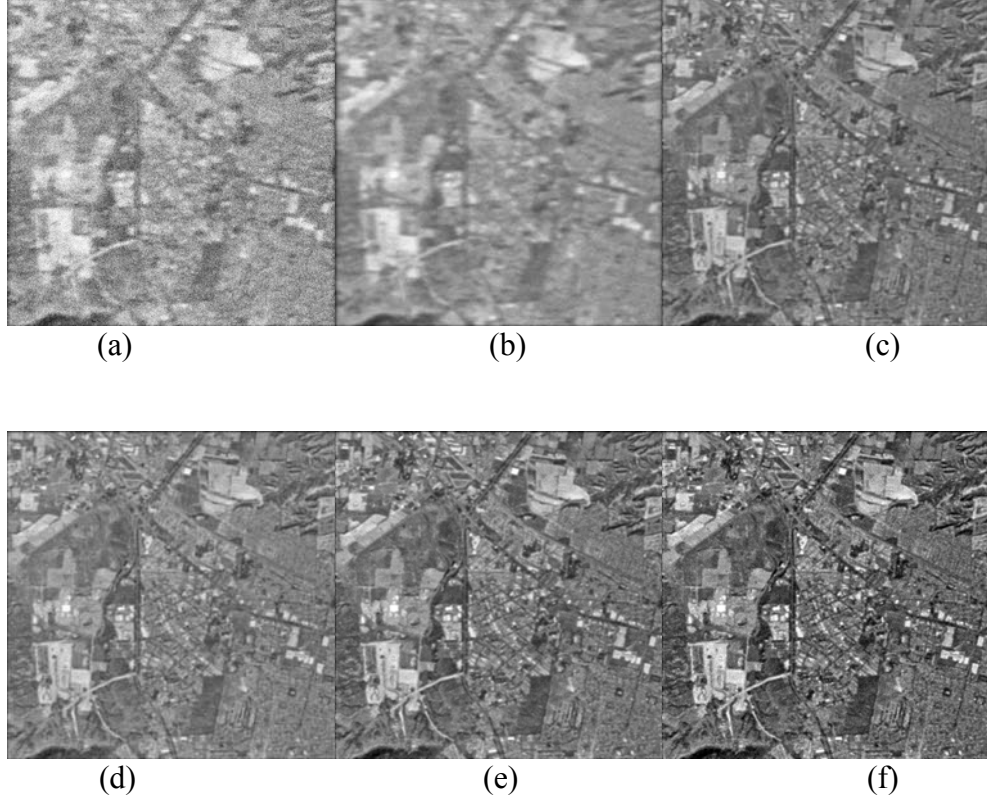


Figure 2.7. Simulation results for the *first* uncertain fractional SAR imaging scenario for the large-scale (1024-by-1024 pixels) test scene and 5% random Gaussian perturbations in the SFO, $\langle \|\mathbf{\Delta}\|^2 \rangle / \|\mathbf{S}\|^2 = 5 \cdot 10^{-2}$: (a) degraded scene image formed applying the MSF method corrupted by composite noise (fractional SAR parameters: range PSF width (at $\frac{1}{2}$ from the peak value) $\kappa_r = 10$ pixels, azimuth PSF width (at $\frac{1}{2}$ from the peak value) $\kappa_a = 30$ pixels, composite SNR $\mu_{\text{SAR}} = 10$ dB); (b) adaptively despeckled MSF image [10]; (c) image reconstructed applying the locally selective RSF method [16] after 30 performed iterations; (d) image reconstructed with the APES method [17] after 30 performed iterations; (e) image reconstructed applying the POCS-regularized RASF technique [17] after 7 performed iterations (f) image reconstructed applying the NN-fused RSF [20] and the DEDR-VA technique (2.49) after 7 performed iterations.

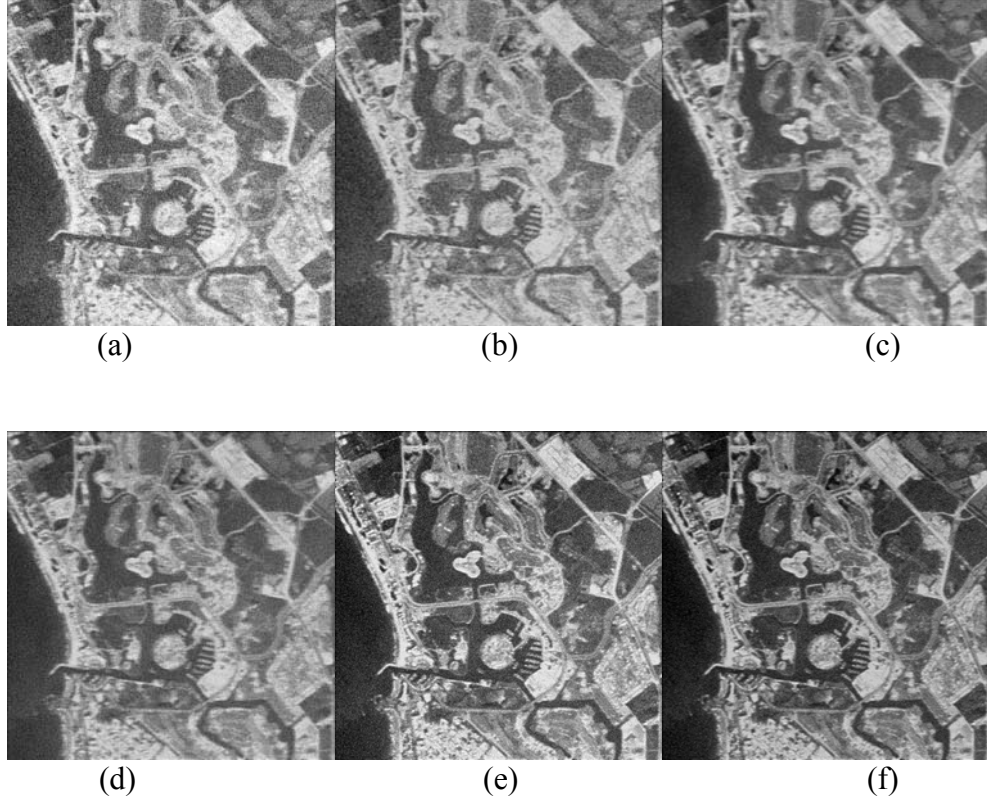


Figure 2.8. Simulation results for the *second* uncertain fractional SAR imaging scenario for the large-scale (1024-by-1024 pixels) test scene and 5% random Gaussian perturbations in the SFO, $\langle \|\mathbf{\Delta}\|^2 \rangle / \|\mathbf{S}\|^2 = 5 \cdot 10^{-2}$: (a) degraded scene image formed applying the MSF method corrupted by composite noise (fractional SAR parameters: range PSF width (at $\frac{1}{2}$ from the peak value) $\kappa_r = 7$ pixels, azimuth PSF width (at $\frac{1}{2}$ from the peak value) $\kappa_a = 20$ pixels, composite SNR $\mu_{\text{SAR}} = 15$ dB); (b) adaptively despeckled MSF image [10]; (c) image enhanced using the AD technique [4] after 30 performed iterations; (d) image reconstructed applying the locally selective RSF method [16] after 30 performed iterations; (e) image reconstructed applying the POCS-regularized RASF technique [16] after 7 performed iterations (f) image reconstructed applying the NN-fused RSF [20] and the DEDR-VA technique (2.49) after 7 performed iterations.

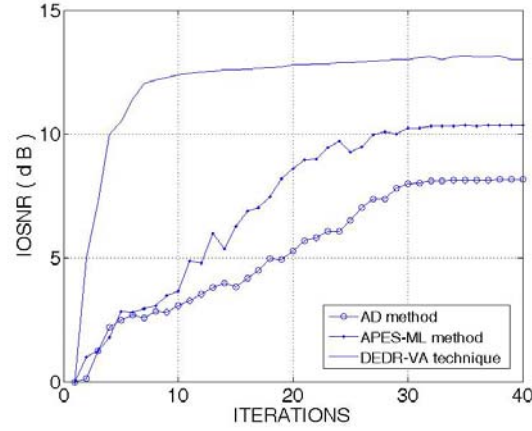


Figure 2.9. Convergence rates evaluated via the IOSNR metric (26) versus the number of iterations evaluated for three most prominent high-resolution iterative enhanced RS imaging methods: DEDR-RASF method [10], APES – ML-optimal amplitude phase estimation method [17], and the developed unified DEDR-VA-NN technique (2.49).

2.8. Summary of Part II

We have reported the results of developing the descriptive experiment design regularization (DEDR) method for high-resolution imaging and estimation of spatial remote sensing signatures (RSS) of remotely sensed (RS) scenes as required for the purposes of high-resolution RS imaging, search, discovery, discrimination, mapping and problem-oriented analysis of the diverse RS data as it is stipulated in the SOW of the subrecipient agreement (S/A) No. C09-00485. Approaching these goals, we have performed the following research and development tasks.

- First, we have established that to alleviate the RS imaging problem ill-posedness and reduce the overall computational load of the large-scale image enhancement/reconstruction tasks at the algorithmic processing level, some special form of descriptive experiment design projection-type numerical regularization must be employed. This stage was developed and addressed as the unified DEDR method, and the efficient fixed-point numerical iterative technique that incorporates the proper construction of the relevant orthogonally factorized regularizing projector onto convex sets (POCS) in the solution domain was designed and specified for the particular employed RS sensor system, namely, for the side-looking fractional imaging SAR.
- We have examined how such SAR-adapted POCS-regularized fixed-point iterative technique can be executed concurrently over the orthogonal range-azimuth coordinates with the optimal use of the sparseness properties of the overall SAR system point spread function characteristics.
- Next, the DEDR framework has been combined with the dynamic variational analysis (VA) approach for perceptually enhanced and considerably speeded up reconstruction of the RS imagery particularly adapted for multimode array sensor and fractional SAR imaging systems operating in the uncertain RS environment. The addressed DEDR-VA

framework was next put into the unified neural network (NN)-adapted computational frame addressed as a unified DEDR-VA-NN method.

- Connections have been drawn between different types of enhanced RS imaging approaches, and it has been established that the convex optimization-based unified DEDR-VA-NN framework provides an indispensable toolbox for high resolution RS imaging system design offering to observer a possibility to control the order, the type and the amount of the employed two-level regularization (at the DEDR level and at the VA level, correspondingly). Algorithmically, this task is performed via construction of the proper POCS operators that unify the desirable image metrics properties in the convex image/solution sets with the employed radar/SAR motivated data processing considerations.
- The addressed family of the efficient contractive progressive mapping iterative DEDR-VA-related techniques has been particularly adapted for the NN computing mode with sensor systems/method fusion. The efficiency of the proposed fusion-based enhancement of the fractional SAR imagery has been verified for the two method fusion example in the reported simulation experiments.
- Our algorithmic developments and the simulations revealed that with the NN-adapted POCS-regularized DEDR-VA techniques, the overall RS imaging performances are improved if compared with those obtained using separately the most prominent in the literature despeckling, anisotropic diffusion or locally selective RS image reconstruction methods that do not unify the DEDR, the VA and the NN-adapted method fusion considerations. Therefore, the developed unified DEDR-VA-NN framework puts in a single optimization frame, radar/SAR image formation, speckle reduction and adaptive dynamic scene image enhancement/fusion performed in the rapidly convergent NN-adapted computational fashion.

Also, following the SOW, we have elaborated the end-user-oriented “Virtual Remote Sensing Laboratory” (VRSL) software to accomplish computationally different DEDR-specified numerical optimization and processing tasks. The VRSL provides the necessary tools for computer-aided simulation and analysis of different DEDR-related RS image formation/enhancement/reconstruction/fusion/post-processing techniques developed using the unified KB DEDR methodology. The reported simulation results are illustrative of the VRSL usefulness and capabilities in computer simulations of different RS imaging tasks performed with the artificial and real-world RS imagery.

PART III

SIGNAL PROCESSING, DATA ARCHIVING AND SIMULATIONS SOFTWARE FOR HIGH-RESOLUTION MULTIPLE TARGET IMAGING WITH GeoSTAR- CONFIGURED SENSOR ARRAY SYSTEM THAT EMPLOYS DEDR-ROBUST IMAGE FORMATION TECHNIQUES

3.1. Background: General Technical Information on Data Acquisition Formats

The sensor array system is composed of 24 sensors, configured in a Y-shaped GeoSTAR multi-sensor imaging radar geometry (GeoSTAR MIR-Y), with 3 arms referenced beneath as A, B and C, with 8 equally spaced sensors in each arm. A system layout is exemplified in Fig.3.1 (see the details of the system configuration in section 3.2).

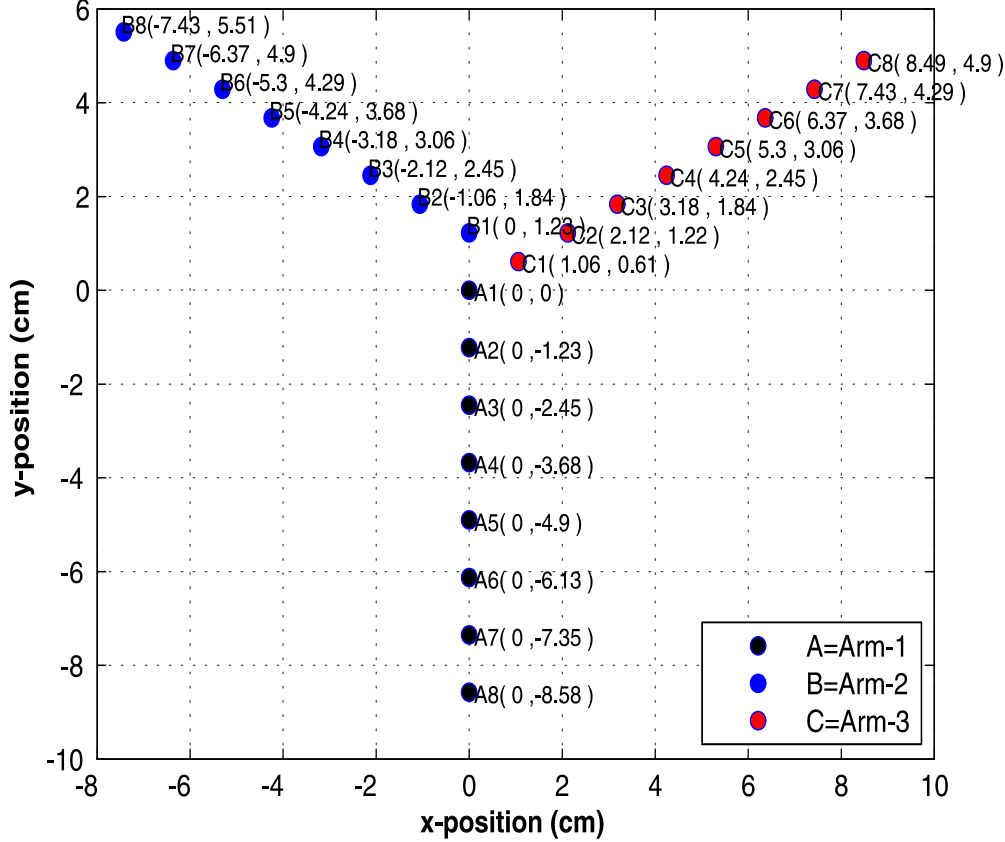


Figure 3.1. GeoSTAR-configured sensor array layout, where d is the inter-element spacing (mm), in this case $d = 12.25$ mm.

The sensors provide two measurements for each data snapshot, In-phase and Quadrature components of the sensor output signals as summarize in Table 3.1.

Table 3.1. Measurement Data Format.

$$\begin{array}{c}
 \left[\begin{array}{cccc} (I_{11VVr}, Q_{11VVr}) & (I_{11VHr}, Q_{11VHr}) & (I_{11HVR}, Q_{11HVR}) & (I_{11HHR}, Q_{11HHR}) \\ \vdots & \vdots & \vdots & \vdots \\ (I_{JMNVr}, Q_{JMNVr}) & (I_{JMVHr}, Q_{JMVHr}) & (I_{JMHVR}, Q_{JMHVR}) & (I_{JMHR}, Q_{JMHR}) \end{array} \right] \\
 \vdots \\
 \left[\begin{array}{cccc} (I_{11VVr}, Q_{11VVr}) & (I_{11VHr}, Q_{11VHr}) & (I_{11HVR}, Q_{11HVR}) & (I_{11HHR}, Q_{11HHR}) \\ \vdots & \vdots & \vdots & \vdots \\ (I_{JMNVr}, Q_{JMNVr}) & (I_{JMVHr}, Q_{JMVHr}) & (I_{JMHVR}, Q_{JMHVR}) & (I_{JMHR}, Q_{JMHR}) \end{array} \right]
 \end{array}
 \quad \begin{array}{l} R_r = 165 \\ \vdots \\ r = 1 \end{array}$$

$$\left\{ \mathbf{u}_j = \left[\begin{array}{cccc} (I_{11VVr}, Q_{11VVr}) & (I_{11VHr}, Q_{11VHr}) & (I_{11HVR}, Q_{11HVR}) & (I_{11HHR}, Q_{11HHR}) \\ \vdots & \vdots & \vdots & \vdots \\ (I_{JMNVr}, Q_{JMNVr}) & (I_{JMVHr}, Q_{JMVHr}) & (I_{JMHVR}, Q_{JMHVR}) & (I_{JMHR}, Q_{JMHR}) \end{array} \right]; r = 1, \dots, R_r = 165 \right\} \quad (3.1)$$

Here, the first subindex $j = 1, \dots, J$ indicates the number of the snapshot corresponding to the j th transmitted pulse $j = 1, \dots, J$; the second subindex $m = 1, \dots, M$ corresponds to the m th sensor, $m = 1, \dots, M = 24$; the third and fourth subindexes correspond to four cross polarization modes VV, VH, HV, and HH, respectively; the last subindex $r = 1, \dots, R_r$ corresponds to the range gate, $r = 1, \dots, R_r = 165$; i.e.:

- I_{jmVVr} = in-phase j th snapshot for the r th range gate at the output of the m th sensor at VV cross polarization;
- Q_{jmVVr} = quadrature j th snapshot for the r th range gate at the output of the m th sensor at VV cross polarization;
- $R_r = 165$ – Total number of range gates numbered by $r = 1, \dots, R_r = 165$;
- J – Number of transmitted pulses for each range gate with the pulse repetition time (PRT) numbered by $j = 1, \dots, J$;
- M – Total number of Sensors, numbered by $m = 1, \dots, M = 24$;

Thus, for each range gate (RG) $\{r = 1, \dots, R_r = 165\}$, we have to record and store the following Amount of Accumulated Data (AAD):

$$AAD = (J) \times (AD) = 4800$$

where $AD = (M) \times (\# \text{Cross Polarization Modes} \times 2) = (24 \times 4 \times 2) = 192$

and $J = 25$ (recall that J defines a number of transmitted pulses for each range gate).

The data are next recorded in a binary file format. Data binary files have the following basic characteristics:

- Binary files require less memory space than text files.
- Binary files are not subject to loss errors as all bits are stored in a register.
- Binary files cannot be read or modified with a text editor, and the reading and writing functions are faster and more efficient than in the case of text files.

Binary files contain collections of identical structures (records). Thus, to recover a data binary file, we specify the format used to compose the file and the size of the data type employed.

Hence, in the adopted binary file format each saved (recorded) data fragment occupies a memory space equal to the size of the data type employed.

We adopt the short integer data type, which size is 2 bytes (we use this data type in all simulations reported in the next section). Each binary file generated in the PC requires the following amount of memory:

$$\begin{aligned}\text{Binary Data File Size} &= (\text{Data Type Size}) \times (AAD) = (2 \text{ bytes})(4800) \\ &= 9600 \text{ bytes for each } RG \quad \{r = 1, \dots, R_r\}.\end{aligned}$$

Here beneath, in Table 3.2 we clarify the employed data acquisition format.

Table 3.2. Recommended data acquisition format for the frequencies band modes ($f_{0(1)} = 24.5GHz$ and $f_{0(2)} = 34.5GHz$)

PRT (j)	SENSORS (m)	CROSS POLARIZATION MODE ($f_{0(1)} = 24.5GHz$ AND $f_{0(2)} = 34.5GHz$)											
		RANGE GATE ($r=1$)								RANGE GATE ($r=2$)			
		VV (1)		VH (2)		HH (4)		HH (4)		VV (1)		VH (2)	
		I_{jmVVr}	Q_{jmVVr}	I_{jmVHr}	Q_{jmVHr}	I_{jmHHr}	Q_{jmHHr}	I_{jmHHr}	Q_{jmHHr}	I_{jmVVR_r}	Q_{jmVVR_r}	I_{jmVHR_r}	Q_{jmVHR_r}
1	1	I_{11VV1}	Q_{11VV1}	I_{11VH1}	Q_{11VH1}	I_{11HH1}	Q_{11HH1}	I_{11HH1}	Q_{11HH1}	I_{11VVR_r}	Q_{11VVR_r}	I_{11VHR_r}	Q_{11VHR_r}
	2	I_{12VV1}	Q_{12VV1}	I_{12VH1}	Q_{12VH1}	I_{12HH1}	Q_{12HH1}	I_{12HH1}	Q_{12HH1}	I_{12VVR_r}	Q_{12VVR_r}	I_{12VHR_r}	Q_{12VHR_r}
	\vdots	\vdots	\vdots	\vdots	\vdots	\vdots	\vdots	\vdots	\vdots	\vdots	\vdots	\vdots	\vdots
	\vdots	\vdots	\vdots	\vdots	\vdots	\vdots	\vdots	\vdots	\vdots	\vdots	\vdots	\vdots	\vdots
	$M = 24$	$I_{1M\bar{V}V1}$	$Q_{1M\bar{V}V1}$	$I_{1M\bar{V}H1}$	$Q_{1M\bar{V}H1}$	$I_{1M\bar{H}H1}$	$Q_{1M\bar{H}H1}$	$I_{1M\bar{H}H1}$	$Q_{1M\bar{H}H1}$	$I_{1M\bar{V}VR_r}$	$Q_{1M\bar{V}VR_r}$	$I_{1M\bar{V}HR_r}$	$Q_{1M\bar{V}HR_r}$
\vdots	\vdots	\vdots	\vdots	\vdots	\vdots	\vdots	\vdots	\vdots	\vdots	\vdots	\vdots	\vdots	\vdots
\vdots	\vdots	\vdots	\vdots	\vdots	\vdots	\vdots	\vdots	\vdots	\vdots	\vdots	\vdots	\vdots	\vdots
\vdots	\vdots	\vdots	\vdots	\vdots	\vdots	\vdots	\vdots	\vdots	\vdots	\vdots	\vdots	\vdots	\vdots
$J \geq 25$	1	I_{J1VV1}	Q_{J1VV1}	I_{J1VH1}	Q_{J1VH1}	I_{J1HH1}	Q_{J1HH1}	I_{J1HH1}	Q_{J1HH1}	I_{J1VVR_r}	Q_{J1VVR_r}	I_{J1VHR_r}	Q_{J1VHR_r}
	2	I_{J2VV1}	Q_{J2VV1}	I_{J2VH1}	Q_{J2VH1}	I_{J2HH1}	Q_{J2HH1}	I_{J2HH1}	Q_{J2HH1}	I_{J2VVR_r}	Q_{J2VVR_r}	I_{J2VHR_r}	Q_{J2VHR_r}
	\vdots	\vdots	\vdots	\vdots	\vdots	\vdots	\vdots	\vdots	\vdots	\vdots	\vdots	\vdots	\vdots
	\vdots	\vdots	\vdots	\vdots	\vdots	\vdots	\vdots	\vdots	\vdots	\vdots	\vdots	\vdots	\vdots
	$M = 24$	$I_{JM\bar{V}V1}$	$Q_{JM\bar{V}V1}$	$I_{JM\bar{V}H1}$	$Q_{JM\bar{V}H1}$	$I_{JM\bar{H}H1}$	$Q_{JM\bar{H}H1}$	$I_{JM\bar{H}H1}$	$Q_{JM\bar{H}H1}$	$I_{JM\bar{V}VR_r}$	$Q_{JM\bar{V}VR_r}$	$I_{JM\bar{V}HR_r}$	$Q_{JM\bar{V}HR_r}$

Therefore, the total number of generated binary files is equal to the number of the used *RGs* ($R_r = 165$) and each file of the stored data requires approximately 9604 bytes. The file format specified in Table 3.2 and the structure of the transmitted data frame of Table 4.3 (see below) is used to generate the binary files containing all the data from each *RG* (range gate). The structure of the generated files is shown in Figure 3.2.

Table 3.3. Structure of Transmitted Data Frame (using 165 pairs of delimiters).

Start Flag (8-bits)	DATA	End Flag (8-bits)		Start Flag (8-bits)	DATA	End Flag (8-bits)
	$r=1$ $AAD=(J) \times (AD)$...		$R_r=165$ $AAD=(J) \times (AD)$	

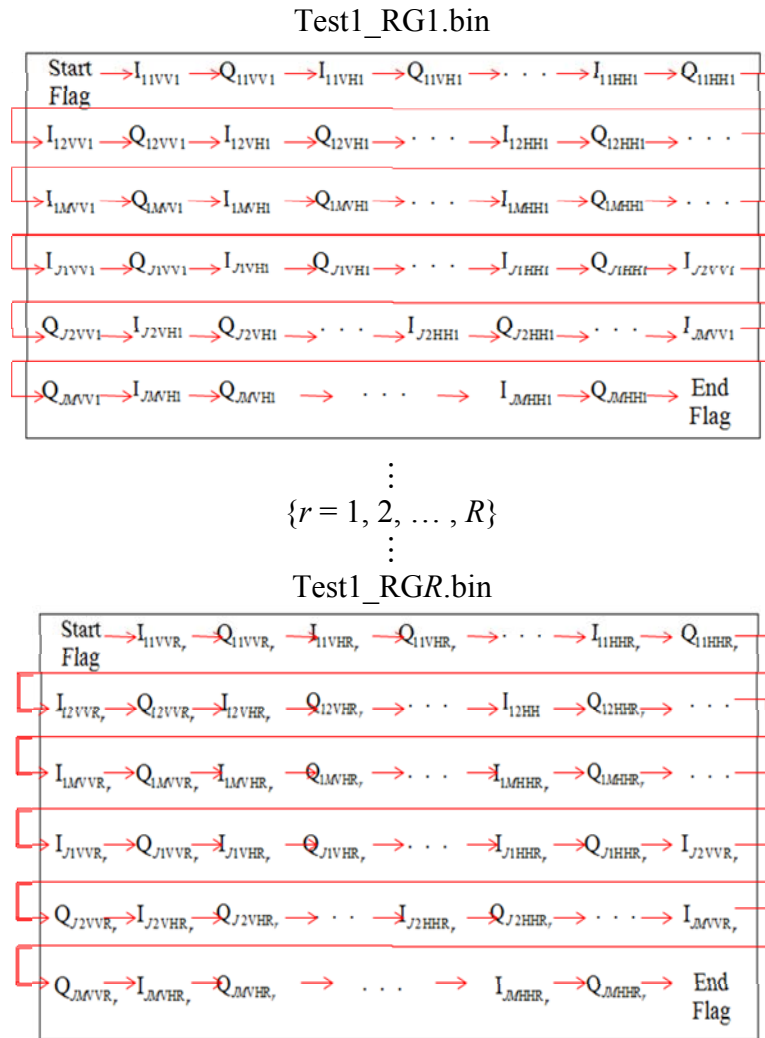


Figure 3.2. Binary File Structure (StartFlag = $11110001_2 = 241_{10}$;
EndFlag = $11111111_2 = 255_{10}$).

In the captions to Figure 3.2, we specified the structure of the StartFlag byte as

$$\text{StartFlag} = 11110001_2 = 241_{10}.$$

Also, we specified the structure of the EndFlag byte as

$$\text{EndFlag} = 11111111_2 = 255_{10}.$$

We next compose the binary file as a continuous data stream strictly following the order specified in Figure 3.2. Therefore, blank spaces or line breaks (enters) between each written or recorded data are avoided. Otherwise, the file size would be unnecessarily increased and would require more computational time for file generation. Thus, the Total Binary File Size is as follows:

$$\begin{aligned} \text{Total Binary Data File Size} &= \text{Binary Data File Size} + \text{Length of StartFlag} \\ &\quad + \text{Length of EndFlag} \\ &= 9600 + 4 \\ &= 9604 \text{ bytes for each } RG. \end{aligned}$$

Each generated file corresponds to its RG number $\{r = 1, \dots, R_r = 165\}$ that ensures all these files be identifiable to each other. Thus, each generated binary file owns a unique name that allows a user to recognize different RG s in a particular test experiment. For this reason we name the generated binary data files using the syntax specified in Table 3.4.

Table 3.4. Binary File syntax.

BINARY FILE NAME SYNTAX	DESCRIPTION
Test1_RG1.bin	Data Binary File for the 1st RG
Test1_RG2.bin	Data Binary File for the 2nd RG
Test1_RG3.bin	Data Binary File for the 3rd RG
:	:
Test1_RGR.bin	Data Binary File for the last R th RG
Test2_RG1.bin	Data Binary File for the 1st RG
Test2_RG2.bin	Data Binary File for the 2nd RG
Test2_RG3.bin	Data Binary File for the 3rd RG
:	:
Test2_RGR.bin	Data Binary File for the last R th RG
:	:

So far, it is important to emphasize the following formatting conventions employed in the test simulations of the elaborated signal processing (SP) software (SW).

1. To recover uniquely information contained in a binary file, the size of the employed data type is pre-specified. We adopt a short integer data type of 2 bytes size. Following this formatting conventions, each binary file generated in the PC requires approximately 9600 bytes for each of 165 RG s (in our test simulations experiment).

2. The total number of generated binary files is equal to the number of the RG s ($R = 165$ in our simulations experiment). Using the format specified in Table 3.2 and following the structure of the transmitted data frame of Table 3.3, we generated binary files containing all the data from each particular RG (Range Gate) $\{r = 1, \dots, R_r = 165\}$ of the structure exemplified in Figure 3.2.

3. The binary data file is composed of a continuous data stream strictly following the order specified in Figure 3.2. Therefore, blank spaces or line breaks (enters) between each written or recorded data are definitely avoided.

4. Finally, each generated file corresponds to its particular RG number $\{r = 1, 2, \dots, R_r = 165\}$. Because all these files must be identifiable to each other, each generated binary file owns a unique name that allows a user to recognize different RG s in a particular test experiment. For this reason we name the generated binary data files using the syntax specified in Table 3.4.

3.2 Feasible Geometries of GeoSTAR-Configured Sensor Array

Considering the inter-element spacing(s) proposed by the TAMU HW Design Team $\rightarrow d = 4 \text{ mm}$, $d = 8.5 \text{ mm}$, $d = 12.25 \text{ mm}$ for two carrier frequencies $f_0 = 24.5 \text{ GHz}$ and $f_0 = 35 \text{ GHz}$, we have performed the HW-SW co-design of system geometry for a series of feasible options. These are exemplified in the following figures.

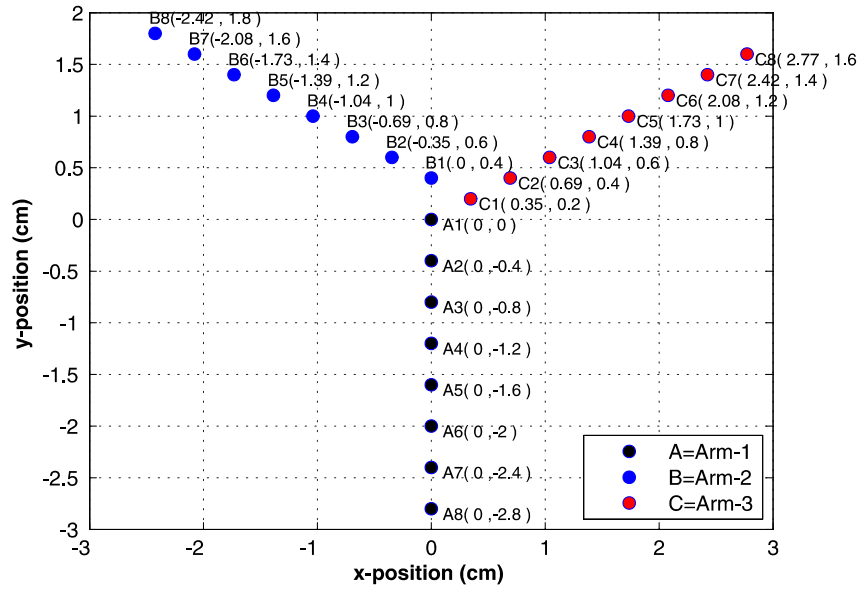


Figure 3.3. GeoSTAR-configured sensor array layout for the inter-element spacing $d = 4 \text{ mm}$.

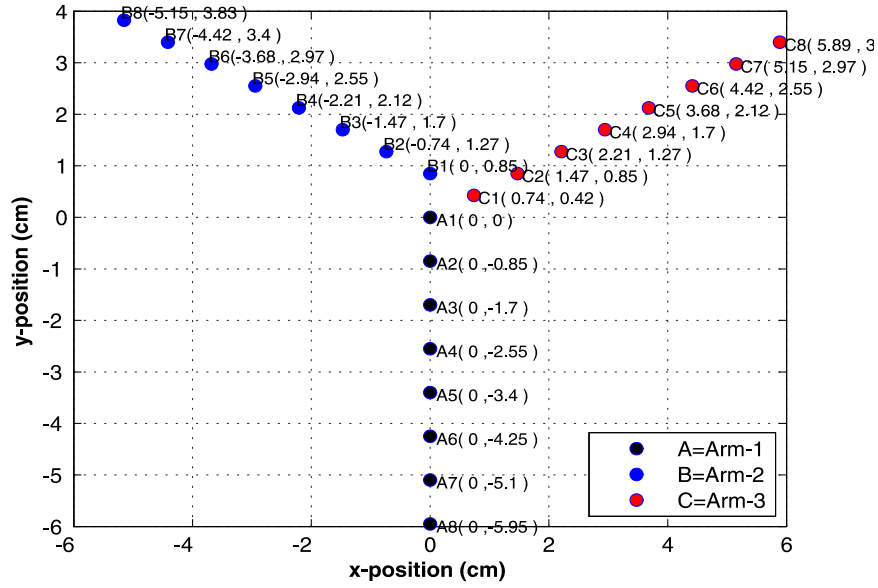


Figure 3.4. GeoSTAR-configured sensor array layout for the inter-element spacing $d = 8.5$ mm.

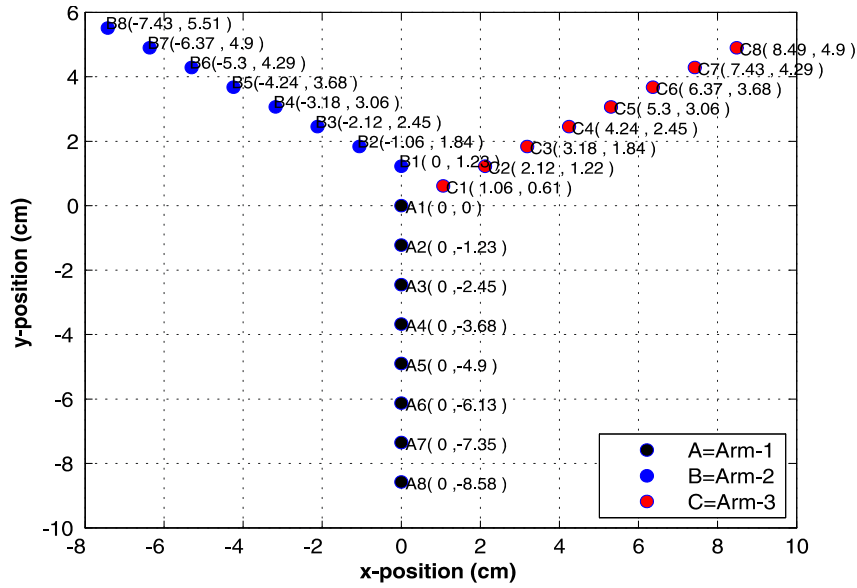


Figure 3.5. GeoSTAR-configured sensor array layout for the inter-element spacing $d = 12.25$ mm.

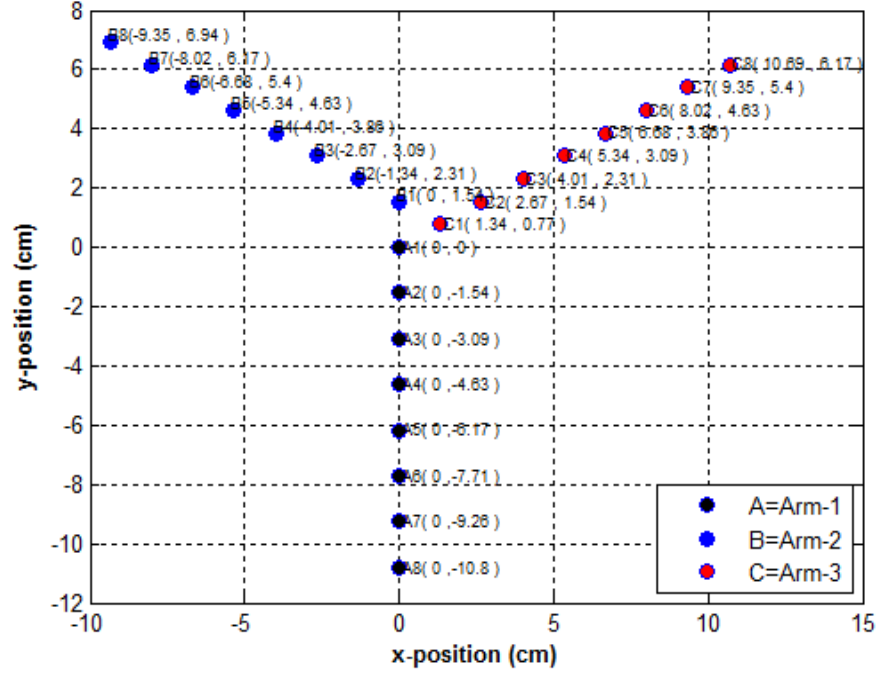


Figure 3.6. GeoSTAR-configured sensor array layout. Recommended inter-element spacing $d \approx 1.8\lambda_{0(2)} = 15.429$ mm.

Table 3.5. Relationship between the arm-related sensor numerations (A_{1-8} ; B_{1-8} ; C_{1-8}) and the m th sensor number ($m = 1, \dots, 24$).

ARM-1	ARM-2	ARM-3
$A_1 = m_1$	$B_1 = m_9$	$C_1 = m_{17}$
$A_2 = m_2$	$B_2 = m_{10}$	$C_2 = m_{18}$
$A_3 = m_3$	$B_3 = m_{11}$	$C_3 = m_{19}$
$A_4 = m_4$	$B_4 = m_{12}$	$C_4 = m_{20}$
$A_5 = m_5$	$B_5 = m_{13}$	$C_5 = m_{21}$
$A_6 = m_6$	$B_6 = m_{14}$	$C_6 = m_{22}$
$A_7 = m_7$	$B_7 = m_{15}$	$C_7 = m_{23}$
$A_8 = m_8$	$B_8 = m_{16}$	$C_8 = m_{24}$

MIR-Y Antenna Array uv spacing normalized to the wavelength

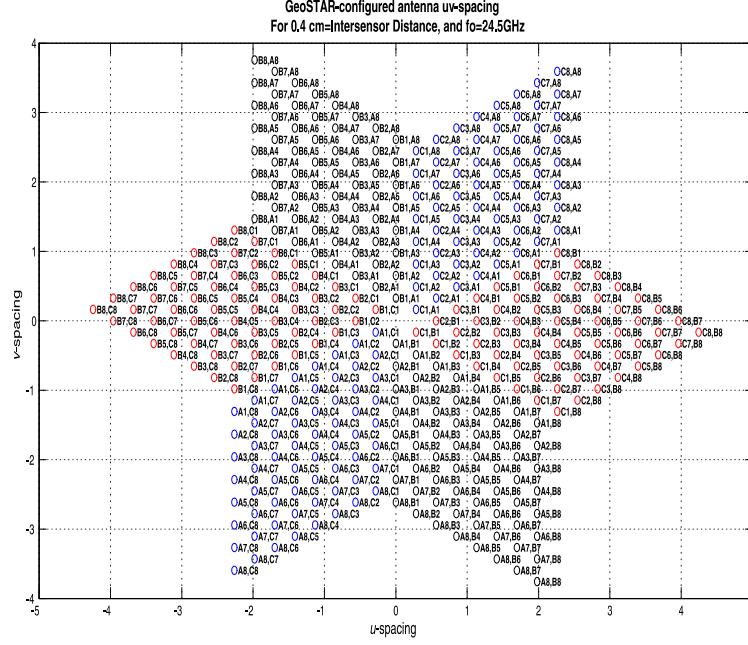


Figure 3.7. \mathcal{U}, \mathcal{V} samples of the GeoSTAR-configured antenna baselines (for $f_{0(1)} = 24.5$ GHz) and $d = 4$ mm. Each \mathcal{U}, \mathcal{V} sample is a difference between x - y position of two corresponding sensors (A specifies Arm-1, B specifies Arm-2, and C specifies Arm-3).

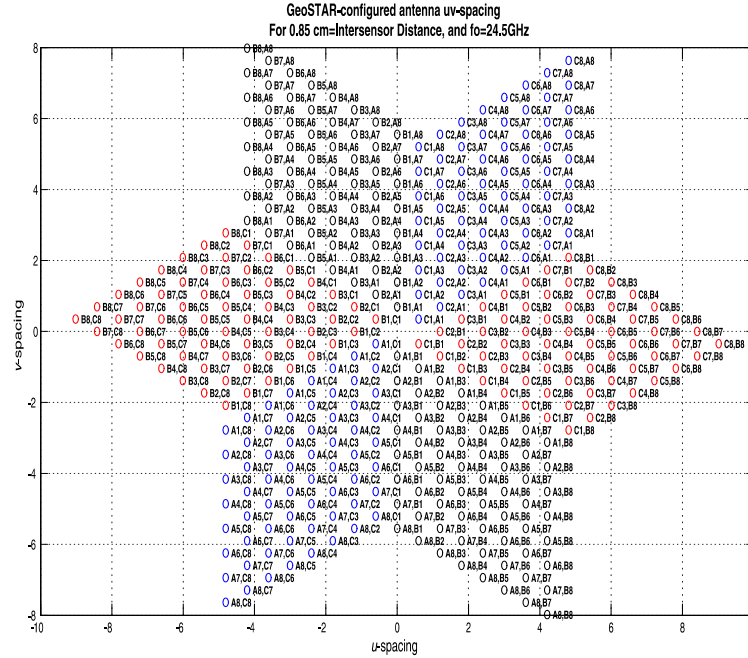


Figure 3.8. \mathcal{U}, \mathcal{V} samples of the GeoSTAR-configured antenna baselines (for $f_{0(1)} = 24.5$ GHz) and $d = 8.5$ mm. Each \mathcal{U}, \mathcal{V} sample is a difference between x - y position of two corresponding sensors (A specifies Arm-1, B specifies Arm-2, and C specifies Arm-3).

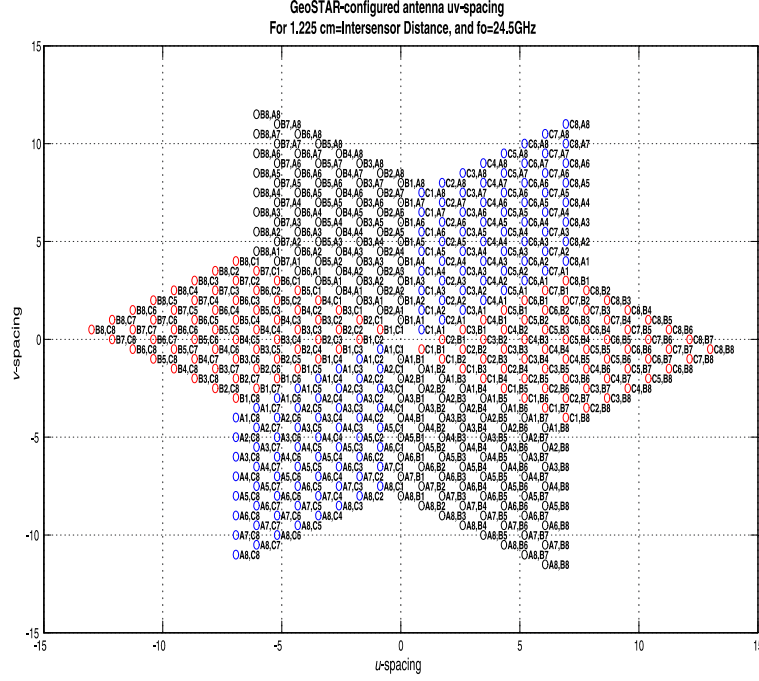


Figure 3.9. u, v samples of the GeoSTAR-configured antenna baselines (for $f_{o(1)} = 24.5$ GHz) and $d = 12.25$ mm. Each u, v sample is a difference between x - y position of two corresponding sensors (A specifies Arm-1, B specifies Arm-2, and C specifies Arm-3).

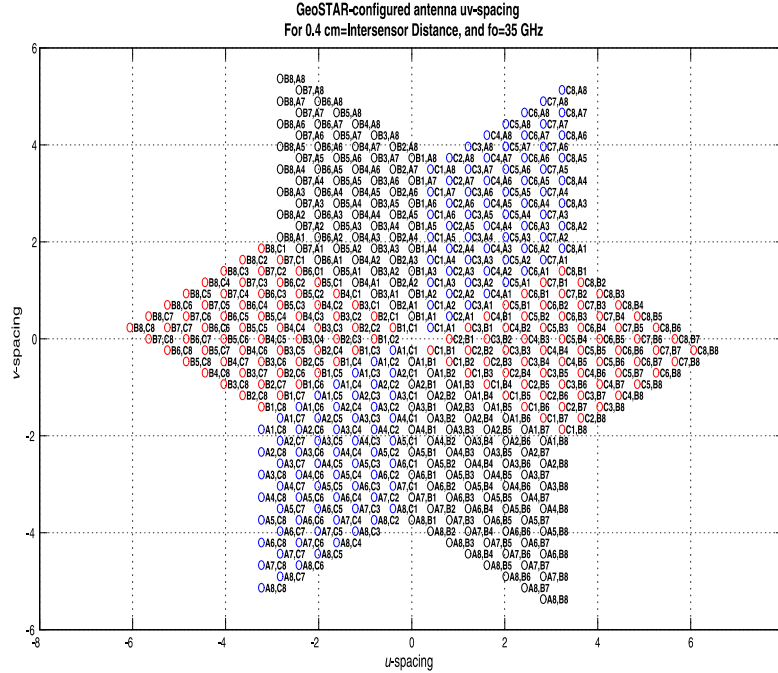


Figure 3.10. u, v samples of the GeoSTAR-configured antenna baselines (for $f_{o(2)} = 35$ GHz) and $d = 4$ mm. Each u, v sample is a difference between x - y position of two corresponding sensors (A specifies Arm-1, B specifies Arm-2, and C specifies Arm-3).

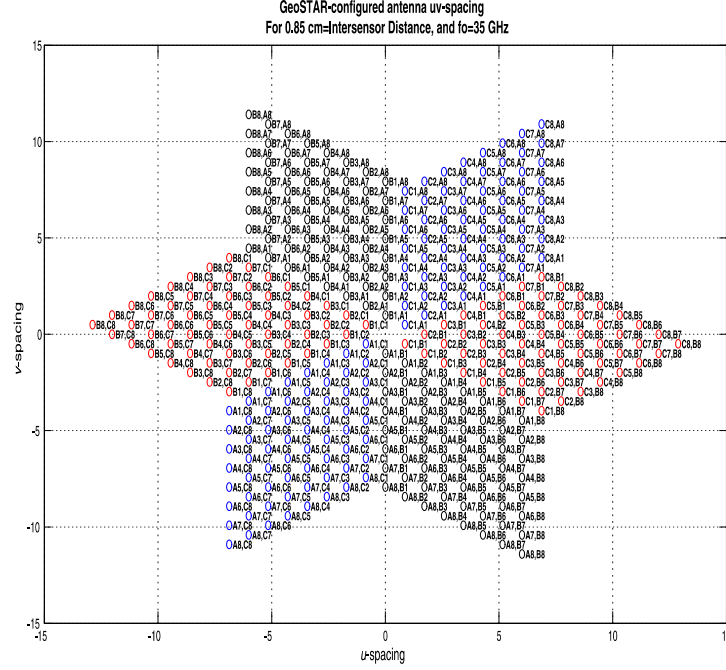


Figure 3.11. \mathcal{U}, \mathcal{V} samples of the GeoSTAR-configured antenna baselines (for $f_{o(2)} = 35$ GHz) and $d = 8.5$ mm. Each \mathcal{U}, \mathcal{V} sample is a difference between x - y position of two corresponding sensors (A specifies Arm-1, B specifies Arm-2, and C specifies Arm-3).

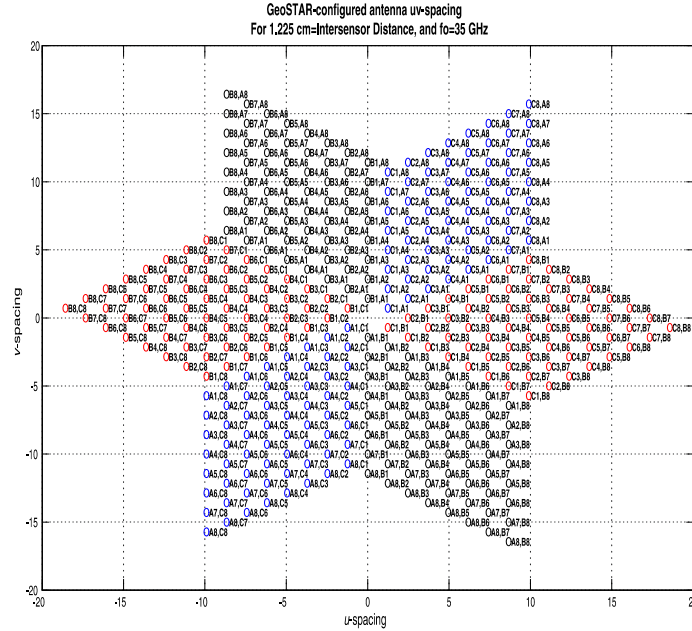


Figure 3.12. \mathcal{U}, \mathcal{V} samples of the GeoSTAR-configured antenna baselines (for $f_{o(2)} = 35$ GHz) and $d = 12.25$ mm. Each \mathcal{U}, \mathcal{V} sample is a difference between x - y position of two corresponding sensors (A specifies Arm-1, B specifies Arm-2, and C specifies Arm-3).

3.3 DEDR - based SP considerations

Once the measurement data has been recorded and archived, according to the previously specified format, the next step is to perform the following calculations of the array correlation function:

$$\mathbf{Y}_r = \frac{1}{J} \sum_{j=1}^J \mathbf{u}_r^{(j)} \mathbf{u}_r^{+(j)} \leftarrow \text{Averaged over } J \text{ Pulse Repetition Time for each range gate.} \quad (3.2)$$

The superscript (+) defines the Hermitian transpose, which is the transpose conjugate (*T). In the real-form representation format, the corresponding real and imaginary parts of the complex correlation coefficients become:

$$\text{Re}\{\mathbf{Y}_r\} = \frac{1}{J} \left[\sum_{j=1}^J \left(\mathbf{u}_{(\mathbf{I})r}^{(j)} \mathbf{u}_{(\mathbf{I})r}^{\mathbf{T}(j)} \right) + \sum_{j=1}^J \left(\mathbf{u}_{(\mathbf{Q})r}^{(j)} \mathbf{u}_{(\mathbf{Q})r}^{\mathbf{T}(j)} \right) \right] \quad (3.3)$$

$$\text{Im}\{\mathbf{Y}_r\} = \frac{1}{J} \left[\sum_{j=1}^J \left(\mathbf{u}_{(\mathbf{Q})r}^{(j)} \mathbf{u}_{(\mathbf{I})r}^{\mathbf{T}(j)} \right) - \sum_{j=1}^J \left(\mathbf{u}_{(\mathbf{I})r}^{(j)} \mathbf{u}_{(\mathbf{Q})r}^{\mathbf{T}(j)} \right) \right] \quad (3.4)$$

The structure of the DEDR-optimally sparse signal data correlation matrix \mathbf{Y} is shown in Figure 3.13. The matrix is composed of six data blocks of 8-by-8 matrices and three diagonal blocks composed of zeros, corresponding to correlations of sensors in the same arm. In the simulation protocol results, we have included calculations with the complete matrix \mathbf{Y} (with correlation of elements of the same arm, no-zero blocks) and the DEDR-optimally sparse signal correlation matrix \mathbf{Y} (as presented in Figure 3.13).

The employed here matched spatial filtering (MSF) algorithm for image formation using the Multi-sensor Imaging Radar (MIR) measurement data is a descriptive experiment design regularization (DEDR) – based generalization of the celebrated Van-Cittert-Zernike theorem from radio astronomy, according to which, the noise-free data visibility function $R_S(u, v)$ and the related spatial spectrum pattern (SSP) $b(\theta_x, \theta_y)$ or angular brightness distribution over the 2-D observation space with spatial frequencies θ_x, θ_y are related through the 2-D spatial Fourier transform

$$R_S(u, v) = c \mathfrak{T}_{\Theta}^{-1} \{ b(\theta_x, \theta_y) \} = C \int_{\Theta} b(\theta_x, \theta_y) \exp[i2\pi(u\theta_x + v\theta_y)] d\theta_x d\theta_y \quad (3.5)$$

where $\theta_x = \cos(\hat{\mathfrak{G}}, \hat{\mathbf{x}}^\circ)$; $\theta_y = \cos(\hat{\mathfrak{G}}, \hat{\mathbf{y}}^\circ)$ are the *directional cosines* related to the direction of arrival (DOA) vector $\hat{\mathfrak{G}}$ defined by (1.4), (1.5). The DOA vector is a unitary vector, thus has length equal to 1, i.e. $|\hat{\mathfrak{G}}| = |\mathbf{r}| / |\mathbf{r}| = 1$ and C is the normalizing constant (not critical for image formation and simulations). The visibility function arguments $(\mathcal{U}, \mathcal{V})$ represent the x - y projections of the normalized sensor baseline vectors (normalized to the employed wavelength λ_o) in the visibility domain $(\mathcal{U}, \mathcal{V}) \in P/\lambda_o$ (see Part I for details).

The robust MSF method for RS image formation implies formation of the observed noised visibility function $R(\mathbf{U}, \mathbf{V})$ via computing proper correlations (3.2) performed via averaging the outer data vector product $\mathbf{U}\mathbf{U}^+$ over multiple snapshots (related to different transmitted pulses) over a range of normalized spacings $(\mathbf{U}, \mathbf{V}) \in P/\lambda_0$ followed by the 2-D Fourier transform that yields the MSF image of the scene

$$\hat{b}(\theta_x, \theta_y | r) = \int_R R(u, v | r) \exp[-i2\pi(u\theta_x + v\theta_y)] du dv \quad (3.6)$$

as a function of normalized spatial frequencies (directional cosines) θ_x, θ_y ; $|\theta_x| < 1$; $|\theta_y| < 1$ at a particular fixed range gate r from the range observation domain $R \ni r$. The corresponding Cartesian cross – range scene coordinates $(x_{(r)}, y_{(r)} | r)$ are related to the directional cosines θ_x, θ_y (in the r th range gate) as

$$x_{(r)} = \theta_x \left(\frac{r}{\sqrt{1 - (\theta_x^2 + \theta_y^2)}} \right), \quad y_{(r)} = \theta_y \left(\frac{r}{\sqrt{1 - (\theta_x^2 + \theta_y^2)}} \right). \quad (3.7)$$

In the pursued nonparametric imaging problem treatment, the resulting resolution quality is assessed by the shape of the system point spread function (PSF) associated with the image (3.6) of a single point-type target located at the scene origin in the corresponding range gate $r \in R$. In particular, the desired system PSF is associated with the shape that provides the lowest possible sidelobes (and grating lobes) level balanced over the minimum achievable effective width of the main beam.

Using (4.6) we performed the simulation study of the PSF's of the MIR imaging systems that employ the GeoSTAR-configured arrays. In the next section, we report the results related to the interelement (sensor) spacing $d_A = 4$ mm, $d_A = 8.5$ mm, $d_A = 12.25$ mm and our recommended $d_A = 15.43$ mm ($1.8\lambda_{0(2)}$) for the two range gates $r = 10$ m and $r = 50$ m, respectively. The PSF's cross-sections in the x - y image scene provide explicit information on the spatial resolution cells achievable with such GeoSTAR-configured sensor array that employ the same 2-D DEDR-related MSF method for image formation.

$0's_{(8 \times 8)}$								A ₁ B ₁	A ₁ B ₂	A ₁ B ₃	A ₁ B ₄	A ₁ B ₅	A ₁ B ₆	A ₁ B ₇	A ₁ B ₈	A ₁ C ₁	A ₁ C ₂	A ₁ C ₃	A ₁ C ₄	A ₁ C ₅	A ₁ C ₆	A ₁ C ₇	A ₁ C ₈
								A ₂ B ₁	A ₂ B ₂	A ₂ B ₃	A ₂ B ₄	A ₂ B ₅	A ₂ B ₆	A ₂ B ₇	A ₂ B ₈	A ₂ C ₁	A ₂ C ₂	A ₂ C ₃	A ₂ C ₄	A ₂ C ₅	A ₂ C ₆	A ₂ C ₇	A ₂ C ₈
								A ₃ B ₁	A ₃ B ₂	A ₃ B ₃	A ₃ B ₄	A ₃ B ₅	A ₃ B ₆	A ₃ B ₇	A ₃ B ₈	A ₃ C ₁	A ₃ C ₂	A ₃ C ₃	A ₃ C ₄	A ₃ C ₅	A ₃ C ₆	A ₃ C ₇	A ₃ C ₈
								A ₄ B ₁	A ₄ B ₂	A ₄ B ₃	A ₄ B ₄	A ₄ B ₅	A ₄ B ₆	A ₄ B ₇	A ₄ B ₈	A ₄ C ₁	A ₄ C ₂	A ₄ C ₃	A ₄ C ₄	A ₄ C ₅	A ₄ C ₆	A ₄ C ₇	A ₄ C ₈
								A ₅ B ₁	A ₅ B ₂	A ₅ B ₃	A ₅ B ₄	A ₅ B ₅	A ₅ B ₆	A ₅ B ₇	A ₅ B ₈	A ₅ C ₁	A ₅ C ₂	A ₅ C ₃	A ₅ C ₄	A ₅ C ₅	A ₅ C ₆	A ₅ C ₇	A ₅ C ₈
								A ₆ B ₁	A ₆ B ₂	A ₆ B ₃	A ₆ B ₄	A ₆ B ₅	A ₆ B ₆	A ₆ B ₇	A ₆ B ₈	A ₆ C ₁	A ₆ C ₂	A ₆ C ₃	A ₆ C ₄	A ₆ C ₅	A ₆ C ₆	A ₆ C ₇	A ₆ C ₈
								A ₇ B ₁	A ₇ B ₂	A ₇ B ₃	A ₇ B ₄	A ₇ B ₅	A ₇ B ₆	A ₇ B ₇	A ₇ B ₈	A ₇ C ₁	A ₇ C ₂	A ₇ C ₃	A ₇ C ₄	A ₇ C ₅	A ₇ C ₆	A ₇ C ₇	A ₇ C ₈
								A ₈ B ₁	A ₈ B ₂	A ₈ B ₃	A ₈ B ₄	A ₈ B ₅	A ₈ B ₆	A ₈ B ₇	A ₈ B ₈	A ₈ C ₁	A ₈ C ₂	A ₈ C ₃	A ₈ C ₄	A ₈ C ₅	A ₈ C ₆	A ₈ C ₇	A ₈ C ₈
B ₁ A ₁	B ₁ A ₂	B ₁ A ₃	B ₁ A ₄	B ₁ A ₅	B ₁ A ₆	B ₁ A ₇	B ₁ A ₈	$0's_{(8 \times 8)}$								B ₁ C ₁	B ₁ C ₂	B ₁ C ₃	B ₁ C ₄	B ₁ C ₅	B ₁ C ₆	B ₁ C ₇	B ₁ C ₈
B ₂ A ₁	B ₂ A ₂	B ₂ A ₃	B ₂ A ₄	B ₂ A ₅	B ₂ A ₆	B ₂ A ₇	B ₂ A ₈									B ₂ C ₁	B ₂ C ₂	B ₂ C ₃	B ₂ C ₄	B ₂ C ₅	B ₂ C ₆	B ₂ C ₇	B ₂ C ₈
B ₃ A ₁	B ₃ A ₂	B ₃ A ₃	B ₃ A ₄	B ₃ A ₅	B ₃ A ₆	B ₃ A ₇	B ₃ A ₈									B ₃ C ₁	B ₃ C ₂	B ₃ C ₃	B ₃ C ₄	B ₃ C ₅	B ₃ C ₆	B ₃ C ₇	B ₃ C ₈
B ₄ A ₁	B ₄ A ₂	B ₄ A ₃	B ₄ A ₄	B ₄ A ₅	B ₄ A ₆	B ₄ A ₇	B ₄ A ₈									B ₄ C ₁	B ₄ C ₂	B ₄ C ₃	B ₄ C ₄	B ₄ C ₅	B ₄ C ₆	B ₄ C ₇	B ₄ C ₈
B ₅ A ₁	B ₅ A ₂	B ₅ A ₃	B ₅ A ₄	B ₅ A ₅	B ₅ A ₆	B ₅ A ₇	B ₅ A ₈									B ₅ C ₁	B ₅ C ₂	B ₅ C ₃	B ₅ C ₄	B ₅ C ₅	B ₅ C ₆	B ₅ C ₇	B ₅ C ₈
B ₆ A ₁	B ₆ A ₂	B ₆ A ₃	B ₆ A ₄	B ₆ A ₅	B ₆ A ₆	B ₆ A ₇	B ₆ A ₈									B ₆ C ₁	B ₆ C ₂	B ₆ C ₃	B ₆ C ₄	B ₆ C ₅	B ₆ C ₆	B ₆ C ₇	B ₆ C ₈
B ₇ A ₁	B ₇ A ₂	B ₇ A ₃	B ₇ A ₄	B ₇ A ₅	B ₇ A ₆	B ₇ A ₇	B ₇ A ₈									B ₇ C ₁	B ₇ C ₂	B ₇ C ₃	B ₇ C ₄	B ₇ C ₅	B ₇ C ₆	B ₇ C ₇	B ₇ C ₈
B ₈ A ₁	B ₈ A ₂	B ₈ A ₃	B ₈ A ₄	B ₈ A ₅	B ₈ A ₆	B ₈ A ₇	B ₈ A ₈									B ₈ C ₁	B ₈ C ₂	B ₈ C ₃	B ₈ C ₄	B ₈ C ₅	B ₈ C ₆	B ₈ C ₇	B ₈ C ₈
C ₁ A ₁	C ₁ A ₂	C ₁ A ₃	C ₁ A ₄	C ₁ A ₅	C ₁ A ₆	C ₁ A ₇	C ₁ A ₈	C ₁ B ₁	C ₁ B ₂	C ₁ B ₃	C ₁ B ₄	C ₁ B ₅	C ₁ B ₆	C ₁ B ₇	C ₁ B ₈	$0's_{(8 \times 8)}$							
C ₂ A ₁	C ₂ A ₂	C ₂ A ₃	C ₂ A ₄	C ₂ A ₅	C ₂ A ₆	C ₂ A ₇	C ₂ A ₈	C ₂ B ₁	C ₂ B ₂	C ₂ B ₃	C ₂ B ₄	C ₂ B ₅	C ₂ B ₆	C ₂ B ₇	C ₂ B ₈								
C ₃ A ₁	C ₃ A ₂	C ₃ A ₃	C ₃ A ₄	C ₃ A ₅	C ₃ A ₆	C ₃ A ₇	C ₃ A ₈	C ₃ B ₁	C ₃ B ₂	C ₃ B ₃	C ₃ B ₄	C ₃ B ₅	C ₃ B ₆	C ₃ B ₇	C ₃ B ₈								
C ₄ A ₁	C ₄ A ₂	C ₄ A ₃	C ₄ A ₄	C ₄ A ₅	C ₄ A ₆	C ₄ A ₇	C ₄ A ₈	C ₄ B ₁	C ₄ B ₂	C ₄ B ₃	C ₄ B ₄	C ₄ B ₅	C ₄ B ₆	C ₄ B ₇	C ₄ B ₈								
C ₅ A ₁	C ₅ A ₂	C ₅ A ₃	C ₅ A ₄	C ₅ A ₅	C ₅ A ₆	C ₅ A ₇	C ₅ A ₈	C ₅ B ₁	C ₅ B ₂	C ₅ B ₃	C ₅ B ₄	C ₅ B ₅	C ₅ B ₆	C ₅ B ₇	C ₅ B ₈								
C ₆ A ₁	C ₆ A ₂	C ₆ A ₃	C ₆ A ₄	C ₆ A ₅	C ₆ A ₆	C ₆ A ₇	C ₆ A ₈	C ₆ B ₁	C ₆ B ₂	C ₆ B ₃	C ₆ B ₄	C ₆ B ₅	C ₆ B ₆	C ₆ B ₇	C ₆ B ₈								
C ₇ A ₁	C ₇ A ₂	C ₇ A ₃	C ₇ A ₄	C ₇ A ₅	C ₇ A ₆	C ₇ A ₇	C ₇ A ₈	C ₇ B ₁	C ₇ B ₂	C ₇ B ₃	C ₇ B ₄	C ₇ B ₅	C ₇ B ₆	C ₇ B ₇	C ₇ B ₈								
C ₈ A ₁	C ₈ A ₂	C ₈ A ₃	C ₈ A ₄	C ₈ A ₅	C ₈ A ₆	C ₈ A ₇	C ₈ A ₈	C ₈ B ₁	C ₈ B ₂	C ₈ B ₃	C ₈ B ₄	C ₈ B ₅	C ₈ B ₆	C ₈ B ₇	C ₈ B ₈								

Figure 3.13. DEDR-optimally sparse signal data correlation matrix \mathbf{Y} . Each element of the matrix is labeled by the corresponding arm and sensors, i.e., A_1B_1 is the correlation between sensor 1 in arm A and sensor 1 in arm B.

3.4 Protocols of Simulations Experiments

In this Section, we report protocols of simulation studies of the PSFs of GeoSTAR-configured imaging array systems that employ three interelement spacings specified by the hardware development team (TAMU) and the DEDR-optimized interelement spacing of 15.43 mm recommended by the software development team (CINVESTAV Unidad Guadalajara).

In Figure 3.14, the original simulated 5-TAG scene is depicted.

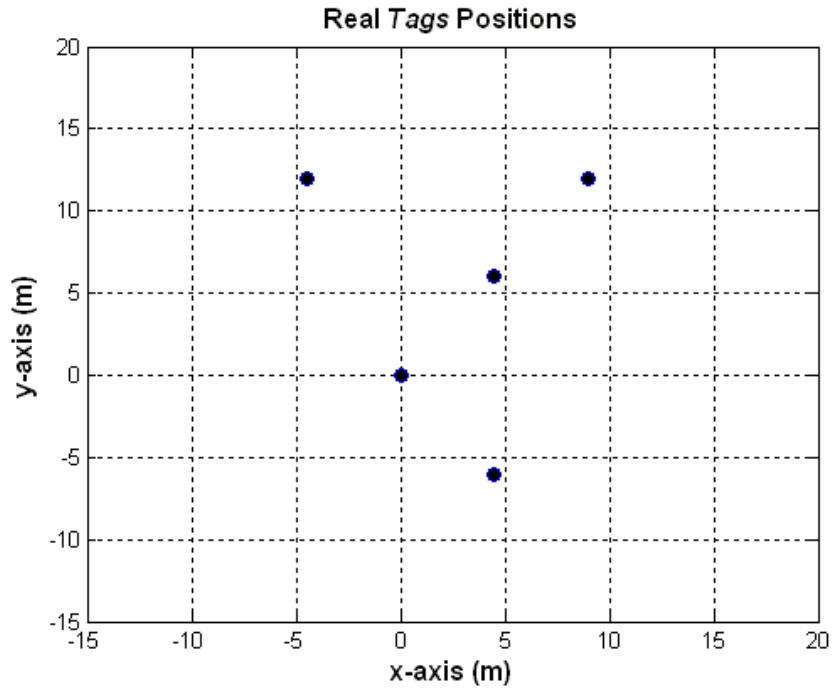


Fig.3.14. Original simulated 5-TAGs scene (Positions of 5 TAGs on the scene).

3.4.1. Simulations Protocols 1

Preliminary Specifications:

- Interelement spacing = 4 mm (recommended by the TAMU team).
- Two types of correlation matrix employed in the MSF SP algorithm: complete and DEDR-optimally sparse data signal correlation matrices.
- Tested range gates: 10 m and 50 m.

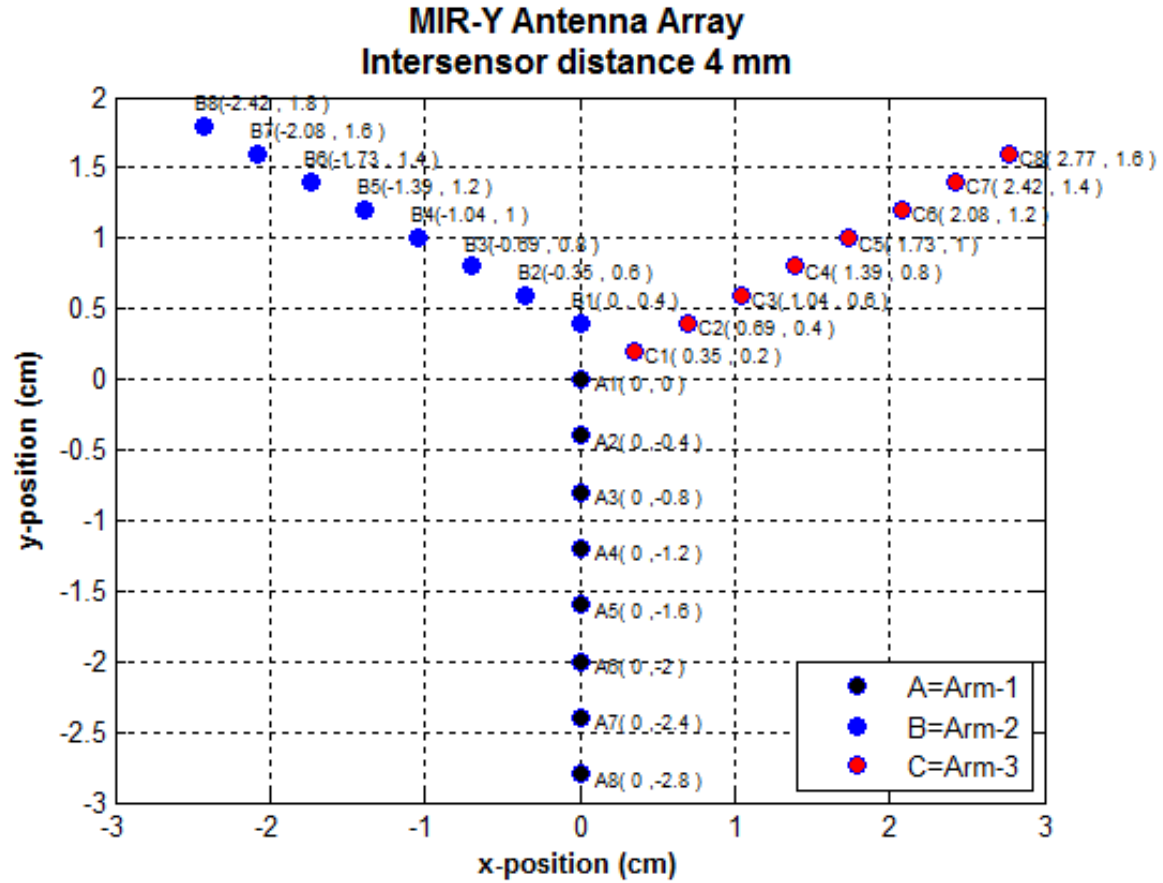


Fig. 3.15. Antenna array layout for interelement spacing = 4mm.

A. Simulations protocols. Case 1: MSF processing for incomplete data correlation matrix (DEDR-optimally sparse).

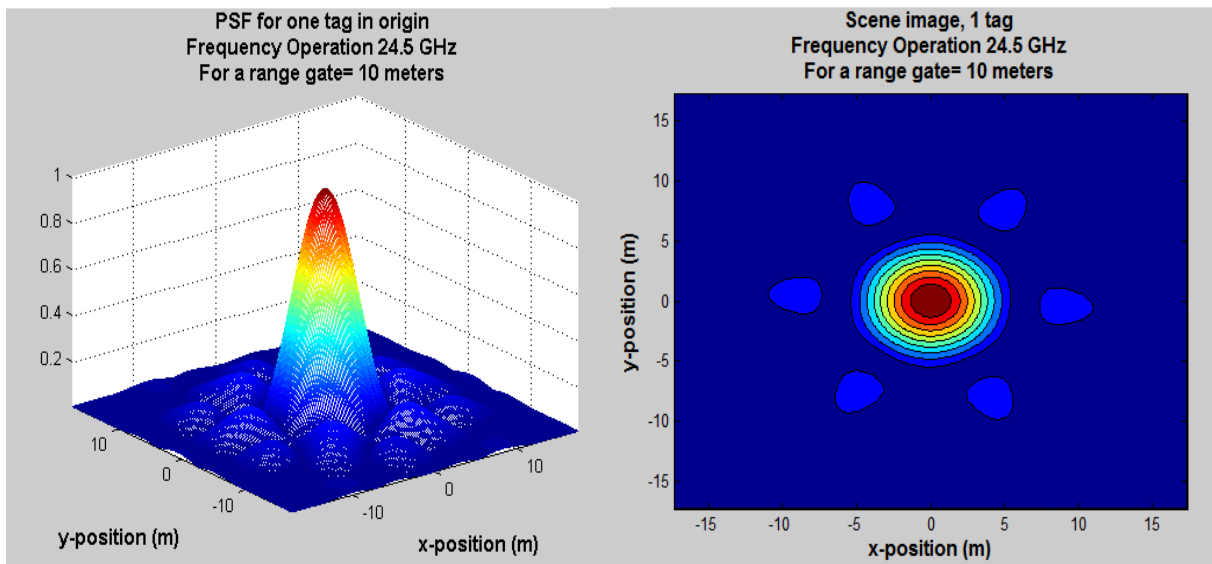


Fig. 3.16. (a) Point Spread Function for $f_{o(1)} = 24.5\text{GHz}$;

(b) Scene image for a single TAG in the origin.

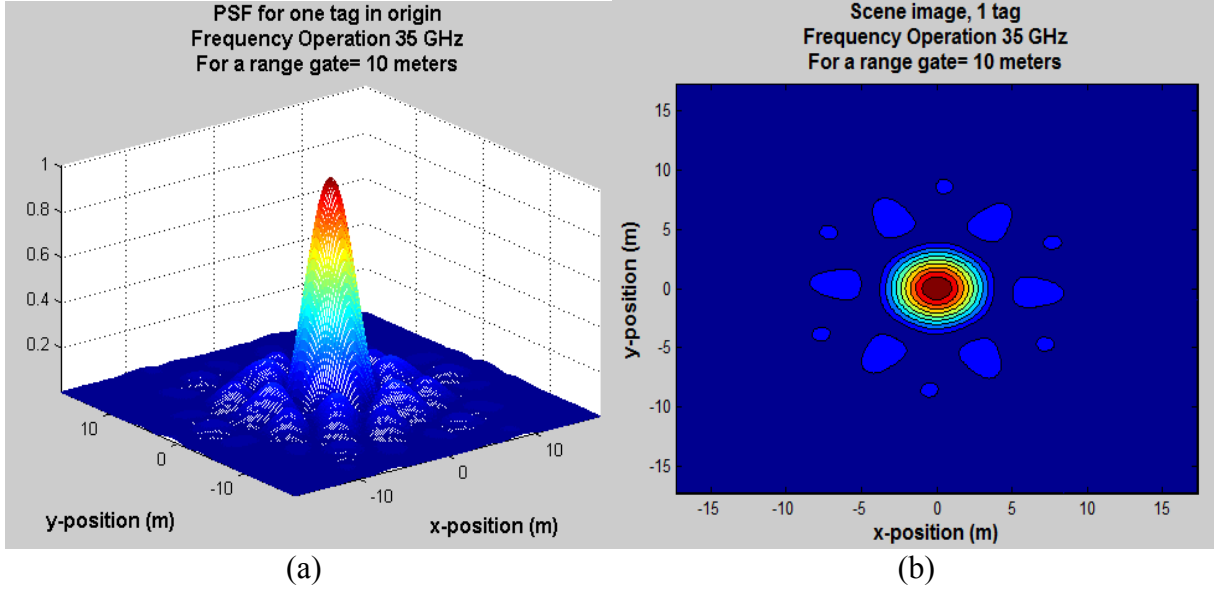


Fig. 3.17. (a) Point Spread Function for $f_{o(2)} = 35$ GHz;

(b) Scene image for a single TAG in the origin.

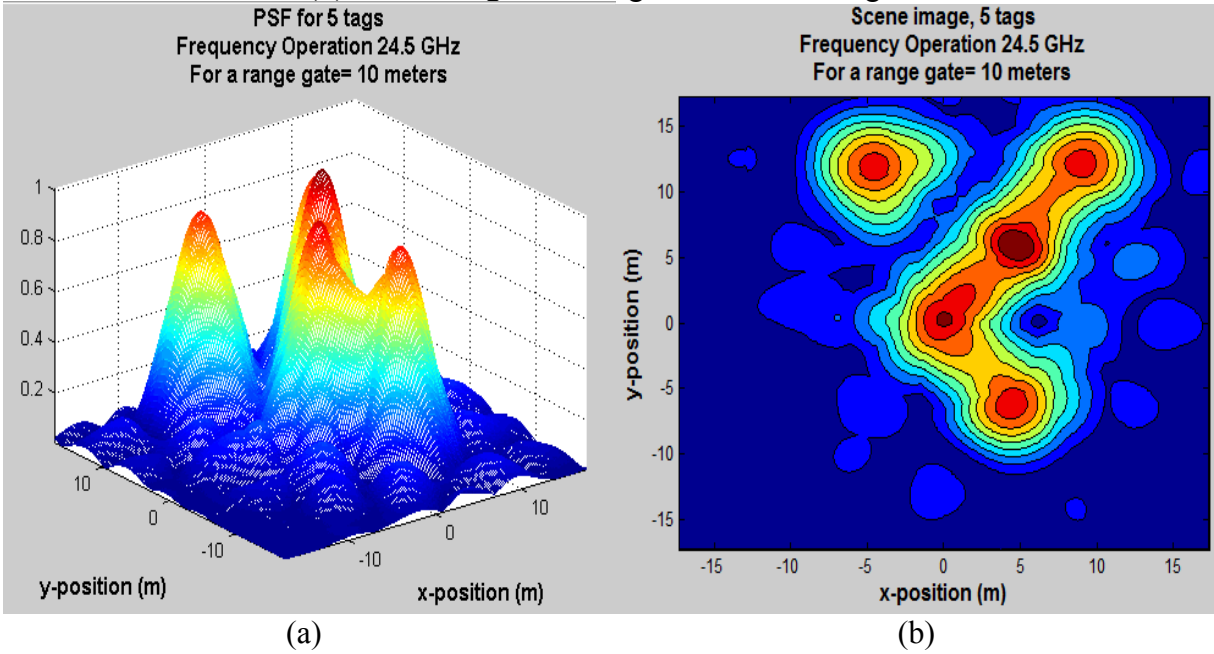


Fig. 3.18. (a) 3-D imaging system output for $f_{o(1)} = 24.5$ GHz and 5 TAGs;

(b) 5-TAG scene image for the same SP specifications.

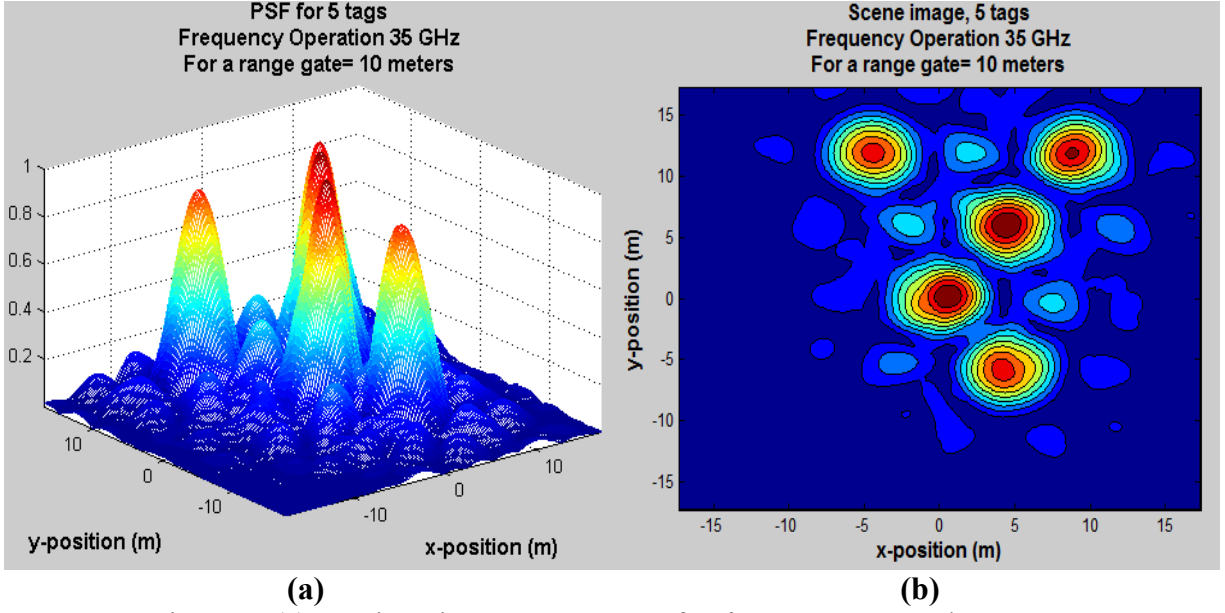


Fig.3.19. (a) 3-D imaging system output for $f_{o(2)} = 35$ GHz and 5 TAGs;
(b) 5-TAG Scene image for the same SP specifications.

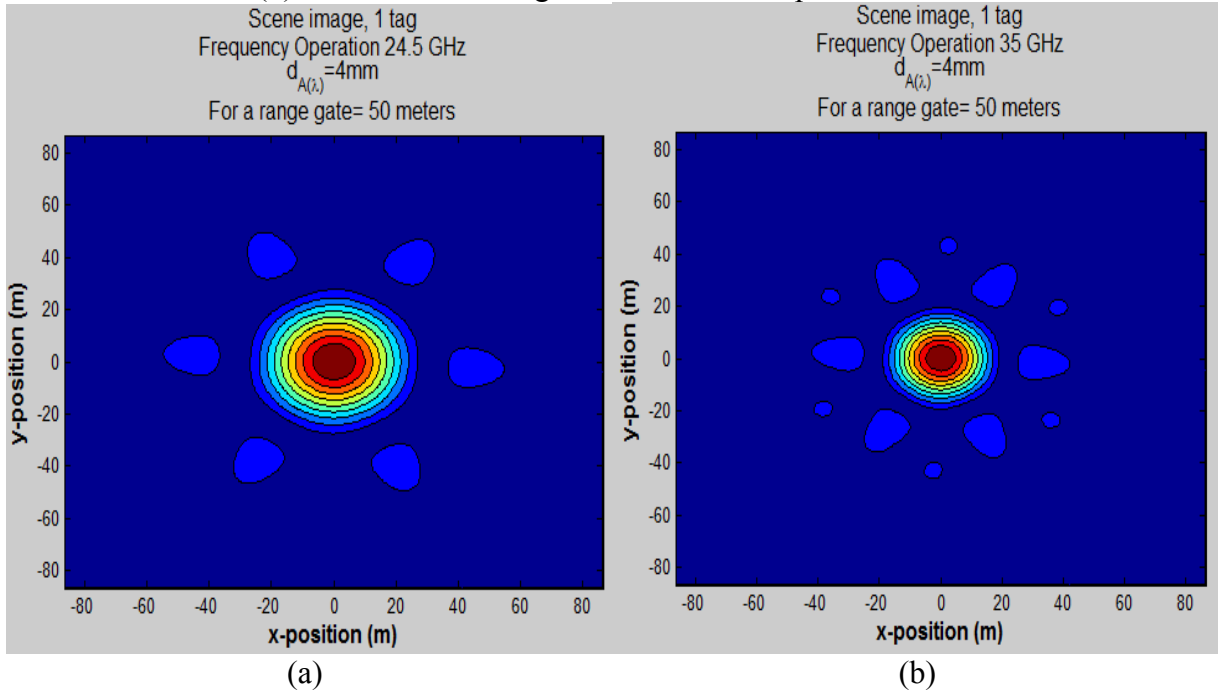


Fig. 3.20. (a) Scene image for a single TAG for $f_{o(1)} = 24.5$ GHz and 50 m range gate;
(b) Scene image for a single TAG for $f_{o(2)} = 35$ GHz and 50 m range gate.

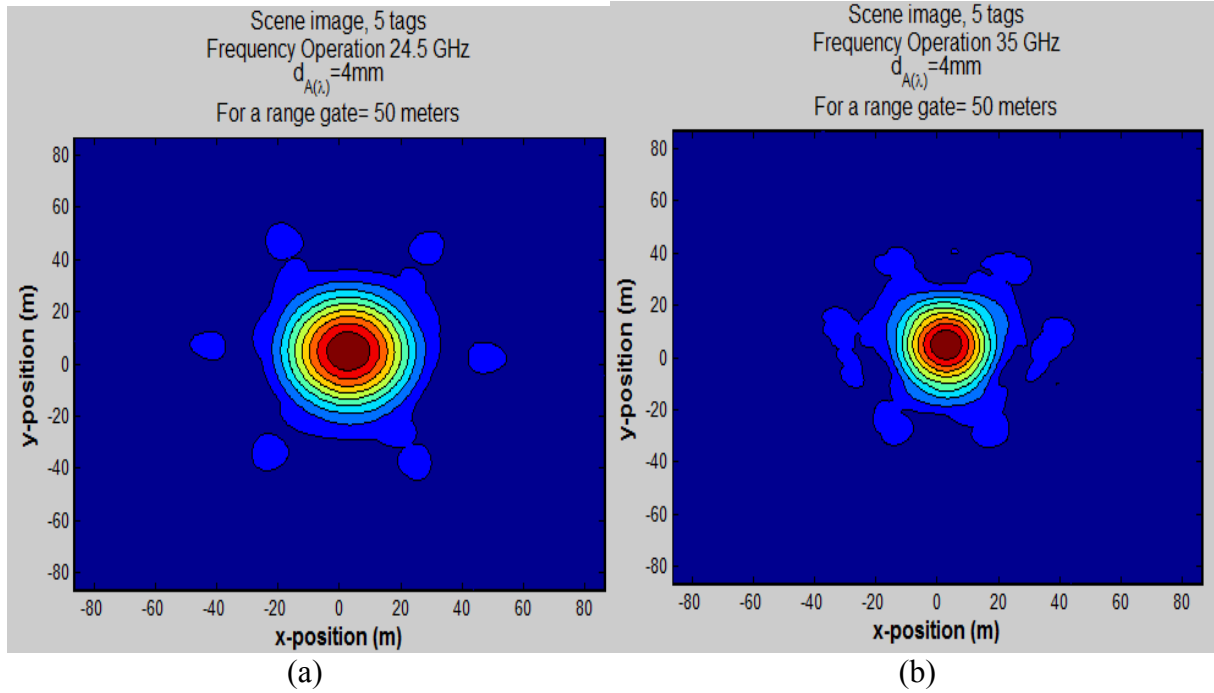


Fig. 3.21. (a) Scene image for five TAGs and $f_{o(1)} = 24.5$ GHz and 50 m range gate;
 (b) 5-TAG Scene image for $f_{o(2)} = 35$ GHz and 50 m range gate.

B. Simulations protocols. Case2: MSF processing for complete data correlation matrix (that involve correlations between elements of the same arm).

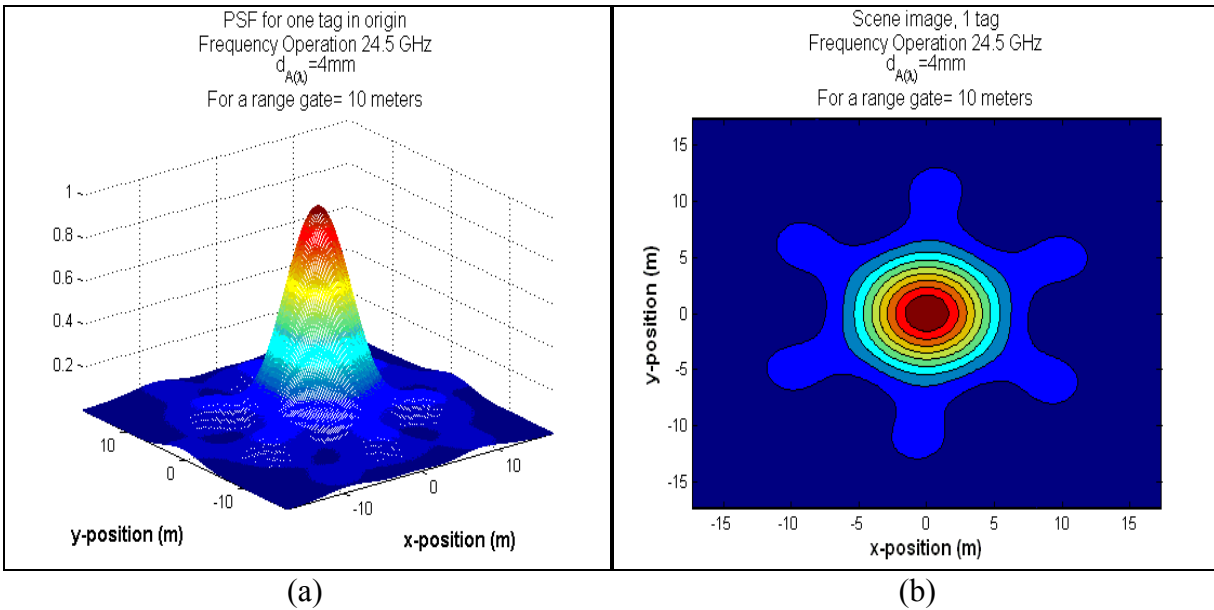
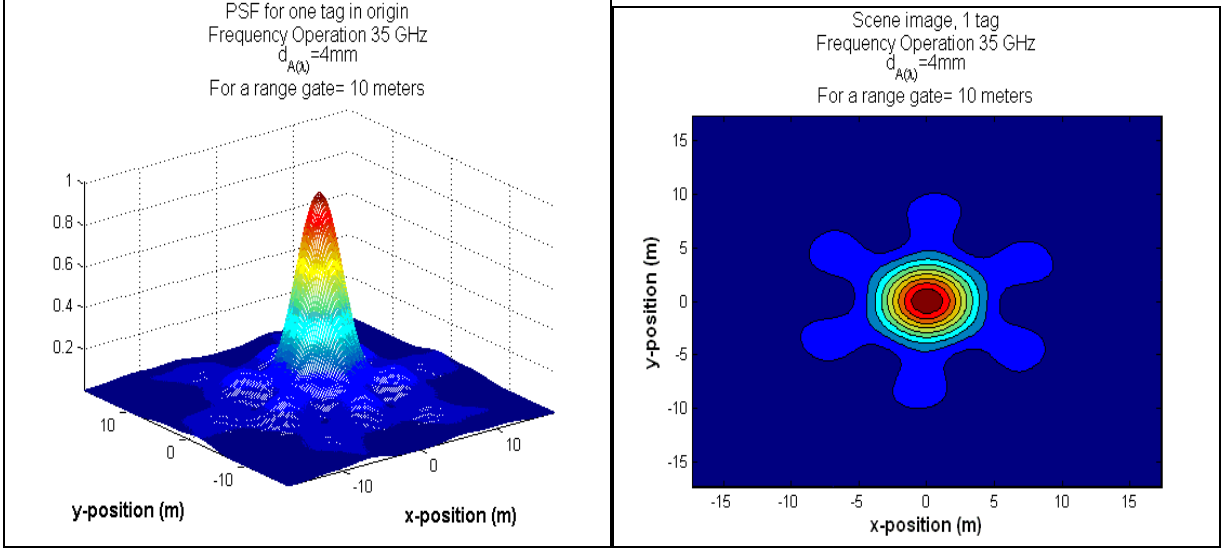
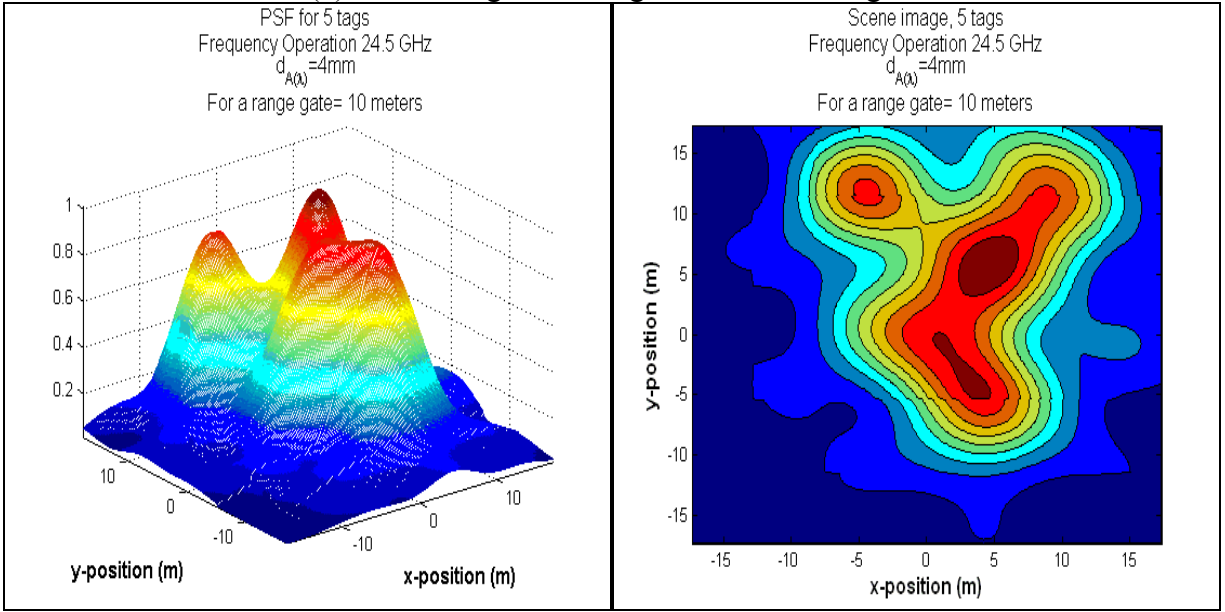


Fig. 3.22. (a) Point Spread Function for $f_{o(1)} = 24.5\text{GHz}$;
 (b) Scene image for a single TAG in the origin.



(a) (b)
Fig. 3.23. (a) Point Spread Function for $f_{o(2)} = 35$ GHz;
(b) Scene image for a single TAG in the origin.



(a) (b)
Fig. 3.24. (a) 3-D imaging system output for $f_{o(1)} = 24.5$ GHz and 5 TAGs;
(b) 5-TAG Scene image for the same SP specifications.

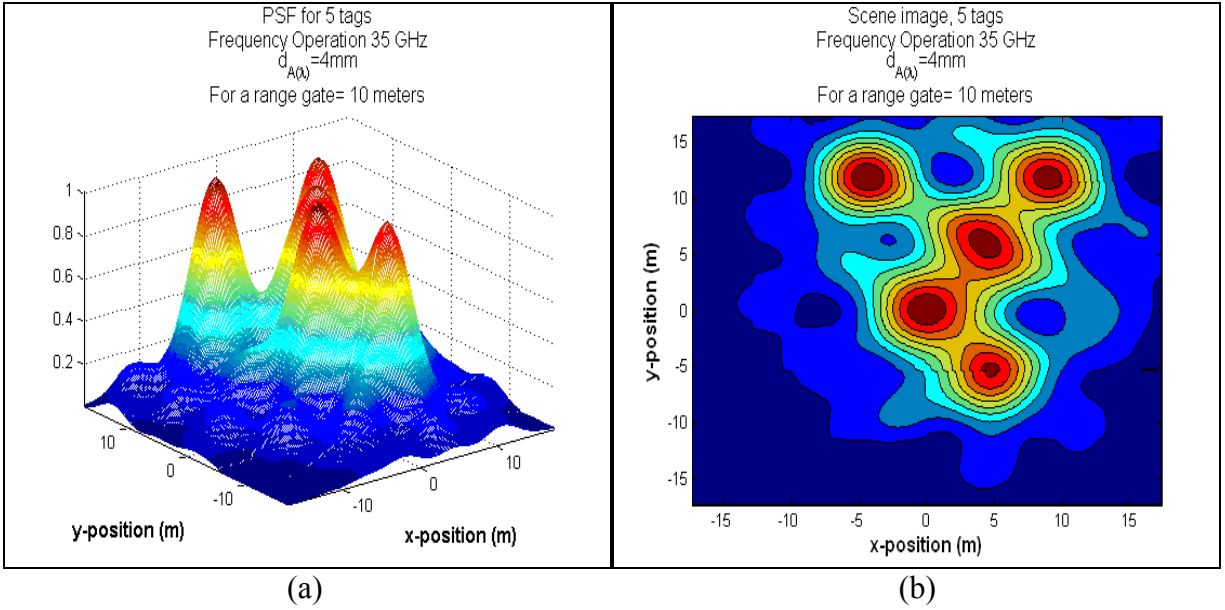


Fig. 3.25. (a) 3-D imaging system output for $f_{o(2)} = 35$ GHz and 5 TAGs;
(b) 5-TAG Scene image for the same SP specifications.

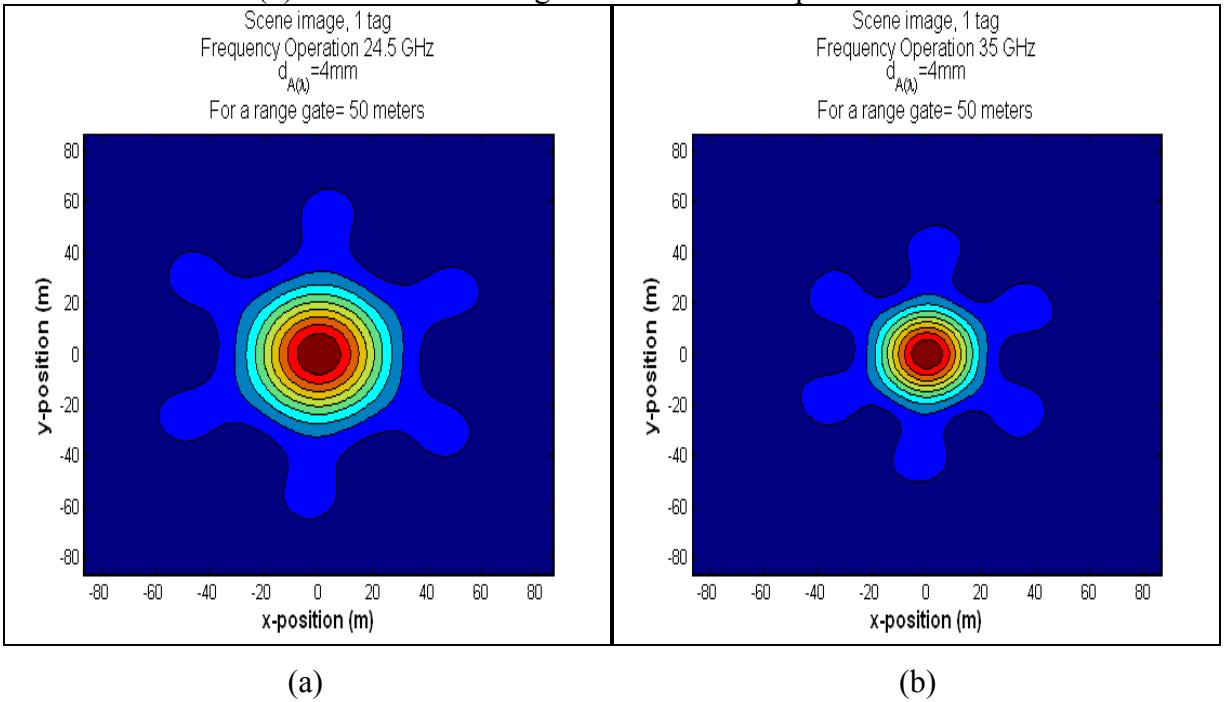


Fig. 3.26. (a) Scene image for a single TAG for $f_{o(1)} = 24.5$ GHz and 50 m range gate;
(b) Scene image for a single TAG for $f_{o(2)} = 35$ GHz and 50 m range gate.

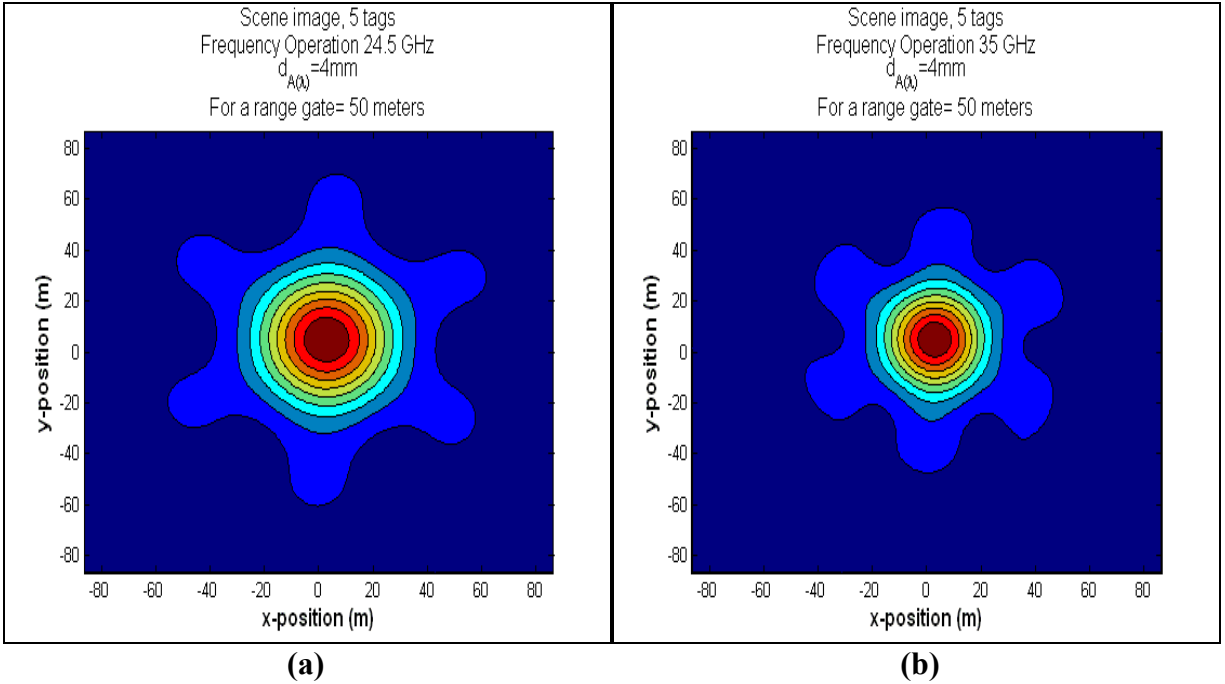


Fig. 3.27. (a) Scene Image for five TAGs and $f_{o(1)} = 24.5$ GHz and 50 m range gate;
(b) 5-TAG Scene image for $f_{o(2)} = 35$ GHz and 50 m range gate.

3.4.2 Simulations Protocols 2

Preliminary Specifications:

- Interelement spacing = 8.5 mm (recommended by the TAMU team)
- Two types of correlation matrix employed in the MSF SP algorithm: complete and DEDR-optimally sparse data signal correlation matrices.
- Tested range gates: 10 m and 50 m.

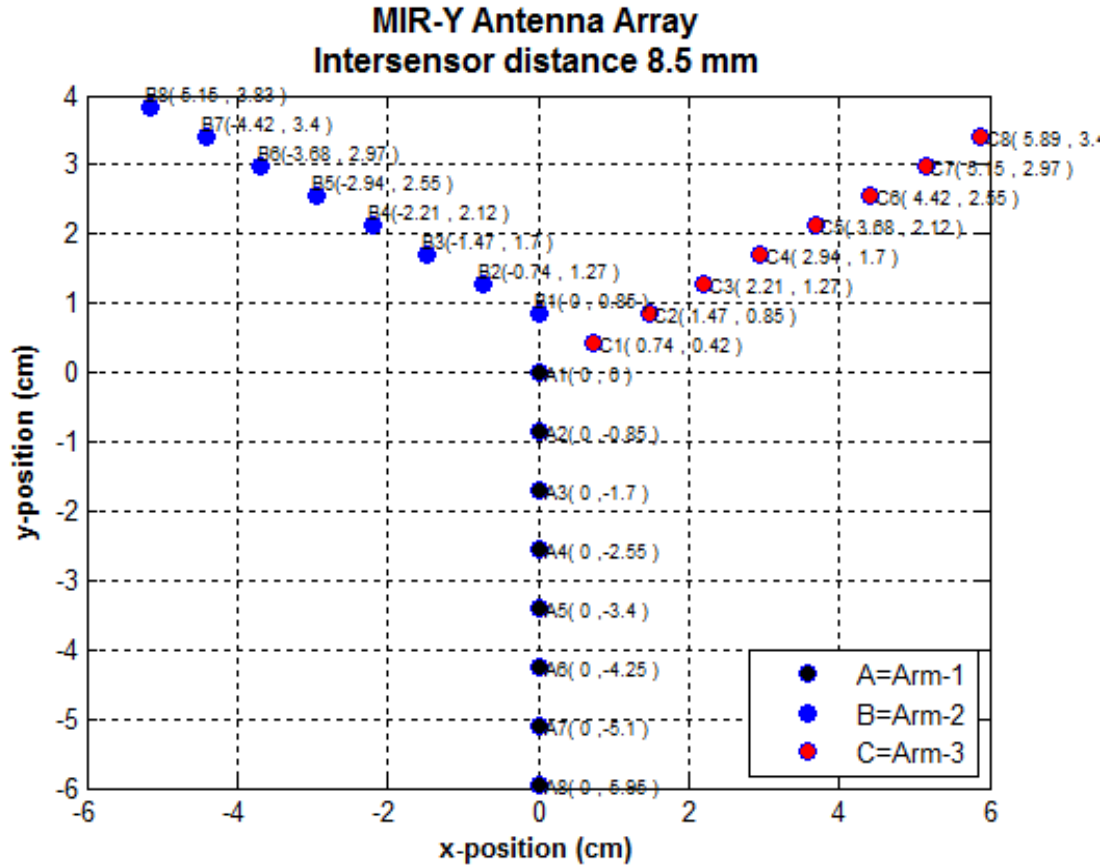


Fig. 3.28. Antenna array layout for interelement spacing = 8.5 mm.

A. Simulations protocols. Case 1: MSF processing for incomplete data correlation matrix (DEDR-optimally sparse).

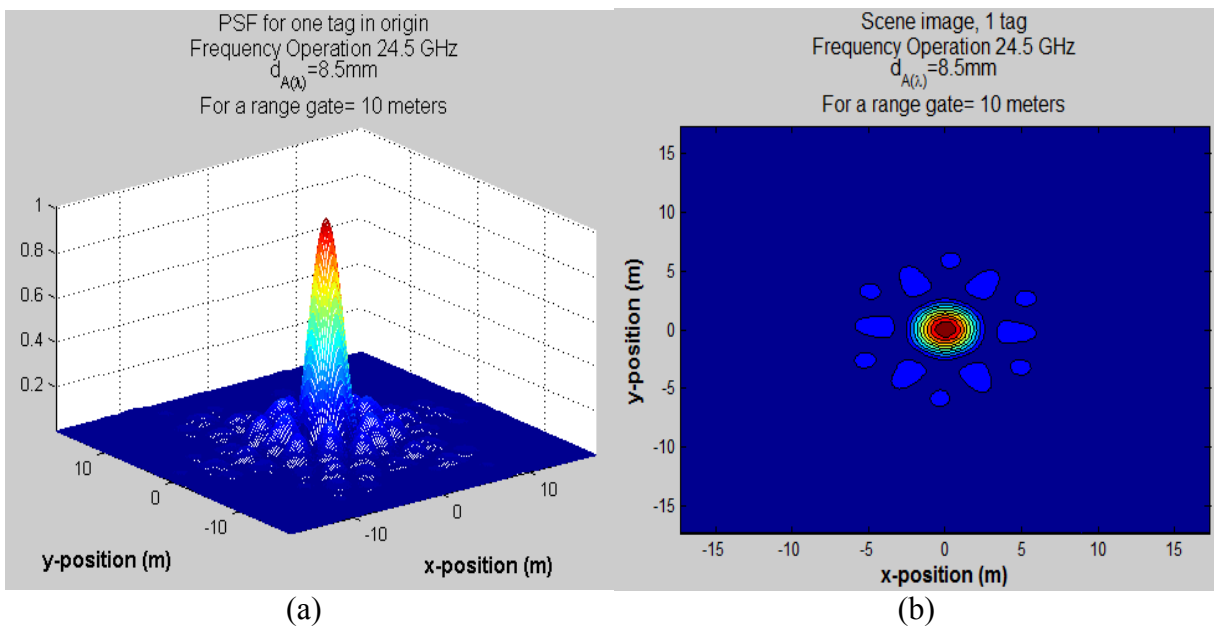


Fig. 3.29. (a) Point Spread Function for $f_{o(1)} = 24.5\text{GHz}$;
(b) Scene image for a single TAG in the origin.

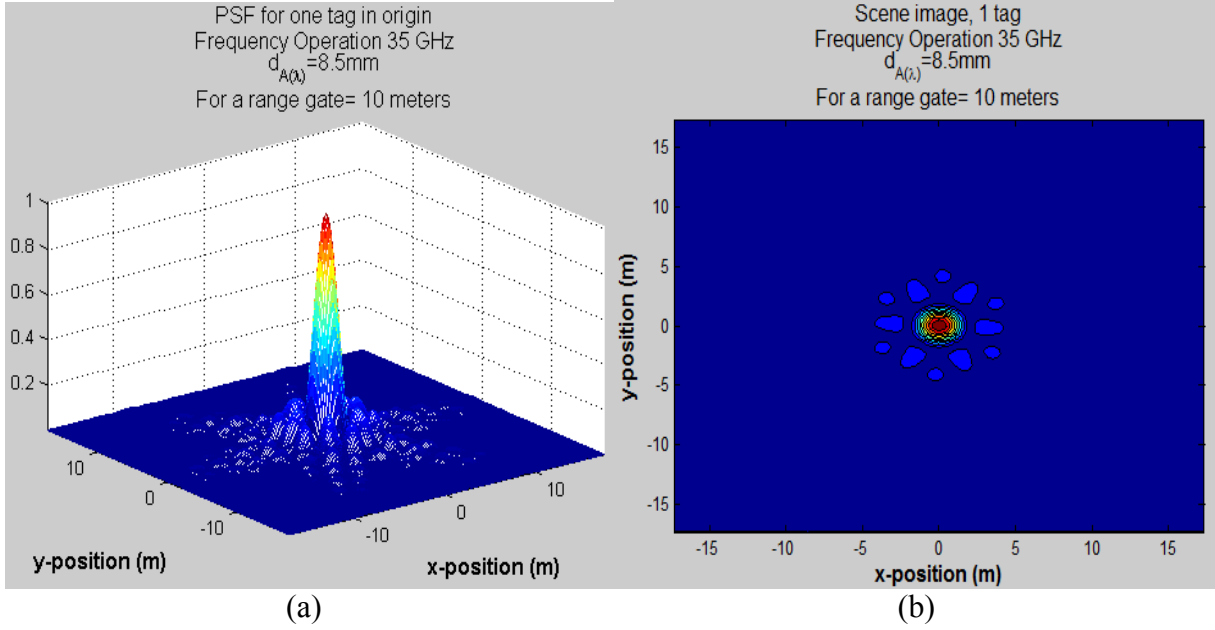


Fig. 3.30. (a) Point Spread Function for $f_{o(2)} = 35\text{ GHz}$;
(b) Scene image for a single TAG in the origin.

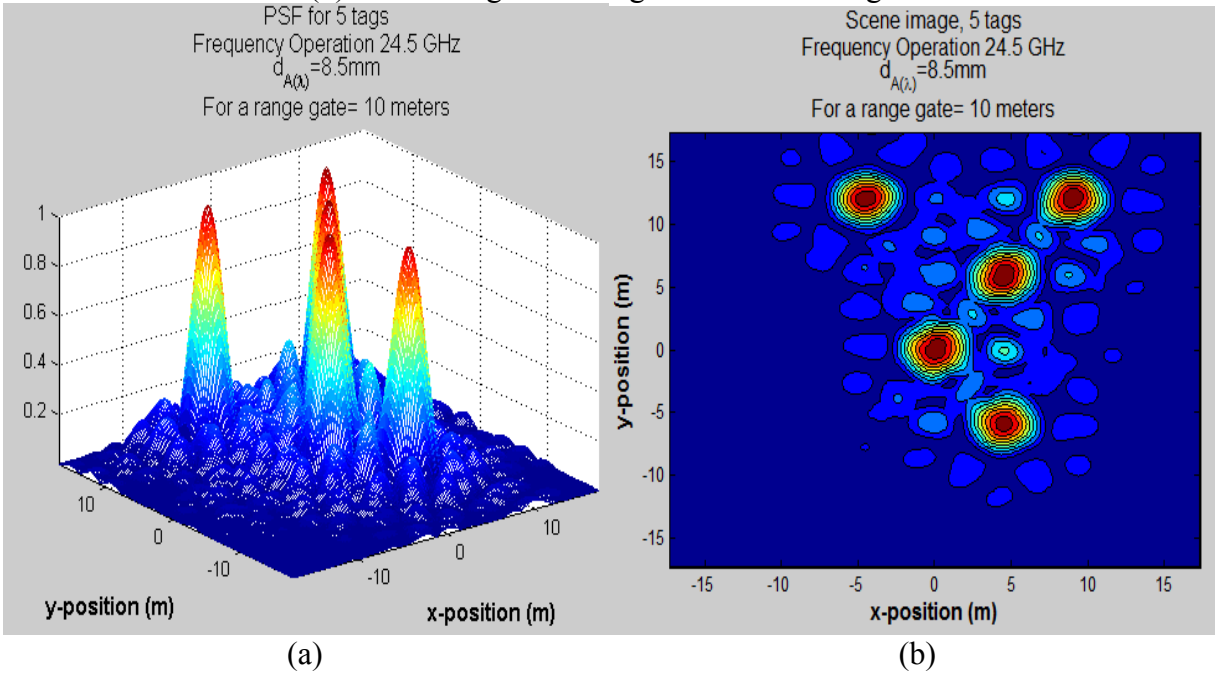


Fig. 3.31. (a) 3-D imaging system output for $f_{o(1)} = 24.5\text{ GHz}$ and 5 TAGs;
(b) 5-TAG Scene image for the same SP specifications.

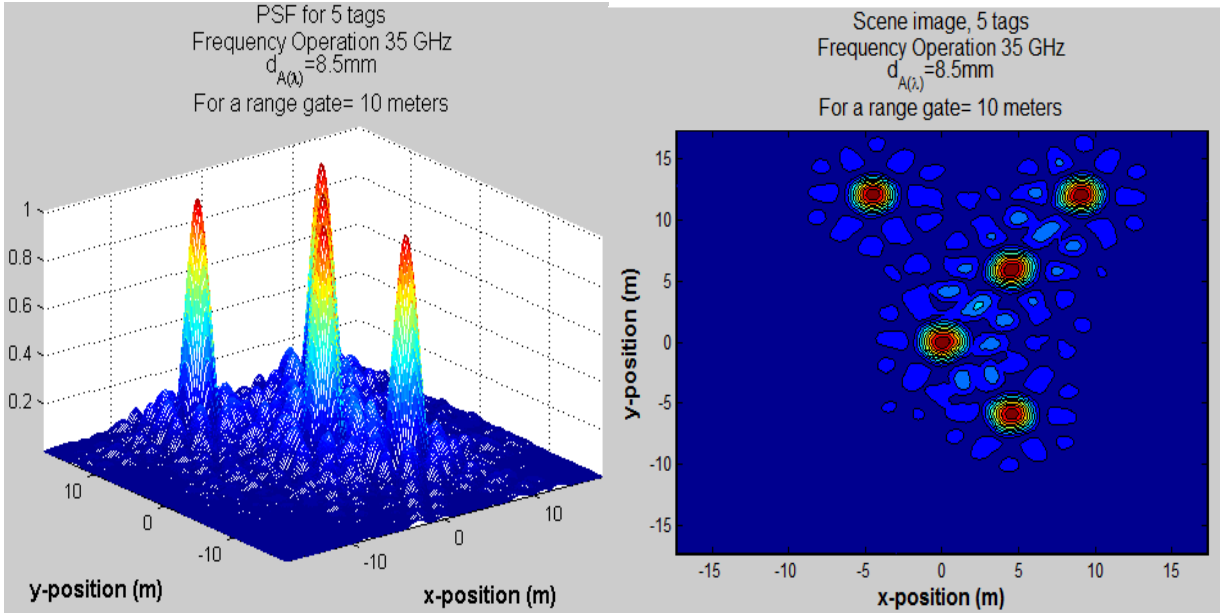


Fig. 3.32. (a) 3-D imaging system output for $f_{o(2)} = 35$ GHz and 5 TAGs;
 (b) 5-TAG Scene image for the same SP specifications.

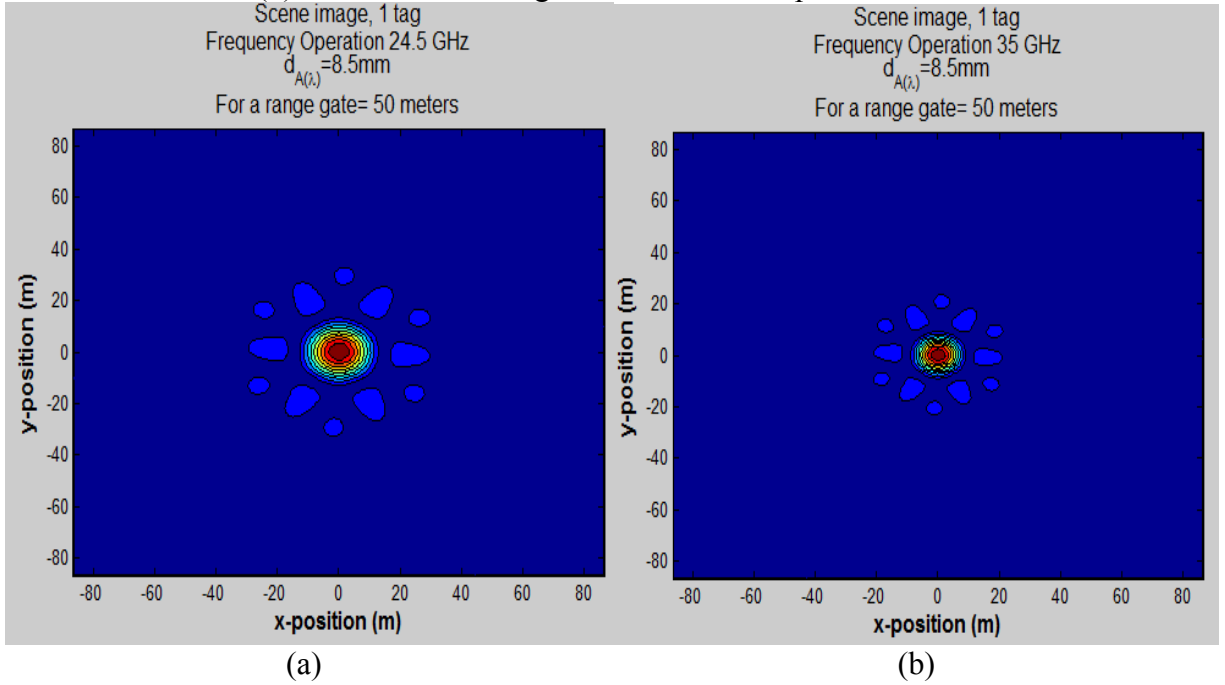


Fig. 3.33. (a) Scene image for a single TAG for $f_{o(1)} = 24.5$ GHz and 50 m range gate,
 (b) Scene image for a single TAG for $f_{o(2)} = 35$ GHz and 50 m range gate.

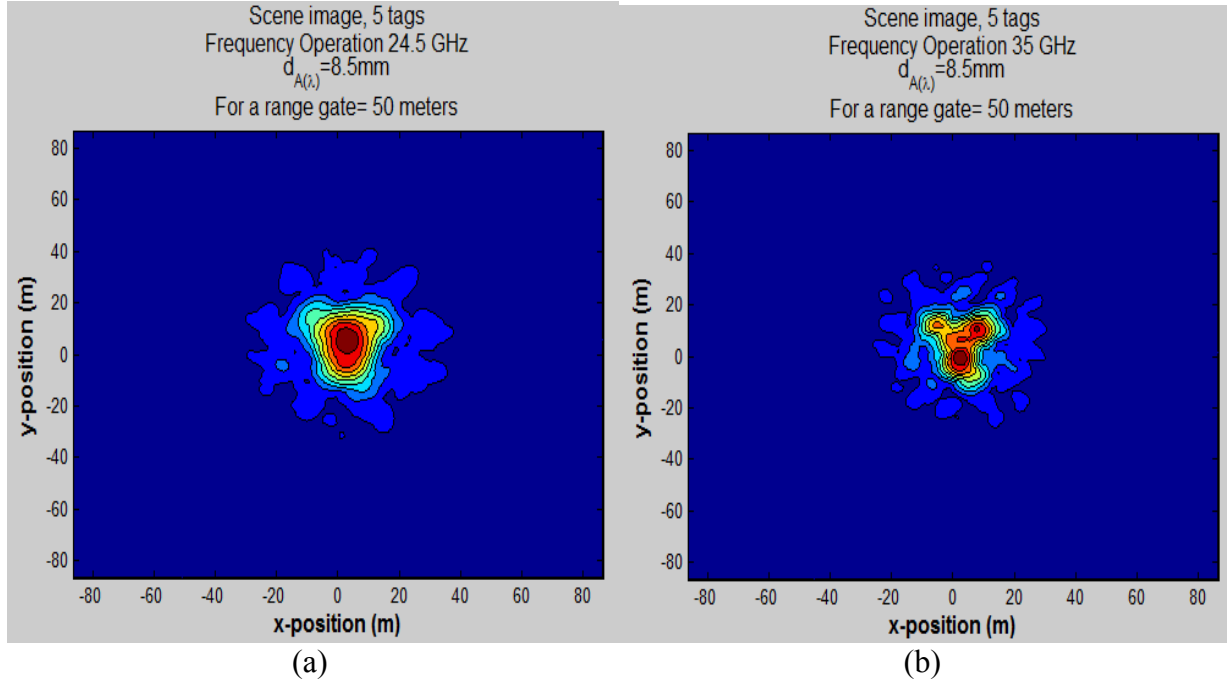


Fig. 3.34. (a) Scene image for five TAGs for $f_{o(1)} = 24.5$ GHz and 50 m range gate,
(b) 5-TAG Scene image for $f_{o(2)} = 35$ GHz and 50 m range gate.

B. Simulations protocols. Case 2: MSF processing for complete data correlation matrix (that involve correlations between elements of the same arm).

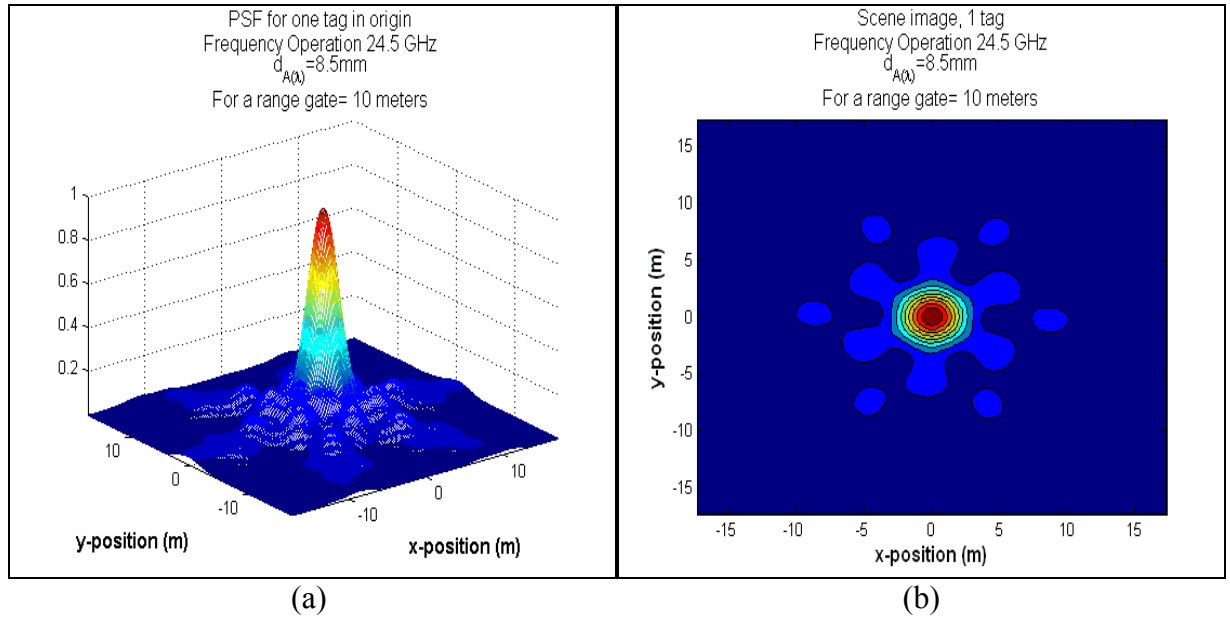


Fig. 3.35. (a) Point Spread Function for $f_{o(1)} = 24.5\text{GHz}$;
(b) Scene image for a single TAG in the origin.

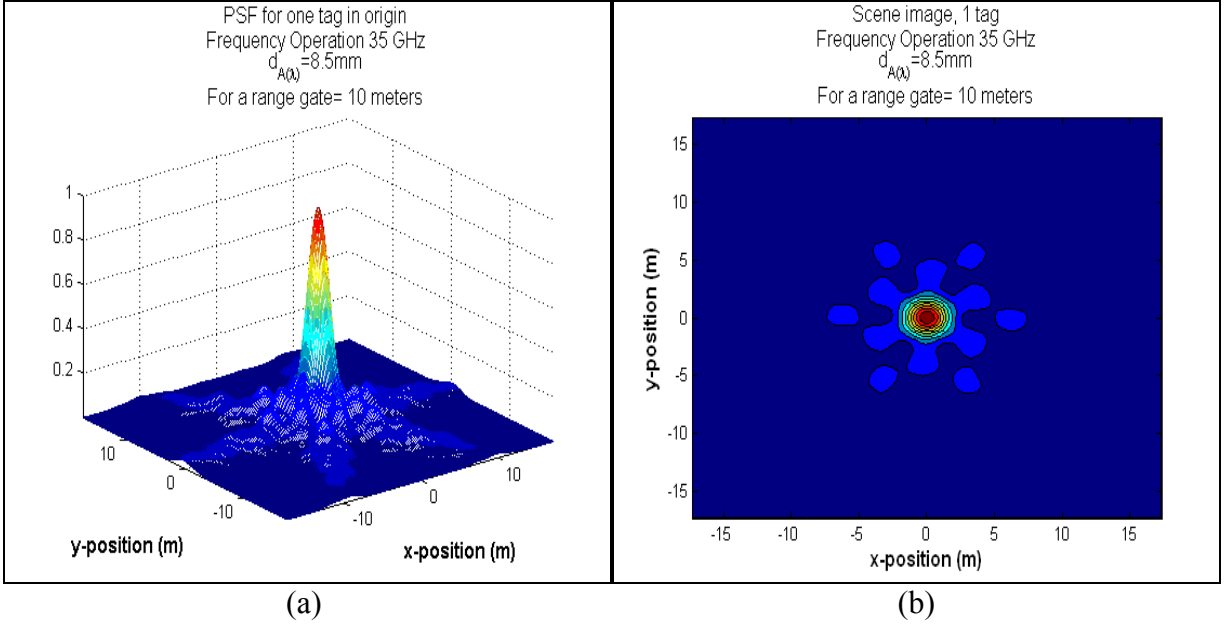


Fig. 3.36. (a) Point Spread Function for $f_{o(2)} = 35$ GHz;
(b) Scene image for a single TAG in the origin.

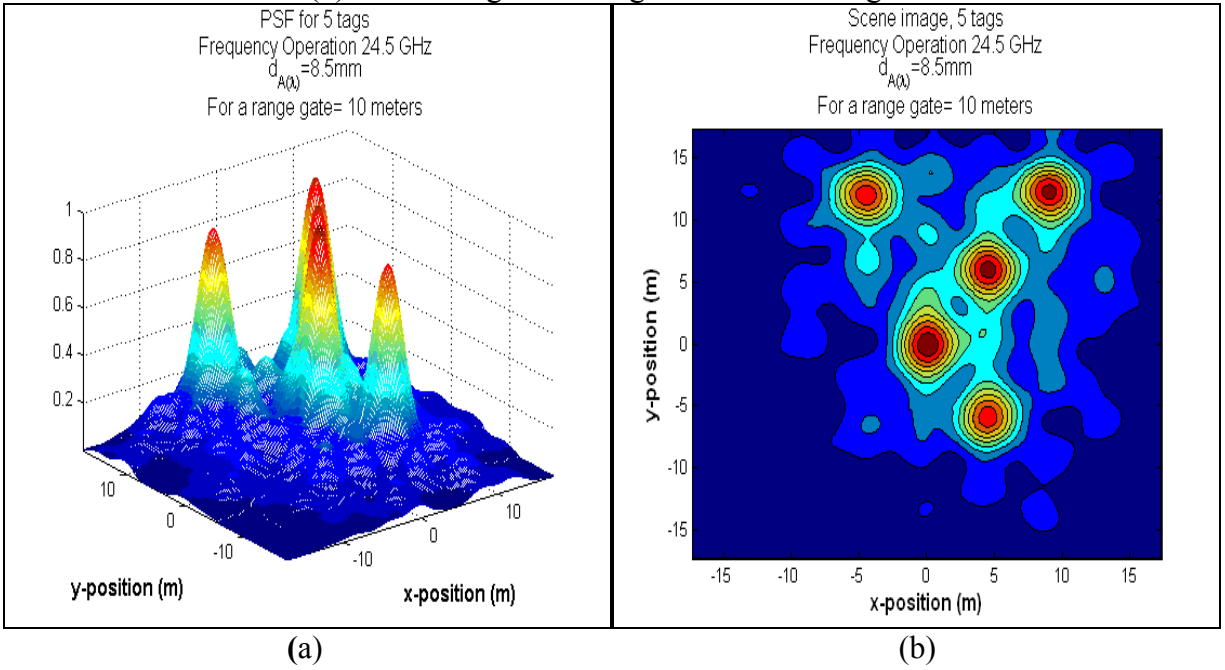
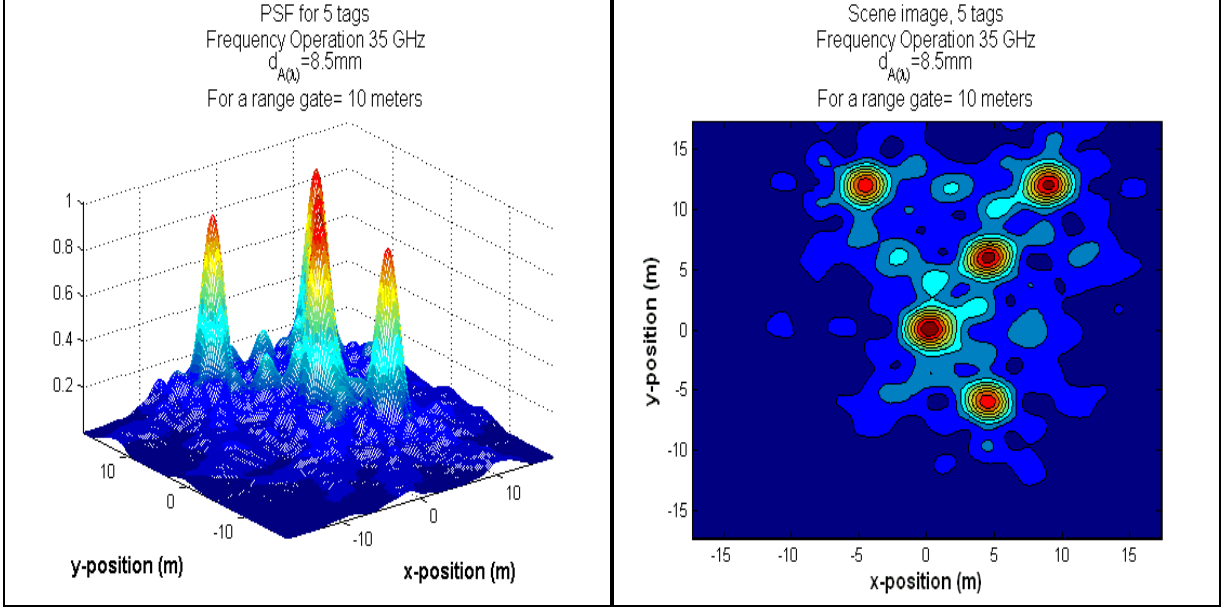
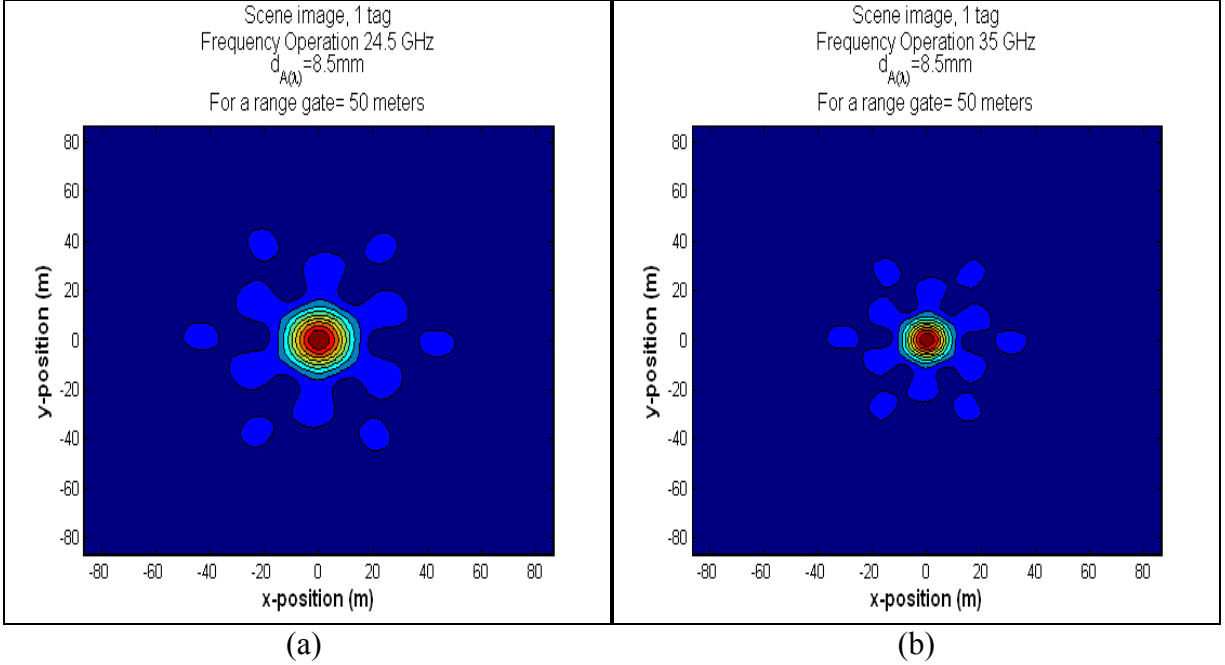


Fig. 3.37. (a) 3-D imaging system output for $f_{o(1)} = 24.5$ GHz and 5 TAGs;
(b) 5-TAG Scene image for the same SP specifications.



(a) (b)
Fig. 3.38. (a) 3-D imaging system output for $f_{o(2)} = 35$ GHz and 5 TAGs;
(b) 5-TAG Scene image for the same SP specifications.



(a) (b)
Fig. 3.39. (a) Scene image for a single TAG for $f_{o(1)} = 24.5$ GHz and 50 m range gate;
(b) Scene image for a single TAG for $f_{o(2)} = 35$ GHz and 50 m range gate.

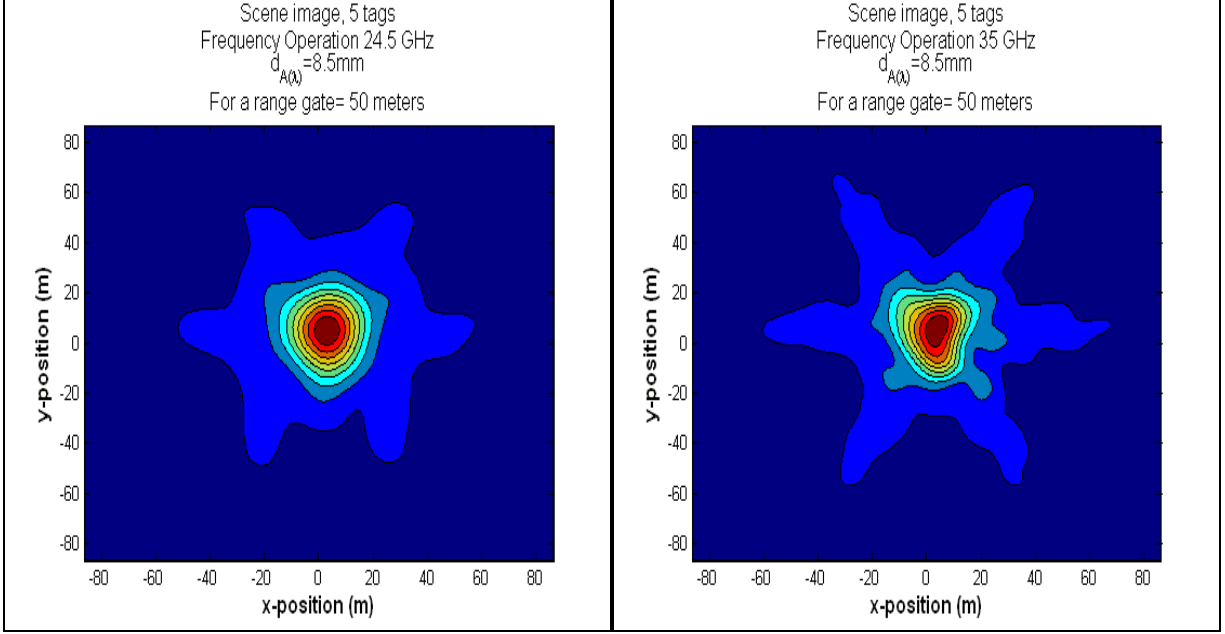


Fig. 3.40. (a) Scene image for five TAGs for $f_{o(1)} = 24.5$ GHz and 50 m range gate;
(b) 5-TAG Scene image for $f_{o(2)} = 35$ GHz and 50 m range gate.

3.4.3 Simulations Protocols – 3

Preliminary Specifications:

- Inter-element spacing = 12.25 mm (recommended by the TAMU team).
- Two types of correlation matrix employed in the MSF SP algorithm: complete and DEDR-optimally sparse data signal correlation matrices.
- Tested range gates: 10 m and 50 m.

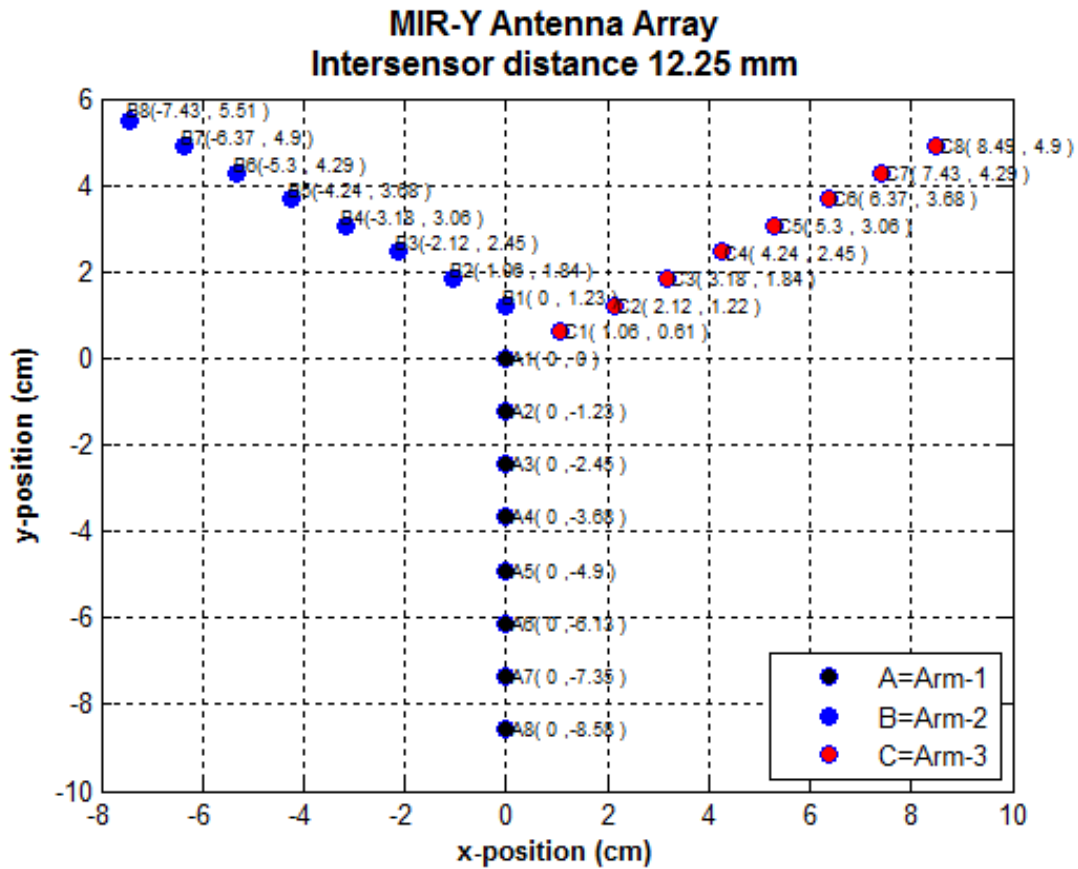
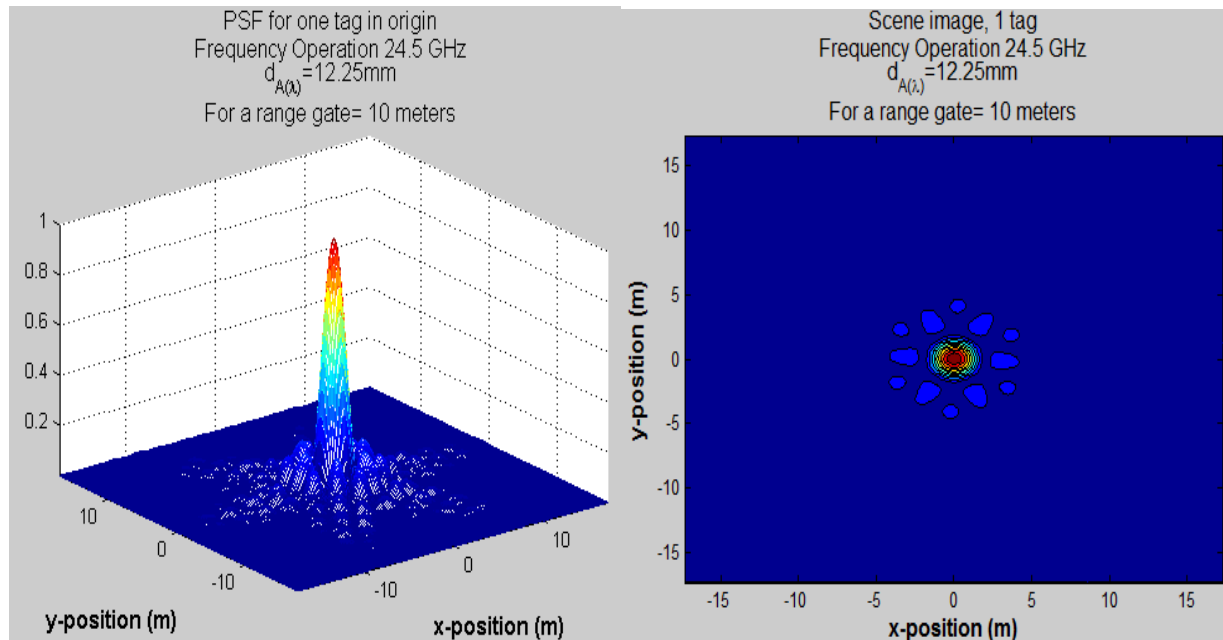


Fig. 3.41. Antenna array layout for interelement spacing = 12.25 mm.

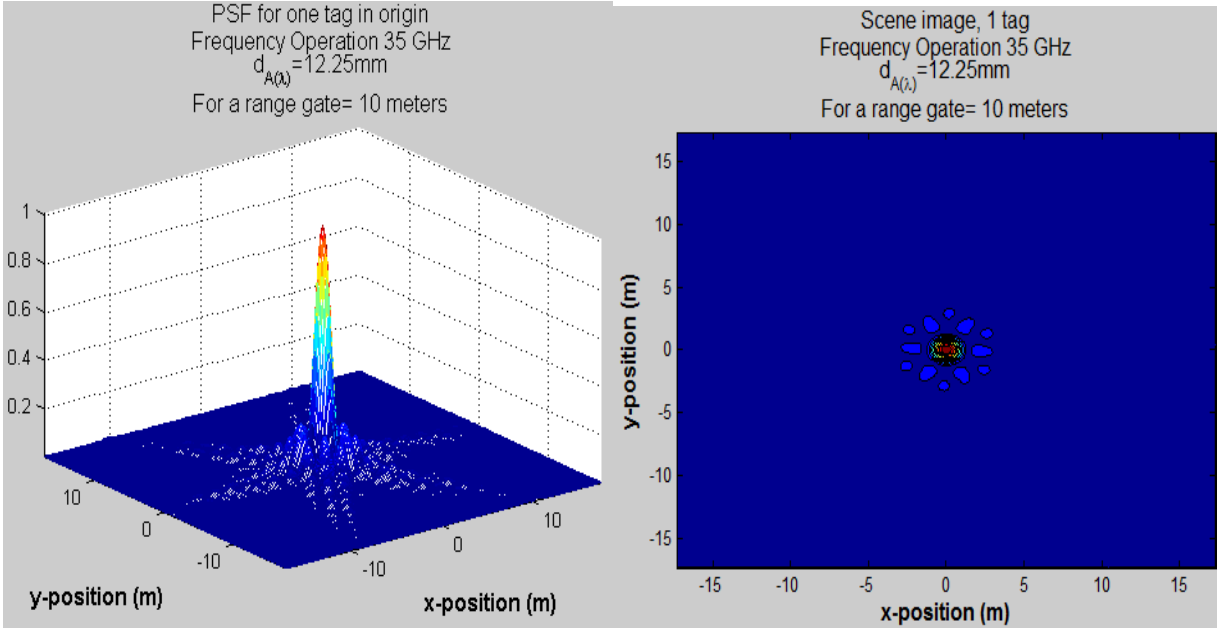
A. Simulations protocols. Case 1: MSF processing for incomplete data correlation matrix (DEDR-optimally sparse).



(a)

(b)

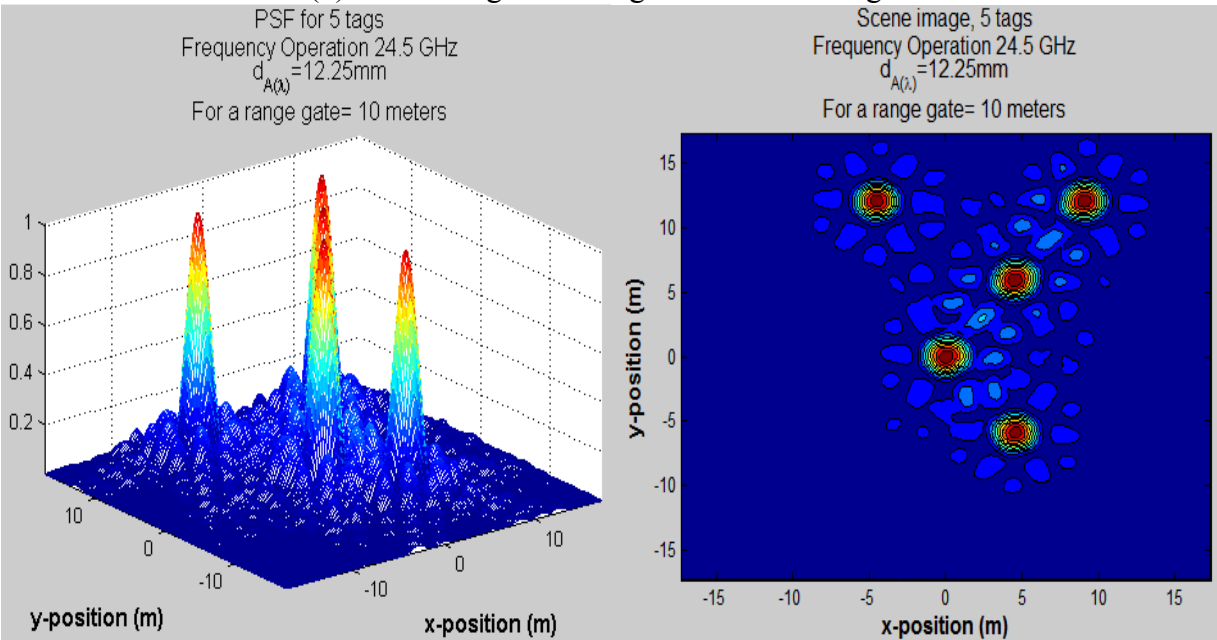
Fig. 3.42. (a) Point Spread Function for $f_{o(1)} = 24.5\text{GHz}$;
(b) Scene image for a single TAG in the origin.



(a)

(b)

Fig. 3.43. (a) Point Spread Function for $f_{o(2)} = 35\text{ GHz}$;
(b) Scene image for a single TAG in the origin.



(a)

(b)

Fig. 3.44. (a) 3-D imaging system output for $f_{o(1)} = 24.5\text{ GHz}$ and 5 TAGs;
(b) 5-TAG Scene image for the same SP specifications.

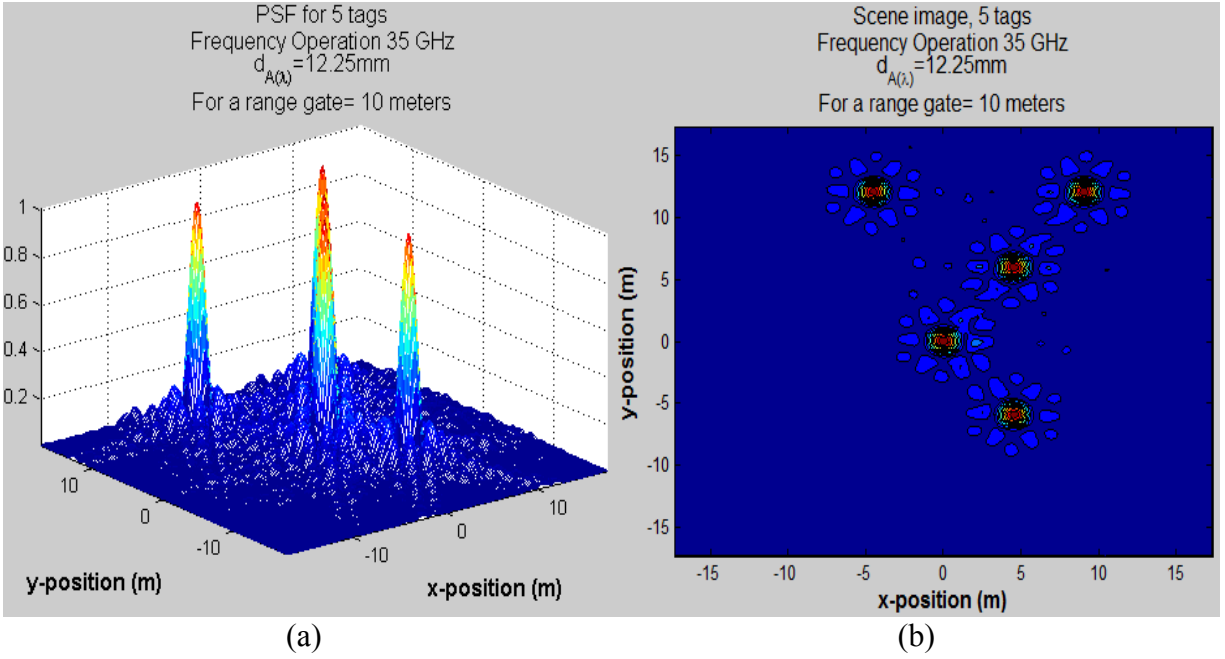


Fig. 3.45. (a) 3-D imaging system output for $f_{o(2)} = 35$ GHz and 5 TAGs;
(b) 5-TAG Scene image for the same SP specifications.

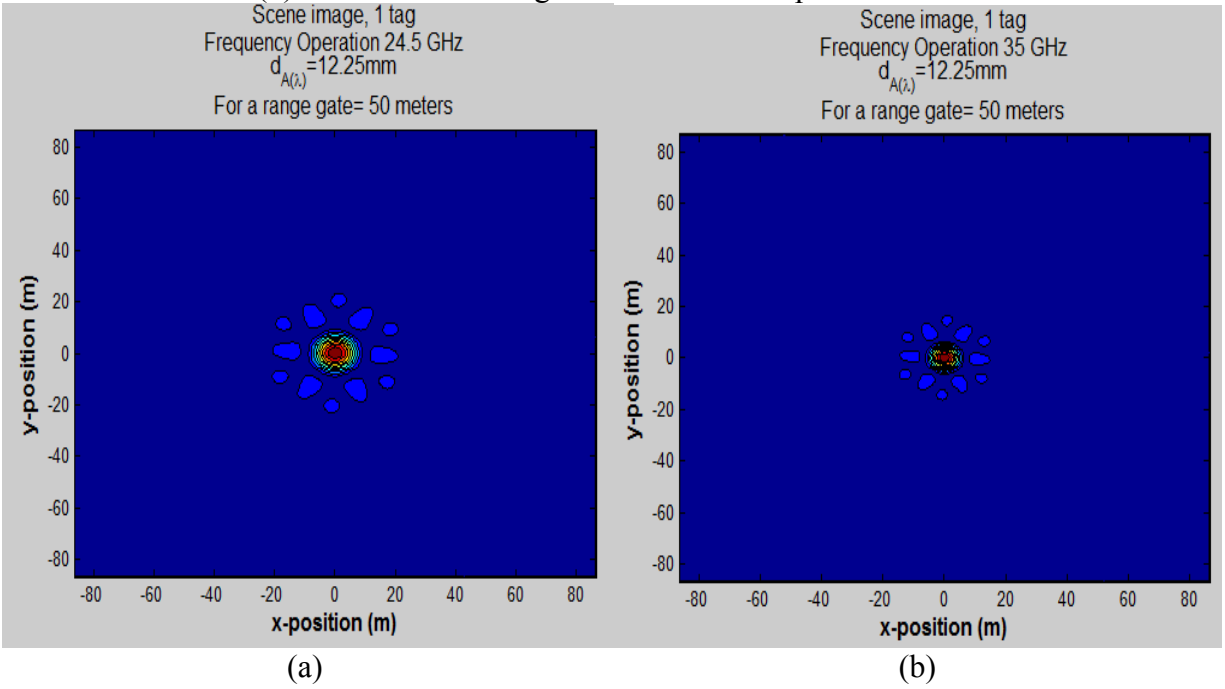


Fig. 3.46. (a) Scene image for a single single TAG for $f_{o(1)} = 24.5$ GHz and 50 m range gate;
(b) Scene image for a single TAG for $f_{o(2)} = 35$ GHz and 50 m range gate.

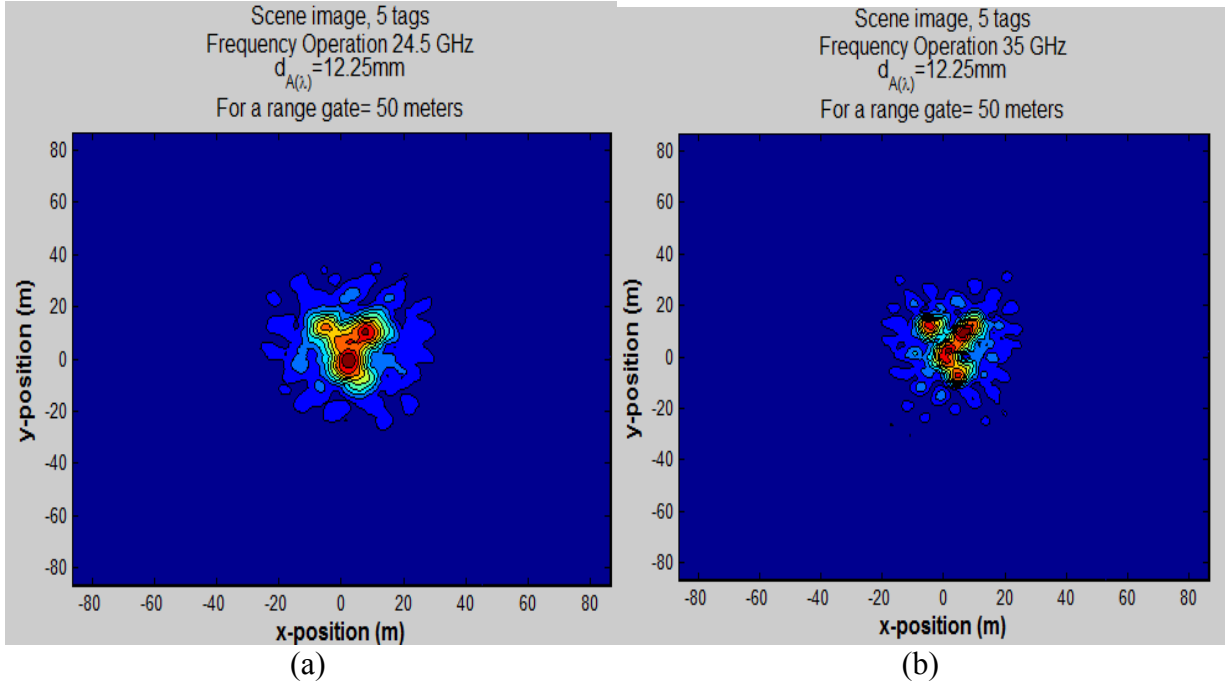


Fig.3.47. (a) Scene image for five TAGs for $f_{o(1)} = 24.5$ GHz and 50 m range gate;
 (b) 5-TAG Scene image for $f_{o(2)} = 35$ GHz and 50 m range gate.

B. Simulations protocols. Case 2: MSF processing for complete data correlation matrix (that involve correlations between elements of the same arm).

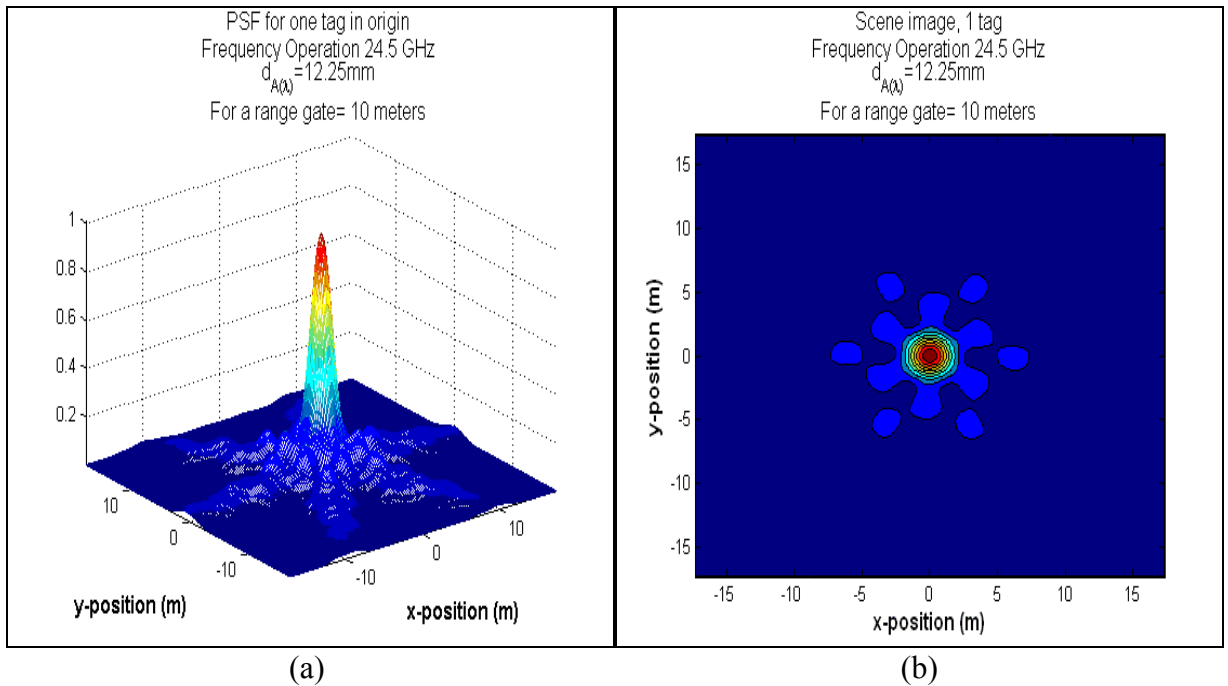
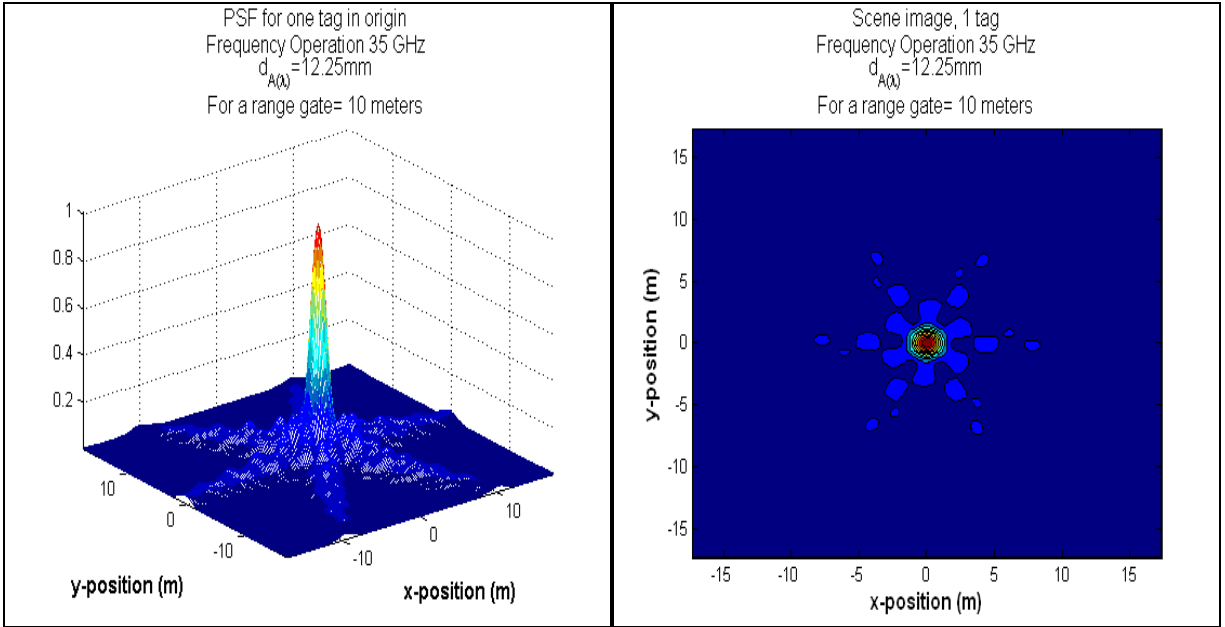


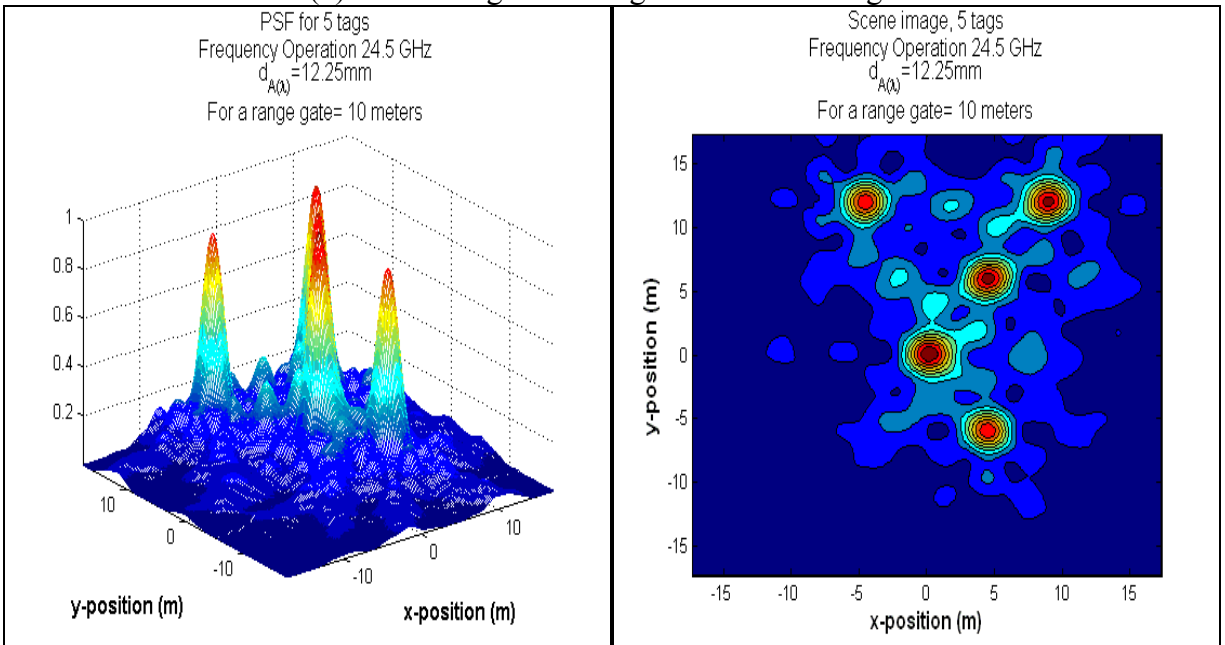
Fig. 3.48. (a) Point Spread Function for $f_{o(1)} = 24.5\text{GHz}$;
 (b) Scene Image for of a single TAG in the origin.



(a)

(b)

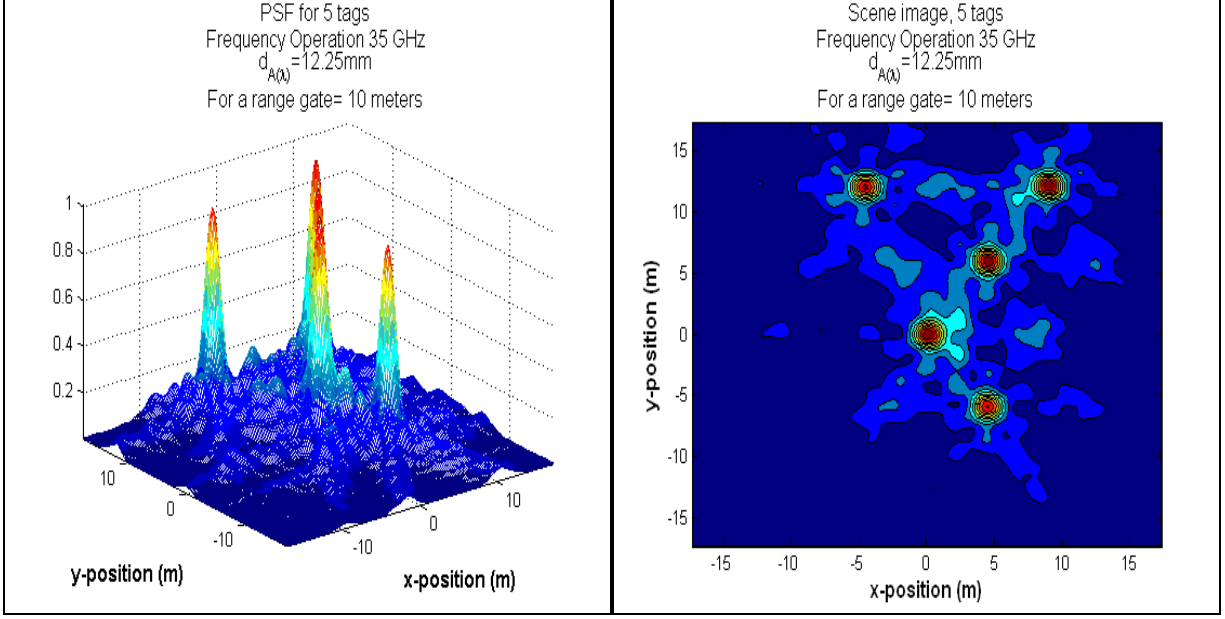
Fig. 3.49. (a) Point Spread Function for $f_{o(2)} = 35\text{ GHz}$;
(b) Scene image for a single TAG in the origin.



(a)

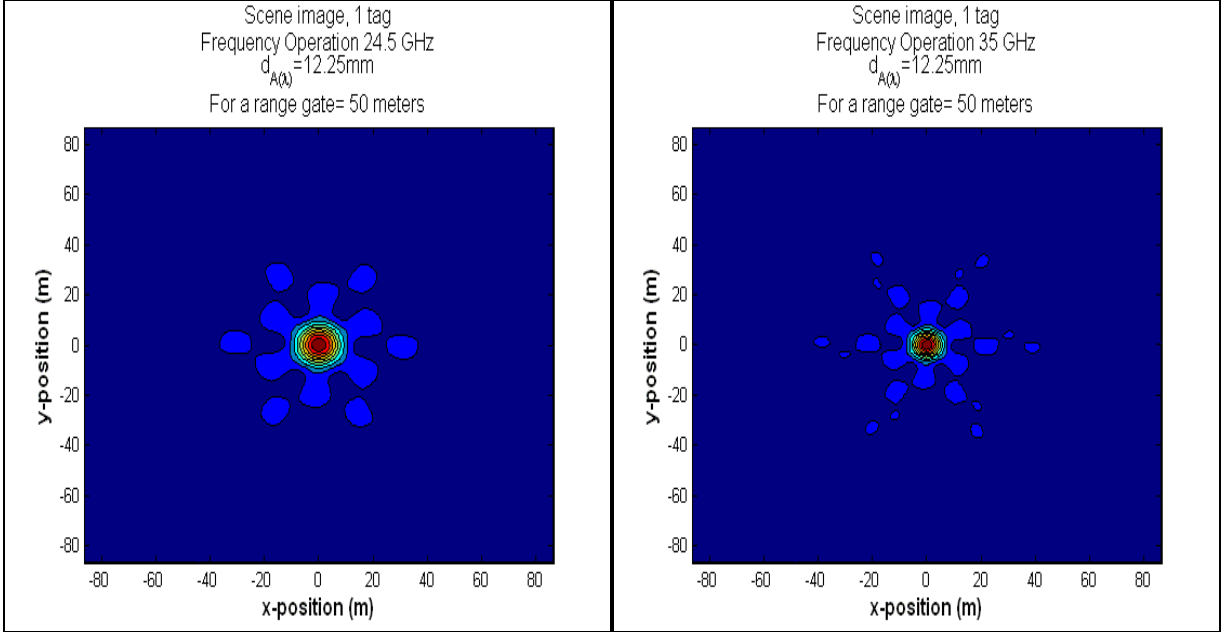
(b)

Fig. 3.50. (a) 3-D imaging system output for $f_{o(1)} = 24.5\text{ GHz}$ and 5 TAGs;
(b) 5-TAG Scene image for the same SP specifications.



(a) (b)

Fig. 3.51. (a) 3-D imaging system output for $f_{o(2)} = 35$ GHz and 5 TAGs;
(b) 5-TAG Scene image for the same SP specifications.



(a) (b)

Fig. 3.52. (a) Scene image for a single TAG for $f_{o(1)} = 24.5$ GHz and 50 m range gate;
(b) Scene image for a single TAG for $f_{o(2)} = 35$ GHz and 50 m range gate.

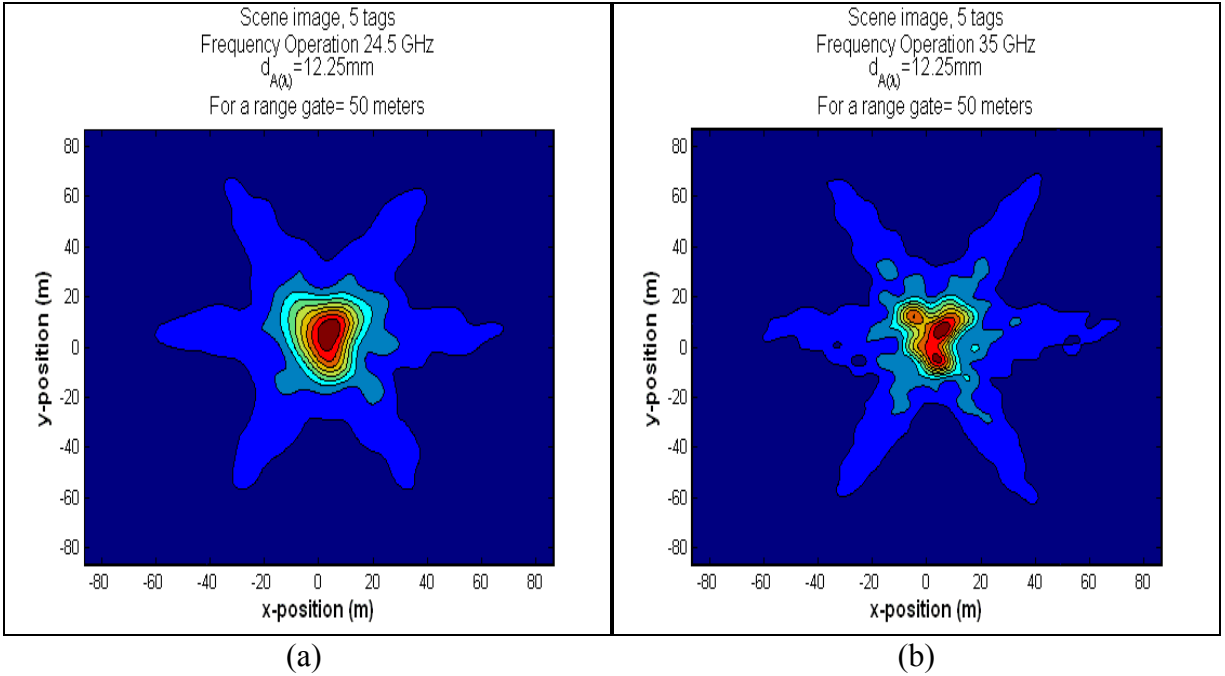


Fig. 3.53. (a) Scene image for five TAGs and $f_{o(1)} = 24.5$ GHz and 50 m range gate; (b) 5-TAG Scene image for $f_{o(2)} = 35$ GHz and 50 m range gate.

3.4.4 Simulations Protocols – 4

Preliminary Specifications:

- Interelement spacing = 12.25 mm (recommended by the CINVESTAV-Guadalajara SW development team).
- Two types of correlation matrix employed in the MSF SP algorithm: complete and DEDR-optimally sparse data signal correlation matrices.
- Tested range gates: 10 m and 50 m.

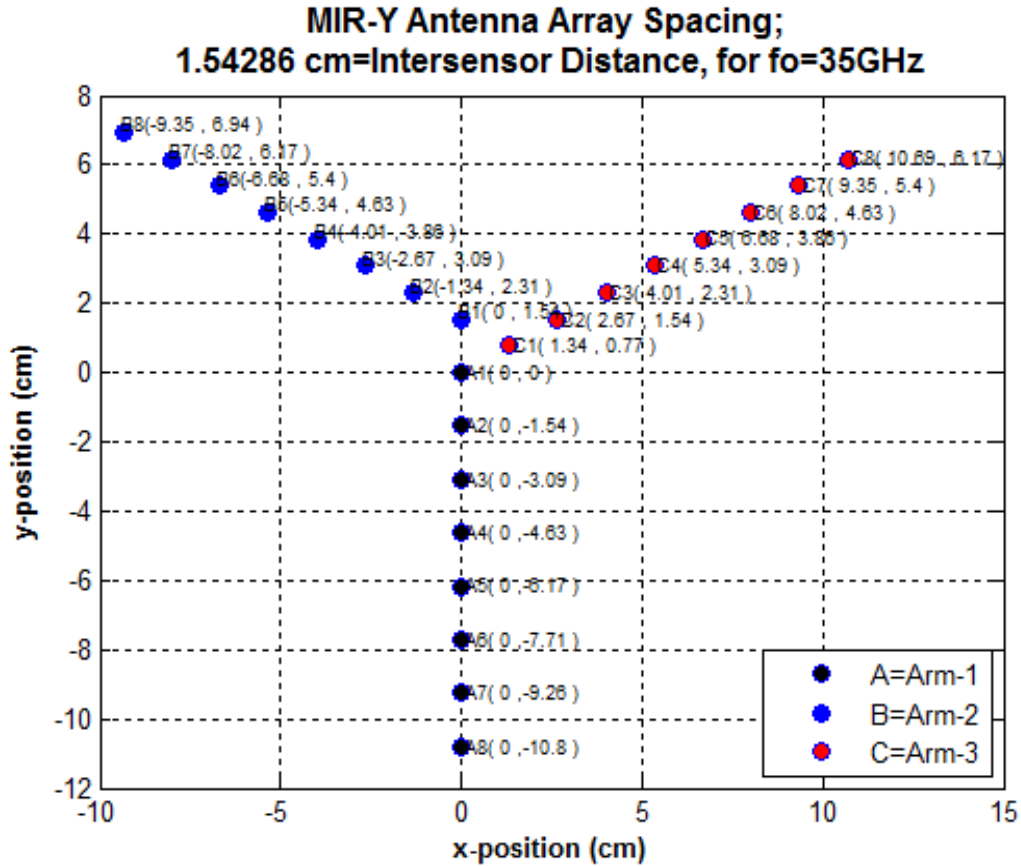
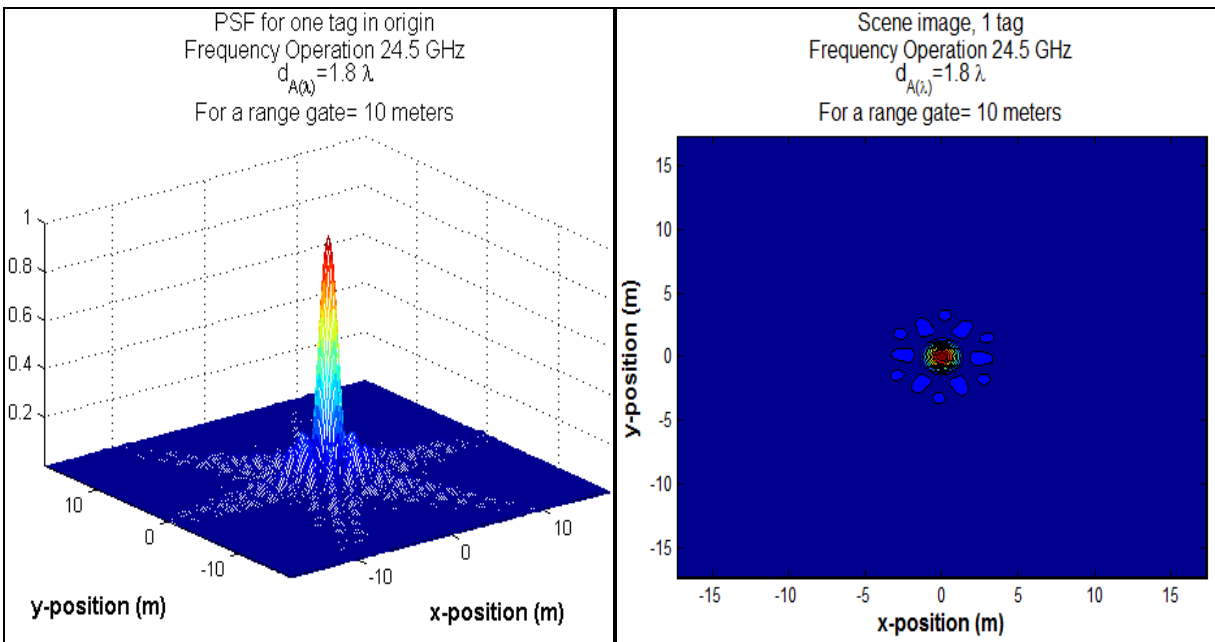
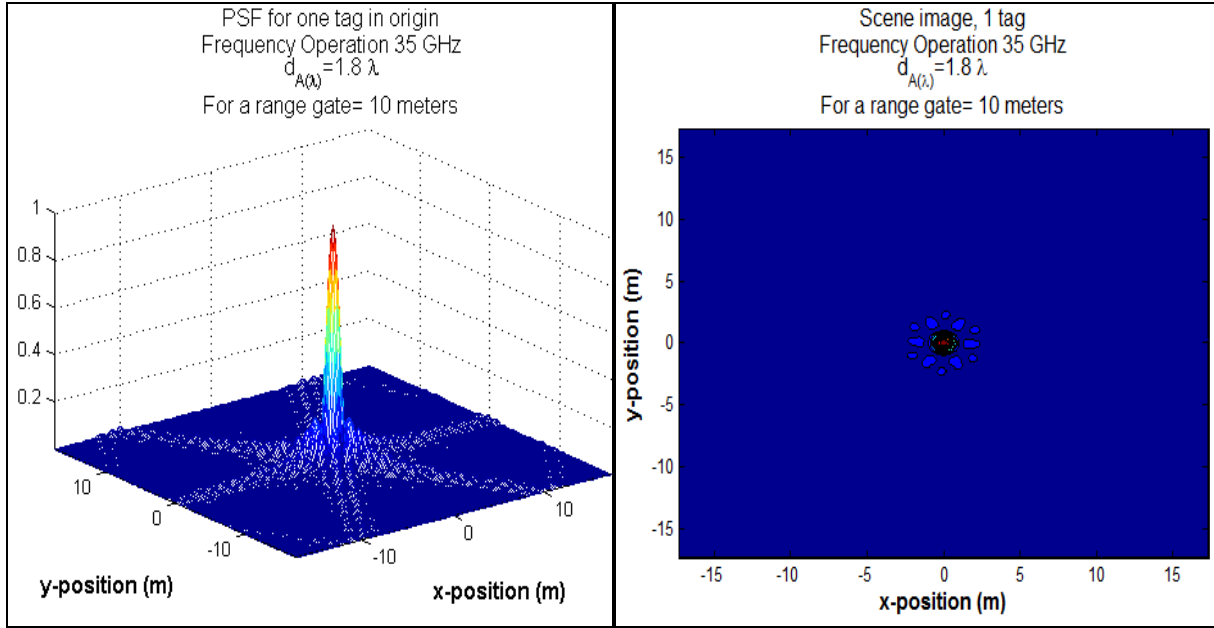


Fig. 3.54. Antenna array layout for interelement spacing = 15.429 mm.

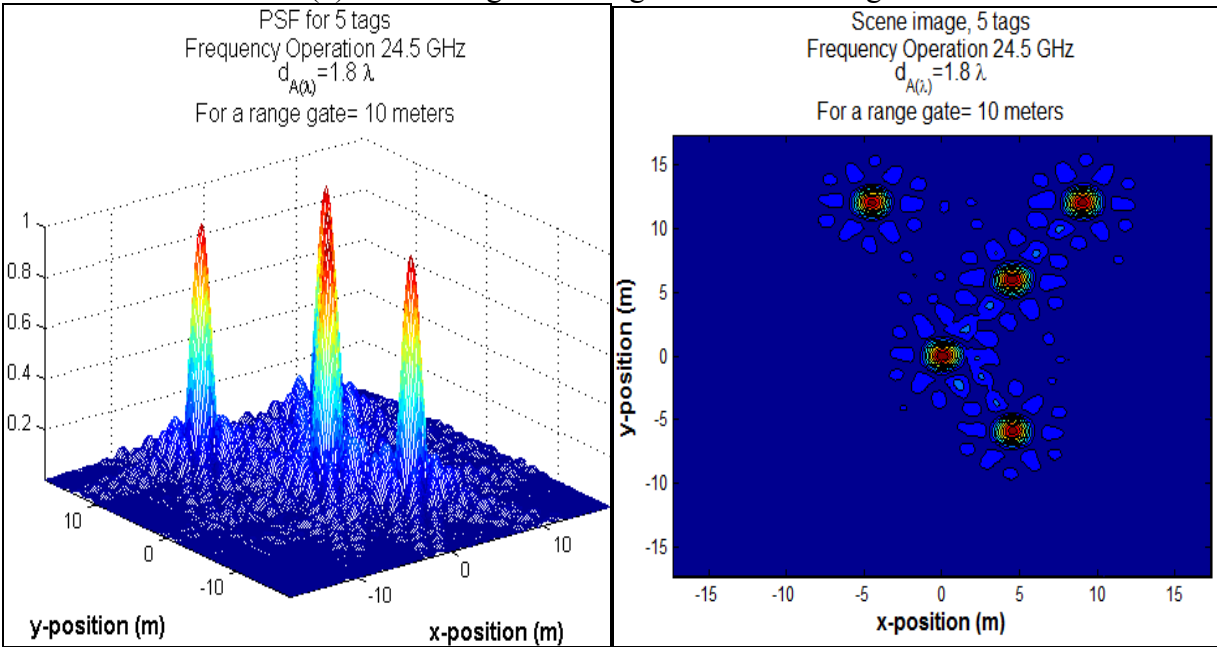
A. Simulations protocols. Case 1: MSF processing for incomplete data correlation matrix (DEDR-optimally sparse).



(a) (b)
Fig. 3.55. (a) Point Spread Function for $f_{o(1)} = 24.5\text{GHz}$;
(b) Scene image for a single TAG in the origin.



(a) (b)
Fig. 3.56. (a) Point Spread Function for $f_{o(2)} = 35\text{ GHz}$;
(b) Scene image for a single TAG in the origin.



(a) (b)
Fig. 3.57. (a) 3-D imaging system output for $f_{o(1)} = 24.5\text{ GHz}$ and 5 TAGs;
(b) 5-TAG Scene image for the corresponding specifications.

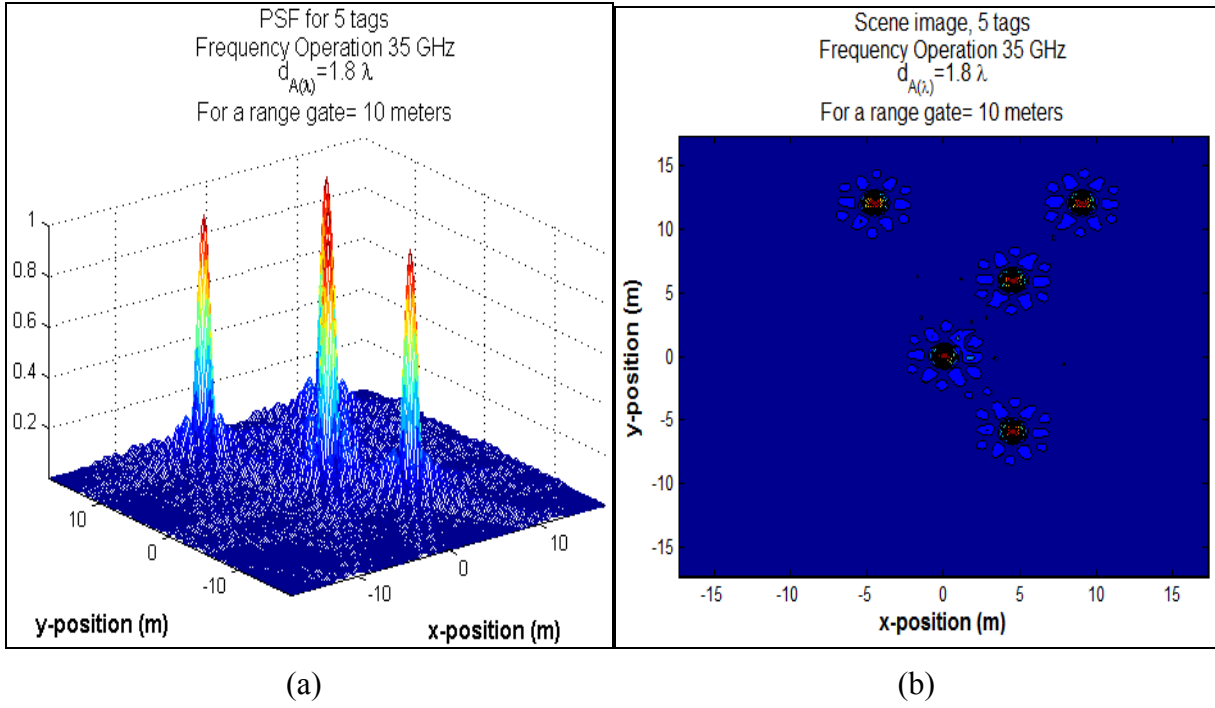


Fig. 3.58. (a) 3-D imaging system output for $f_{o(2)} = 35$ GHz and 5 TAGs;
(b) 5-TAG Scene image for the corresponding specifications.

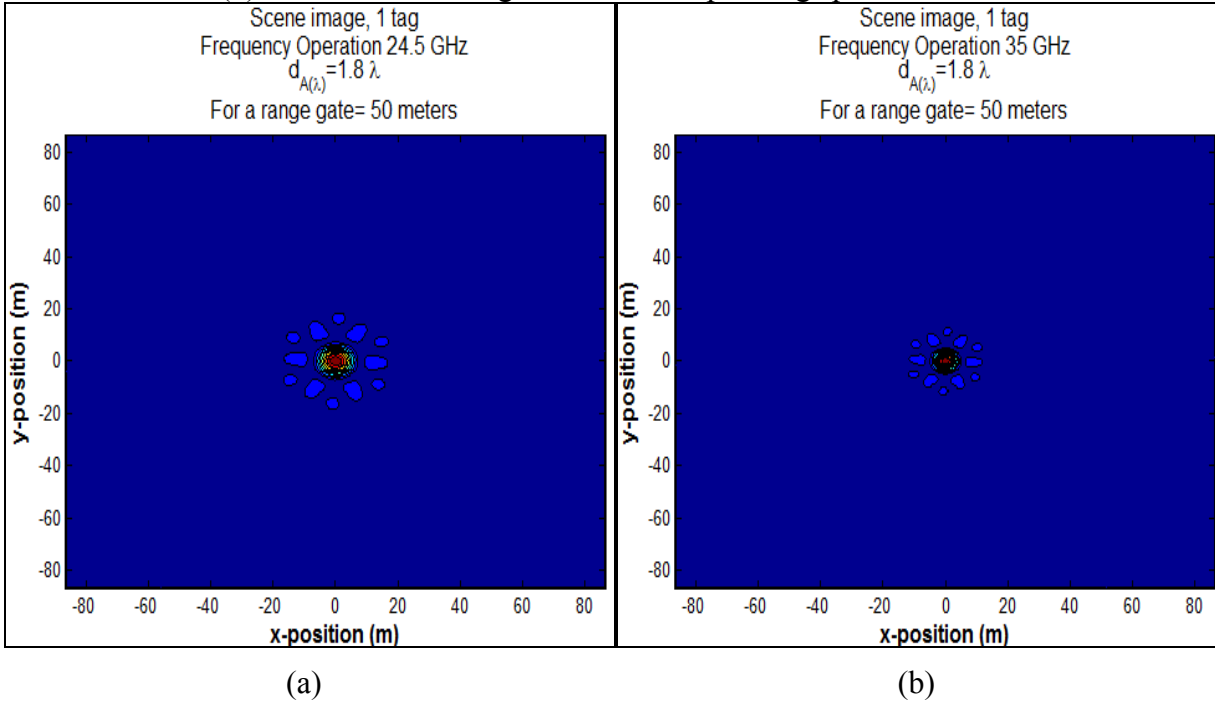


Fig. 3.59. (a) Scene image for a single TAG for $f_{o(1)} = 24.5$ GHz and 50 m range gate;
(b) Scene image for a single TAG for $f_{o(2)} = 35$ GHz and 50 m range gate.

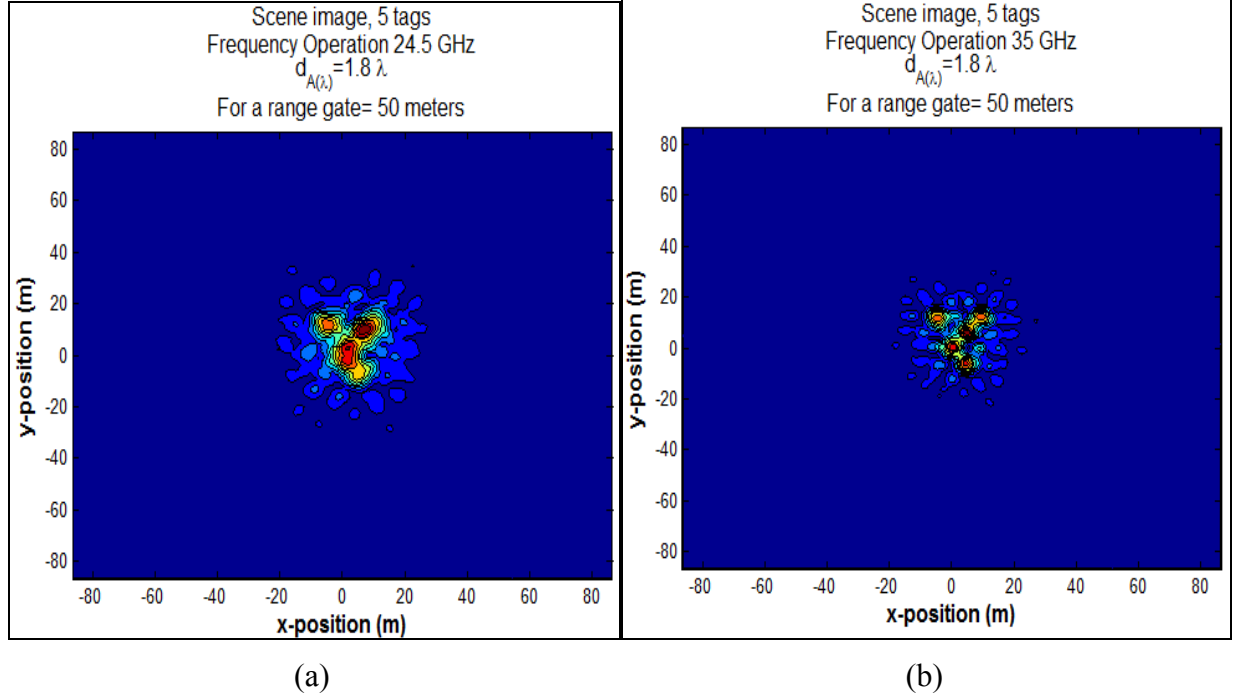


Fig. 3.60. (a) Scene image for five TAGs for $f_{o(1)} = 24.5$ GHz and 50 m range gate;
 (b) 5-TAG Scene image for $f_{o(2)} = 35$ GHz and 50 m range gate.

B. Simulations protocols. Case 2: MSF processing for complete data correlation matrix (that involve correlations between elements of the same arm).

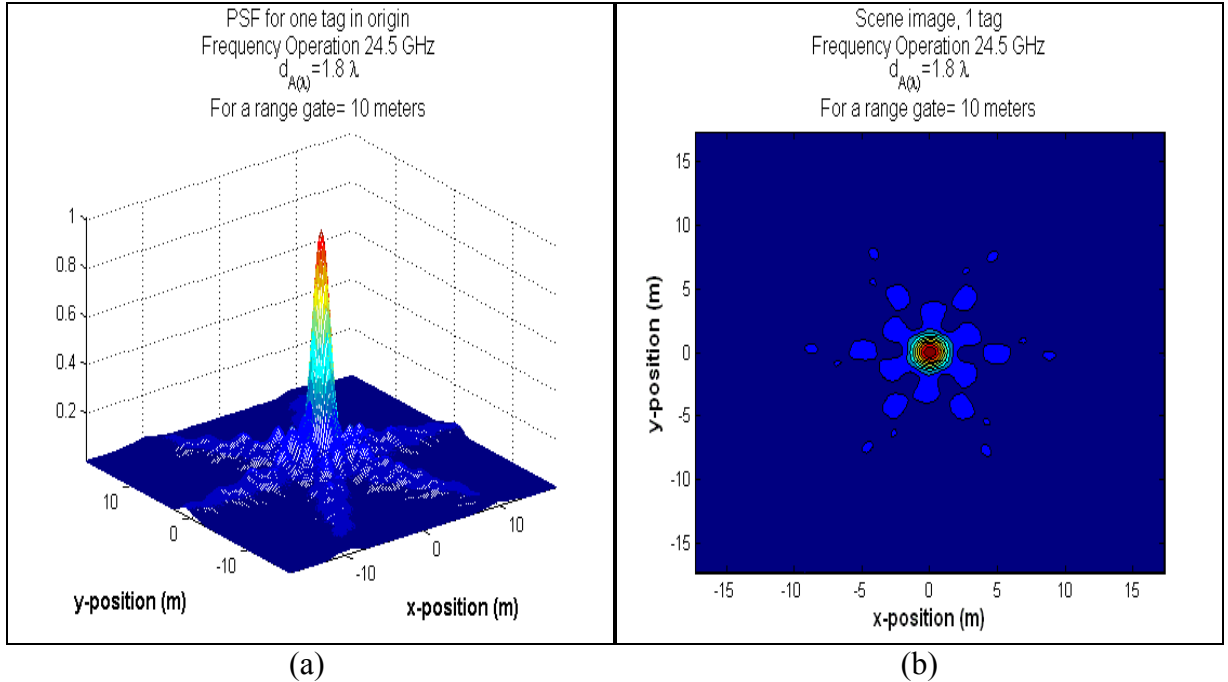
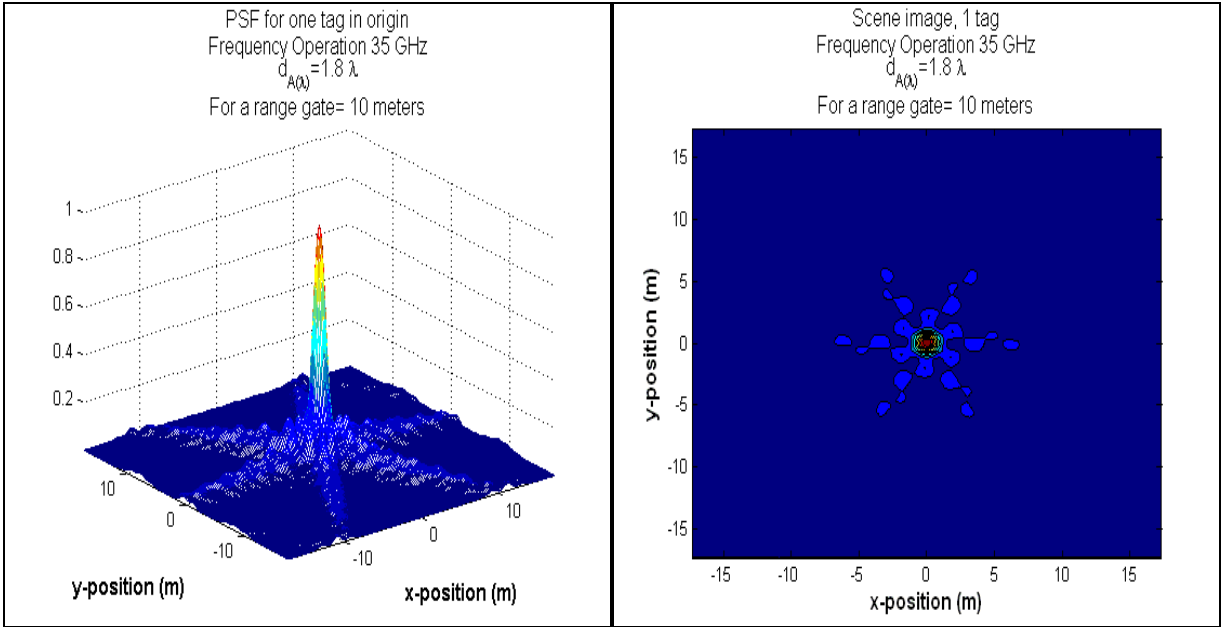


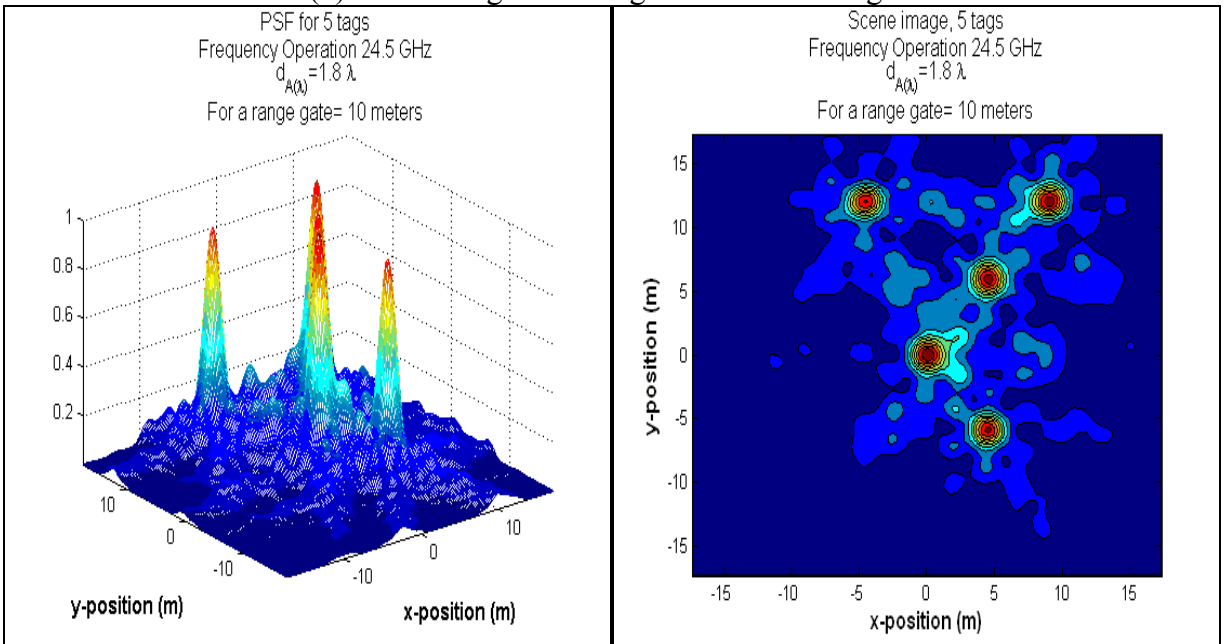
Fig. 3.61. (a) Point Spread Function for $f_{o(1)} = 24.5$ GHz;
 (b) Scene image for a single TAG in the origin.



(a)

(b)

Fig. 3.62. (a) Point Spread Function for $f_{o(2)} = 35$ GHz;
(b) Scene image for a single TAG in the origin.



(a)

(b)

Fig. 3.63. (a) 3-D imaging system output for $f_{o(1)} = 24.5$ GHz and 5 TAGs;
(b) 5-TAG Scene image for the corresponding specifications.

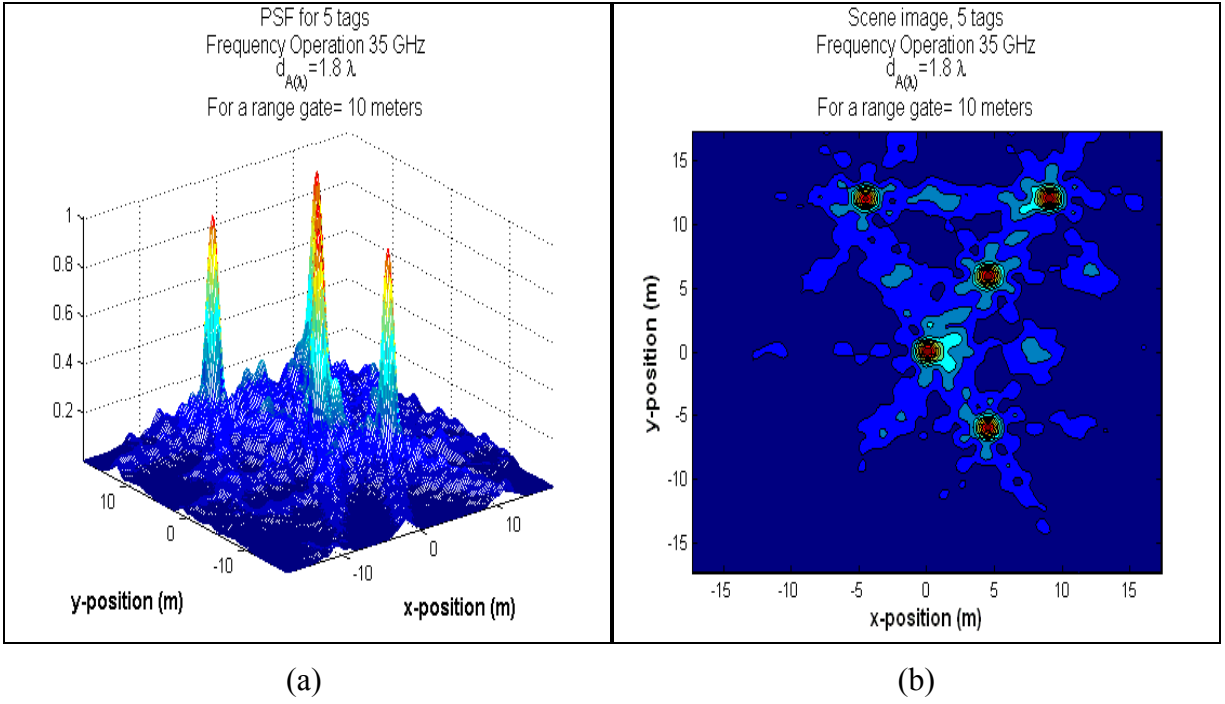


Fig. 3.64. (a) 3-D imaging system output for $f_{o(2)} = 35$ GHz and 5 TAGs;
(b) 5-TAG Scene image for the corresponding specifications.

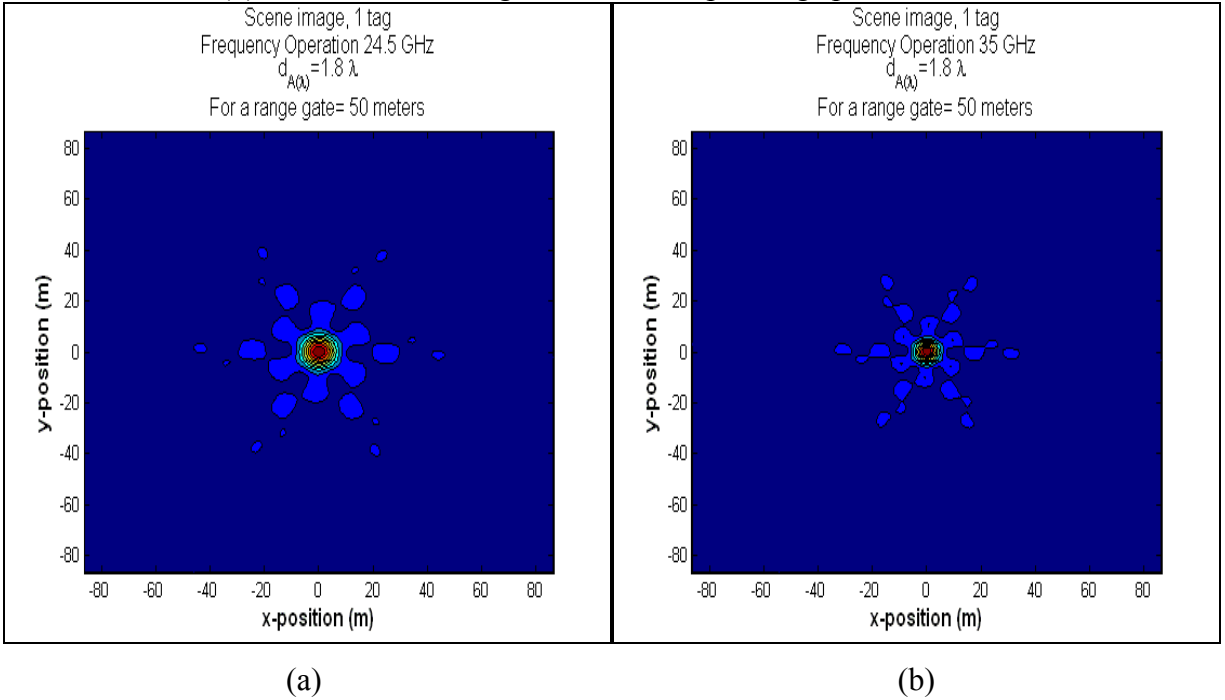


Fig. 3.65. (a) Scene image for a single TAG for $f_{o(1)} = 24.5$ GHz and 50 m range gate;
(b) Scene image for a single TAG for $f_{o(2)} = 35$ GHz and 50 m range gate.

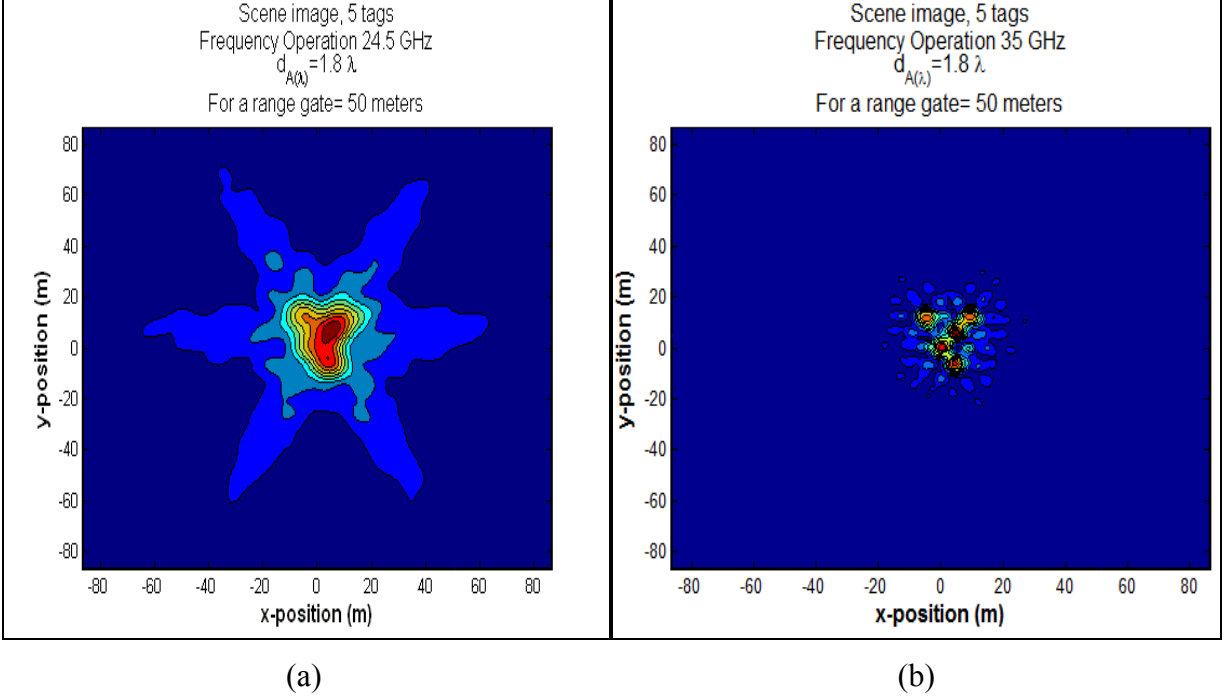


Fig.3.66. (a) Scene image for five TAGs for $f_{o(1)} = 24.5$ GHz and 50 m range gate;
(b) 5-TAG Scene image for $f_{o(2)} = 35$ GHz and 50 m range gate.

3.5. Resuming Summary of Part III

We have elaborated and reported the HW/SW co-designed signal processing (SP), data acquisition and archiving protocols accompanied with the corresponding test sensor simulations results that evaluate the functionality and reliability of the elaborated VRSL SW developed in conceptual connection with such HW-SW co-design based on the DEDR signal/image processing framework developed and detailed in Part II. The performed simulations experiments are particularly oriented at the sensor system HW under current development by the TAMU HW design team. The required test binary data files have been composed of continuous simulated data streams for a variety of feasible tested operational scenarios specifications following the developed SP data acquisition, storing and archiving protocols. At this final stage of research, we present the following concluding remarks.

- To make all the test data files identifiable to each other, each generated binary data file owns a unique file name. The required file syntax has been specified (see Table 3.4), and the reliability of the developed data acquisition, storing and archiving protocols was validated via performed simulations experiments. The code for binary data files generation, storing and archiving is presented in Appendix A.
- The simulations test experiment protocols reported in Section 3.2 present the results of evaluation of the attainable resolution performances of the developed DEDR-related robust MSF signal processing technique for RS image formation characterized via the resulting point spread function(s) (PSF's) provided by the GeoSTAR-configured sensor system for a variety of feasible sensor geometries (inter element spicing) for both tested operational frequency bands, $f_{o(1)} = 24.5$ GHz and $f_{o(2)} = 35$ GHz, respectively. The resulting PSF's and the related resolution performances were evaluated through extended

computer simulations experiments. The presented target localization protocols are indicative of the considerably superior operational efficiency provided with the GeoSTAR-configured multisensor imaging radar system that employs the developed DEDR-optimized MSF signal processing technique with the DEDR-optimally sparse test data correlation matrices. The simulations protocols have been reported in a graphical form in Section 3.2.

- The simulations were performed for 4 feasible tested interelement spacing, namely, $d_{A(1)} = 4$ mm, $d_{A(2)} = 8$ mm, $d_{A(3)} = 12.25$, (all these specified by the TAMU HW development team) and $d_{A(4)} = 1.8\lambda_{o(2)} = 15.43$ mm (recommended by the CINVESTAV-Guadalajara SP design team). The highest resolution performances and imaging quality have been attained for $d_{A(4)} = 1.8\lambda_{o(2)}$ for both frequency bands. The reported test simulation results are indicative of the SP efficiency of the elaborated SW and its effectiveness for real-time RS image formation employing the GeoSTAR-configured sensor system HW under current development by the TAMU HW design team for a variety of the feasible tested SP operational scenarios.

SUMMARY

We provided, first, the necessary foundations, basic methodological and algorithmic developments related to the new hardware (HW) software (SW) codesign paradigm developed for the purposes of robust high-resolution processing of cross-polarization sensor data obtained from multiple sensor modalities aimed at high-resolution sensing, detection and localization of point-type targets in uncertain remote sensing (RS) environment. Our study verify that in the target localization scenario, the Y-shaped array (virtual synthetic GeoSTAR-configured array) provides the best operational performances in the sense of the compromise between the resulting resolution cell cross-section and artifacts due to the sidelobes and grating lobes in the resulting point spread function. Optimization of the Y-shaped array geometry via adjusting the interelement spacing and employing the directional sensors array were investigated and reported. The recommendations concerning the optimal array geometry were verified via reported extensive simulations.

Next, the descriptive experiment design regularization (DEDR) approach for high-resolution estimation of spatial remote sensing (RS) signature (RSS) fields has been developed as required for the purposes of high-resolution RS imaging, search, discovery, discrimination, mapping and problem-oriented analysis of the diverse RS data provided in the fractional SAR mode. First, we have established that to alleviate the RS imaging problem ill-posedness and reduce the overall computational load of the large-scale image enhancement/reconstruction tasks at the algorithmic processing level, some special form of descriptive experiment design projection-type numerical regularization must be employed. This stage was developed and addressed as the unified DEDR method, and the efficient fixed-point numerical iterative technique that incorporates the proper construction of the relevant orthogonally factorized regularizing projector onto convex sets (POCS) in the solution domain was designed and specified for the particular employed RS sensor system, namely, for the side-looking fractional synthetic aperture radar (SAR) operating in both certain and uncertain scenarios. We have also examined how such SAR-adapted POCS-regularized fixed-point iterative technique can be executed concurrently over the orthogonal range-azimuth coordinates with the optimal use of the sparseness properties of the overall SAR system point spread function characteristics. The algorithmic-level advantages of such unified DEDR-POCS-regularized RS image enhancement/reconstruction techniques relate to the theoretically guaranteed convergence of the corresponding fixed-point iterative process with the proper factorization of the numerical reconstructive procedures over the orthogonal range-azimuth directions in the representation image frame.

The extended descriptive experiment design regularization (DEDR) framework has been combined with the dynamic variational analysis (VA) approach for perceptually enhanced and considerably speeded up reconstruction of the RS imagery particularly adapted for the fractional SAR imaging system operating in the uncertain RS environment. Connections have been drawn between different types of optimization-based RS imaging approaches, and it has been established that the convex optimization-based unified DEDR-VA paradigm provides an indispensable toolbox for super-high resolution RS and multimode sensor imaging system design offering to the observer a possibility to control the order, the type and the amount of the employed two-level regularization (at the DEDR level and at the VA level, correspondingly). Algorithmically, this task is performed via construction of the proper POCS operators that unify

the desirable image metrical properties in the convex image/solution sets with the GeoSTAR sensor or fractional SAR motivated data processing considerations. We have developed the family of the efficient contractive progressive mapping iterative DEDR-related techniques for sensor data fusion with the corresponding computational recipes oriented at the neural network computational implementation. The end-user-oriented “Virtual Remote Sensing Laboratory” (VRSL) software (SW) was elaborated and employed in extended simulations experiments to verify, evaluate, and demonstrate the capabilities of the DEDR-related signal and image processing techniques including precise multiple target localization. Our analytical study and the simulations revealed that with the DEDR-related techniques, the overall RS imaging performances are improved if compared with those obtained using separately the most prominent despeckling, anisotropic diffusion or locally selective RS image reconstruction methods that do not employ the unified DEDR considerations. Therefore, the developed DEDR framework puts in a single optimization frame, imaging array radar/SAR focusing, speckle reduction and adaptive dynamic scene image enhancement performed in a consistent rapidly convergent fashion robust against the operational scenario uncertainties.

The test sensor simulations experiment was designed and performed to evaluate the functionality and reliability of the elaborated SW developed in conceptual connection with the HW-SW codesign paradigm. The performed simulations experiments are particularly oriented at the sensor system HW under current development by the TAMU HW design team. The required test binary data files have been composed of continuous simulated data streams for a variety of feasible tested operational scenarios following the developed SP data acquisition, storing and archiving protocols. To make all the test data files identifiable to each other, each generated binary data file owns a unique file name. The required file syntax has been specified, and the reliability of the developed data acquisition, storing and archiving protocols was validated via performed simulations experiments. The code for binary data files generation, storing and archiving is presented in Appendix A.

The simulations test experiment protocols reported in Section 2 of Part III present the results of evaluation of the attainable resolution performances of the developed DEDR-related robust MSF and FTST signal processing techniques for RS image formation characterized via the resulting point spread function(s) (PSF's) provided by the GeoSTAR-configured sensor system for a variety of feasible sensor geometries (interelement spicing) for both tested operational frequency bands, $f_{o(1)} = 24.5$ GHz and $f_{o(2)} = 35$ GHz, respectively. The resulting PSF's and the related resolution performances were evaluated through extended computer simulations experiments. The presented target localization protocols are indicative of the considerably superior operational efficiency provided with the GeoSTAR-configured multisensor imaging radar system that employs the developed DEDR-optimized MSF and FTST signal processing techniques with the DEDR-optimally sparse test data correlation matrices. All algorithmic and SW developments are sufficiently verified via simulations and the SW is ready to implement with the HW measurement data.

REFERENCES

- [1] S.E. Falkovich, V.I. Ponomaryov, and Y. V. Shkvarko, *Optimal Reception of Space-Time Signals in Channels With Scattering*, (in Russian), Moscow: Radio i Sviaz, 1989.
- [2] A. Farina, *Antenna-Based Signal Processing Techniques for Radar Systems*, Norwood, MA: Artech House Inc., 1991.
- [3] Shkvarko Y.V., Shmaliy Y.S., Jaime-Rivas R., Torres-Cisneros M. System fusion in passive sensing using a modified Hopfield network. *Journal of the Franklin Institute*, Vol. 338, pp. 405-427, 2001.
- [4] H.L. Van Trees, *Detection, Estimation and Modulation Theory, Part IV, Optimum Array Processing*. New York: Willey, 2002.
- [5] H.H. Barrett and K.J. Myers, *Foundations of Image Science*, New York: Willey, 2004.
- [6] Y.V. Shkvarko, "Estimation of wavefield power distribution in the remotely sensed environment: Bayesian maximum entropy approach", *IEEE Trans. Signal Proc.*, vol. 50, No. 9, pp. 2333-2346, Sep. 2002.
- [7] Y.V. Shkvarko, "Unifying regularization and Bayesian estimation methods for enhanced imaging with remotely sensed data—Part I: Theory", *IEEE Trans. Geoscience and Remote Sensing*, vol. 42, No. 5, pp. 923-931, May 2004.
- [8] Y.V. Shkvarko, "Unifying regularization and Bayesian estimation methods for enhanced imaging with remotely sensed data—Part II: Implementation and performance issues", *IEEE Trans. Geoscience and Remote Sensing*, vol. 42, No. 5, pp. 932-940, May 2004.
- [9] S. Haykin, "Cognitive radar", *IEEE Signal Proc. Magazine*, vol. 23, No. 1, pp. 30-40, Jan. 2006.
- [10] Y.V. Shkvarko, "From matched spatial filtering towards the fused statistical descriptive regularization method for enhanced radar imaging", *EURASIP J. Applied Signal Processing*, vol. 2006, Article ID 39657, pp. 1-9, 2006.
- [11] A.B. Tanner, *et al.*, "Prototype Development of a Geostationary Synthetic Thinned Aperture Radiometer, GeoSTAR", *IEEE Intern. Symposium on Geoscience and Remote Sensing, IEEE IGARSS 2004*, ISBN 0-7803-8742-2/04, pp. 1256-1259, 2004.
- [12] A.B. Tanner, *et al.*, "Initial Results of the Geosynchronous Synthetic Thinned Aperture Radiometer (GeoSTAR)", *IEEE Intern. Symposium on Geoscience and Remote Sensing, IEEE IGARSS 2006*, ISBN 0-7803-9510-7/06, pp. 3951-3954, 2006.
- [13] Perona P., Malik J.: Scale-space and edge detection using anisotropic diffusion, *IEEE Trans. Pattern Anal. Machine Intell*, Vol. 12, No. 7, pp. 629-639, 1990.
- [14] John S., Vorontsov M.A.: Multiframe selective information fusion from robust error theory. *IEEE Trans. Image Proc*, Vol. 14, No. 5, pp. 577-584, 2005.

- [15] Castillo-Atoche A., Torres-Roman D., Shkvarko Y.V.: Experiment Design Regularization-Based Hardware/Software Codesign for Real-Time Enhanced Imaging in Uncertain Remote Sensing Environment, *EURASIP Journal on Advances in Signal Processing*, Vol. 2010, Article ID 254040, pp. 1–21, 2010.
- [16] Castillo-Atoche A., Torres-Roman D., and Shkvarko Y.V., “Towards Real Time Implementation of Reconstructive Signal Processing Algorithms Using Systolic Array Coprocessors”, *Journal of Systems Architecture*, Vol. 56 (2010), pp. 327–339, 2010.
- [17] Shkvarko Y.V., Tuxpan J., and Santos S.R., “Dynamic Experiment Design Regularization Approach to Adaptive Imaging with Array Radar/SAR Systems”, *Sensors*, Vol. 2011, No. 11, pp. 4483-4511, 2011.
- [18] Shkvarko Y.V., Santos S.R., and Tuxpan J., “Resolution Enhanced Radar/SAR Imaging: An Experiment Design Framework Combined With Neural Network-Adapted Variational Analysis Regularization”, *EURASIP Journal of Advances in Signal Processing*, Vol. 2011, In press, pp. 1-16, 2011.
- [19] Shkvarko Y., Tuxpan J., and Castro D., “Bayesian Dynamic Experiment Design Regularization Framework for High-Resolution Radar/SAR Imaging”, International Radar Symposium (IRS’2011), Leipzig, Germany, pp. 359-364, Sept. 2011.
- [20] Shkvarko Y.V., Santos S.R., Tuxpan J., and Espadas V.E., “Modified Hopfield Neural Network Computational Technique for Real-Time Enhancement of Multimode Radar/SAR Imagery”, International Radar Symposium (IRS’2011), Leipzig, Germany, pp. 385-390, Sept. 2011.

Appendix A

C Code for generating the data test binary files with the format as shown in Figure 3.2 (subsection 3.1.)

```
//Program to create a backup of the u datas
#include <stdio.h>
#include <stdlib.h>
#include <conio.h>
#include <ctype.h>
#include <time.h>

#define NumDatos 4802 //Number of data to be stores in the binary file
int DATO[NumDatos];
int u;

//Data structure for writing in the binary file
struct mystruct
{
    short i;
};
struct mystruct s;
FILE *stream;

int main(void)
{
    //Generation of the values ??to write to the binary file
    for (unsigned int i=1; i<=NumDatos-2; i++)
    {
        //Sets the value of 1 in all positions of the vector DATA[i]
        if ((i!=0) || (i!=NumDatos-1))
        {
            DATO[i]=1;
            u=DATO[i];
            printf("DATO[%d]=%d ",i,u);
        }
    }
    //Set the DATO[0] = StarFlag = 241
    DATO[0]=241;
    //Set the DATO[NumDatos-1] = EndFlag = 255
    DATO[NumDatos-1]=255;

    //Creates and opens a binary file for writing
    if ((stream = fopen("Test1_RG1.bin", "w+b"))== NULL)
    {
        fprintf(stderr, "Cannot open input file.\n");
    }
}
```

```

    return 1;
}

//Writes the contents of the DATO[z] vector in the binary file. through
//the s.i structure
for (unsigned int z=0; z<=NumDatos-1; z++)
{
    s.i=DATO[z];
    fwrite(&s,sizeof(s),1, stream);
}
fclose(stream); //Close the binary file
printf("File created, sizeof(s)=%d \n",sizeof(s));
getche();
return 0;
}

```


Appendix B

SP MATLAB code of the test simulations experiment

```
%%%%%%%%%%%%%%%%%%%%%%%%%%%%%%%%%%%%%%%%%%%%%%%%%%%%%%%%%%%%%%%%%%%%%%%%%
%%%%%%%%%%%%%%%%%%%%%%%%%%%%%%%%%%%%%%%%%%%%%%%%%%%%%%%%%%%%%%%%%%%%%%%%%
%%%%%%%%%%%%%%%%%%%%%%%%%%%%%%%%%%%%%%%%%%%%%%%%%%%%%%%%%%%%%%%%%%%%%%%%% Target Localization Protocol %%%%%%%%%%
%%%%%%%%%%%%%%%%%%%%%%%%%%%%%%%%%%%%%%%%%%%%%%%%%%%%%%%%%%%%%%%%%%%%%%%%% Y GeoStar Array - Equidistant %%%%%%%%%%
%%%%%%%%%%%%%%%%%%%%%%%%%%%%%%%%%%%%%%%%%%%%%%%%%%%%%%%%%%%%%%%%%%%%%%%%% CINVESTAV, Guadalajara, Mexico %%%%%%%%%%
%%%%%%%%%%%%%%%%%%%%%%%%%%%%%%%%%%%%%%%%%%%%%%%%%%%%%%%%%%%%%%%%%%%%%%%%% PhD Student: Eduardo Espadas Aldana %%%%%%%%%%
%%%%%%%%%%%%%%%%%%%%%%%%%%%%%%%%%%%%%%%%%%%%%%%%%%%%%%%%%%%%%%%%%%%%%%%%% Thesis Advisor: Dr. Yuriy Shkvarko %%%%%%%%%%
```

```
function tagprotocol3(d_A,h,tags,frec)
%% opening binary file
% fid=fopen('Test1_RG1.bin');
fid=fopen('T1_RG1.bin');
F=fread(fid,'uint16');

PRT_all_I=zeros(1,24);
for mk=2:192:4610
    M_PRTx_I=[];
    for ik=2:8:(2+184)
        M_PRT_I=(F(ik)+F(ik+2)+F(ik+4)+F(ik+6))/4;%%averaging VV_I to HH_I
        M_PRTx_I=[M_PRTx_I,M_PRT_I];
    end
    PRT_all_I=PRT_all_I+M_PRTx_I;
end
PRT_all_I=(1/25)*PRT_all_I;
%% averaging of cross-polarization modes//Quadrature

PRT_all_Q=zeros(1,24);
for mkk=3:192:4611
    M_PRTx_Q=[];
    for ikk=mkk:8:(mkk+184)
        M_PRT_Q=(F(ikk)+F(ikk+2)+F(ikk+4)+F(ikk+6))/4;%%averaging VV_I to HH_I
        M_PRTx_Q=[M_PRTx_Q,M_PRT_Q];
    end
    PRT_all_Q=PRT_all_Q+M_PRTx_Q;
end
PRT_all_Q=(1/25)*PRT_all_Q;
%% Real part Corr matrix formation
Re_Y=((PRT_all_I')*PRT_all_I+(PRT_all_Q')*PRT_all_Q);
%% Imaginary part Corr matrix formation
Im_Y=((PRT_all_Q')*PRT_all_I+(PRT_all_I')*PRT_all_Q);
%% start variables
```

```

% d=> 1= 4mm, 2 = 8.5mm, 3 = 12.25mm
if tags==1
    N_TAGS=1; %protocol for 1 tag
    TAGS=[0 0]; % TAGS POSITIONS
    title_psf='PSF for one tag in origin';
    title_map='Scene image, 1 tag';
else
    N_TAGS=5; %protocol for 5 tags
    TAGS=[0,0,4.5,6,9,12,4.5,-6,-4.5,12]; %test tags positions
    title_psf='PSF for 5 tags';
    title_map='Scene image, 5 tags';
end

if d_A==1
    d=0.4;
    title_d='d_{A(\lambda)}=4mm'; %Intersensor distances
elseif d_A==2
    d=0.85;
    title_d='d_{A(\lambda)}=8.5mm';
elseif d_A==3
    d=1.225;
    title_d='d_{A(\lambda)}=12.25mm';
else
    d=1.8*((3e8/35e9)*100);
    title_d='d_{A(\lambda)}=1.8 \lambda';
end

if freq==1
    f=24.5e9; %frequency in GHz
    lambda_uv=(3e8/f)*100;%lambda in cm
    title_freq='Frequency Operation 24.5 GHz';
else
    f=35e9; %frequency in GHz
    lambda_uv=(3e8/f)*100;%lambda in cm
    title_freq='Frequency Operation 35 GHz';
end

% f_antenna=35e9;
% c=3e8; %speed of light
% lambda=(c/f_antenna)*100;%lambda in cm
delta=.0045;
tetha_x=-.5:delta:.5;
tetha_y=-.5:delta:.5;
% d=(lambda*1.8);
N=length(tetha_x);
trheshold_main_lobe=.75;

```

```

threshold_second_lobe=.25;
beta=(pi/3);
gamma=(pi/6);
x=h*tan(beta);
delta2=(2*x)/N;
X=linspace(-x,x,N);
Y=X;
ax_x=-111:111; %axis
ax_y=ax_x;
M=8; %(3 Arms, 8 elements in each Arm)

%% antenna configuration %%
%%%%%%%%%%%%%%%%%%%%%%%%%%%%%%%%%%%%%%%%%%%%%%%%%%%%%%%%%%%%%%%%%%%%%%%%Antenna Position - axis X %%%%%%%%%%%%%%
Ro_x_l=[];
for p=-(M-1):0
    Ro_x_l=[ Ro_x_l, d*p*cos(gamma)];
end
Ro_x_d=[];
for p=1:(M)
    Ro_x_d=[ Ro_x_d, d*p*cos(gamma)];
end
Ro_x=[Ro_x_l Ro_x_d];
Mx=length(Ro_x);
Ro_xx=zeros(1,M);
%%%%%%%%%%%%%%%%%%%%%%%%%%%%%%%%%%%%%%%%%%%%%%%%%%%%%%%%%%%%%%%%%%%%%%%%Antenna Position - axis Y %%%%%%%%%%%%%%
Ro_y_d=[];
for p=(M-1):-1:1
    Ro_y_d=[ Ro_y_d, d + d*p*sin(gamma)];
end
Ro_y_d=[Ro_y_d d];

Ro_y_d1=[];
for p=1:(M)
    Ro_y_d1=[ Ro_y_d1, d*p*sin(gamma)];
end
Ro_y_u=[];
for p=-(M-1):0
    Ro_y_u=[ Ro_y_u, d*p];
end
%%%%%%%%%%%%%%%%%%%%%%%%%%%%%%%%%%%%%%%%%%%%%%%%%%%%%%%%%%%%%%%%%%%%%%%%
%%%%%%%%%%%%%%%%%%%%%%%%%%%%%%%%%%%%%%%%%%%%%%%%%%%%%%%%%%%%%%%%%%%%%%%%
Ro_y=[Ro_y_d Ro_y_d1(1) Ro_y_u];
%%%%%%%%%%%%%%%%%%%%%%%%%%%%%%%%%%%%%%%%%%%%%%%%%%%%%%%%%%%%%%%%%%%%%%%%
%%%%%%%%%%%%%%%%%%%%%%%%%%%%%%%%%%%%%%%%%%%%%%%%%%%%%%%%%%%%%%%%%%%%%%%%

```

```

Ro_x_all=[Ro_xx Ro_x_l Ro_x_d];
Ro_y_all=[Ro_y_u Ro_y_d Ro_y_d1];
My=length(Ro_y_all);
%% figure antenna layout %%
% figure(1)
% plot(Ro_x_all,Ro_y_all,'O','markerfacecolor','k')
% grid on;
% for i=1:length(Ro_x_all);
%     text(Ro_x_all(i)+.1, Ro_y_all(i)-.1,num2str(i));
% end
% title({'MIR-Y Antenna Array','Intersensor distance = 0.5 \lambda'});
% xlabel('x-position (cm)');
% % ylabel('10 log_{10} (|X(\omega)|^2)'); EJEMPLO
% ylabel('y-position (cm)');
%%%%%%%%%%%%%%%%%%%%%%%%%%%%%%%%%%%%%%%%%%%%%%%%%%%%%%%%%%%%%%%%%%%%%%%%
%%%%%%%%%%%%%%%%%%%%%%%%%%%%%%%%%%%%%%%%%%%%%%%%%%%%%%%%%%%%%%%%%%%%%%%%
%% %%%%%%%%%% DIRECTIONAL
MASK %%%%%%%%%%
%%%%%%%%%%%%%%%%%%%%%%%%%%%%%%%%%%%%%%%%%%%%%%%%%%%%%%%%%%%%%%%%%%%%%%%%
%%%%%%%%%%%%%%%%%%%%%%%%%%%%%%%%%%%%%%%%%%%%%%%%%%%%%%%%%%%%%%%%%%%%%%%%

%a=1.802; %% 120° directional aperture
a=3.591; %% 60° directional aperture
% a=4.79; %% 45° directional aperture
for q=1:N
    for q2=1:N
        R = sqrt((tetha_x(q))^2 + (tetha_y(q2))^2);
        y(q,q2) = sin(a*R)/(a*R);
    end
end
max_y=max(max(y));
y=y/max_y;
y2=zeros(N,N);
for q=1:N
    for q2=1:N
        y2(q,q2)=(abs(y(q,q2)))^2;
    end
end
max_y2=max(max(y2));
y2=y2/max_y2;
% figure(1)
% mesh(X,Y,y2)
% % axis('tight');
%%%%%%%%%%%%%%%%%%%%%%%%%%%%%%%%%%%%%%%%%%%%%%%%%%%%%%%%%%%%%%%%%%%%%%%%

```

```

%% %%%%%%%%%%
%
%% %%%%%%%%%% GeoSTAR CONFIGURATION %%%%%%%%%%
% %%%%%%%%%% X_Y direction %%%%%%%%%%
psi=zeros(N,N);
% P1=(ones(24)); %with ceros (no samples of sensors-same arms)
% P1(1:8,1:8)=0;
% P1(9:16,9:16)=0;
% P1(17:24,17:24)=0;
P1=Re_Y+1i*Im_Y;
% vec=ones(1,24); %all samples
% vec(1)=0;
% P1=toeplitz(vec);

for q=1:N
    for q2=1:N
        var_ii=[];
        var1_ii=[];
        for p=1:24
            arg_ii=(-2*pi)/lambda_uv*((Ro_x_all(p)*tetha_y(q2)) + (Ro_y_all(p)*tetha_x(q)));
            var_ii=[var_ii, exp(1i*arg_ii)];
            arg1_ii=((2*pi)/lambda_uv*((Ro_x_all(p)*tetha_y(q2)) + (Ro_y_all(p)*tetha_x(q)));
            var1_ii=[var1_ii, exp(1i*arg1_ii)];
        end
        psi(q,q2)=abs(var_ii*P1*var1_ii)*y2(q,q2);
    end
end
max_psi=max(max(psi));
psi=psi/max_psi;

fig2=figure(2);
mesh(X,Y,psi);
title({'Point Spread Function';title_freq;title_d},'fontsize',12);
axis('tight');
xlabel('x-position (m)','fontsize',12,'fontweight','bold');
ylabel('y-position (m)','fontsize',12,'fontweight','bold');
grid on

%% %%%%%%%%%%CONVOLUTION%%%%%%%%%
%here is generated scene image
%% %%%%%%%%%%
A=zeros(N,N);
psi_tag=zeros(N,N);
psi_temp=zeros(N,N);

for j=1:N_TAGS

```

```

x_i=TAGS(1,2*j);
y_i=TAGS(1,(2*j)-1);

for u=1:N
    xx = abs(X(u)-x_i);
    yy = abs(Y(u)-y_i);
    if (xx <= (delta2/2))
        pos_x =u;
    end
    if (yy <= (delta2/2))
        pos_y =u;
    end
end
A(pos_x,pos_y)=1;
psi_temp=conv2(psi,A,'same');
psi_tag= psi_tag + psi_temp;
A=zeros(N,N);
psi_temp=zeros(N,N);
end
max_psitag=max(max(psi_tag));
psi_tag= psi_tag/max_psitag;

figure(3)
mesh(X,Y,psi_tag);
axis('tight');
title({title_psf;title_freq;title_d;sprintf('For a range gate=%3.0f meters',h)},'fontsize',12);
xlabel('x-position (m)','fontsize',12,'fontweight','bold');
ylabel('y-position (m)','fontsize',12,'fontweight','bold');
grid on
figure(4)
contourf(X,Y,psi_tag);
axis('tight');
xlabel('x-position (m)','fontsize',12,'fontweight','bold');
ylabel('y-position (m)','fontsize',12,'fontweight','bold');
title({title_map;title_freq;title_d;sprintf('For a range gate=%3.0f meters',h)},'fontsize',12);

end

```